ROMA TRE
UNIVERSITÀ DEGLI STUDI

Scuola Dottorale in Scienze della Materia,
Nanotecnologie e Sistemi Complessi

XXXI Ciclo di Dottorato

Multiparameter Analysis of Genesis and Evolution of Secondary Electrons produced in the Low Energy Regime

---

Alessandra Bellissimo, *Dottoranda* _____

Prof. Giovanni Stefani, *Docente Guida* _____

Prof. Fabio Bruni, *Coordinatore* _____

Dedicated to those
who have contributed to the construction of
my conciousness, heart and soul
and to all those
who are well aware of bringing these subsystems of my being
to a manifold of excited states
by strong interaction.
Indelibly.

TABLE OF CONTENTS

ACKNOWLEDGEMENTS

I can cope with formalisms, but I tend to dislike formalities. Some circumstances in life happen to coincide with such extraordinary events and encounters that one should not constrain himself by a bland formality perhaps missing the chance to meet that coincidence. But before I start to diverge towards even more further fields, I stop right here and go back to the beginning to the point why I mentioned "formalisms" and "formalities" in the first place. Well, some formalisms (those I claim to be able to cope with) are entailed in the following pages, whereas concerning formalities I would like to stress out that it's actually not because of those that I direct my first thanking words to the person I will mention right away, to the person whom I am profoundly thankful for the constant support and who has enriched my perspectives in many ways. To my Professor Gianni Stefani, I would like to express my deep gratitude for having guided me through this adventurous and exciting path leading me eventually to this node in the space-time continuum, which to me undoubtedly represents one of most desired and relevant ambitions in my existence. Cherishing all the moments spent together: in the lab, either performing experiments or brewing the traditional 10 'o clock coffee, while discussing on life and Physics, I thank you for having helped me to grow both scientifically and humanly!

A very special gratitude goes to all members of my research group, with a special mention to Alessandro Ruocco, Stefano Iacobucci, Francesco Offi, Adriano Verna with whom I have had the pleasure to share in work and friendship these past three years, not forgetting the by-now ex-LASEC dream team trio: Marco Sbroscia, Gian Marco Pierantozzi and Valerio Serpente. Thank you all for all for your encouragement, for the collegiality and the fun!

Furthermore, I consider myself very lucky to have had the great opportunity to conduct my PhD work embedded in the framework of an EU Marie Curie ITN project, namely of SIMDALEE2 (grant number 606988) which has not only provided me with financial support, but foremost it has given me the unique chance to interact with so many scientific fields and perspectives widening my horizon in many ways, and not only by travelling. And first of all, I am grateful to this project because I have had the immense pleasure to meet so many wonderful and interesting colleagues, whom I foremost consider friends by now. I cannot name all of them, but I deeply appreciate each moment that we have all spent together and I tell you: it's definitively not over! Nonetheless, I would like to single out one particular and special person, Prof. Wolfgang Werner, the one who has encouraged me since the very beginning to pursue my motto with gumption and passion (*"In dreams begin responsibilities"*) and with whom I share a unique friendship since many years.

A very special thanks goes also to Dr. Mauro Taborelli with whom I have had the opportunity not only to collaborate scientifically, but to grow in friendship; I also name some of the members in his group, who have contributed to both fruitful science and delightful conversations: Holger Neupert and Paolo Chiggiato.

I send out to the Universe a note entailing my innermost thoughts and feelings, non-perceivable by beings still walking on the upper part of the meadow, to my forever loving, encouraging and always enthusiastic father Umberto, whom I also would like to thank for unconsciously predicting so many things for me; you my personal oracle. (Papi mi manchi!)

And now I come to those two, whom I unconditionally love, fondly:

my caring and loving Mutti, Helga Adele and my beloved step-father Maurizio, the ones whose constant love, support and encouragement have given me the instruments and the motivation to become what I am now today! Thank you all, once more, for accompanying me along this fundamental path of my existence.

Alessandra

ABSTRACT

More than a century after the discovery of the electron, there are still fundamental, yet unresolved, questions concerning the generation-ejection mechanism of the ubiquitous Secondary Electrons (SEs) from a solid surface. Secondary Electron Emission (SEE) plays an important role in a broad range of technological applications and scientific cases. In particular, interaction, generation and ejection mechanisms of these Low-Energy Electrons (LEEs with kinetic energies $\leq 50\,\mathrm{eV}$) from solid surfaces has become increasingly important.

This thesis focusses on electron-induced electron-emission and reports on the dissection of such a tangled process operated by the help of spectroscopic tools of increasing finesse; measuring differential cross sections with an increasing degree of differentiation. To this end, the interaction of LEEs with various targets such as Carbon allotropes, Aluminium and Copper surfaces exhibiting different long-range order, has been investigated by means of measurements of the Total Electron Yield (TEY), single-electron and electron pair spectroscopy.

Measuring the TEY of a material is needed to obtain a quantitative answer to *how many* electrons are effectively scattered and/or generated when one incoming electron approaches the surface of a solid. In the LE-regime, it has been shown that the TEY-response of a material is constituted by the interplay of reflectivity and emissivity of the target, both dictated by the target band structure.

Spectroscopic techniques based on measurements differential in energy and angle of the electrons emitted from the surface, such as angled-resolved Reflection Electron Energy Loss and Secondary Electron Emission Spectroscopy (REELS and SEES) were employed to obtain a doubly-differential information on the scattering of electrons in solids in dependence of these two parameters.

In (e,2e)-coincidence spectroscopy detection of correlated electron pairs enables to disentangle the main scattering mechanisms relevant to SEE by discriminating among the possible excitation channels. This type of *"one electron in–two electrons out"*–measurement represents the most effective way to decompose the SE-cascade into its constituents, because only those SEs, that are ejected in coincidence with a specifically chosen energy loss channel under a selected scattering kinematics of the primary electron, are detected. In particular, measurements of these correlated electron pairs has made possible to pinpoint the fundamental role of both initial and final states of the ionising event.

Carbon allotropes were chosen as targets since they are important in technological applications where both minimisation and maximisation of the SE-yield is a relevant issue. Characteristic excitation channels of the collective modes, i.e. plasmons, are known to play a substantial role in the generation and ejection process of low-energy SEs, reason for which the nearly-free electron (NFE) metal Aluminium was chosen since for this target they are known to represent the dominant inelastic scattering mechanism. Different crystalline faces of Copper were employed to gain further insight on the relevance of the electronic structure for the SEE-mechanism.

This comprehensive investigation has led to the disentanglement of the elementary processes that need to be accounted for the understanding of the SE-generation probability, that fully take into account both energy and momentum conservation in the collision and the band structure of the solid. The gathered results demonstrate that single ionising scattering events, assisted by collective excitations, constitute one of the fundamental ingredients leading to SE-emission.

RIASSUNTO

Più di un secolo dopo la scoperta dell'elettrone, esistono ancora domande fondamentali ed irrisolte, riguardanti il meccanismo di generazione-espulsione degli onnipresenti elettroni secondari (SEs) da una superficie di un solido. L'emissione di elettroni secondari (SEE) svolge un ruolo importante in una vasta gamma di applicazioni tecnologiche e casi scientifici. In particolar modo, i meccanismi di interazione, generazione ed emissione di questi elettroni a bassa energia (LEEs con energie cinetiche $\leq 50\,\mathrm{eV}$) da superfici hanno acquisito sempre più importanza. Questa tesi è focalizzata sull'emissione di elettroni indotta da elettroni incidenti e riporta sulla dissezione di tale aggrovigliato processo studiato con l'aiuto di strumenti spettroscopici di crescente finezza; misuranti sezioni d'urto differenziali con un crescente grado di differenziazione. A tal fine, è stata studiata l'interazione di LEEs con vari bersagli come allotropi di carbonio, superfici di alluminio e rame esibenti diversi ordini a lungo raggio, mediante misure di spettroscopia a singlola particella e a coppia di elettroni come anche misure di resa totale di elettroni (TEY).

Misurare il TEY di un materiale è necessario per ottenere una risposta quantitativa a *quanti* elettroni vengono effettivamente emessi e/o generati quando un elettrone incidente si avvicina alla superficie di un solido. Nel regime a bassa energia (LE), è stato dimostrato che la risposta TEY di un materiale è costituita dall'interazione di riflettività ed emissività del bersaglio, entrambe dettate dalla struttura a banda del solido. Tecniche spettroscopiche basate su misurazioni differenziali in energia ed in angolo degli elettroni emessi dalla superficie, come la perdita di energia di elettroni in riflessione risolta in angolo e la spettroscopia di emissione di elettroni secondari (REELS e SEES) sono state impiegate per ottenere informazioni doppiamente differenziali sulla interazione di elettroni nel solido in dipendenza di questi due parametri. Nella spettroscopia in coincidenza (e,2e) il rilevamento di coppie di elettroni correlate consente di districare i principali meccanismi di collisione rilevanti per SEE, discriminando tra i possibili canali di eccitazione. Questo tipo di misurazione – basato sul principio di *"one electron in–two electrons out"* – rappresenta il modo più efficace per scomporre la cascata di secondari nei suoi costituenti, perché solo quei secondari, che vengono espulsi in coincidenza ad uno specifico canale di perdita, selezionato da una cinematica di collisione dell'elettrone primario, viene rilevato. In particolare, misurando queste coppie di elettroni correlate permette di individuare il ruolo fondamentale degli stati iniziale e finale dell'evento ionizzante.

Gli allotropi di carbonio sono stati scelti come bersagli poiché sono importanti nelle applicazioni tecnologiche in cui sia la minimizzazione che la massimizzazione della resa di SEs rappresentano un problema rilevante. I canali caratteristici di eccitazione rappresentati da modi collettivi, vale a dire i plasmoni, sono noti per svolgere un ruolo sostanziale nel processo di generazione ed emissione di SEs a bassa energia, motivo per cui è stato scelto l'alluminio – un metallo ad elettroni quasi-liberi (NFE) – poiché in questo bersaglio i plasmoni sono noti per rappresentare il meccanismo di diffusione anelastica dominante. Sono state impiegate diverse facce cristalline del rame per ottenere ulteriori informazioni sulla rilevanza della struttura elettronica nel meccanismo di SEE.

Questa esauriente indagine ha permesso di individuare i processi elementari che devono essere considerati per la comprensione della probabilità di generazione dei SEs, che tiene pienamente conto sia della conservazione dell'energia che del momento durante la collisione, sia della struttura a banda del solido. I risultati raccolti dimostrano che singoli eventi di diffusione ionizzante, assistiti da eccitazioni collettive, costituiscono uno degli ingredienti fondamentali che portano all'emissione SEs.

ZUSAMMENFASSUNG

Mehr als ein Jahrhundert nach der Entdeckung des Elektrons gibt es immer noch grundlegende, aber noch ungelöste Fragen bzgl. des Generierungs- und Auswurf-mechanismus der allgegenwärtigen Sekundärelektronen (SEs) aus der Oberfläche eines Festkörpers. Die Sekundärelektronenemission (SEE) spielt eine wichtige Rolle in einem breiten Spektrum technologischer Anwendungen und wissenschaftlicher Fällen . Insbesondere die Wechselwirkungs-, Erzeugungs- und Ausstoßmechanismen dieser niederenergetischen Elektronen (LEEs mit kinetischer Energie $\leq 50\,\mathrm{eV}$) von festen Oberflächen sind zunehmend wichtiger geworden.

Diese Dissertation konzentriert sich auf die elektroneninduzierte Elektronenemission und berichtet über die Dissektion eines solchen verwickelten Prozesses, durchgeführt mit Hilfe von spektroskopischen Werkzeugen von steigernder Finesse, die einem Zugang verschaffen zu der Messung von differentiellen Wirkungsquerschnitten mit zunehmender Differenzierungsgrad. Zu diesem Zwecke, die Wechselwirkung von LEEs mit verschiedenen Proben, wie Allotropen des Kohlenstoffs, Aluminium- und Kupfer-oberflächen unterschiedlicher Fernordnung wurde untersucht mit hilfe von Messungen der Gesamtelektronenausbeute (TEY), der Einzelelektronen- und Elektronenpaar-Spektroskopie.

Das Messen des TEYs eines Materials ist erforderlich, um eine quantitative Antwort auf die Frage *wie viele* Elektronen effektiv gestreut und/oder erzeugt werden, wenn sich ein eintreffendes Elektron der Oberfläche eines Festkörpers nähert, zu erhalten. Im Niederenergetischem Bereich es wurde gezeigt, daß sich die Gesamtelektronenausbeute eines Materials aus einem Zusammenspiel von Reflektivität und Emission des Materials zusammensetzt, welche beide von der Bandstruktur des Materials bestimmt werden. Spektroskopische Verfahren, die auf Messungen der Energie und des Winkels der von der Oberfläche emittierten Elektronen basieren, wie etwa in Winkel aufgelöster Reflektionselektronen Energieverlust Spektroskopie und Sekundärelektronenemissionsspektroskopie (REELS und SEES), wurden verwendet, um eine doppelt differentielle Information über die Streuung von Elektronen zu erhalten in Festkörpern in Abhängigkeit von diesen beiden Parametern. (e,2e)-Koinzidenzspektroskopie ermöglicht die Detektion korrelierter Elektronenpaare, durch welche die für den SEE relevanten Streumechanismen identifiziert werden können, die direkt in Verbindung mit gezielt-selektierten Anregungskanälen gebracht werden können.

Diese Art von Messung *"ein Elektron in–zwei Elektronen aus"* stellt die effektivste Methode dar, um die SE-Kaskade in ihre Bestandteile zu zerlegen, da nur jene SEs detektiert werden, die in Koinzidenz mit einem bestimmten ausgewählten Energieverlustkanal, unter einer ausgewählten Streukinematik des Primärelektrons, emittiert werden. Insbesondere, Messungen dieser korrelierten Elektronenpaare haben es ermöglicht, die grundlegende Rolle sowohl des Anfangszustands als auch des Endzustands des Ionisierungsereignisses zu bestimmen und betonen.

Allotrope des Kohlenstoffs wurden als geeignete Proben ausgewählt, da sie in technologischen Anwendungen wichtig sind, bei denen sowohl die Minimierung als auch die Maximierung der SE-Ausbeute ein relevantes Thema sind. Charakteristische Anregungskanäle der Kollektivmoden, dh. Plasmonen, spielen bekanntermaßen eine wesentliche Rolle bei der Erzeugung und dem Auswurf von niederenergetischen SEs, weshalb Aluminium, ein Metall mit nahezu freien Elektronen (NFE), für diese Untersuchungen gewählt wurde, da in diesem Material, Plasmonen repräsentieren bekanntlich den dominanten inelastischen Streuungsmechanismus. Verschiedene kristalline Oberflächen von Kupfer wurden eingesetzt, um weitere Informationen zur Relevanz der elektronischen Struktur für den SEE-Mechanismus zu erhalten.

Diese umfassende Untersuchung hat zur Entflechtung der elementaren Prozesse geführt,

die für das Verständnis der SE-Erzeugungswahrscheinlichkeit berücksichtigt werden müssen, wobei sowohl die Energie- als auch die Impulserhaltung in einer Kollision und die Bandstruktur des Festkörpers vollständig berücksichtigt werden. Die gesammelten Ergebnisse zeigen, daß einzelne ionisierende Streuereignisse, die durch kollektive Anregungen unterstützt werden, einen wesentlichen Bestandteil für die SE-Emission darstellen.

CHAPTER 1

Introduction and Motivation

Even though the scientific community is aware of the existence of electrons since over a hundred years [1, 2, 3, 4] and extensive investigation of these elementary particles has been ongoing since their discovery [5, 6, 7, 8, 9, 10, 11, 12, 13], there are important facets concerning their interaction with matter that still need to be fully clarified. Since that time, several theories – ranging from simple empirical treatments to highly complex quantum mechanical approaches – have been formulated and a plenitude of experimental evidence has been gathered on their behalf.

Nowadays, one particular area of interest in Science concerns electrons that have kinetic energies of about 50 electronvolts (eV) or less. In fact, these Low-Energy Electrons (LEEs) are found to play a significant role in a broad variety of scientific cases and technological applications. Generation of these LEEs is typically induced whenever charged particles and radiation interact with matter. In such cases one refers to these electrons as "secondary" electrons, since they arise as a consequence of a precedent (primary) collision. For example, one fundamental and seemingly trivial question concerns the number of Secondary Electrons (SEs) that would be ejected from and in vicinity of a solid surface, when this latter is exposed to the impact of a single (primary) electron with a given kinetic energy. Per definition, the number of these secondary electrons generated per incident primary is represented by the Secondary Electron Yield (SEY). Despite the numerous investigations pursued on this physical quantity, a definite answer to this question still needs to be given.

Electrons with energies of a few electronvolts sample only a few atomic layers, hence their interaction with the target is limited to the surface-vacuum interface. Low-Energy Secondary Electrons (LE-SEs) with kinetic energies ranging between $\sim$0 eV and $\sim$10 eV (wrt. vacuum level) can be generated as a consequence of a large number of excitation channels. As the probing electrons approach or exit from the surface, they interact with the vibrational modes of the solid (crystal) surface, or possibly with further elementary excitations localised within this latter. The energy distribution of back-reflected and ejected electrons represents a rich source of information of the dynamical properties, along with selection rules, offering insight into its basic structural features. Even though these excitation channels are qualitatively known and are routinely studied

by means of different electron spectroscopic techniques, a quantitative understanding on the elementary generation mechanisms for SEs is still lacking.

LEEs have a non-negligible influence even on scientific fields where usually it is assumed that only high-energy Physics does play a role. Thinking of the processes that govern chemistry in space, immediate connection to High-Energy (HE) radiation, such as X-rays or gamma rays and high-energetic ions, is generally made. When this HE-radiation strikes atoms and molecules, the knock-out of HE-electrons is induced, these in turn can again interact with matter, thus leading to the generation of low-energy secondary electrons (LE-SEs) . It has been shown [14], that it is these LE-SEs, generated by the interaction of HE-radiation with matter, that seem to play the central role when it comes to forming bonds and making compounds being the precursors to complex organic molecules. Again, it is the low-energy electrons created in biological tissue under the influence of UV-light irradiation, that cause damage leading to bond-breaking of DNA and consequently to possible tumor formation. Dissociation of these DNA-bonds can be already provoked by electrons having an energy of the order of $\leq$1 eV [15, 16, 17]. On the other hand, by exploiting this knowledge, attempts of using low-energy electrons for theurapetic purposes are being investigated [18, 14].

An extensive number of technologies is based on the generation of SEs. Materials used in technological devices need to be meticulously selected in order to achieve the desired performance. In some cases, the choice of a material is based on an intended enhancement of the SEY, e.g. in particle detectors, where the surfaces of electron multipliers and for cathodes in electron sources are treated in such a way as to optimise the secondary emission characteristics [19, 20]

Materials with high SEY are also of interest for potential use in novel transmission dynodes for Photo Multipliers Tubes (PMTs) [21]. Other applications require the employement of materials capable of suppressing the phenomenon of Secondary Electron Emission (SEE) [22]. For example, low-emission materials are sought for coating the grids and the tube walls in the electron optical elements used for the electron transport in surface analysis instrumentation – a typical example is given by Hemispherical Mirror Analysers (HMA). Generally, the walls of the electrodes and the hemispheres are coated with an acqueous solution based on graphitic materials (known to have low-emitting properties).

Despite their low kinetic energies, these electrons dramatically affect the operation of high-energy physics facilities [23], e.g. in the Large Hadron Collider (LHC) at CERN. In the vacuum chambers of these charged particle storage rings, the so-called *"electron cloud"* (EC) formation [24, 25] can lead to a deterioration of the proton beam and to a possible beam-dump during an experiment. For this reason, at CERN (and not only) a big effort has been made in the last decades [26, 27, 28, 29, 30] to develop surface coatings made of low-emitting materials to prevent and limit the formation of this amplified cascade of SEs, also known as the phenomenon of multipackting. Thorough investigation on the partial electron yield of the secondaries (SEY) is routinely performed to study various materials at different stages of cleanliness and also in presence of a variety of adsorbates. Furthermore, attempts to perform *in-situ* studies (e.g.

in an accelerator or in a synchrotron environment) of the SEY are being made to investigate the phenomenon of multipackting leading to the growth of the EC [31]. Besides, measuring the SEY represents nowadays a crucial mean of diagnostics to probe the quality of technical surfaces in many fields of technology. At this point it shall be noted that, in most of these studies the employed instrumentation actually allows one to access to a Total Electron Yield (TEY) measurement rather than to the measurement of a (partial) SEY. This is the reason why throughout this thesis work it was purposely chosen to refer to this electron yield as TEY instead of SEY.

SEs are exploited in the Secondary Electron Microscope (SEM) for the visualisation of sub-micron patterns [7, 32, 33], where these LE-SEs are, among others, responsible for the image contrast. On the other hand, the creation of these very same SEs becomes troublesome in the patterning process itself. For instance, in Electron Beam Lithography (EBL) the attainable lateral resolution can be compromised due to the so-called *"proximity effect"* caused by the random diffusion of *"hot electrons"*[1] within the photo-resist. This problem is also encountered in the patterning technique of Focussed Electron Beam Induced Deposition (FEBID) [34], which is a single-step, direct-write nano-fabrication technique capable of writing three-dimensional metallic-based structures at the nano-scale on surfaces by exploiting electron-induced reactions of organometallic precursors. Currently FEBID is limited in resolution mainly due to unwanted depositions outside the area of the Primary Electron (PE) beam. This limitation is caused by reactions of the precursor molecules with low-energy SEs (<100 eV). These LE-SEs are abundantly generated, both within the area and in the proximate surroundings of the PE-beam, by the interaction of PEs itself with the substrate causing incomplete ligand dissociations from FEBID precursors. For this reason, it is of great interest to understand how these fragmentation processes, initiated by the low energetic SEs can lead to different types of "dissociative" reactions, e.g. dissociative electron attachment, dissociative ionisation, neutral and dipolar dissociation.

The surface charging of spacecraft materials, induced by cosmic radiation, may also limit their perfomance and lifetime and therefore it represents on of the major issues for earth-orbiting spacecrafts [35, 36, 37, 38]. The first investigations dealing with these phenomena were primarily focussed on the sole surface effects and were therefore linked mostly to the external design issues of a spacecraft. However, nowadays it is known that a significant portion of spacecraft anomalies are also caused by the internal charging of the employed materials introduced by penetrating electrons and related reaction processes (buried and deep dielectric charging).

LE-SEs, as well as hot-electrons, can constitute a big nuisance that needs to cautersised, affecting the functioning of semiconductor devices (e.g. transistors) [39] and insulators [40, 41] in electronic systems, but at the same time their existence is exploited in photovoltaic devices [42]. On the one hand, degradation of semiconducting materials can be induced, among others, by the so-called Secondary Generated Hot Electron (SGHE) injection. This effect is due to the generation

[1] These are LEEs with kinetic energies above the Fermi level of a material, however not sufficiently high to overcome the surface barrier and to escape above vacuum level, thus remaining trapped inside the material. Their accumulated energy is generally transferred to the material in form of heat dissipation.

of hot carriers from impact ionisation involving a secondary electron that was likewise created by an earlier collision event (e.g. a hot electron). This phenomenon, among others, is known to produce one of the worst device degradations [43]. On the other hand, exploitation of the very same hot electrons can be used to minimise unwanted losses of current. For example, in solar cells the current production is limited by the fact that when the photon energy is inferior to the semiconductor energy band-gap this photon gets lost before being collected, thus it will not contribute to the current consequently limiting the cell performance. Hot carrier solar cells, instead, could avoid these losses, by bridging this gap with hot electrons [44, 45]. It is well-known by now that, electron bombardment of an insulator leads to a high SEY/TEY electron, resulting from an increase of the escape-depth of these SEs. However, there are still difficulties in the exact modelling of these effects, since although the free-electron scattering theory is applicable to the high-energy PEs, it cannot be applied to the escaping LE-SEs because of the large energy gap in insulators [40].

Surface properties of a material are intrinsically connected to their characteristics at microscopic scale and are determined from their electronic structure, therefore it is of fundamental interest and technological significance to deepen the study of the interaction between matter and charged particles, where electron-induced SEE represents a most prominent phenomenon. For all above-mentioned scientific cases and technological applications a purposely tuning of the surface properties of a material aiming at gaining control on the SEE-process represents a highly desirable scientific goal. To this end, detailed understanding concerning the elementary generation-ejection mechanism of LEEs is mandatory.

1.1 Fundamentals of Electron-Solid Interaction & the Electron Spectrum from Solids

Generally, the irradiation of a solid surface by a charged particle (electrons, ions, protons) beam results in the emission of secondary electrons[2]. In this work, only electron bombardment of solid surfaces is contemplated. Electrons are a convenient probe to be used for the investigation of surfaces, since they are easy to generate, handle and detect [46, 47, 48]. They can be easily focussed and their energy is tunable by electric fields. When a solid surface is exposed to a beam of electrons, further electrons are released from the irradiated target yielding a characteristic energy distribution – commonly known as *electron spectrum*. An analytical technique exploiting electrons both as probing and scattered particles is Electron Energy Loss Spectroscopy (EELS) [11, 49, 50]. The electrons detected in such a spectrum are conventionally subdivided into three main groups of the so-called backscattered, inelastically scattered and secondary electrons. Their energy and angle of impact (which in turn allow to determine the electron momentum) can be analysed using electrostatic fields. The process of both energy and momentum transfer occurring when the electron strikes a surface is of fundamental importance for the understanding and the proper interpretation of the measured electron spectrum. Moreover, when the electron source energies are comprised within the LE-range ($\leq 50\,\mathrm{eV}$), the probing electrons have sufficient momentum to explore vast regions in the Brillouin zone of a material, thus making LEEs additionally advantageous for surface analysis.

Back-Scattered Electrons (BSEs) are those which are either elastically reflected or re-diffused out of the solid interaction volume in the course of an elastic collision with the ionic subsystem of the specimen. This type of interaction, leading to a net change in direction, is defined as *elastic scattering* and is linked to the interaction of the incident electron with the (screened) Coulomb potential of the atomic nuclei. Due to the large mass difference of the scattering partners involved, the electron gets deflected during its interaction and only a negligibly small amount of energy is lost by the the elastically scattered electron. Trajectory deviation from its original direction can vary between 0–180°. The recoil energy – the energy associated to this elastically scattered electron – transferred in an elastic collision is of the order of some tens of meV, therefore, per definition, in an elastic event the kinetic energy of the electron remains unchanged, i.e. $\mathrm{E}_s \cong \mathrm{E}_0$, where E_0 is the incoming electron energy, whereas E_s stands for the kinetic energy of the scattered electrons.

The *inelastically scattered* electrons are those which get re-diffused from the target after having transferred part (or all) of their energy (E_0) and momentum ($\vec{k}_0$) to the ensemble of

[2]Also emission of sputtered atoms, ions and molecules can occur, however in this work only electron-induced SE-emission processes are considered.

solid-state electrons. The energy lost by the primary electron (PE) and transferred to the electronic sub-system is generally linked to a small momentum transfer – $\Delta\vec{K} = \vec{k}_0 - \vec{k}_s$. In an inelastic collision, the PE and its scattering partners have similar mass, hence its deflection (involving scattering angles of the order of 0.1° or less when the energy of the PEs are high) from their original trajectory can be neglected (*forward scattering*).

Both energy and momentum of the total system (incident electron and target) are always conserved, thus any energy loss is accompanied by a momentum transfer. Due to this energy deposition and momentum transfer, the electronic subsystem of the target is perturbed, i.e is brought into an excited state and its response to this energy absorption can manifest itself via different excitation channels. The deposited energy can be re-distributed and dissipated away over all sorts of degrees of freedom available in a target. Depending on the primary energy of the incoming electron beam different excitation processes are possible.

For the energy range of interest in this work, the LE-regime ($\leq 100\,\text{eV}$), the most prominent excitation channels involve the valence band of a solid, where the energy loss of the electron is directly linked to an excitation process. In the LE-regime, these include *inter*- and *intra*-band transitions, consisting in the promotion of electrons from the valence to the conduction band or within a same band, respectively. Electrons generated during such an excitation process feel the response of the solid to the sudden appearance of the hole left behind.

Another important excitation channel is given by the collective modes of the electron gas, also known as plasmon oscillations [51, 52, 53]. *Plasmon excitations* are characteristic losses, or eigen-losses, visible in the electron spectrum as sharp distinct features, which stand out in an electron spectrum. This phenomenon is due to the fact that conduction electrons in metals (or valence electrons in semiconductors) are loosely bound to atoms, however coupled to each other by electrostatic forces. When an external perturbation occurs (e.g. an incident electron approaches the target surface), the solid-state electrons undergo a displacement due to Coulomb repulsion – hence a polarisation of the surface takes place – forming a correlation hole, that moves along with the incident electron. This correlation hole is a region exhibiting a net positive charge, which is considered to be of the size of ca. 1 nm [54]. The response of the electron sub-system to this external perturbation is oscillatory, giving rise to regions of charge density fluctuations (alternating positive and negative space charges) along the electron trajectory. As stated by Ferrell and Quinn in Ref. [55] and later also by Egri in Ref. [56] these collective modes can be regarded as a coherent superposition and aggregate oscillation of electron-hole pairs in the valence (or conduction) bands, corresponding to electronic transitions from occupied to unoccupied states. In the second quantisation formalism, these plasmon oscillations are also describable as quasi-particles, known as *"momentum-excitons"* or more commonly known as *"plasmons"*, with an effective mass, m^*_{eff}, and a own momentum, $\vec{k}_{pl}$. Plasmons can be distinguished as (i.) *bulk* or *volume plasmons*, occurring inside a medium of infinite extension, where the polarisation field represents the response to the probing electron or as (ii.) *surface plasmons* linked to the collective

response of solid-state electrons due to the boundary conditions of Maxwell's equations at both sides of the solid-vacuum interface; two media exhibiting different electrical susceptibility and with it different dielectric properties.

In their works, Ferrell, Quinn and Egri showed that both the magnitude of these plasmon losses as well as their sharpness can be described on the basis of a quantum-mechanical treatment for one-electron excitation. Goel *et al.* in Ref. [57] derived an expression for calculating the total number of electrons participating in such a plasmon oscillation for metals. In general, it is assumed that in metallic surfaces, plasmon oscillations are formed by the coherent superposition of *all* valence electrons in the target. However according to their formula, the calculated number of electrons participating to a plasmon wave ranges between 1 (for elements like Ag and Cu) and 5 for Bismuth. In Ref. [58], Egri *et al.* discuss the internal structure of a plasmon and according to their formulation, for the number of electron participating to this collective motion, one would obtain a result ranging between 1 and 10 electrons. The line shape and width of a plasmon peak is inversely related to its lifetime after which the plasmon oscillation is damped. Relaxation of all the above-mentioned excited states of the electronic system, generally results in the emission of SEs above vacuum level, either promoting them to empty states (conduction band) or to the continuum, provided that they have sufficient energy to overcome the surface barrier, in either case.

A detailed description of the three types of inelastic interactions for the case of non-crystals is given Refs. [59, 60, 54].

"True secondary" electrons are per definition those generated and ejected from the target as a consequence of inelastic collisions between the impinging electrons and the solid-state electrons. If the herewith generated SE has sufficient energy to escape right after over the vacuum level, without undergoing additional energy losses, then this SE was generated in the course of a single scattering event. In other cases, during their transport through the specimen these liberated (secondary) electrons can in turn undergo additional scatterings with other electrons or with the ionic sub-system of the target. Also the inelastically scattered PE can experience further inelastic collisions along its path towards the surface. These latter can act as new sources for SEs, by suffering additional energy losses on their way towards the surface-vacuum interface, thus being subject to *plural* (1–20 scattering events) or even *multiple* scattering (more than 20 scattering events)[3]. The probability for these two types of collisions to occur is described by the scattering cross-section, σ, and by the distance travelled on average by an electron within a solid before undergoing an inelastic collision, the so-called Inelastic Mean Free Path (IMFP), λ_{inel}. When treating with bulk materials, with typical thickness larger than twice the IMFP, plural and

[3]The number of scattering events reported here, to make a distinction between the plural and the multiple scattering regimes, represents those commonly used in electron scattering models assuming medium to high kinetic energies for the incident electron beams. Since the number of inelastic collisions undergone by an electron depends on its inelastic mean free path, it becomes clear that in the LE-regime the amount of collision events mentioned above becomes rather meaningless. An electron with only 50 eV is very unlikely to be subject of plural scattering exceeding 2-3 events, since its mean free path becomes larger and larger after each energy loss.

multiple scattering are likely (if the energy of the PE is sufficiently high). Consequently, as stated above these SEs can be also produced in the course of plural (or subsequent) inelastic scattering events.

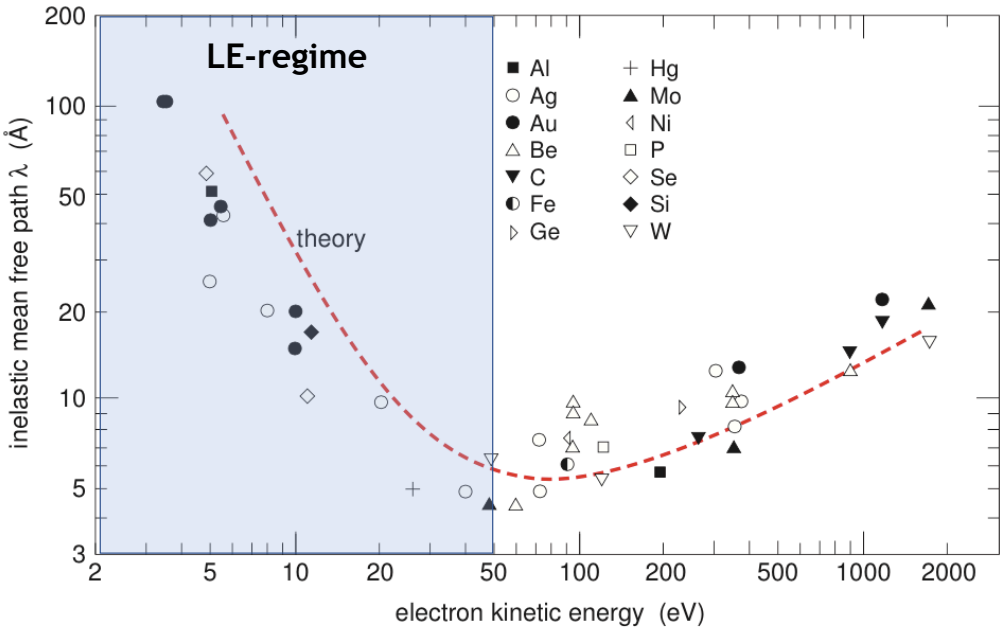

Figure 1.1: The "universal curve" showing the IMFP of electrons in solids. The dashed red curve is obtained from calculations, whereas the dots are experimental values measured for different materials. [Figure extracted from Ref. [61] where the range of LE-regime has been highlighted by the blue rectangular area].

One of the most relevant properties of LEEs relies in their *surface sensitivity*, hence their capability to sample regions near the surface-vacuum interface of a solid and this is a consequence for their short IMFPs. The trend for this physical parameter is given in figure 1.1 as a function of the kinetic energy, ranging between a few eV and several hundred eV. The red dashed line represents the IMFP as calculated based on the Drude model for electron collisions in metals [61]. The data points represents experimental values for the IMFP obtained for different materials (see legend in Fig. 1.1). Since the behaviour of the IMFP seems to be independent of the material, this curve is often known as *"universal curve"*. The blue shaded area highlights the energy range of interest treated in this work. The IMFP exhibits a minimum for energies between 20–100 eV where it becomes less than 10 Å, hence undoubtedly surface sensitive. Furthermore, for low incident energies of the primary electrons, the internally generated secondary electrons manage to escape more efficiently, since their points of liberation are closer to the surface. By looking at this universal curve, it becomes clear that by adjusting the excitation energy of the electron beam, it is possible, in turn, to tune the surface sensitivity for an experiment. For the experimental energy range explored in this work we reach highest surface sensitivity.

The energy distribution of all these electrons, $j(E)$, of all these electrons is characteristic for the microscopic properties of the bombarded material and is intrinsically linked to its electronic

structure and geometrical arrangement (i.e. degree of long-range order).

Figure 1.2 shows a typical energy distribution of these electrons for the case of polycrystalline Aluminium, measured in reflection geometry by impact of ∼100 eV primary electrons. This energy distribution shows again a prominent peak at E_0, composed of electrons that have only suffered elastic scattering and it can exhibit peaks at lower kinetic energy, arising from electrons that have participated to inelastic scattering events. In general, these scattered electron energy distributions can be detected for any desired scattering angle. The electron spectrum is conventionally subdivided into three spectral regions (numbered and explained in Fig. 1.2):

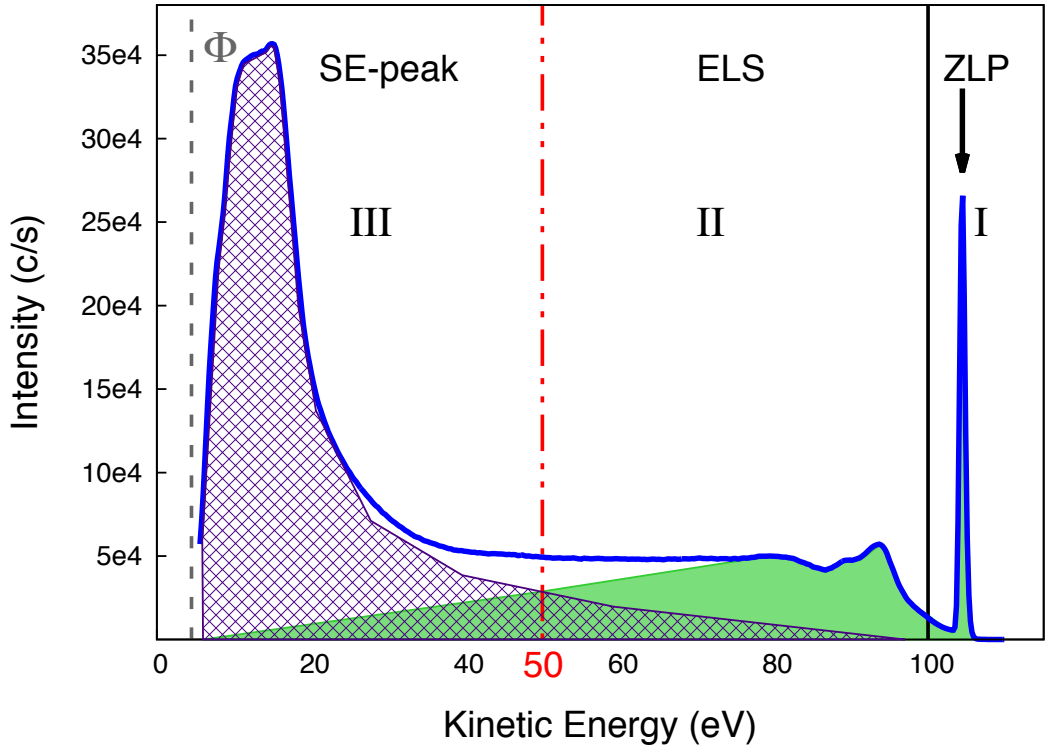

Figure 1.2: REELS from poly Al measured for E_0 = 104.45 eV. Region **I** confines the elastically reflected and backscattered electrons; region **II** is composed of inelastically scattered electrons giving rise to the energy loss range, where characteristic spectral features, such as plasmon peaks are visible. At the kinetic energy of E_s = 93.95 eV a surface plasmon loss (with $\hbar\omega_s$ =10.5 eV) and for E_s ≃89.55 eV the bulk plasmon (with $\hbar\omega_b$ =15 eV) are recognisable. All electrons with kinetic energies ⩽50 eV are labelled as SEs (region **III**). Contributions to the total energy distributions are essentially given by backscattered primary and secondary electrons, whose spectral portions are symbolically highlighted by the light-green coloured and dashed regions, respectively.

I. The *"Zero-Loss"-Peak* (ZLP) or elastic peak composed of all elastically reflected and scattered electrons, which have not experienced any energy loss process and which therefore have (nearly) the same kinetic energy as the impinging electron beam. In the specific case of the spectrum shown in Fig. 1.2 the central primary energy, E_0 is of 104.45 eV. By studying the energy and angular distributions of the elastically reflected electrons, it is possible to obtain information on the geometrical atomic structure (long-range order or crystallinity) of a material. Accounting for the wave-nature of electrons, this latter can be associated

to a de Broglie wavelength $\lambda_e = {}^{2\pi}/_{k}$. When this wavelength, λ_e is of the same order as the inter-atomic distance in a target, this electron (and/or wave) is subject to Bragg's scattering. Constructive interference from scattered electrons can be only observed if the Bragg conditions are fulfilled, meaning that the exchanged momentum $\Delta\vec{K}$ matches the reciprocal lattice vector, $\vec{G}$. By means of diffraction of elastically scattered electron it is possible investigate the degree of order present in a target.

II. The *Energy Loss Spectrum* (ELS) is given by the energy distribution of all inelastically scattered electrons, which have therefore undergone an energy (and momentum) transfer to the solid-state electronic system. The momentum transferred during such an inelastic collision is determined by the electron energy and the scattering geometry. By means of Electron Energy Loss Spectroscopy (EELS), information on the excitation channels, carrying the signature of all accessible degrees of freedom available in a target can be studied. Within the considered LE-regime we shall see that the majority of these inelastic events can be related to collective excitations such as plasmons (or phonon[4]). Inelastic scattering processes associated to these collective oscillations, are visible in the spectrum within an energy loss region typically below a few tens of eV. The average energy corresponding to loosely-bound valence electrons in a target is generally of the order of one Hartree (E_H), hence the mean excitation energy that can be induced by an electron interacting with the electronic system during an inelastic collision.

III. Finally, the third spectral region is represented by the *Secondary Electron Emission Spectrum* (SEES or SE-peak) ranging from the workfunction, Φ, up to the conventionally chosen kinetic energy of 50 eV. Together with the ZLP, the SE-peak represents the most prominent contribution to the electron spectrum making up nearly the total electron current. The energy distribution of SEs is considered to be essentially independent from the primary energy.

This subdivision of the electron spectrum represents a simplistic (but nonetheless practical) attempt at categorising electrons into groups characterised by their origin and interaction type. Strictly speaking such a categorisation is rather inappropriate, since electrons are per se indistinguishable fermions. Furthermore, it is demostrated [62, 48, 63] that a non-vanishing amount of so-called secondary electrons with kinetic energies higher that 50 eV can be ejected and that their contribution to the spectrum reaches up to the elastic peak (symbolically highlighted as crossed area in Fig. 1.2). Likewise, also contributions from the BSEs (given in light-green) can extend beyond region (I and II) thus participating to building up part of the intensity of the SE-spectral region (III). Even if in practice, a distinction between these types of electrons is common, in reality there are no experiments capable of distinguishing between a true secondary

[4]Phonons are an omni-present excitation channel that occurs in any material. However, in most materials, the phonon energies are considerably lower than 100 meV, which is an energy out of the sensitivity range aimed at in the present work.

electron and a backscattered primary electron. In spite of the fact that some SEs leave the sample with energies higher than 50 eV and that a number of BSEs and scattered electrons escape with less than this energy, these numbers are considered to be small (see also fig. 2.1). Thus, 50 eV was defined as a reasonable threshold to classify the true secondary electrons emitted from a sample.

Independently from the primary electron energy, E_0, all types of scattering mechanisms (occurring in region II) will eventually contribute to the production of SEs in the same low energy range of the SE-peak extending from Φ to approximately 30 eV (or E_H). Escape of secondary electrons can only take place if their kinetic energy is sufficient to overcome the surface barrier. This potential-barrier at the surface-vacuum interface ultimately influences both the energy and angular distributions of the ejected secondaries. In metallic systems, this barrier is represented by the workfunction, or Φ which is defined as the energy difference between the vacuum level (E_{vac}) and the Fermi-edge (E_{Fermi}). Thus in order to be ejected, SEs need to have a kinetic energy higher than Φ of the target (if the energy is defined wrt. E_{Fermi}). As previously mentioned, liberated electrons with kinetic energies just below E_{vac}, which eventually remain trapped in target are classified as hot electrons. Since these low energy secondaries (LE-SEs with $E_{kin} \leq$30 eV as visible from figure 1.2) constitute the most abundant yield in an electron spectrum, it is evident that to elucidate and to quantify the processes inherent to SEE is a scientific objective of fundamental interest. In fact, the phenomenon of electron-induced SEE describes one of the most relevant manifestations of the interaction between matter and probing electrons.

1.2 Why understanding on SEE is still lacking?

The most simple and fundamental questions that one can ask concerning the phenomenon of the emission of slow electrons induced by electron bombardment are in essence: *"how many"* and *"how"*.

Quantification of the SEE-properties of a material has been pursued since almost a century where one important physical parameter in this context is given by the SEY measured as a function of the primary electron energy $\delta(E_0)$ [64, 65, 32, 66, 33].

As previously shown, on the basis of the electron spectrum characteristics depicted in Fig. 1.2, it is experimentally impossible to distinguish between backscattered primary electrons and true SEs. Therefore Based on this fact, when measuring the currents associated to the energy distribution of scattered electrons, the only experimentally accessible quantity is constituted by the Total Electron Yield (TEY). Nonetheless, many authors still refer to this physical quantity as SEY, which indeed might lead to confusion. As previously said, all the yields shown throughout this thesis work are referred to as total yields (TEY).

The TEY or σ represents the ratio between the total current, which makes up the complete electron spectrum, with respect to the current of the source electrons, I_0. Hence, the SEY, or δ represents a partial yield, which along with the reflection coefficient η makes up the TEY [7].

$$\sigma = \delta + \eta \tag{1.1}$$

Since electrons are emitted (and scattered) over the entire solid angle, by measuring the currents associated to the total number of re-diffused and ejected electrons, after the interaction between the probing electrons and the electronic structure of the target, one obtains the TEY as a physical quantity, which therefore stands for an *integral* response of the target. Generally, these measurements are performed for an E_0-range going from 50 eV up to several keV and the typical trend of such curves is shown in figure 1.3. For low primary energies, with $E_0 \leq 80$ eV ca. the yield is much less than unity and increases to a maximum, δ_{max} (σ_{max}) at some $E_{0,max}$, generally at a few hundred eV, after which it slowly decreases as E_0 is further increased. The secondary (total) electron yield is a highly surface sensitive quantity. The slight presence of impurities, oxidation, recrystallisation or irregularities present at the surface immediately affects the whole trend of these curves, especially at which primary energy $E_{0,max}$ one finds which maximal yield σ_{max}.

Many authors have researched the secondary electron yield and the relevant parameters involved in its formation; they have attemped to set up formulae describing and predicting the SEY [67, 41, 68, 69, 70], however some of them are semi-empirical formulae and describe experimental results only qualitatively, thus still lacking of *quantitative* understanding.

Lin and Joy [71] have performed a thorough examination of this parameter as a function

of the incident energy and atomic number Z by analysing a data set for 44 elements, they have gathered from a whole manifold of sources. By compiling this data base, they provided a basis upon which they formulated a semi-empirical universal law to describe at best these collected data. However, as shown in figure 1.3 (a.), there is a non-negligible discrepancy among

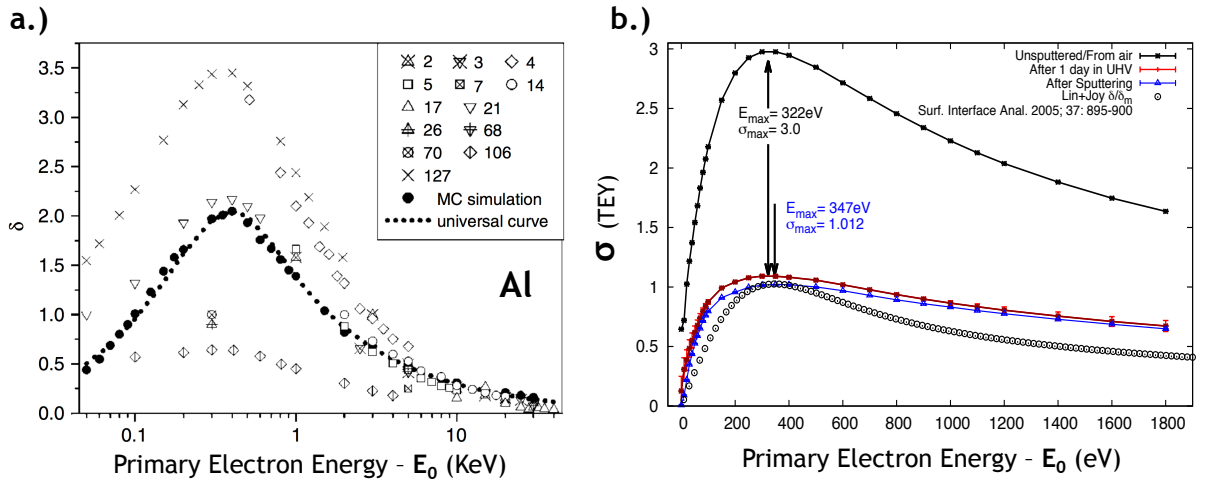

Figure 1.3: SE yields from Al: (a.) shows 13 experimental δ-curves exhibiting a maximal discrepancy of a factor 7. The black-dotted curve is the MC-simulation result obtained by Lin and Joy [71] with their semi-empirical formula describing the optimal SEY. Numbers in the legend stand for the references from where these data are taken. (b.) Comparison of SEY-data acquired in this work: (black) dirty poly Al surface with a $\sigma_{max} = 3.0$; (blue) freshly sputter-cleaned Al surface exhibiting a TEY of ca. 1.0; (purple/red) after one day in UHV. These three experimental curves were compared with the result computed by means of the universal formula by Lin&Joy, showing discrepancies at both the very LE-range and at higher energies. All experimental curves in this plot are displayed with their error-bars assuming an overestimated error of ca. 10%.

the measured SEY-curves, which in case of Al exhibits a variation in the maximal yield value, δ_{max}, of a factor 7. From fig. 1.3 (a.) it is evidently recognisable that the first main problem for performing a reliable quantification is given by the huge variations in the measured SEY itself. These discrepancies may be attributed to the different sample preparation methods and to the variation of the experimental arrangements used, which consequently lead to measuring the electron yield from "different" surfaces. As also demonstrated in several other works [29, 71, 72, 73] (to name a few) the SEY behaviour is strongly influenced by the chemical state and the cleanliness of the surface and for this very same reason it is often difficult to establish a *de facto standard* value for the SEY (TEY).

Even sorting out accurately these SEY-curves, they still found striking differences, which in turn made the modelling of the SEY rather difficult. The main aim of their work was to find a suitable formula capable to reliably provide the "optimal" SEY-curve, i.e. the one suiting at best the most reliable measurements. The results of their semi-empirical formula, obtained by means of Monte Carlo (MC) simulations, are plotted as black dots in fig. 1.3 and tend to fit the central data sets.

On the right-hand side of the same figure, panel (b.) shows the total electron yields measured at CERN (using the set-up discussed in subsection 3.3.1) on a polycrystalline sample at three stages

of cleanliness. The black curve, exhibiting a σ_{max} of ca. 3.0 was measured on the dirty sample, right after insertion into the Ultra-High Vacuum vessel (UHV). This value of σ_{max} resembles the one measured in the highest curve of panel (a.), suggesting that also the measurement from the data base was probably acquired on a contaminated Al surface. Further in panel (b.), the blue curve is the TEY measured on the freshly sputtered Al surface, for which a σ_{max} of 1.0 was obtained and the purple curve shows a subtle rise in the σ after the sample has remained for one day in the UHV-chamber. Many authors nowadays confirm that the σ_{max} of a clean polycrystalline sample is around 1.0 [72, 74]. The subtle rise in yield seen in the purple curve stresses once more the surface sensitivity of the TEY. If comparison between the measured TEY of the Al sample in fig. 1.3 (b.) and the MC-simulation shown in fig. 1.3 (a.) is made, the first evident difference is given by the value of δ_{max} or σ_{max} which in (a.) is about 2.0 whereas in (b.) is of 1.0. The curve displayed with open circles (in panel b.) was obtained by using Lin and Joy's formula and fixing the pair ($E_{0,max}$; σ_{max}) to the experimentally determined values (for the clean surface). Although this normalisation is arbitrarily chosen, what still can be said is that there are substantial differences between the experimental σ and the semi-empirical formulation, both at high-energies and in the LE-range. These discrepancies might suggest that the commonly employed theory does not cover all the details of the mechanisms playing a role in secondary electron emission.

Even though their approach is capable to qualitatively describe these SEY trends, following open questions remain:

- Which are the truly relevant parameters acting on $\delta(E_0)$ – or more precisely on the $\sigma(E_0)$? i.e. how shall the empirical quantities, utilised in this formulation, be "translated" into Physics?
- Would such a semi-empirical theoretical approach also apply to primary energies below 50 eV? – at least from a qualitative point of view.

Despite the lack of a complete physical picture, their semi-empirical formulation remains one of the most commonly used.

One of the parameters which is known to act on the TEY is given by the impact angle θ [68, 69]. In general, σ_{max} increases for an increasing angle of incidence ($\theta > 0°$) and the primary energy where its maximum is then observed is higher than when measured at normal incidence. This behaviour is recognisable in figure 1.4 where three angle-dependent σ-curves from a clean Highly Oriented Pyrolytic Graphite (HOPG) surface are displayed. The curves shown in fig. 1.4 were acquired starting from a primary energy of ~ 0 eV, which provides with information on this parameter also in the LE-range. The inset of the same figure shows the enlargement of the energy range $0 < E_0 < 50$ eV, where a prominent feature can be recognised centred around 10 eV. Detailed explanation on the origin of this energy-dependent structure will be discussed in subsection 4.1.1 in chapter 4, but it shall serve here as an additional indicator demonstrating

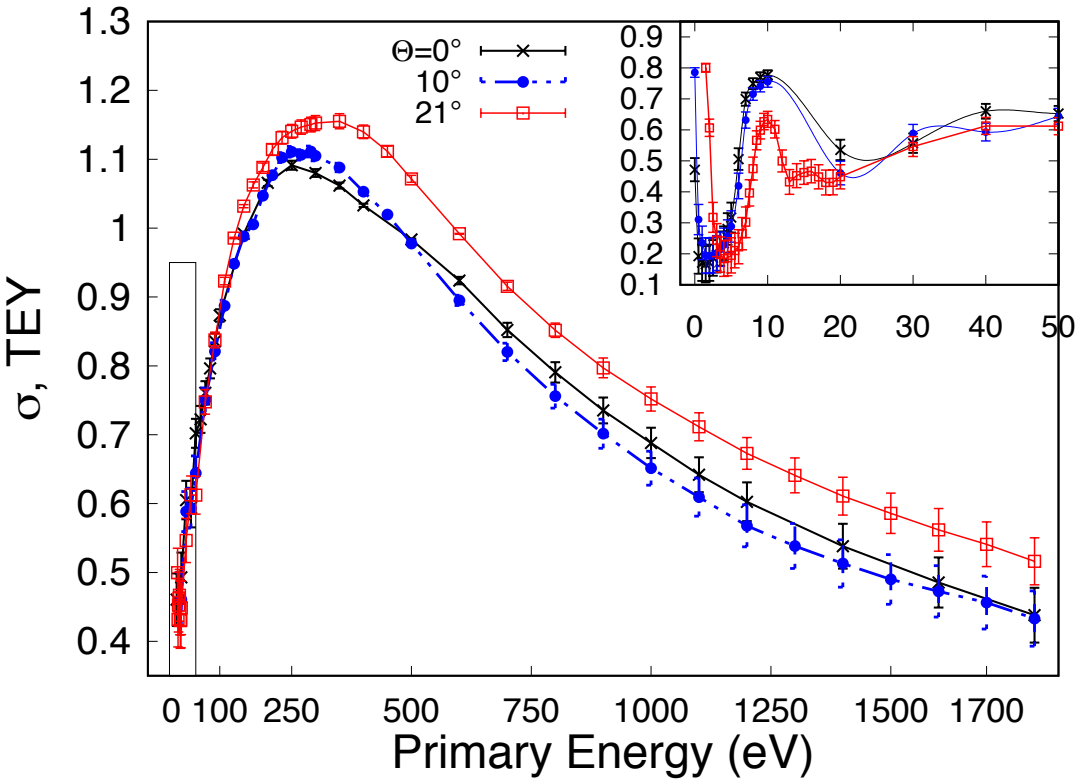

Figure 1.4: SEY-curves from a clean HOPG surface acquired at three angles of incidence (see legend). The inset enlarges the low kinetic energy range of landing energies up to 50 eV, where characteristic modulations, linked to the electronic structure of this 2D-semi-metal crystalline surface, are observed. (More information on the LE-structures is given in subsection 4.1.1 of chapter 4).

that in the LE-regime, the TEY-behaviour is evidently influenced by other factors, which up to date do not seem to have been considered in any model describing the TEY (or SEY). This is not too surprising if one acknowledges that the majority of the SEY/TEY measurements available up to day have been always performed for energies higher than 50 eV. On the other hand, to improve the understanding and the tuning in and for all technological applications mentioned in the beginning, it will be necessary to extend these TEY and SEE-models also to the very low-energy range.

Nowadays, the majority of the available models for SEE manage to reproduce most of the physical characteristics of a material, as long as the considered kinetic energies involved are high (~ 1000 eV and beyond) and its surface is either amorphous or polycrystalline. A more detailed overview of these models can be found in section 2.1 of chapter 2. In order to understand the complex phenomenon of SEE, which is nowadays generally attributed to be the consequence of a sequence of incoherent plural or multiple scattering processes (as sketched in figure 1.5), it is first necessary to unveil which is the most elementary "brick" upon which this electron cascade is built. Each individual interaction vertex (indicated as stars in the figure) shall represent an event at which energy and momentum are transferred during one collision. Particularly, when the

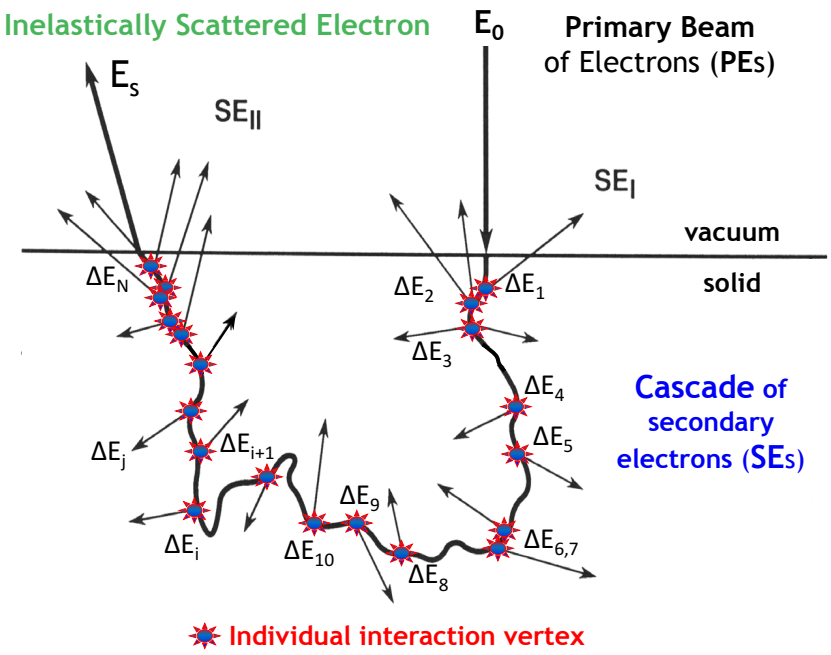

Figure 1.5: Common view on the SEE-mechanism nowadays: Series of subsequent incoherent multiple scattering events producing a *cascade* of LE-SEs. In each single interaction vertex a discrete amount of ΔE- and $\Delta\vec{K}$ are transferred in form of inelastic collisions, inducing the generation of SEs.

PE has already a low kinetic energy, which are the most relevant aspects in the electron-solid interaction that need to be taken into account? To find answers to the question on *"how"* the LE-SEs are generated and ejected from a target in the LE-regime, we pose ourselves some more specific questions:

- Which are the main excitation channels, through which the transferred energy and momentum lead to the generation-ejection mechanism of a SE?
- Which is the role played by the electronic structure of a target in the process of SEE?
- What is the influence of the long-range order of a surface on the SEE and TEY?
- Which is the elementary process constituting the fundamental brick of the SE-cascade?

Herewith, the focus of this work is devoted to the investigation of the processes linked to each such single interaction vertex (symbolised in fig. 1.5) of which the final aim is to elucidate its nature and mechanism. To this end, it is mandatory to first understand *how* energy and momentum are handled in such individual processes, for which the single scattering regime in an electron spectrum is the process ideally suited to conduct such investigation.

The complexity of the phenomenon of SEE becomes already evident if one considers the steps involved in this process merely from a qualitative point of view. One of the most common ways to describe the electron-solid interaction and the consequent emission of SEs is by means of the so-called *"three-step-model"* [65, 75, 64, 76, 33, 77]. In a nutshell, this theory treats the *excitation* (1) of the ejected electrons, their *transport* (2) throughout the solid from their point of liberation to the surface barrier and their *escape* (3) over this latter as three distinct steps.

However, already the first step can be additionally subdivided into two more steps, since the primary electron beam impinging upon the surface of a material first interacts with the surface barrier and can be split into two components, a.) electrons that are (directly) reflected and b.) electrons which penetrate the surface.

The second step (2) involves those electrons that have managed to penetrate the surface. After trespassing the surface, they interact with the ionic subsystem and with the solid-state electrons of the material and get thus re-distributed via elastic collisions with the nuclei, whereas energy is lost during their interaction with the solid-state electrons (inelastic collisions).

The elastic collisions cause the original electron beam to be separated again into various directions, some of which are redirected toward the surface. These reflected PEs can in turn produce further secondaries, part of which will escape into free space, after overcoming the surface-vacuum barrier. A portion of these SEs may additionally undergo further inelastic collision with the solid-state electrons, thus only those with sufficient kinetic energy will eventually manage to escape. Others, with kinetic energies lower than the surface barrier remain trapped under the vacuum level (hot electrons) and their energy may be then be dissipated away over other excitation channels, e.g. phonons.

The interactions of the PEs and the material electrons, as well as the possible interactions of the SEs with further solid-state electrons will *cascade* through the material each causing further interactions or scattering (this is the reason why one generally refers to this process as "secondary electron cascade"). Only a finite number of all these (scattered and generated) electrons will eventually reach the surface and escape above vacuum.

Finally, depending on the excitation energy a whole manifold of different electron excitation channels can be accessed and each one of these channels can lead to the generation of a "secondary" electron with the very same kinetic energy through different combinations of energy dissipation mechanisms.

This simplified picture of the three-step model manages to describe qualitatively most of the important characteristics of SEE. On the other hand, all of these theories can predict only the functional dependence of SEE, but not the magnitude of the emission process itself, therefore also in this case quantitative understanding of this phenomenon still awaits a complete answer.

1.3 Employed Approach

This thesis is dedicated to the investigation of the process of electron-induced secondary electron emission in the low energy regime, by employing electron sources of kinetic energies below and around 100 eV.

Knowledge about connection between microscopic electronic properties and the phenomenon of SEE has been pursued employing several electron spectroscopic techniques, each one of which capable to provide with distinctive information on the mechanisms involved in SEE. The differential cross-sections obtainable by these spectroscopic techniques enable to study the same SE-generation-ejection mechanism with a gradually increasing degree of differentiation. By combining the results obtained by means of these different investigation tools, it is aimed at obtaining a more detailed insight on the very same phenomenon with increasing peculiarity and supplementary information.

Total Electron Yield (TEY) measurements deliver the *integral* response (in terms of emission, reflection and back-scattering events) of a system to electron bombardment. A certain degree of differentiation can be accessed, if the total yield is separated in its partial components, of a Reflection Electron Yield (REY or η) and of the SEY or δ.

Low-Energy Electron Diffraction (LEED) studies permit to determine the long-range order of a target and to select specific symmetry directions, thus enabling to study the yield of SEs in dependence of the sampled band structure of a target.

A *double-differential response* (in energy and momentum) on the relevant interactions occurring in a target and on the predominant ejection channels is obtained by means of *Reflection Electron Energy Loss Spectroscopy* (REELS) and by *Secondary Electron Emission Spectroscopy* (SEES), respectively.

In practice, one uses REELS to measure the kinetic energy distribution and propagation vector of an electron inelastically scattered from the sample above vacuum. What in fact is actually measured is the energy and a relative momentum of a temporarily excited many-body electronic state with a given life-time, which has been created during the interaction. Such a picture makes it clear how remarkably complex the interaction between an incoming electron and the many-body system of the target in reality is.

While the various excitation channels – recognisable as characteristic spectral features (e.g. surface and bulk plasmon peaks visible in the electron spectrum of figure 1.2) in the energy loss range of a spectrum – are easily distinguished and routinely studied by means of EELS, the

(almost) featureless SE-peak makes it inherently difficult to study the mechanisms by means of which the deposited energy is effectively dissipated away over the solid-state electrons. Hence, only by using REELS it cannot be elucidated to which extend the scattering processes ultimately contribute to the intensity of the SE-spectrum and yield.

Solely by studying the blandly-shaped secondary electron spectrum or the TEY of a material, it is an exigent (if not impossible) task to identify which are the mechanisms responsible for their creation and ejection. As previously mentioned, an abundant variety of inelastic processes can lead to the production of a SE having the exact same kinetic energy. For this reason, the intensity of the SE-peak is built-up by a mixture of all possible excitation mechanisms by means of which the deposited energy is differently distributed over the various degrees of freedom available in the target.

In materials, where the electronic structure exhibits a rather engaged (i.e. a band structure with a complexity higher than that of simple metals) conduction energy band structure in the (unoccupied) density of states (DoS) it is possible to exploit SEE-spectra to study the conduction band DoS above vacuum level, thus obtaining information on the availability of escape channels through which the generated LE-SEs can leave the solid after their excitation. However, no knowledge on their origin in the valence band can be determined.

This makes it clear, that by using conventional single-electron spectroscopies, the causal-connection or correlation between the PE and the SE is not accessible and with this no information on the complete interaction-creation-ejection mechanism for LE-SEs can be obtained.

On the other hand, if a so-called *(e,2e)-coincidence experiment* is performed, a direct link between the energy loss spectrum and the SE-spectrum can be made by detecting simultaneously, or coincident in time, *correlated* electron pairs. (e,2e)-spectroscopy – a *"one electron in, two electrons out"*-spectroscopic tool – permits to detect both scattering partners involved in an inelastic collision. This type of measurement represents the most effective way to decompose the SE-cascade into its constituents, because only those SEs, that are ejected in coincidence with a specifically chosen energy loss under a specifically chosen scattering kinematics (and herewith momentum transfer) of the primary electron, are detected.

By means of this two-particle spectroscopic technique, it becomes possible to disentangle the main scattering mechanisms relevant to SEE by discriminating among the possible excitation channels.

The main aim of the present work is to scrutinise the fundamental mechanism governing the most-elementary interaction between electrons – the *single scattering interaction* – in the very low energy regime. For achieving this purpose, the one to observe and analyse a single scattering event, ideal conditions are obtained when the kinematics of collision events can be controlled and opportunely tuned. For doing so most of the targets used for the following investigations are single-crystalline surfaces. The long range order of these surfaces permits

to properly adjust the scattering conditions to be used in an electron collision experiment. Additional experiments, performed on non-crystalline surfaces, have the scope to provide one with complementary comparative information, which is exploited to interpret and to separate contributions to the TEY and to the SE-spectrum linked to the sole electronic structure from those linked to the long-range order of a same material.

Furthermore, the set of samples used for these investigations was selected in order to highlight the importance of the electronic structure (both in the occupied and in the unoccupied state) and the role played by characteristic excitation channels (e.g. plasmons) in the processes leading to the emission of LE-SEs. All of these measurements were performed both in dependence of the primary energy and also in dependence of the employed scattering geometry.

CHAPTER 2

Theoretical Framework for Secondary Electron Emission

The phenomenon of secondary electron emission induced by electron bombardment is a complex process and its theoretical treatment is manifold. Along with numerous experimental studies, in the past century a plenitude of theories have been developed to describe the SE-generation mechanism from solids. In general, these proposed theories, which have been confirmed and refined in the high energy (HE) regime, are capable to deliver a good prediction of both the energy-dependent secondary electron yield, $\delta(E_0)$, and of the energy distribution of the ejected SEs, j(E), which are in satisfactory agreement with experimental results – as long as the excitation energies involved are high (of the order of some keV and beyond).

As previously emphasised, SEE is still not quantitatively understood. The simple fact that in an experiment it is never possible to distinguish between a so-called "*true SE*" and a back-scattered primary, makes quantitative interpretation intrinsically difficult.

This limitation can be overcome in theoretical models and simulations, in which these types of electrons can be indeed distinguished and treated separately as visible in the Monte Carlo simulation by Ridzel [78] presented in figure 2.1, where the total energy distribution of electrons is separated into (true) SEs and elastically (and inelastically) back-scattered primaries (BSEs). This model calculation – performed for the case of a polycrystalline Au surface and for primary electrons of 1000 eV – clearly shows that SEs (red curve figure 2.1) with considerable kinetic energies, of the order of the elastic peak energy, may be emitted from the surface, although the majority is released with energies below ~ 50 eV. For such low energies, the contribution of backscattered primaries (green curve in figure 2.1) to the total spectrum is more than an order of magnitude smaller than the contribution of secondaries, which is the reason why, *by convention* electrons with energies below ~ 50 eV are designated as (*true*) secondary electrons. The physical reason for the peak at energies below ~ 50 eV is the fact that the typical energy of the solid state electrons is of the order of 1 Hartree (27.22 eV), giving rise to a mean energy loss in an inelastic collision of the same order of magnitude, for arbitrary incident energies [62, 80].

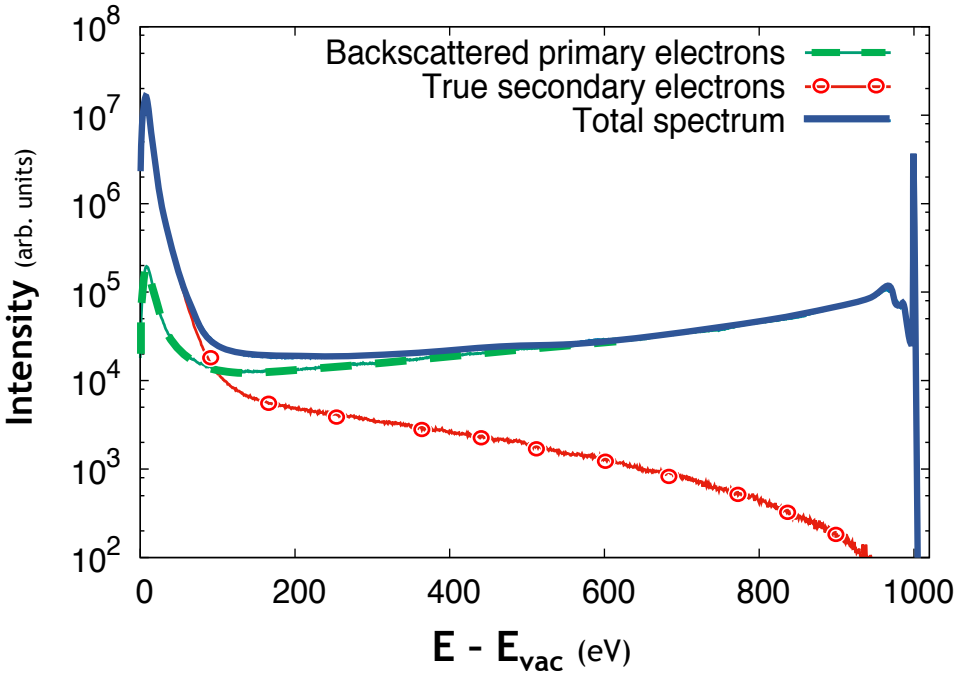

Figure 2.1: Simulation of an electron spectrum from a polycrystalline Gold surface for a primary electron energy of 1000 eV (given w.r.t vacuum level). The simulation is performed using a Monte Carlo (MC) code developed at TUV by Werner *et al.* (see also Ref. [63, 79]) and relies on the calculation of the inelastic mean free path (IMFP). The total energy distribution (blue curve) is made up of backscattered primary electrons (green curve) and secondary electrons (red curve).

When the kinetic energies of the source electrons enter the low energy (LE) range – around 100 eV and below – agreement of these very same models with experimental results is rather poor and the admissibility of their usage starts to become questionable.

In fact, in this LE-regime, several of the assumptions which are admissible and routinely accepted at HEs are no longer valid.

For example, as explained by Ding and Shimizu in Ref. [81] several theoretical simulations schemes describing the behaviour of SEE rely on Bethe's stopping power [82]. The stopping power, S(ΔE), defines the retarding force acting on charged particles – on electrons in this case – due to their interaction with matter, resulting in an energy loss suffered by the interacting electrons. It depends on the source energy, as well as on the properties of the target material. Hence, the S(ΔE) of a material corresponds to the energy loss, ΔE per unit path length, x, with S(ΔE)= $\frac{d\,\Delta E}{dx}$.

First of all, Bethe's model was originally developed to describe the interaction with free atoms and only by making suitable assumptions it can be adapted also for the interaction of charged particles with solids. This formulation accounts for all types of inelastic collisions and all sorts of excitation channels and once again it is valid for high energies only. At high kinetic energies the wave vector of the primary electron (PE) can be assumed to be much larger than the wave vector of lattice electrons – i.e. the electron wavelength is much smaller than the inter-atomic

distance – so that the electron behaves rather as a particle, allowing to disregard its wave nature and making the binary encounter approximation reasonable. This approach assumes that the volume occupied by an atom significantly exceeds the volume in which the electron interaction takes place [59].

A further loophole of most of these models is represented by the treatment used to describe the electron transport, when these charge carriers have very different kinetic energies.

At high and medium kinetic energies – hence at energies where the wave nature of an electron can be neglected, since then the electron wavelength is much smaller than the inter-atomic distance – the binary encounter approximation becomes applicable and is well-established. This approach assumes that the volume occupied by an atom significantly exceeds the volume in which the electron interaction takes place [59].

Whereas for low energy electrons with $E \leq 100\,eV$ and for SEs this is no longer valid since the electron wavelengths become comparable or even larger than the inter-atomic distance or the electron correlation lengths.

For example, for an electron of 100 eV the correspondent De Broglie wavelength is of the order of 1 Å, which is already comparable with inter-atomic distances, at which interference effects would occur. For an electron just above the vacuum level, e.g. of 1 eV, the electron wavelength exceeds the inter-atomic distance by a factor of ca. 4 or 6 (depending on the lattice parameter), since it becomes about 12 Å. However, inside the solid the maximum wavelength for an electron detected in vacuum is dictated by an energy equal to the height of the inner potential (about 20 eV), i.e. is about 3 Å.

Furthermore, when modelling the emission of LEEs just above the vacuum level it is essential to properly account for the potential barrier at the surface, which represents the main parameter influencing the energy and angular distribution of slow electron emission, comparable to deflection of light at the interface between media with different refraction index (Snell's law).

In addition, if one wanted to include in the modelling also the production of the so-called *"hot electrons"* – electrons exhibiting kinetic energies below vacuum level – thus remaining trapped beneath the vacuum level one would be forced to use alternative approaches. On the other hand, these trapped hot electrons generally do not contribute to the detected electron signal in electron scattering experiments and their energy is dissipated away over other excitation channels, e.g. phonons.

At primary energies below 100 eV, true secondary and backscattered electrons cannot be distinguished, i.e., a separation of the primary and secondary electrons is impossible. Consequently, stage (1) of the three-step model must be included in a complete solution of the electron transport problem with suitable boundary conditions. In such cases, most of the models regard only the current of PE at the surface as source term.

In addition, when dealing with such low kinetic energies, a multitude of additional effects, which are commonly neglected in the HE-regime, become relevant. One of these aspects, which is

demonstrated by a whole series of experiments performed throughout this thesis, is given by the role played by the band structure (BS) of the target. Depending on the characteristic energy band distribution of the irradiated target, when this latter is bombarded by LEEs (with $E \leq 50\,eV$) both the reflectivity of the PEs as well as the emissivity of SEs is strongly dependent on both the conduction (unoccupied) and valence (occupied) bands of the target BS.

Since slow electrons play a relevant role in a broad variety of fields, also influencing processes occurring at much higher kinetic energies, it is of paramount importance to properly treat electron generation, transport and emission in the LE-range and for this novel theoretical approaches, that take the aspects mentioned here above, are required.

2.1 State of the Art & Historical Overview

After the first experiments performed by J.J. Thomson in 1904 when it was demonstrated that emission of slow electrons followed the bombardment of metal plates by alpha particles, a whole series of experiments dedicated to the study of SEE and in particular the study of their energy distribution, j(E), followed. Most of these experiments were first performed on (non-crystalline) metallic surfaces. In 1925 Becker [5] was the first to find that the j(E) of electrons was rather independent of the bombarded metal as well as of the primary energy, E_0. In his experiments he employed both ion sources as well as alpha rays with excitation energies around 1 keV and in either case the function j(E) showed a maximum at E$\sim$ 2 eV. On the basis of these experiments he was the first one who proposed to subdivide the energy distribution curve in three parts ranging from true secondary electrons, the re-diffused primary electrons, to the elastically reflected primary electrons. He also was the first to assume the angular dependence of the SEs to be a cosine distribution, additionally presuming that their energy distribution is independent of the escape angle.

Some time later, for the description of the SEY, a simple semi-empirical theoretical expression was developed by Lukyanov and Bernatowitch (1937), who wrote an expression for $\delta\,(E_0,\,\theta)$ as a path integral over all rectilinear path lengths of the incoming PE, also dependent on some empirical values [83]. They focussed mainly on the θ)-dependence of the SEY. Only some time later, improved semi-empirical expressions were derived which were capable to describe more accurately the SEY-distributions observed.

Further early models were proposed by McKay in his extensive review [75], by Dekker and Van der Ziel [84] who gave a general formulation of the SEE-process and compared basic features of the theories available at their time.

During the early 1940s experiments dedicated to measure the energy distribution of SEs both in dependence of the primary energy E_0 and on the type of irradiated target (mostly metals) lead to the conclusion that the $j(E)$ in metallic surface was nearly independent of the PE-energy. Also in this case, the energy distributions measured on metal surfaces exhibited very similar trends, showing all their maximal intensity around 2 eV. The fact that independently from the irradiated surface and for the source energy used the SE-peak showed its maximum around the same kinetic energy suggested that the phenomenon of SEE has a "universal" character.

Bruining [85, 86] followed by Dionne [67], who described the parameters influencing the SEY, contributed essentially with their phenomenological models on SE-emission, of which the most famous is represented by the "universal law" describing the SE yield as a function of primary energy. In their models, it is assumed that the incident electron looses energy, ΔE, along a straight-linear path with a power law energy loss and the herewith generated internal SEs are proportional to the stopping power. Escape of these secondaries is described by an exponential

law assuming either single scattering events or in some cases assuming diffusion processes (large number of collisions). Even though in these models the electron cascade formation is disregarded, they nonetheless managed to reproduce the main features of the energy-dependent SEY, $\delta(E_0)$.

Wolff [87] followed with one of the first comprehensive models developed to describe the transport treatment for electron-induced SEE. He obtained the spectrum of emitted secondaries, as well as an estimate for the maximum SE-yield. He was the first to formulate a theoretical description for SE-multiplication by cascade processes, thus explaining the possibility for a PE to generate more than one SE. The calculated energy spectrum of ejected electrons was obtained by solving the Boltzmann kinetic equation in an infinite medium with a uniformly distributed source.

In Ref. [88], Schou's model calculations assume primary particles (both electrons and ions) of high non-relativistic energies, in the keV-energy range, leading to a general expression for the yield (δ) and the energy distribution of the slow SEs. Devooght, Dubus and Dehaes [76] derived a mixed analytical-numerical electron transport model for SEE induced by what they call "low-energy" electrons, which are assumed to be in the keV-energy range. They propose an approximate solution to the Boltzmann equation designed for SEE induced by electrons and protons. In their model they considered also the semi-infinite character of the target, thus automatically including the escape process of SEs (3). In their work, both Schou and Devooght also used the Boltzmann transport equation to describe the cascade of SEs during their transport towards the surface-vacuum interface.

Ganachaud and Cailler [89, 90] developed a more elaborate model from the microscopic point of view, where they employed microscopic cross-sections including elastic and inelastic collisions. They solved the electron transport problem by Monte Carlo methods.

Koshikawa and Shimizu [91] employed a Monte Carlo method to describe the emission properties of Copper, and calculated the radial distribution of outgoing secondaries. Chung and Everhart [92, 93] investigated the role of plasmon decay in SEE from nearly free electron metals, in particular, they applied this model for the case of Aluminium, the material which best fits the free-electron model (Heine 1957 [94, 95, 96]). The transport process was treated in a very simplified way by taking only electron-electron scattering into account. The calculated results of the function j(E) were in good agreement with the experimentally observed one. Contemporaneously, Chung and Everhart also showed that the inelastic mean free path $\lambda_{inel}(E)$ derived by Quinn on the basis of Lindhard's dielectric function yielded a function j(E) reproducing the experimental energy distribution much better than the employment of a constant mean free path.

They treat electron transport on the basis of Berglund and Spicer's model [97], who developed their *three-step model* for photo-emission experiments and where only non-scattered and singly inelastically scattered electrons are considered. Some considerations on the limitations of the three-step model were already discussed in section 1.1 of chapter 1.

Even 20 years after Chung and Everhart, the most established model for the description of the SEE-process is based on this three-step model, as discussed in detail by Shih and co-workers in Ref. [33]. They describe in detail each of the three-steps subdividing them into (1) penetration

of the primary electrons, (2) transmission of the secondary electrons through the material, and (3) final escape of the secondary electrons over the vacuum barrier. They found that one of the critical factors in determining the magnitude of the secondary-electron yield is given by the transmission of SEs within the target and studied the behaviour of the SE-yield in insulating materials and on hydrogen-terminated diamond samples. In general, insulating materials have high SEYs, this is due to the fact that the SEs escaping towards the surface encounter a band-gap in the conduction band, wherein no additional energy can be lost via inelastic collisions (due to the absence of collision partners within a gap). For this reason also SEs liberated at deeper locations inside the solid manage to escape, thus resulting in a overall higher SEY, since their increased IMFP will result in a thicker effective layer of material contributing to the SEY. In the specific case of the hydrogenated diamond surfaces, where the vacuum-barrier is lower, they also observed an enhancement of the yield, thus assessing the relevant role played by the vacuum barrier height in the SE-emission mechanism.

Having obtained a solution to the Boltzmann equation, one arrives at statements concerning the quantities j(E) and $\delta(E_0)$, provided the mean free path of the electrons is known. Another approach is based on the use of the experimentally determined dielectric constant for the calculation of the excitation function (or Energy Loss Function, ELF) and the inelastic mean free path (IMFP). These semi-empirical models generally use macroscopic properties as input quantities. It has been shown that, if such a parameter is appropriately chosen, the calculated IMFP describes the experimental data with considerable success and despite this physical quantity varies from material to material it was often found to be in sufficient good agreement with some of the empirical formulae, as the one proposed by Seah and Dench in Ref. [98].

In spite of the existence of more advanced investigations based on quantum mechanical theories and Monte Carlo simulation techniques available nowadays, the large number of semi-empirical models developed between the '40s and '60s by Bethe [99], Baroody [100], Barut [101], Bruining [85] and Lye and Dekker in Ref. [102] (to name a few) is still used nowadays due to their simplicity and effectiveness. Even though in semi-empirical models, only the generation and transport mechanisms are considered – all secondaries that manage to reach the surface are assumed to escape – the errors arising from their use are often found to be negligible, thus making them still a suitable model to rely on when working at high energies.

At this point it shall be noted that any model based on a semi-empirical formulation is de facto a rough "approximation", since the introduction of empirically determined parameters intrinsically implies that fundamental physical understanding is still lacking.

A great effort has been made by many authors, among others by Lin and Joy [71], to improve this semi-empirical formulations, thus to extrapolate a "*universal law*" suitable for the description

of the SEY. They compiled and examined a huge database of experimentally measured SEY curves acquired over a period of 80 years by many (of the order of hundred) authors, covering 51 elements and 42 compounds. After scrutinising this data base, containing data of vary different quality and exhibiting a rather large spread among SEY curves for a same material. Even for commonly studied materials, e.g. Al and Ti, substantial discrepancies could be found among data-sets measured by different sources. An example for such a huge discrepancy was shown for the case of Al in figure 1.3 in section 1.2. Such a divergence between SEY data can be brought in connection to different surface preparation and measurement methods. In addition, it shall be mentioned, that in the case of so-called "technical surfaces" – e.g. those of an accelerator beam pipe or those employed in the construction of space-crafts – which are generally covered by an oxide layer and other contaminants, this formula is not applicable.

After scrutinising this data base the authors derived a "universal law" by fitting MC calculations employing the Continuous Slowing Down Approximation (CSDA) – a modified Bethe-model for the stopping power – in the form of eq. (2.1) thus to describe the experimental data. This nowadays commonly employed semi-empirical formula to predict the SEY (or $\delta(E_0)$) as a function of the incident energy is given below:

$$\frac{\delta}{\delta_m} = 1.28 \left(\frac{E_0}{E_0^m}\right)^{-0.67} \times \left(1 - \exp\left(-1.614 \left(\frac{E_0}{E_0^m}\right)^{1.67}\right)\right) \tag{2.1}$$

where the yield is parametrised in terms of the maximum SE-yield δ_m and the corresponding primary energy E_0^m. where the yield is parametrised in terms of the maximum SE yield δ_m and the corresponding primary energy E_0^m. The scope of this formula was intended to be used as a tool to examine sets of experimental results, to identify possible sources of error in the data, and to generate an optimised SE-yield profile for the element of interest.

As previously stated, it is generally assumed that the shape of Secondary Electron Emission Spectra (SEES) is rather bland and nearly independent from E_0. This is generally true, especially in case of polycrystalline and amorphous materials and if the angle of incidence is kept constant. Whereas in case of single crystals, or in materials such as Highly Oriented Pyrolytic Graphite (HOPG) – characterised by a high degree of in-plane order extended over a 3D-crystalline structure – exhibiting a band structure with a complexity beyond those of simple metals, the SE-spectrum can display a whole manifold of distinct spectral features. These SE-spectral features are linked to ejected electrons having a well-defined momentum, which is characteristic for the unoccupied electron band through which they escape. The shape and intensity of these characteristic peaks in the SEES of these crystals are therefore dictated by the electronic structure of the conduction bands of the irradiated material.

By varying the primary energy, E_0, of the incoming electron beam (at constant angle of incidence) a same spectral feature in the SEES is found at a same kinetic energy for the ejected electrons. However, it shall be noted that, the intensity of these spectral features can by all means

vary in dependence of the excitation energy as recognisable (even though on arbitrary intensity scale) by the energy-dependent SEES shown in panel (a.) of figure 2.2. These SEES acquired by Ueno *et al.* [103] exhibit distinct spectral features superimposed over the smooth SE-peak background.

Panel (b.) in the same figure shows Angle-resolved (Ar) SEES acquired by Hoffman *et al.* [104] for primary electrons of 200 eV. In this experiment the incident angle is kept fix and the emission angle for the SEs is changed between 20° and 75°. In this case, the appearance (disappearance) or the dispersion of peaks highlights once more the relevant role in the emission process played by the electronic structure of the irradiated target. From these two examples, it becomes clear that

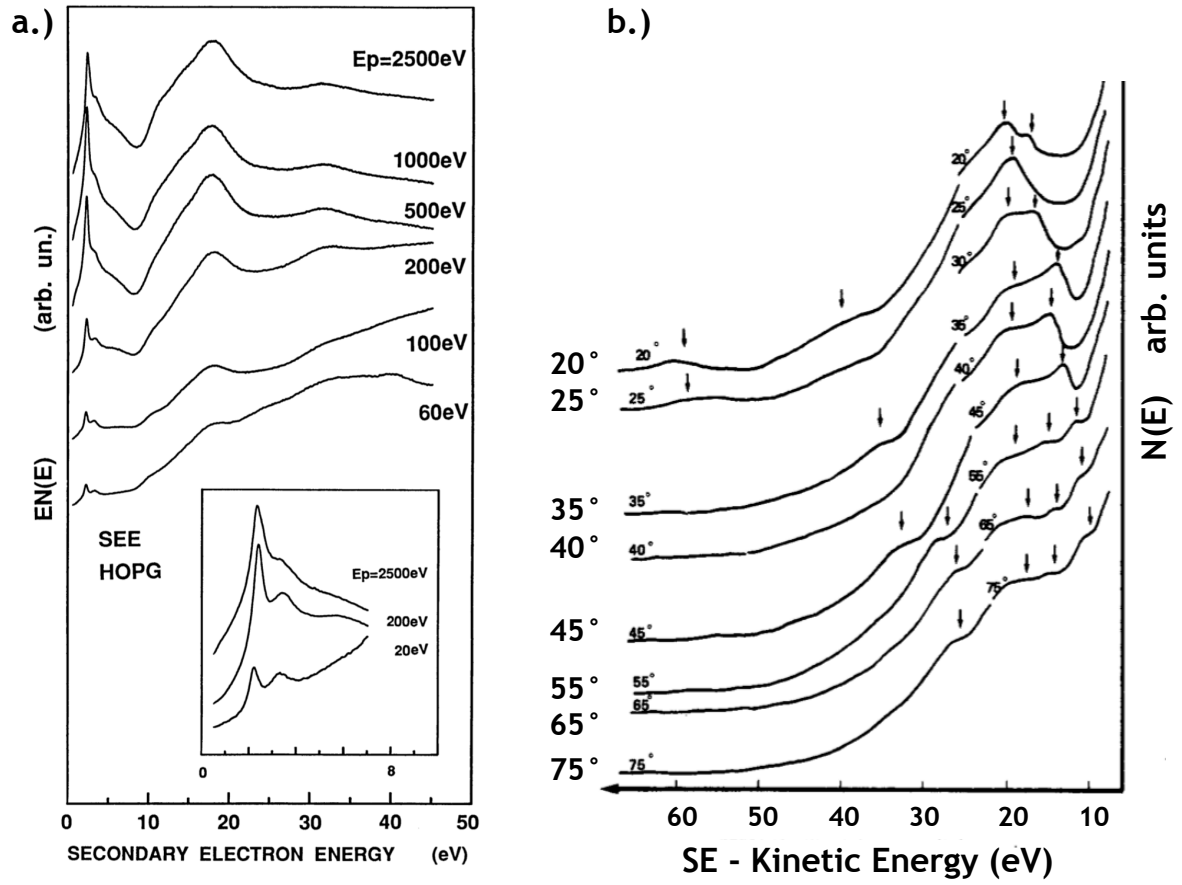

Figure 2.2: Secondary Electron Emission Spectra from Highly Oriented Pyrolytic Graphite (HOPG) extracted from literature: Panel (a.) shows a series of experimental SEES taken from Ref. [103] and acquired for a varying primary energy ranging from $E_0 = 60$ eV up to 2500 eV and at constant scattering geometry. These SEES exhibit a richness of spectral features, visible at all excitation energies. The intensity of these features may however vary with E_0. Panel (b.) shows Angle-resolved (Ar)-SEES performed by Hoffman *et al.* [104] at a constant primary electron energy of 200 eV and for varying emission angle (see legend). Depending on the emission angle different spectral features can be identified and brought into connection with unoccupied energy bands of HOPG. Some spectral features also exhibit a slight dispersion.

for a proper modelling of SEES it would be necessary to take into account also the band structure of the target, thus to simulate and predict these spectral features, their shape and intensities.

This is a further aspect, which is generally not considered in most of the already existing models simulating SE-emission spectra.

In fact, the energy distribution of SEs has been less investigated than the yield of SEs, some empirical approaches to predict the shape and intensity of a SE-spectrum was for example introduced by Chung and Everhart [105]:

$$\frac{d\,j(E)}{dE} = k\frac{E}{(E+\phi)^4} \tag{2.2}$$

Here, $d\,j(E)/dE$ is the differential energy distribution of SEs at the emitted energy E measured with respect to the vacuum level, and k is a pre-factor, responsible for the magnitude of $d\,j(E)/dE$ and ϕ is the target workfunction.

Figure 2.3 shows the comparison of measured[1] SEES of HOPG and randomly oriented Glassy Carbon (Cl-C) with eq. (2.2). As visible from fig. 2.3, for such a material, like HOPG or even for its less ordered allotrope, the prediction of the SEE-spectrum using this formula does not provide a reasonable description of the experimental data. In all the models presented up to now, in fact,

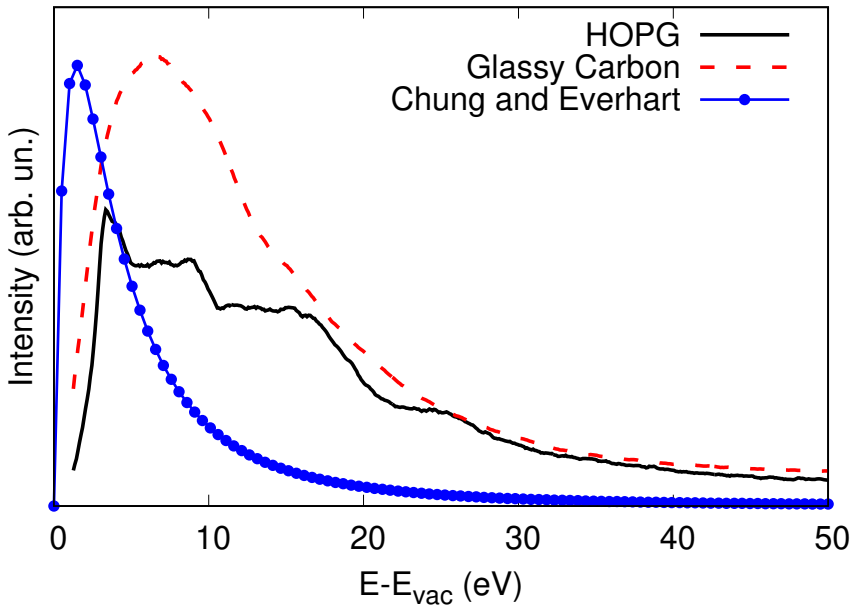

Figure 2.3: SEE-spectrum from HOPG compared with the randomly oriented Glassy Carbon (Gl-C) and the result of an empirical formula for the prediction of a SEES by Chung and Everhart [105]. Both experimental spectra were acquired for a primary energy of $E_0 = 173\,eV$ by Astašauskas at TUV. (See also Ref. [79, 106])

the energy transfer process is assumed to occur in non-crystalline solids. For many applications, where indeed materials with short-range order are employed, the transport of electrons can

[1]Measurements conducted by Astašauskas at TUV [106, 79].

be conveniently described by means of *incoherent* scattering and transport of the interacting electrons, which can be dealt by solving the Boltzmann-type kinetic equation.

For a proper prediction of SEES in case of crystalline surfaces – as previously discussed on the basis of figures 2.2 and 2.3 – these models are rather inadequate since they do not consider either the long-range order, or the band structure of the irradiated target. When crystalline samples are involved, it is necessary to take into account the wave nature of electrons and their *coherent* (Bragg) scattering. For finding a solution in such a case the Schrödinger equation must be solved, where coherence and therefore constructive(destructive) interference of the electron wave-functions can be treated quantum mechanically.

In this connection, it should be mentioned that theories for electron transport in crystalline media exist for different surface characterisation techniques [107, 108, 109, 110] and are based on a rigorous treatment of the Schrödinger equation. However, the description is usually restricted to (elastic) peak intensities, whereas consistent treatment of energy loss processes is usually lacking (except for Ref. [110]). In these theoretical approaches, the creation, propagation and emission of SEs, which is the main subject of the present thesis, does not seem to have been even attempted presently. Loss of coherence, e.g. due to imperfections in a crystal, may formally be understood by the vanishing of the off-diagonal terms in the density matrix [111, 112, 113, 114], which describe quantum-mechanical interference. The problem of describing the electron transport in solids then reduces again to solving a Boltzmann-type kinetic equation.

The non-coherent electron transport in a solid is assumed to comprise elastic and inelastic scattering. Elastic scattering describes the interaction of an electron with the ionic subsystem of the solid. Such an interaction between the electron and a nucleus involves a deflection of the electron by the (screened) Coulomb field of the nucleus, accompanied by a small recoil energy loss. Due to the large mass difference between electron and nucleus this energy loss is negligible compared to any energy loss experienced in inelastic collisions. Inelastic scattering involves the interaction of an electron with the solid state electrons, accompanied by a small momentum transfer and a large energy loss compared to the recoil energy loss in elastic collisions.

Nonetheless, already for the non-crystalline case, where incoherent transport is admissible, to find a solution to the Boltzmann transport equation is a complicated task. Therefore, one has to resort to numerical solution techniques or to employ approximate approaches [115, 116].

Nowadays, a standard tool used for the simulation of particle transport and trajectories of scattered electrons employs the Monte Carlo method, which is based on a statistical sampling approach using random numbers[2] to solve determinable problems [9, 81]. Monte Carlo (MC) simulations for electron transport are therefore based on a stochastic description of the scattering process. These statistical calculations also employ different approximations for the microscopic scattering cross sections of electrons in targets and have managed to confirm many properties of SEE. The accuracy of a MC simulation, strongly depends upon the modelling of these scattering

[2]The solution to a problem by means of the Monte Carlo approach is obtained as a statistical estimate of a parameter describing the hypothetical population/ensemble considered. This latter is approximated by a random sequence of numbers constructing a sample of this population/ensemble.

processes, upon which formulae and assumptions are made. The MC technique has been described in detail by many authors in the literature, e.g. Refs. [117, 118, 59, 119]. Many of them employ the continuous slowing down approximation (CSDA) to describe multiple electron scattering assuming that energy fluctuations after a given path length are weak [59]. However, the CSDA-approach becomes questionable in the LE-regime, where the energy loss is not negligible with respect to the incident energy of the PE, having then an energy within the same order of magnitude.

In literature, various approaches based on different assumptions on how to treat electron interactions and transport in solid surfaces can be found. In Ref. [120], Dubus *et al.* presented a comparison of a series of Monte Carlo results, obtained using different sets of cross-sections for the case of a polycrystalline Al target. The various assumptions for the interaction cross-sections of the LEEs lead to significantly different calculated values for the SE-yields, thus reconfirming that the accuracy of a MC-simulation is determined by the underlying individual scattering model.

For practical reasons, in MC modelling, it is generally assumed that the sample is homogeneous in its chemical composition and that it exhibits an amorphous (or polycrystalline) structure. This assumption is necessary since in Monte Carlo simulations the scattering centres are randomly distributed within the interaction volume (which should be always larger than the grain size[3] of the target) and therefore electron transport is incoherent and relies on the solution the Boltzmann kinetic equation. For many applications, in which materials with short-range order are, in fact, employed, it is justifiable to handle electron transport by means of non-coherent scattering.

MC simulations usually do not treat crystalline samples, even though in principle it could be possible to describe a scattering process in a single crystal by employing Bloch waves instead of using plane waves [117]. Theories treating the electron transport in crystalline media exist for different techniques [107, 108, 122, 110] and they are all based on a rigorous treatment of the Schrödinger equation. However, the description is usually restricted to elastic peak intensities, whereas a consistent treatment of energy loss processes is usually lacking (except for Ref. [110]). In these theoretical approaches, the creation, propagation and emission of secondary electrons, which is the main subject of the present thesis, does not seem to have been even attempted presently.

At present, a number of different MC calculations are routinely applied to specific scattering problems. In general they employ already existing models with the implementation of variations on the electron scattering cross sections. In most of the cases these theoretical treatments were conducted on nearly-free electron (NFE) materials such as Aluminium [120] and seldom on insulators. In the latter case, to describe electron transport and emission is far more compli-

[3]Grains are crystallites in bulk materials. According to the American Society for Testing and Materials (ASTM) a grain is defined as the area within the confines of an original boundary observed on the 2D-plane of the volume enclosed by the original boundary in the 3D-object. The ASTM grain size number G defines the number of grains per unit area at a particular magnification. This number is defined as G= -2.9542 + 1.4427· $\log N$, where N is the number of grains/mm^2, G needs then to be compared in ASTM grain size chart to obtain the actual grain size [121]. According to this chart, average grain sizes range between 0.011 and 0.51 mm

cated, since in insulators also surface charging effects need to be considered. From experimental work, in fact, it is very well known that due to primary electron bombardment, the surface of an insulator charges up (either negatively or positively) thus enhancing or suppressing the yield of SEs.

For the case where incoherent electron transport is assumed, the description of elastic scattering requires the implementation of data describing the elastic mean free path (EMFP), the total and differential elastic cross section (DECS). Different codes are available for the calculation of the DECS. One of the most reliable and frequently used approaches is the ELSEPA code [123].

To describe inelastic scattering, data for the inelastic mean free path (IMFP), the total inelastic cross section and the differential inverse inelastic mean free path (DIIMFP) are required. The IMFP is defined as the path length an electron travels in between two successive inelastic collisions measured along the electron trajectory. The DIIMFP describes the distribution of single energy losses during the inelastic scattering process. The DIIMFP and IMFP can be obtained on the basis of linear response theory using optical constants [124, 125]. However, there is a huge spread in low energy ($< 100\,\mathrm{eV}$) IMFP values reported in the literature [63], which introduces limitations for the reliability of the MC simulation at low energies. A more detailed review on these physical quantities can be read in Refs. [9, 59, 60], to name a few.

During an inelastic interaction between a source electron and a valence band electron, generally the energy loss, ΔE, suffered by the incoming electron leads to a subsequent generation of a SE. Usually it is assumed that secondary electrons are mainly ejected from the Fermi level [117]. There was an attempt made by the authors of Ref. [119] to consider electron emission from anywhere within the valence band. As soon as in their model, a SEE-process considered to involve also electrons from valence bands with energies below Fermi, the resultant SEY exhibited an overall reduction of the yield, which no longer matched the experimental data. This reduction in the SEY was assigned to the fact that a larger fraction of SEs was assumed to have a smaller energy and consequently could not escape over the surface barrier.

Another related question is whether one should always consider in each energy loss the generation of a single secondary electron. Earlier work [126] as well as all experiments in this thesis suggest that the single electron generation process is dominant. However, the possibility of creating multiple electrons in a single collision cannot be ruled out.

Taking into account all the assumptions and limitations mentioned above, this makes the MC approach questionable, in particular for the investigation of LEEs. Nevertheless, MC simulations seem to work quite reasonably for many applications such as calculations of energy loss spectra and secondary electron yields [63] and is frequently employed by many authors.

In summary: most of the above-mentioned models were developed to describe experimental results obtained at HEs, where, despite the several simplifications and assumptions made on the SE-generation mechanism, they have been found to be a suitable description.

These theories are applicable only to homogeneous and non-crystalline targets, since the description of electron transportation is treated via the Boltzmann kinetic equation, which implies incoherent particle transport. Crystalline materials require the coherent electron transport to be solved quantum mechanically, which is seldom done.

The widely used "universal curve" for the SEY is based on a semi-empirical formulation, which per se implies that the underlying physical processes are not yet completely understood, evidencing once more the necessity for an improved theoretical approach to describe not only the yield of SEs, but also their energy distribution.

Most of these models fail in the LE-regime, due to the ineffectiveness and invalidity of some of the approximations they are based on and they turn out to be rather inadequate to describe electron scattering in ordered solid surfaces, where interference effects play a relevant role.

As it will be demonstrated by the experiments presented in this thesis, in the LE-regime – especially for electron energies below 50 eV – the influence of the target band structure dominates both the reflection and emission behaviours of both incoming and emitted electrons. At present, no rigorous treatment of these aspects, relevant to the generation and ejection of LEEs has been incorporated in any theoretical model.

For this reason, in order to describe the scattering mechanisms in surfaces with a long-range order, it is necessary to rely on models accounting for coherence and interference effects.

2.2 Electron Scattering and Secondary Electron Emission (SEE): The (e,2e) Process

The fundamental reaction channels of emission of SEs from a solid is represented by a single collision resulting in two electrons leaving the target (the *scattered* and the *ejected* secondary). To obtain the complete picture of the generation-ejection mechanism of this SE, it is necessary to collect information from both scattering partners participating to such an inelastic collision. Energy and momentum resolved measurements of these two electrons done by means of the so-called (e,2e)-coincidence spectroscopy enable to fully determine the kinematics and to give evidence of correlation effects. The (e,2e) technique consists in the impact ionisation of a bound electron induced by an incident electron [127, 128]; by measuring simultaneously the energy E_0 of the incident electron, both energies E_1 and E_2 of the two final electrons – which can be identified as scattered and ejected electrons (therefore in the following we shall refer to them with the subscripts *"s"* and *"e"*). By fixing the energy loss (ΔE) of interest and herewith the momentum transfer ($\Delta\vec{K}$) occurring during the collision, and the energy and momentum of the ejected secondary (E_e and $\vec{k}_e$) a large variety of kinematics can be selected, which in turn permit to choose certain conditions for which selected correlation effects can be either enhanced or diminished [129].

In the past 50 years the (e,2e) technique has gained more and more interest and has been already extensively applied by several research groups for the investigation of ionisation cross-section and for the understanding of surface properties.

The pioneering works by Amaldi *et al.* [130] followed by the work of Camilloni *et al.* [131, 132] had already demonstrated how (e,2e)-coincidence spectroscopy is an ideal tool for the detailed investigation of the ionisation mechanisms. (e,2e)-spectroscopy has been extensively and successfully employed for mapping the momentum distribution in gaseous targets [133, 134, 135] where the (e,2e)-reaction consists of an incident electron knocking-out (directly) an electron from the target. The principles describing these ionisation events, which are also applicable in case of solid targets, were further exploited in the study of bulk materials.

The study of solid targets is more complicated due to the fact that the energy transferred to the target by the primary electron can be re-distributed over the solid-state electron subsystem also via a sequence of plural and multiple scattering events (constituting the "cascade"), before an electron eventually manages to escape the surface-vacuum barrier. At first (e,2e) on solid targets was performed in transmission mode [136, 137, 138, 139] with high-energy incident electrons, later other groups started to perform (e,2e)-measurements in back-reflection geometry [140, 141, 142], where lower energetic primary electron beams could be employed.

(e,2e)-experiments performed in transmission mode need to be conducted employing high-

energetic primary electrons (or the order of 20 keV), with the advantage of the applicability of the binary-encounter approximation and the plane-wave description of both the incident and ejected electrons. On the other hand, in order to perform (e,2e)-measurements in transmission the specimen preparation is tedious since they have to be very thin ($\sim$80 Å).

Coincidence experiments between energy losses and secondary electrons have been performed by several groups in transmission mode [136, 143, 144, 145, 146] and in some of these experiments a direct link between the plasmon-decay process and the emission of SEs could be observed.

However not all of these experiments could lead to an unanimous statement concerning the role played by the bulk plasmon decay process in the production of SEs. It shall be noted that most of these earlier coincidence experiments were devoted to the study of SEs associated to energy losses in thin films of Carbon. Firstly, in most of these works, the authors report on the total number of secondary electrons detected in coincidence with specific energy losses, however do not fully resolve the coincident SE-spectrum. For this reason alone it is more difficult to associate the yield of SEs to a certain plasmon decay.

Even though their coincident energy loss spectra clearly exhibit a spectral feature associated to the bulk plasmon[4] in Carbon, in the coincident SE-spectrum no direct evidence for a bulk plasmon decay contribution could be established.

On the contrary, more recent (e,2e)-experiments conducted in reflection mode on Aluminium surfaces (single- and poly-crystalline) by Werner *et al.* [147, 148, 126, 149] and on a Beryllium single crystal by Di Filippo *et al.* [150] emphasise the relevance of plasmon decay in the generation of secondary electrons. In all of these experiments a large increase in the SE-yield was observed when the energy loss of the primary corresponds to the characteristic excitation energies of a surface and bulk plasmons, respectively. When measured in coincidence, the line-shape of the SE-spectrum together with the plasmon excitation, it becomes clear that a relevant portion of the ejected SEs is created when the plasmon energy and momentum are transferred directly to a valence band electron in the solid.

Owing to its high surface sensitivity, the (e,2e)-coincidence technique in reflection mode enables a better investigation of all those processes involving SEE at a surface-vacuum interface, thus unambiguously demonstrating that surface and bulk plasmon excitation/decay leads to secondary electron emission.

(e,2e)-coincidence spectroscopy in the reflection mode has been extensively applied by several groups since its first realisations. In Kirschner's group [141, 151, 152] (e,2e) experiments with LEEs were conducted using a time-of-flight (TOF) detection technique, which enables in-parallel acquisition of the correlated electron pair with with a significantly reduced accumulation time.

[4] A more appropriate and commonly known designation for this plasmon excitation in Carbon and graphitic surfaces is actually the $(\pi + \sigma)$-plasmon

Using this set-up they investigated how the distributions of the correlated electron pairs varies in dependence of the scattering experimental conditions, i.e. the sampled volume in the phase-space of the valence electrons changed according to the scattering geometry, which in turn lead to a variation in the detected (e,2e)-yield, since the valence electrons contributing (or not) to the (e,2e)-process also varied. Furthermore, they assessed that the asymmetry observed in the energy-sharing of the two final electrons originated from the asymmetry of the scattering kinematics, whereas in symmetric scattering conditions the correlated pairs, mostly generated by the specularly reflected beam, also lead to a symmetric energy-sharing of E_e and E_s.

The momentum density in Highly Oriented Pyrolytic Graphite (HOPG) was investigated by Iacobucci *et al.* [153, 140, 154] in grazing incidence with 300 eV-primary electrons; their experiments demonstrated that this technique is capable of resolving the complete electronic band structure in a solid.

The high surface sensitivity of this technique has been also exploited in experiments performed by further groups [142, 155, 126, 149] by studying the contributions to the correlated emission of electron pairs induced by the characteristic plasmon losses and by the surface states. In some other cases, also the spin effects were studied along with the observation of exchange and correlation effects [156, 157, 158].

The (e,2e)-experiments presented in this thesis were conducted in reflection geometry. When performed in reflection geometry, (e,2e)-measurements can be conducted on bulky targets, thus facilitating the sample preparation. Furthermore, the usage of reflection geometry enables to significantly decrease the source energies, which from the keV-range can then reach few hundreds of eV and below. These kinematics allows to investigate scattering phenomena occurring at the surface-vacuum interface due to their short probing depth [62]. In addition to its high surface sensitivity, by choosing suitable scattering conditions for (e,2e)-experiments in the LE-regime (for $E_0 \leq 100$ eV) it becomes possible to explore multiple Brillouin zones in the binding-energy-momentum-phase-space of the target [61].

In reflection (e,2e)-experiments, it is no longer possible to neglect elastic scattering; on the contrary, elastic scattering plays a crucial role in the whole kinematics of an (e,2e)-event.

In fact, the theoretical framework needed to properly interpret these experiments have to account for both the elastic scattering event and the inelastic collision, wherein the primary electron transfers energy and momentum to the solid-state electron system. In the case of crystalline targets, it has been furthermore demonstrated that the inelastic collision occurring during the (e,2e)-event is actually assisted by the elastic scattering event [159, 154]. In the next section only the kinematical conditions obtainable during an (e,2e)-experiment in reflection geometry are explained.

2.3 The Kinematics of (e,2e) in Reflection Geometry

In a well-ordered crystalline surface, the energy transfer and the kinematics occurring in an (e,2e)-event are fully defined through energy and momentum conservation laws:

$$E_0 + \varepsilon_{bin}(\vec{q}) = E_s + E_e + \Phi \tag{2.3}$$

$$\left(\vec{k}_{0,\parallel},\, k_{0,\perp,in}\right) + \left(\vec{q}_{\parallel},\, q_{\perp}\right) = \left(\vec{k}_{s,\parallel},\, k_{s,\perp,in}\right) + \left(\vec{k}_{e,\parallel},\, k_{e,\perp,in}\right) + \left(\vec{G}_{\parallel},\, G_{\perp}\right) \tag{2.4}$$

Here, E_l (with $l = 0, s, e$), represent the electron energies of the three electrons participating to the collision, $\vec{k}_l$ – separated in their parallel and perpendicular components – represent the total momentum components of the three electrons inside the solid. Φ is the workfunction of the target, $\varepsilon_{bin}(\vec{q})$ is the binding energy of the valence electron prior to its emission with its momentum $\vec{q} = (\vec{q}_{\parallel},\, q_{\perp})$ and finally $\vec{G} = (\vec{G}_{\parallel},\, G_{\perp})$ is the reciprocal lattice vector of the crystal, with it in-plane component for a given crystalline symmetry direction and the perpendicular component given along the $\hat{c}$-axis. Equation (2.4) is separated in the $\parallel$ and $\perp$ components to emphasise that, at a vacuum-surface interface only the parallel component of the electron momentum, namely $\vec{k}_{l,\parallel}$, is fully conserved, whereas in the bulk of the solid its energy and herewith the perpendicular component of its momentum ($k_{l,\perp,in}$) is changed upon transmission through the surface, under the influence of the crystal mean inner potential U_{in}.

When the incoming free-electron approaches and trespasses (or also when the scattered/ejected electron leaves) the solid-vacuum interface it undergoes refraction at the surface (Snell's law). Due to U_{in} when one of the l-electrons, involved in the (e,2e)-process, is inside the target it has a shorter wavelength, i.e. its kinetic energy increases to $\mathrm{E}_{l,in} = (\mathrm{E}_l + \mathrm{U}_{in})$, by means of which it gets accelerated inside (or decelerated when escaping into vacuum) of the material. Since $\vec{k}_{l,\parallel}$ remains constant, the excess in energy is compensated by a larger perpendicular component of its wave-vector, which then becomes

$$|\, k_{l,\perp,in}\,| = \frac{1}{a_0}\sqrt{\frac{2\,(E_l + U_{in})}{E_H}} \cdot \cos\theta_l{}^{in} \tag{2.5}$$

where $a_0 = 0.5291\,\text{Å}$ is the Bohr-radius, $\mathrm{E}_H = 27.2113\,\mathrm{eV}$ is the Hartree energy and $\theta_l{}^{in}$ is the angle (w.r.t. surface normal) inside of the solid, i.e. the $\theta_l{}^{vac}$ modified upon refraction. Hence, the perpendicular component of the electron momentum measured in vacuum is different (smaller) from $\vec{k}_{l,\perp,in}$. Due to refraction, the polar angle $\theta_l{}^{in}$ enclosed by this new $k_{l,\perp,in}$-direction inside of the target becomes smaller with respect to the actual angle of incidence/emission in vacuum

(${\theta_l}^{in} < {\theta_l}^{vac}$) and can be determined by

$$ {\theta_l}^{in} = \arccos \sqrt{\frac{\vec{k}^2_{l,in} - \vec{k}^2_{l,\parallel}}{\vec{k}^2_{l,in}}} \qquad with \qquad |\,\vec{k}_{l,in}\,|^2 = |\,\vec{k}_l\,|^2 \cdot \sin^2 {\theta_l}^{vac} + |\,\vec{k}_{l,in}\,|^2 \cdot \cos^2 \theta_{l,in} \quad (2.6) $$

The equation on the right-hand side of formula (2.6) is the modulo squared of the total electron momentum inside the solid, separated in its parallel and perpendicular components. The *conserved* parallel component $\vec{k}_{l,\parallel}$ can be calculated by using the known scattering polar angle ${\theta_l}^{vac}$ on the vacuum side.

In an (e,2e)-experiment, the three electrons with subscripts "0,s,e" are those being detected and their energies and momenta are known, since fixed by the experimental conditions. The bound electron with its $\varepsilon_{bin}(\vec{q})$ is then fully defined by means of equations (2.3) and (2.4), hence it is possible to determine from where in the band structure of the crystal the ejected electron originated. The (e,2e)-cross-section, i.e. the probability to detect correlated electron pairs, can be displayed in different forms. It can be expressed as the probability to detect a SE with a given kinetic energy (E_e) in correspondence of a specific energy loss process ($\Delta\mathrm{E}$) undergone by the incident electron, hence as an intensity of the pair ($\Delta\mathrm{E}, \mathrm{E}_e$). Alternatively, instead of $\Delta\mathrm{E}$, the scattered electron energy E_s can be used. In certain cases, it is however more significant to display this correlated electron intensity as a function of the initial state, hence with respect to the bound electron state, defined through its pair ($\vec{q}_\parallel$, ε_{bin}). By means of this representation it becomes possible to analyse the relevance of the initial state in the (e,2e)-event, thus finding out from where in band structure of the solid the ejected electron is more likely to escape under the given kinematical conditions. The (e,2e)-intensity associated to a specific initial state can be then displayed by projecting it onto the 2D (surface) Brillouin zone along the symmetry direction of interest.

For this reason, in most of the (e,2e)-experiments discussed in literature, it is the conserved parallel momentum components that play the role of major interest, whereas the perpendicular momenta are often left out of the discussion. As it will be shown in chapter 4 this is not always applicable, especially in materials exhibiting anisotropy such as in the case of HOPG. In (e,2e)-experiments performed at kinematics yielding a transferred momentum having both non-null parallel and perpendicular components it is essential to consider all symmetry directions for the proper interpretation of the (e,2e)-cross section.

Commonly, during an inelastic collision the impinging electron with (E_0 ,$\vec{k}_0$) looses energy ($\Delta\mathrm{E} = \mathrm{E}_0 - \mathrm{E}_s$) and its trajectory undergoes a rather small deviation, thus the momentum of the resulting inelastically scattered electron – defined by (E_s ,$\vec{k}_s$) – is diminished in magnitude, but it essentially remains directed in nearly the same direction as the incoming electron (*forward-scattering*). Such an inelastic process requires only small momentum transfers.

On the other hand, in reflection geometry, for an inelastically scattered electron to be detected

on the same side of the target, this implies that rather large momentum transfers – $\Delta\vec{K} = (\vec{k}_0 - \vec{k}_s)$ – are necessary. Only via large $\Delta\vec{K}$ it would then be possible to revert the direction of motion of the scattered electron for it to reach again the surface (*back-ward scattering*).

The scattering sequence describing such an inelastic collision is shown in figure 2.4 and is labelled as a "L" (loss) event. Here the vectors associated to the incoming electron are given in black and those associated to the scattered and ejected electrons are displayed in blue and red, respectively. Their polar angles $\theta_{0,s,e}$, defined with respect to the surface normal, are indicated in the same colour code. The situation depicted in fig. 2.4 shows all steps of the electron-solid

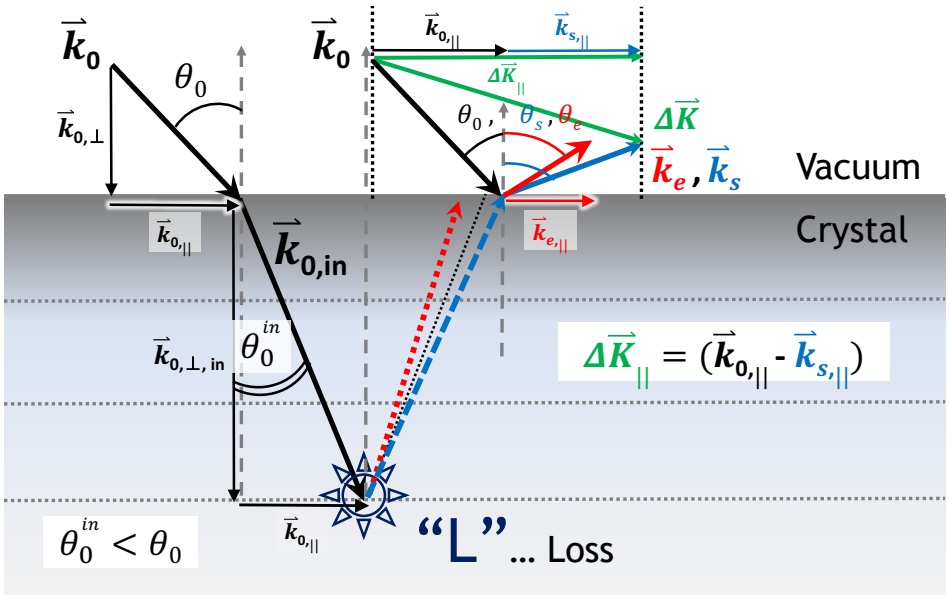

Figure 2.4: The "L"-kinematics describes the inelastic scattering process by means of one single energy loss event occurring at a large momentum transfer (see also Ref. [154]).

interaction. The incoming electron (black arrow on the left side) undergoes refraction as explained above, for it to undergo an inelastic collision inside the solid (marked by the blue star labelled "L"). The scattered and ejected electrons, originating in such event, reach the surface and after its crossing they are detected in vacuum with their respective energies and momenta ($E_{s,e}$,$\vec{k}_{s,e,\parallel}$). In the scheme shown on the left-hand side of the same plot, on the vacuum-side all three electron vectors are drawn as originating from the same point thus to facilitate the envision of their vectorial components and their projections onto the surface. The momentum transfer $\Delta\vec{K}_\parallel$ required in such an event is very large as visible by the length of the green arrow.

However, it has been experimentally demonstrated [153, 160, 154] and theoretically described [159] that in reflection geometry the probability for such large momentum transfers to be associated to only one single scattering event (as given in the "L"-sequence) is rather small. It is more likely for the momentum reversal of the scattered electron and for its inelastic collision to occur in the course of a two-step scattering mechanism composed of an elastic collision – a diffraction ("D")

event responsible for the back-scattering of the electron – and of an inelastic process wherein the incoming electron transfers energy and momentum to the solid.

The cross-sections measured in the experiments conducted by Iacobucci *et al.* [153, 161, 162] at medium kinetic energies (300 eV) under grazing incidence demonstrated that the ionisation mechanism is significantly enhanced when the alignment of the experiment is symmetric with respect to the direction of the specular reflected beam, thus confirming the two-step mechanism. Their (e,2e)-yield measured in dependence of the scattering angle exhibited the strongest assonance with theoretical predictions made upon assumption of an inelastic collision assisted by the elastic process, which in specular reflection conditions can be either given by a "LD"- or "DL"-sequence. Whereas, the theoretical prediction for the distribution of correlated electron pairs in the sole "L"-sequence expected a rather uniformly bland distribution, such as not detected by the experiment.

Soon after this was also confirmed by Artamonov *et al.* [160], who conducted (e,2e)-experiments in back-scattering kinematics employing very low-incident energies (20 eV). Their (e,2e)-CS was highest when the correlated electron pair was generated in a dual-step process, which also produced a more symmetric energy-sharing distribution.

Liscio *et al.* [154] performed a thorough investigation on the angular dependence of their (e,2e) differential-cross-section (DCS) analysing the validity of both scattering sequences, comparing the one single-collision sequence ("L") to the two-step scattering sequence – made of one diffraction ("D") and one loss ("L") event. They derive a six-fold differential-cross section[5] where the matrix element entails all possible interactions leading to the (e,2e) process. These include both the single- and the double-step scattering sequences.

Furthermore, they also investigated the DCS differentiating upon the sequence of the double-scattering mechanism, distinguishing whether the "L"-process, i.e. the electron-electron interaction, is precedent to or posteriorly assisted by the elastic scattering event of diffraction ("D"). These double-scattering mechanisms – "LD" or "DL" – can couple the elastic collision of the electron with the crystal lattice to its energy loss process either in an incoherent or in a coherent fashion. The kinematics in these two cases is discussed in the following.

In the "LD"-sequence (displayed in figure 2.5) the energy loss process occurs at a small momentum transfer and anticipates the elastic collision of the then scattered electron and can be therefore described as two following incoherent events. Figure 2.5 shows, just like in fig. 2.4, the source electron penetrating the target and undergoing refraction, followed by the "L"-event. However, this time the inelastic process is assumed to occur at small momentum transfers, hence as a forward-scattering event. The ejected electron (red) arising in the course of the loss-step reaches the surface and after its refraction is emitted into vacuum with its $\vec{k}_e$. The forward inelastically scattered electron (blue) undergoes an elastic scattering at the crystal lattice, in the

[5] Their DCS is differentiated over all available degrees of freedom: the energies of the two detected electrons, $E_{s,e}$ and the solid angles wherein these are detected, $\Omega(\theta, \varphi)_{s,e}$.

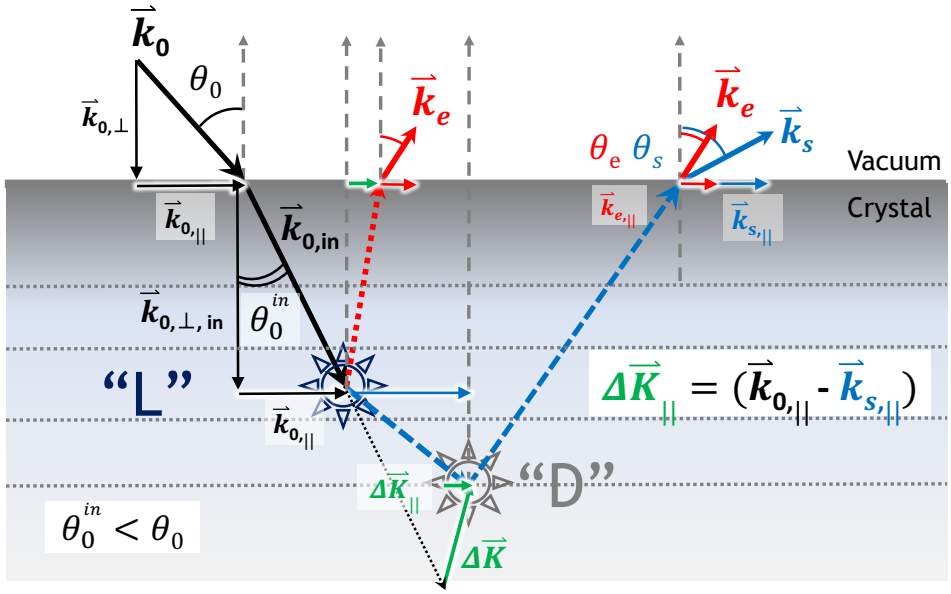

Figure 2.5: The "LD"-kinematics describes the ionisation process occurring in an (e,2e)-event as an incoherently coupled two-step mechanism, where the inelastic collision "L" precedes the diffraction event at the crystal lattice "D", the elastic collision responsible for the momentum reversal of the scattered electron. (see also Ref. [154]).

course of which its momentum is reversed, thus directing it towards the surface. After trespassing the surface it is detected in vacuum with its $\vec{k}_s$. Considering only the momentum components of the electrons in vacuum, it is possible to reconstruct the $\Delta\vec{K}_{\parallel}$, which now is visibly smaller than in the "L"-case.

Liscio et. Al. [154] demonstrated that the "LD"-sequence indeed better reproduces the measured (e,2e)-cross-section, however they obtained the best agreement between the measured intensity of the correlated electron pairs and the theoretical prediction for their angular distribution, when a coherent coupling of these two-scattering events – described by the "DL"-mechanism – was taken into account (consult fig. 4 in Ref. [154]). However, it shall be noted that when measuring in specular reflection, these two-step sequences are *per se* indistinguishable. Figure 2.6 shows the most probable sequence for the correlated electron emission in reflection geometry. After refraction at the surface the incident electron undergoes a coherent elastic collision, i.e. is diffracted by the crystalline lattice, for which its momentum is reversed. The wave-vector of the incident electron (in vacuum) after the "D"-process is labelled as $\vec{k}_0'$ to highlight the fact that due to the Bragg scattering event, the following ionisation process occurs as if the source electron originated from inside the crystal. In the subsequent "L"-step only small momentum transfers are required to explain the measured (e,2e)-intensity.

Once again, on the vacuum-side of the interface all three electrons participating to the (e,2e)-event are displayed with their wave-vectors – $\vec{k}_0'$, $\vec{k}_s$ and $\vec{k}_e$ – and their parallel components are projected onto the surface. The parallel component of the incident electron remains constant also for the $\vec{k}_0'$ vector. The magnitude of $\Delta\vec{K}_{\parallel}$ is very small in this dual-step sequence with respect to

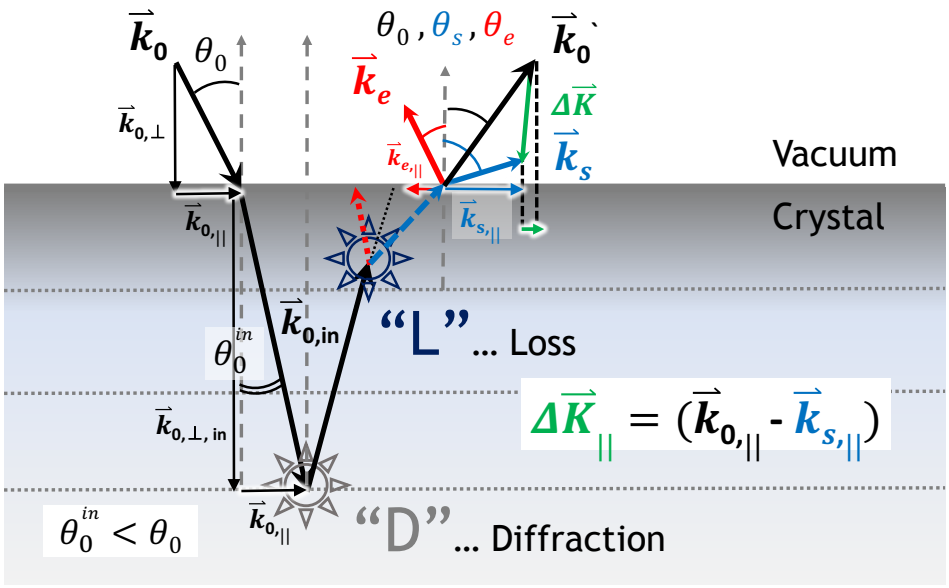

Figure 2.6: The "DL"-scattering sequence: here the inelastic process is preceded by the coherent elastic collision of the incoming electron with the crystal lattice. (consult also Ref. [154]).

the "L"-sequence.

Under the assumption that either path – "LD" or "DL" – leads to a same final state characterised by $|\vec{k}_s, \vec{k}_e\rangle$ it shall be pointed out that they nonetheless reconstruct two different initial states for the bound electron $|\vec{q}\rangle$ due to the different perpendicular components $q_\perp$ involved in the scattering process, as schematically illustrated by the vertical vectors in the mechanisms given in figures 2.5 and2.6.

All (e,2e)-experiments discussed in chapter 4 were interpreted according to this kinematics, for which the triple-differential (e,2e)-cross-section is described in the next section.

2.4 The (e,2e)-Cross-Section in the LE-regime

In this section the (e,2e)-cross-section for and experiment performed in the reflection geometry at low-incident energies ($E_0 \leq 100\,eV$) is described on the basis of the "DL"-scattering sequence previously presented. For the following experiments it is always assumed that in an ordered crystalline solid the ionisation process occurring in the (e,2e)-interaction is accompanied and sustained by a precedent elastic collision and these two processes can be treated incoherently.

In an (e,2e) collision in reflection geometry the two electrons participating to the ionising collision (labelled "s" and "e" in the following) are detected coincident in time and their energy and momentum, (E_s, $\vec{k}_s$) and (E_e, $\vec{k}_e$), are measured. In this way the kinematics under which the process takes place is fully determined and the probability for them to be collected into the solid angles $\Omega_s(\theta_s, \varphi_s)$ and $\Omega_e(\theta_e, \varphi_e)$ is measured. The herewith measured probability-flux corresponds to a yield of SEs obtained for each considered ejected electron energy at a specifically selected energy loss process.

The differential cross-section for such an (e,2e)-event can be written as a two-body interaction approximation yielding a triple-differential cross-section (TDCS):

$$\frac{d^3\sigma_{(e,2e)}}{d\Omega_s\, d\Omega_e\, dE_e} \propto \left(\frac{k_s\, k_e}{k_0}\right) \sum_{j_{occ}} |\langle \vec{k}_s, \vec{k}_e\, |\bar{T}_{(e,2e)}\, |\, \vec{k}_0, \vec{q}_j\rangle \times \langle \psi^{ion}\, |\psi^{N-1}\rangle|^2 \Big|_{\varepsilon_{bin}=-\Delta E+E_e+\Phi} \tag{2.7}$$

which is the six-fold DCS defined by Liscio in Ref. [154] integrated over the energy conservation. The TDCS in eq. (2.7) expresses the probability for the correlated electron emission differentiated in the two solid angles Ω_s and Ω_e. Furthermore, the measured correlated flux is expressed as a function of the ejected electron energy, which means that the previously six-fold DCS was integrated over the total energy E of the the process for all occupied valence electrons admissible by conservation law. The electron state $|\,\vec{k}_0,\, \vec{q}_j\rangle$ describes the initial state composed of the incident particle and the bound electron in the valence band, while $|\,\vec{k}_e,\, \vec{k}_s\rangle$ gives the final state of the two detected electrons. The sum is then performed over all occupied valence electron states $|\,\vec{q}_j\rangle$ in the target available for the defined binding energy. The amplitude $|\,\langle\psi^{ion}\,|\psi^{N-1}\rangle|^2$ represents the probability for a valence electron to be removed from a given j^{th} state $|\vec{q}_j\rangle$ from the ground state entailing N electrons, thus leaving the system in an ionised state $|\psi^{ion}\rangle$ with $N-1$ electrons. Under the assumption of the so-called frozen-core approximation[6] the amplitude $|\,\langle\psi^{ion}\,|\psi^{N-1}\rangle|^2$ assumes the value of a delta-function $\delta_{ion,N-1}$. The matrix element $\bar{T}_{(e,2e)}$ considers all possible

[6]For many quantum mechanical investigations it is convenient to employ the so-called "frozen-core approximation" (FCA) as the inter-atomic interactions are largely governed by the valence electrons. In the FCA it is assumed that, when condensed matter is formed by free atoms, only the valence electrons contribute to the interaction between atoms. The electrons close to the nuclei (core electrons) will only have a small influence on the properties of the solid. In the FCA nucleus and core electrons are regarded as a unit, i.e., the neutral atom consists of a positive, spherically symmetric ion and of valence electrons.

interactions leading to the correlated pair emission, entailing effective potentials accounting for various probable scattering events, e.g between electron and nucleus, electron-electron interactions.

This matrix element reduces to an effective one-electron transition operator projecting the initial valence state $|\,\vec{q}_j\rangle$ onto the final state $\langle\,\vec{k}_e\,|$, which equals the time-reversed scattering state of the ejected electron. This step brings the TDCS to following form

$$\frac{d^3\sigma_{(e,2e)}}{d\Omega_s\,d\Omega_e\,dE_e} \propto \left(\frac{k_s\,k_e}{k_0}\right) \sum_{j_{occ}} |\langle \vec{k}_s,\, \vec{k}_e\,|F(\vec{k}_0,\, \vec{k}_s)\,|\,\vec{k}_0,\, \vec{q}_j\rangle\,|^2 \Big|_{\varepsilon_{bin}=-\Delta E+E_e+\Phi} \tag{2.8}$$

with the simplified matrix element $F(\vec{k}_0,\, \vec{k}_s) = F_L + F_{LD} + F_{DL}$ consisting of three terms, representing the kinematical factors, each one of which describing one of the possible scattering sequences explained in the previous section. Incoherent summing of these three scattering sequences was found to be admissible based on the fact that all paths, in particular the ones considering the dual-step mechanism ("DL" and "LD") lead to the same final state for the free electrons.

As previously discussed, among all three of these possible scattering sequences, in our (e,2e)-coincidence experiment performed in reflection mode, it is admissible to consider only the "DL"-process, thus additionally simplifying the TDCS to

$$\frac{d^3\sigma_{(e,2e)}}{d\Omega_s\,d\Omega_e\,dE_e} \propto \left(\frac{k_s\,k_e}{k_0}\right) \sum_{j_{occ}} |\langle \vec{k}_s,\, \vec{k}_e\,|F_{DL}\,|\,\vec{k}_0,\, \vec{q}_j\rangle\,|^2 \Big|_{\varepsilon_{bin}=-\Delta E+E_e+\Phi} \tag{2.9}$$

In the quasi-free-electron approximation the wave-functions of both bound and ejected electrons – basically the wave-functions describing the same electron prior and after its emission over the vacuum barrier – can be both approximated by plane waves. The valence (bound) state is described as a plane Bloch-state of the following form:

$$\Psi_j = \langle \vec{r}_e\,|\,\vec{q}_j\rangle \propto \sum_{\vec{G}} c_{\vec{q}_j-\vec{G}}\, \exp\Big(i(\vec{q}_j - \vec{G})\cdot \vec{r}_e\Big) \tag{2.10}$$

Here the $c_{\vec{q}_j-\vec{G}}$ is the Bloch coefficient defined through the reciprocal lattice vector $\vec{G}$, of which the modulus squared $|c_{\vec{q}_j-\vec{G}}|^2$ yields the density of occupied states ϱ_j.

The wave-function of the ejected electron is then given by

$$\Psi_e = \langle \vec{r}_e\,|\,\vec{k}_e\rangle \propto c_{\vec{k}_e}\, \exp\Big(i\,\vec{k}_e\cdot \vec{r}_e\Big) \tag{2.11}$$

in this case $|c_{\vec{k}_e}|^2 \propto \varrho_{unocc}(\vec{k}_e)$ is proportional to the DOS of the unoccupied states with momentum $\vec{k}_e$ for the ejected electron.

The (e,2e) reaction that we want to describe, in fact, is not only modulated by the availability of occupied energy bands, whose density is described by the ϱ_j, but as it will be shown in particular for those (e,2e)-experiments performed on HOPG at low-impact energies yielding low-energy

secondaries (LE-SEs) the TDCS is also modulated by the momentum density of unoccupied states in the conduction band $\varrho_{unocc}(\vec{k}_e)$, hence above vacuum level.

For experiments conducted at a fixed final state, i.e. where energy and momentum of the ejected electron are fixed, while the energy losses measured allow to scan over different initials states for the bound electron, the obtained (e,2e)-cross-section is then essentially modulated by the matrix element, $F(\vec{k}_0, \vec{k}_s)$, and the momentum density of the initial states, ϱ_j. However, in such an experiment it is essential to make sure that availability of empty states is granted, through which the knocked-out electron manages to escape. In presence of energy gaps above vacuum level, even if the initial state of the bound electron is available for the kinematics of an experiment, its Bloch-wave-function will not match any free-electron wave-function above vacuum level, hence its promotion to the conduction band fails[7].

The effective (e,2e) interaction between the electron and the crystal can be approximated by a Coulomb interaction occurring between the electron and the ion-cores distributed over the whole lattice, where the crystal potential is represented by a screened-Coulomb potential of the ionic cores. A screened-Coulomb potential serves also to account for the electron-electron interaction potential.

If under these approximations, only the "DL"-sequence is considered (being the mostly relevant kinematics) the TDCS can be re-written as follows:

$$\left.\frac{d^3\sigma_{(e,2e)}}{d\Omega_s\, d\Omega_e\, dE_e}\right|_{DL} \propto \left(\frac{k_s\, k_e}{k_0}\right) \cdot |\, S_{\vec{k}_0'-\vec{k}_0}\,|^2 \cdot \Gamma_D(\vec{k}_0',\, \vec{k}_0)\, \Gamma_L(\vec{k}_0',\, \vec{k}_s) \cdot \varrho_{unocc}(\vec{k}_e) \cdot \left.\sum_{j_{occ}} \varrho_j \right|_{\varepsilon_{bin}=-\Delta E+E_e+\Phi} \tag{2.12}$$

where the term $|\, S_{\vec{k}_0'-\vec{k}_0}\,|^2$ accounts for the refraction at the surface, the sudden interruption of the crystal periodicity. The kinematical factors $\Gamma_D(\vec{k}_0',\, \vec{k}_0)$ and $\Gamma_L(\vec{k}_0',\, \vec{k}_s)$ are the square moduli of the Fourier transform of the interaction potentials. In the case of a screened-Coulomb potential these assume the form of

$$\frac{1}{\left[|\Delta\vec{K}|^2 + \vec{k}^2_{screen}\right]^2} \tag{2.13}$$

with $|\Delta\vec{K}|$ being the modulus of the momentum transfer in the collision and the $\vec{k}_{screen}$ the screening wave-vector, which equals the inverse of the screening wavelength $2\,\pi/\lambda_{screen}$. This latter describes the electric potential in a medium, when charges are increasingly screened. Screening of charges occurs for example, if a locally neutral electron plasma – given by an electron ensemble superimposed over a background of fixed positive ionic cores – is disturbed by the introduction of

[7]Some experiments conducted on HOPG in the LE-regime (for $E_0 = 50\,eV$) were performed for a fix final state of the ejected electron, in one case for a pair of (E_e, $\vec{k}_e$) coinciding with accessible unoccupied bands and in another case coinciding with a region in phase-space exhibiting an energy gap. Whereas in the formed case the (e,2e)-yield was found to follow the distribution of the occupied DOS, in the second case the TDCS was null, yielding no coincidence events at all. Such experiments highlight the relevance of the band structure playing a role in the SEE-process. The mentioned experiments are discussed in subsection 4.3.1 of chapter 4.

an external additional point charge of positive polarity. The sudden appearance of such positive charge in the electrically neutral medium can be for instance caused by the ionisation of this latter, wherein an electron is extracted from the background, thus leaving a positively charged hole behind. The remaining electrons in the medium will rearrange to compensate the additional positive charge of the hole, hence they will *screen* the hole-charge. This screening has the effect of annihilating the presence of this electric field at far distances. The higher the electron density n, the shorter the range over which electrons have to rearrange in order to establish an effective shielding.

In metallic surfaces, where the free-electron density is of the order of $10^{22}\,\mathrm{cm}^{-3}$ screening lengths are rather short, of the order of inter-atomic distances. In semi-metallic systems instead, such as for example Graphite and HOPG, the free-carrier concentrations are usually much lower (of ca. $10^{17}\,\mathrm{cm}^{-3}$) thus much larger screening lengths, of the order of hundreds of Ångstroms are to be expected [62].

In a nearly-free electron (NFE) metal like Al (characterised by high electron densities) λ_{screen} is very short and this also relates to strong plasmon resonances. Since both the short screening length λ_{screen} as well as the plasma oscillation ω_{pl} are related to a high electron density n, the former represents an alternate way to describe the collective behaviour of electrons inside a medium with metallic properties. In such a system, the plasma frequency is given by:

$$\omega_{pl} = \left(\frac{4\,\pi\,n\,e^2}{m_e} \right)^{1/2} \tag{2.14}$$

where m_e and e are the electron mass and charge, respectively. For Al the NFE-model is sufficient to describe its electronic properties, at least in the frequency range around the plasma frequency [163, 51], whereas in other materials, e.g. HOPG, to properly describe the electronic and screening properties (and consequently the energy loss spectrum) of the material, it is necessary to take the band structure into account, i.e. the assumption of a homogeneous background as given by a jellium is inadequate.

For a longitudinal electric wave (i.e. plasmon oscillation) to be sustained in a medium the real part of the complex dielectric function $\epsilon(\omega_{pl}) = \epsilon_1 + i\,\epsilon_2$, describing the polarisability (susceptibility) of this material, must vanish. Also to induce the oscillation of a plasmon, perturbation of the charge equilibrium in the medium is required (just like as previously described for the screening length). It is well-known that in an electron energy loss spectrum (EELS) many characteristic spectral features are intrinsically linked to the excitation(relaxation) of plasmons, for this reason it is generally convenient to express the EELS via the dielectric constant of a medium.

The TDCS given in equation (2.12) fully describes the (e,2e)-process, however accounting only for the "DL"-sequence of the ionising scattering process. The factors entailed in this TDCS are representative for the most relevant aspects to be accounted in a material.

In a material such as HOPG, an optically anisotropic and inhomogeneous material with lower

charge carrier density n, it seems more convenient to describe the collective response of this medium employing the quantity of λ_{screen} and to take inter-band transitions into account, which is then solved by the consideration of ϱ_j and $\varrho_{unocc}(\vec{k}_e)$.

The series of (e,2e)-experiments performed on HOPG and discussed in subsection 4.3.1 of chapter 4 are suitably interpreted by means of the TDCS defined in eq. (2.12).

On the other hand, for the case of Aluminium, which is among all NFE-metals, the one exhibiting strongest and sharpest plasmon resonances, our interpretation of (e,2e)-experiments relies on the formalism described by Kouzakov and Berakdar in Ref. [164]. Experimental results shown in subsection 4.3.2 of chapter 4 are compared with the theoretical model developed by these authors.

In their work Kouzakov and Berakdar set up the theoretical framework to theoretically describe plasmon-assisted (e,2e) interactions for metallic surfaces contemplating a direct-scattering mechanism. Presence of the characteristic plasma resonances of a *surface* and *bulk plasmon* losses, whose excitation is induced by the incident primary, leads to the promotion of a secondary above E_{vac}. To model the target, they employ a jellium, hence disregarding its real band structure, and describe its collective response utilising the dielectric function of the considered metal. In a jellium the electrons of the degenerate electron gas move within a positive uniformly distributed background created by the ionic cores. These electrons are bound solely via the definition of the surface potential barrier. Treatment of the potential barrier at the surface-vacuum interface is also included, which introduces abrupt changes in the response function. They contemplate a single electron-hole pair formation assisted by the plasmon excitation, in the framework of the random phase approximation (RPA) [165] for which it occurs at the critical value of the wave-vector, i.e. when the plasmon momentum exceeds the critical wave-vector $\vec{k}_c$ and merges with the electron-hole continuum. In the RPA, electrons are assumed to respond to the total electric potential (constituted by the sum of the potentials associated to the external perturbation and to the screening). In this environment only the potential associated to a specific wave-vector contributes to the dielectric function describing the medium, whereas contributions from the total electric potential are averaged out.

The electron is then ejected as a consequence of a single electron-electron interaction due to the screened-Coulomb potential of the surrounding medium. These screening effects lead to a resonant enhancement of the potential when the energy loss occurring during the electron-solid interaction coincides with the characteristic excitation energy of the surface and bulk plasmons. Their theoretical (e,2e)-cross-section exhibits highest intensity, i.e. highest SE-yield, exactly in correspondence of these two collective modes – i.e. in correspondence of the characterisitc excitation energies of a surface ($\hbar\omega_s = 10.5\,\mathrm{eV}$) and bulk ($\hbar\omega_b = 15\,\mathrm{eV}$) plasmon.

Their *Ansatz* for the determination of the fully-differential cross-section (FDCS), as they

name it, which was also assumed by Liscio, is defined as follows:

$$\frac{d\sigma}{dE_s\, d\Omega_s\, \Omega_e\, dE_e} = \left(\frac{\vec{k}_s\, \vec{k}_e}{(2\pi)^5\, \vec{k}_0}\right) \sum_{j_{occ}} \left\{ \frac{1}{4} \left| \langle \vec{k}_s \vec{k}_e \left| \mathbb{T} \right| \vec{k}_0 \vec{q}_j \rangle + \langle \vec{k}_e \vec{k}_s \left| \mathbb{T} \right| \vec{k}_0 \vec{q}_j \rangle \right|^2 \right\} + \tag{2.15}$$
$$+ \sum_{j_{occ}} \left\{ \frac{3}{4} \left| \langle \vec{k}_s \vec{k}_e \left| \mathbb{T} \right| \vec{k}_0 \vec{q}_j \rangle - \langle \vec{k}_e \vec{k}_s \left| \mathbb{T} \right| \vec{k}_0 \vec{q}_j \rangle \right|^2 \right\}$$
$$\times \delta(E_s + E_e + E_0 - {\varepsilon_{bin}}^j)$$

Just like in the case of the TDCS shown in eq. (2.7) the quantum states of $|\, \vec{k}_0 \vec{q}_j \rangle$ and $|\vec{k}_e \vec{k}_s \rangle$ describe the initial and the final two-electron states, where in this case the momenta of the final electrons, $\vec{k}_e$ and $\vec{k}_s$ have asymptotic character (plane-waves), the momentum of the projectile is given by $\vec{k}_0$ and of the valence electron in its unperturbed j^{th}-state by $\vec{q}_j$. The sum is performed over all occupied single-electron states having a binding energy of ${\varepsilon_{bin}}^j$. The matrix-operator $\mathbb{T}$ is and effective transition operator that induces the (e,2e) reaction under the assumption of a spin-independent system. This transition operator has the same form as the $\bar{T}_{(e,2e)}$ of eq. (2.7) and is treated within the FCA, which leads it to the following structure:

$$\mathbb{T} = V_s + W + (V_s + V_e + W)\, {G^+}_{se}\, (E_{tot})\, (V_s + W) \tag{2.16}$$

where V_s, V_e and W describe the effective electron-solid and electron-electron potentials, the ${G^+}_{se}\, (E_{tot})$-propagator describes the retarded two-electron motion in the overall potential, v, constituted by $(V_s + V_e + W)$ evaluated at the total energy given by the sum of E_s and E_e. This overall potential satisfies the Lippmann-Schwinger equation, thus allowing to treat the matrix element given in equation 2.16 up to the first order, leading to the distorted-wave Born approximation, which in simple words allows to treat the electron-solid interaction-potential separately from the electron-electron potential.

This brings the FDCS to a form where the wave-function of the incident, scattered and ejected electrons can be described by a superposition of a plane wave and the integral of this plane-wave interacting with the Green's function in the potential v. The matrix-element then reduces to the sole W-interaction potential which describes only the bare electron-electron interaction v_{ee}.

The dielectric response of the metallic sample (modelled by a degenerate electron gas) is used to calculate the (e,2e) rate. Within the framework of the RPA, the surface dielectric function $\epsilon(\vec{r},\, \vec{r}^{\,\prime};\, \omega)$ is used to describe the (dynamical) screening effects arising as a consequence of v_{ee}, thus yielding to the following expression for this electron-electron potential:

$$W(\vec{r},\, \vec{r}^{\,\prime};\, \omega) = \int d\vec{r}^{\,\prime\prime}\, \frac{1}{\epsilon(\vec{r},\, \vec{r}^{\,\prime\prime};\, \omega)}\, v_{ee} \quad , \quad v_{ee}(\vec{r}^{\,\prime\prime},\, \vec{r}^{\,\prime}) = \frac{1}{|\vec{r}^{\,\prime\prime} - \vec{r}^{\,\prime}|} \tag{2.17}$$

In eq. (2.17) the inverse of the dielectric function is evaluated at the energies $\hbar\omega = E_0 - E_{s,e}$, depending on the final state.

The theoretical treatment adopted for the description of the collective response of the medium was done in two different ways and details on these different approaches can be read in Ref. [164].

In essence, the authors proceed with the description of the bulk and surface dielectric response in the framework of the RPA and try two different paths. The model which yields the best results, thus resembling the most the experimental data which were available at the time of their publication (2012), defined both the bulk and the surface dielectric responses in the so-called hydrodynamic approximation (HA). The HA is a well-established way to describe the electron transport and optical properties of metallic (conducting) surfaces. Introducing a bulk dielectric function derived in this hydrodynamic limit and considering an infinite surface barrier, the theoretical (e,2e)-cross-section obtained was capable of describing most of the features observed in experimental (e,2e)-data of Refs. [147, 126].

The experiments discussed in Refs. [147, 126] were performed on two Al surfaces exhibiting different long-range order, an Al(100) single crystal and a polycrystalline surface. A third experiment, performed in the course of this thesis project is presented in subsection 4.3.2 and is discussed along with both experimental TDCS from Aluminium obtained by Werner *et al.* in 2008 and later in 2013. All experimental (e,2e)-cross-sections are compared with the theoretical predictions described by the presented formalism.

CHAPTER 3

Experimental

This chapter reports all experimental details relevant to the performed multiple investigations of the set of samples. A brief overview of the cardinal experimental requirements and precautions to be heeded when working on surface analysis experiments involving electrons of low kinetic energies are described in section 3.1. A survey on the physical properties and basilar characteristics of the chosen set of specimens, along with the procedure adopted for the preparation of their surfaces can be found in section 3.2. The instrumentation used for the investigations is described along with its fundamental characteristics. The most relevant notions concerning the experimental methods are discussed, highlighting those aspects which are particularly relevant for the performance of a certain measurement. For the acquisition of the data discussed in chapter 4 two different experimental apparatus were employed:

- The "SPECS-TEY"-chamber, described in subsection 3.3.1, was used for the measurement of Total and Partial (Secondary and Reflection) Electron Yields (TEY, SEY & REY). These experiments were conducted in the surface analysis laboratories under the supervision of Dr. Mauro Taborelli in the Vacuum Surface and Coatings (VSC) group of the Technology Department (TE) at CERN, where I spent a period of secondment within the EU ITN Project of SIMDALEE2[1].

- Results collected by means of single-electron spectroscopy – i.e. Angle-resolved Reflection Electron Energy Loss and Angle-resolved Secondary Electron Emission Spectroscopies (Ar-REELS & Ar-SEES) as well as Low-Energy Electron Diffraction (LEED) – and (e,2e)-coincidence spectroscopy experiments were measured in the "LASEC"[2] laboratory (treated in subsection 3.3.3) in the Science department of the Università degli Studi Roma Tre (RM3), where I conducted most of my thesis work. The experimental chamber of the "LASEC"-apparatus was modified during the first year of my PhD-project, where a novel

[1] SIMDALEE2 is a research and training network dedicated to the investigation of Low Energy Electrons near solid surfaces. The acronym of SIMDALEE2 stands for Sources, Interaction with Matter, Detection and Analysis of Low Energy Electrons. It is a Marie Curie Initial Training Network (ITN) financed by the European Commission (grant number 606988 under the FP7-PEOPLE-2013-ITN action of the EC).

[2] LAboratorio di Spettroscopie Elettroniche e Correlazioni

home-built electrostatic energy hemispherical mirror analysers (HMA) was assembled and then mounted into UHV. Among others, I was in charge of this assembly process and of the testing and calibration of this novel HMA (which in the following will be also called "R66" – due to its mean radius R_0 of 66 mm). After its calibration, this analyser was employed for the acquisition of both double- and triple-differential electron spectra. Some details on the characteristics of this HMA can be found in sub-subsection 3.3.3.1.

The characteristics of these two instruments are explained in detail followed by an accurate description of all experimental steps and strategies that are needed to (successfully) perform a given type of measurement. Especial emphasis is dedicated to the description of the experimental aspects of (e,2e)-Coincidence Spectroscopy, since this technique represents the main experimental tool exploited throughout this work.

3.1 Requirements and Precautions to heed when working with Low-Energy Electrons (LEEs)

The requirements for a correct performance of a surface science experiment employing LEEs are in short listed below:

- UHV-conditions to guarantee cleanliness and to minimise electron scattering with the rest-gas in the chamber.
- Thorough preparation of the sample surface: cleaning of the surface layers and restoring of the crystalline order at the surface.
- The (secondary) electrons must not be subjected to any stray magnetic or electric fields from the point of emission to the collector. Therefore, particular care shall be dedicated to the compensation and suppression of all such fields, e.g. Earth's $\vec{B}$-field.
- Space charge effects in the field free region must be avoided at all costs. All experimental parts have to be properly grounded or polarised accordingly.
- All contact potentials of the electrodes must be known and controlled. Therefore, the calibration of the energy scales and of the electron optical parts used for the transport of electrons towards the analysers are of paramount importance.

Low-energy electrons represent an ideal probe to investigate the surface and crystalline structure of a material. As already mentioned in the introduction, these LEEs have a short IMFP (with $\lambda \leq 10$ Å) which makes any spectroscopic technique based on such electrons very surface sensitive. Another aspect, which makes LEEs ideally suited to monitor the crystalline structure of surfaces is given by their de Broglie wavelength $\lambda_e = h/m \cdot v$, which for low-energies assumes values similar to typical distances in crystals and thus diffraction phenomena are to be expected and can be exploited for investigation.

The above-mentioned advantages of LEEs as a probe imply some experimental complications, which, on the other hand, need to be considered and cured to guarantee the correct performance of a surface science experiment.

Cleanliness is a mandatory key-requirement for all above-mentioned aspects. Impurities absorbed on the surface even in monomolecular layers may falsify the results. Thorough preparation of the sample surface is absolutely necessary. Common cleaning methods include flashing at high temperatures (to get rid of some of the adsorbed contaminants, such as water vapour) and erosion with energetic ions of noble gases (sputtering). To guarantee that the surface remains clean for several hours (or for the duration of an experiment) all procedures and measurements need to be performed in a ultra-high vacuum (UHV) environment (ideally in the low 10^{-9} to

10^{-10} mbar range) [166, 167, 61]). Furthermore, High-Vacuum (HV) and UHV conditions are also advantageous to guarantee that the electron mean-free path remains long with respect to the typical distances in an experimental vessel, otherwise scattering of electrons with residual gas would interfere with the actual measurement.

Typically, during a surface science experiment the analysis chamber is kept at a pressure in the low 10^{-9} mbar range, ideally even below (in the 10^{-10} mbar range). For example, in the LASEC laboratory during a running measurement the analysis chamber exhibits a pressure between $4.5–7.5\times 10^{-10}$ mbar [3]. Whereas in the SPECS–SEY laboratory, where the routinely performed surface science experiments are of short duration (in the order of few minutes), the base UHV pressure is of ca. $1.5–2.0\times 10^{-9}$ mbar.

To reach UHV pressures the removal of water vapour and other contaminants, e.g. Oxygen, Nitrogen, Carbon, CO, airborne Hydrocarbons, from the inside walls is required. This can be achieved only by baking the system to temperatures of about 150°C. The need of baking dictates a thorough selection of the materials that shall be used in the construction of the experimental chamber and impose the avoidance of materials with low vapour pressure [168].

To maintain UHV-conditions the experimental set-up is generally equipped with ion pumps, in addition to the "standard" pumping systems consisting of a series of primary rotary pumps, membranes, followed by turbo-molecular pumps [169].

Contaminants on the surface (even well below a mono-layer (ML) which is of the order of 10^{15} atoms/cm^2) can drastically influence the SEY, since they modify the surface workfunction and can also influence the Density-of-States (DoS) at the Fermi level, thus consequently inducing a variation of the SEY intensity and trend. For example, Hydrocarbons have per se a higher electron yield, therefore when present on a surface, the SEY will result to be higher than the SEY of the same, but clean surface. Whereas, if Carbon prevails in the ensemble of surface contaminants, the electron yield in this case could result lower than the expected value for the clean surface. (Carbon and graphitic materials are known to have a low SE-yield and this property, in fact, is exploited in many technological applications as stated in the introductory chapter). Furthermore, presence of such surface contaminants is known to induce a strong change of the elastic scattering at low energy [170].

Generally, the removal of the above-mentioned impurities as well as the topmost atomic layers of the sample by means of noble gas ion bombardment (Ar, Ne, etc.)[4] does not induce chemical reactions with the surface, but occasionally (depending on the surface morphology and electronic structure) some noble gas ion, e.g. Ar^+-ion implantation and adsorption, may occur. In most of the cases, these implanted ions can be removed by annealing the sample over 300°C. However,

[3] These "oscillations" in the base pressure are dependent on the surface type and its cleanliness, on the source used for the experiment (electron gun or X-ray source), it may depend on the outgassing of the filaments and of course it depends on the ambient temperature of the lab, which in spite of being furnished with an air-conditioning system, to maintain the temperature as steady as possible, it can be nonetheless subject of seasonal variations

[4] In both apparatus (at CERN and RM3) sputtering of the targets is performed employing Ar^+-ions.

there are some cases where implantation of Ar^+-ions cannot be effectively cured by "flashing" the target in UHV. One such a case is represented by the surface of Highly Oriented Pyrolytic Graphite (HOPG) due to its lamellar structure, which is also known to favourise intercalation [171]. Based on our experience, if Ar^+-ion (or also any other contaminant i.e. Nitrogen) implantation occurs on a graphite or a HOPG surface [172] the only possibility to cure it is to mechanically exfoliate the surface to guarantee removal of the first monolayers.

In case of single crystalline surfaces, the habitual sputtering procedure induces disruption and discontinuities, thus the crystalline order at the surface is no longer maintained. For this reason, the cleaning procedure of single crystals always combines several sputtering and annealing cycles of the target. To recover surface crystallography it is necessary to heat the sample up to a temperature characteristic for its surface melting point (*"flash-annealing"*). This is generally done in the final stage of the sample preparation procedure for the duration some minutes.

The sample and the quality of its surface preparation can be controlled by means of conventional surface analysis techniques, such as X-ray Photoelectron Spectroscopy (XPS) and Auger Electron Spectroscopy (AES), which are used to determine the chemical composition of the surface. XPS enables easy and fast identification of the elements present on the surface – with atomic numbers $Z \geq 3$ – and has a detection limit close to 1 at% (*atomic percentage*) in the probed depth of 1–3 nm for most elements. To check whether the long-range order of the surface has been properly restored during the procedure, Low-Energy Electron Diffraction (LEED) scans of the elastically reflected electrons are acquired [167, 173, 174]. The cleaning cycles are stopped when the checking methods, XPS, AES and LEED, show satisfactory results concerning contamination and the degree of crystallographic order (exhibiting sharp LEED patterns). The recipe adopted for the sputter cleaning and annealing of a sample varies with the type of target, but is also dependent on the UHV-conditions present in the experimental apparatus. Some examples of surface preparation recipes are given in the following section 3.2.

When working with very low energy electrons (of the order of few eV) it is mandatory to have complete control over stray and fringe fields of both electrostatic and magnetostatic nature, which may be present in the chamber.

A *stray* electric field $\vec{E}$ can occur on the surface of a conducting part in the chamber having in principle zero potential, with $V = 0\,V$ (i.e. at ground potential) across its surface, but due to the presence of some (accumulated) electrical charge the electric field, which is given by the gradient of the potential at its surface, thus results to be non-zero. For example, if the "snout" (the entrance) of the electron optical elements of a hemispherical mirror analyser (HMA) is not properly grounded, charge can accumulate onto its surface, due to the impingement of electrons coming from the target and entering the analyser slit. This can result in the presence of a stray electric field, which of course can lead to deflection and even repellence of further electrons, which will no longer be able to enter the analyser slit and therefore will not be detected.

The formation of a *fringe* electric field occurs for example at the entry and exit of a *real* hemispherical deflector or mirror analyser (HDA or HMA). These fringe fields can significantly degrade the focussing conditions, thus compromising the real energy resolution [175, 176].

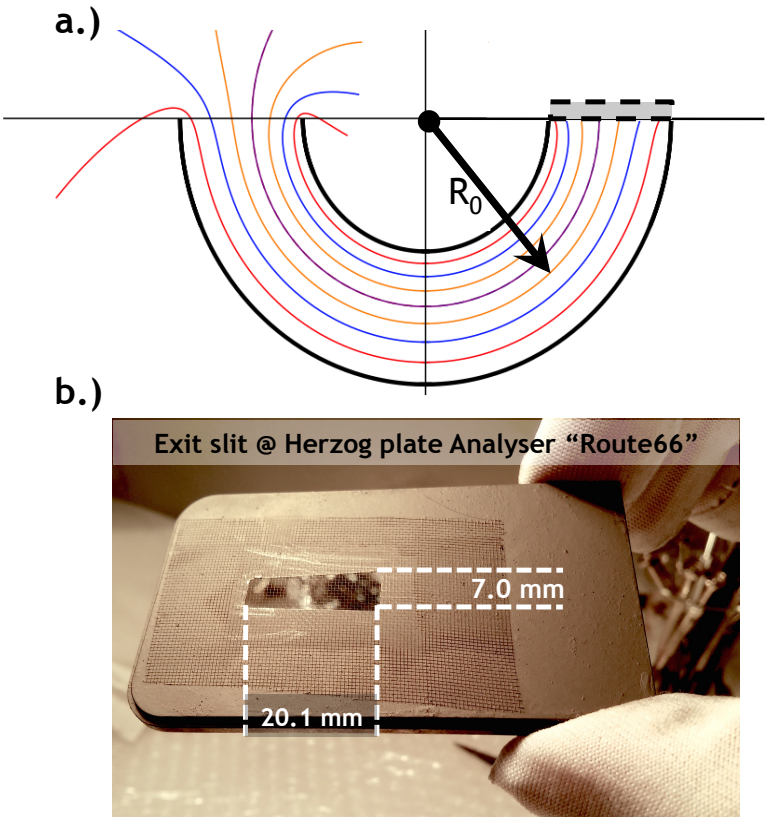

Figure 3.1: a.) Equipotential lines, equally spaced in voltage for cylindrical plates (a similar, but simplified geometry with respect to our real hemispheres in the analyser). On the left side, the sudden termination of the cylindrical surfaces induces the formation of *stray* fields, whereas on the right side the placement of a fine grid is symbolised. The presence of a mesh interrupts the transmission of the equipotential lines, thus diminishing the effects caused by the stray field. On the other hand, such grid-termination may introduce *fringe* field effects. **b.)** Tungsten grid with 96% transmission [177] on the exit slit of the HMA "R66", mounted on the Herzog-plate at the end of the electron path within the hemispheres before reaching the MCP-detector.

For example, at the ending part of finite hemispherical plates the equipotential lines of the electric field can reach outside the plates, thus giving rise to a so-called *stray* $\vec{E}$-field (see left-side of figure 3.1). Such stray field influences the electric field outside of the hemispherical plates (in nearby parts of the detection or transport system). As shown from the equipotential lines at the endings of the hemispherical plates, if not corrected, electrons moving within a stray field could either diverge or converge at the end of their paths in the hemispherical section, undesirably. Typically to improve the field termination conditions in a real HMA metallic mashes or grids are placed at the entrance/exit slits. This ensures a termination of the field at the end of the interested area and stray fields are diminished (as symbolised by the right-side of figure 3.1).

During the assembly of the HMA "R66" (see sub-subsection 3.3.3.1), the exit slit on the Herzog-plate[5] of this HMA was furnished with a fine Tungsten mesh of ca. 96 % nominal transmission [177] thus to avoid that the fringe field arising at the ending of the hemispheres would deflect electrons away from the microchannel plate (MCP) detector or could reach and interfere with the potential set at the MCP itself (see picture (b.) in figure 3.1).

[5]These are plates positioned at the entrance and exit of the electrostatic dispersive element, e.g. the hemispheres in a HMA, accommodating entrance and exit slits, respectively.

When electrons originating from the sample reach the entrance slit of the electron optic of an HMA they are transported (throughout the electrostatic lenses) towards the entrance slit on the Herzog-plate at the hemispheres. Electron scattering occurring within the various electrodes and hemispheres of the analyser may lead to an unwanted scattered background of (secondary) electrons. To suppress as much as possible this background and also to minimise the emission of additional SEs in the electrodes, the internal surfaces of analyser parts are generally coated with an aqueous graphitic solution (known as "aquadag" [178]). As already noted, graphite is per se a low-emitting electron material and therefore often used to minimise undesired effects linked to SEE. All parts of our "R66" analyser were uniformly coated by this graphitic paint before assembly.

A particularly sensitive issue, when making use of spectroscopic techniques based on the impingement and detection of LEEs concerns the presence of remnant magnetic fields in the scattering region and along particle trajectories. To minimise the Earth's magnetic field ($\vec{B}$) in the chamber parts one can either make use of a so-called *passive* magnetic shielding system, e.g. μ-metal shielding or place the instrumentation within a "Helmholtz cage" (representing an *active* magnetic shielding system).

Static magnetic fields or low-frequency magnetic fields can be minimised – ideally even compensated – by a μ-metal shielding, which consists of a concentric arrangement of thin shells of a high permeability (ferromagnetic) material[6] diverting the external magnetic flux around a region of interest – i.e. the $\vec{B}$-field lines are directed along these shells. In case of an *active* magnetic compensation, the apparatus is surrounded by a system of Helmholtz coils. The current flowing inside the coils is opportunely adjusted to generate an internal $\vec{B}$-field which has the opposite orientation of the Earth's magnetic field and its strength shall compensate the outer field at best in the region of scattering. Most of our measurements (shown in Chapter 4) are dedicated to the detection of very low-energy electrons (VLEEs) with typical kinetic energies of 3–20 eV. In order to be able to perform those measurements, we need to have full control of the magnetic field compensation in the experimental chamber. B-field compensation in the "LASEC" laboratory is done by means of a Helmholtz cage composed of three main coils and two intermediate coils, through which the currents I_x, I_y, I_z can be independently adjusted.

Minimisation of the Earth's $\vec{B}$-field influence inside the experimental chamber was performed by optimising the currents in the Helmholtz coils, thus achieving a remnant $|\vec{B}| \simeq 2\,\mathrm{mG}$ in the centre of scattering and of ca. 10 mG at a distance of 20 mm (from the centre of scattering). This is sufficient enough to ensure that for LEEs there is no sizeable deflection of the trajectories [179].

All the aspects mentioned above make clear that, especially when dealing with LEEs, a high degree of control on the instrumentation and its parts are indispensable to ensure an accurate apparatus performance.

[6]Generally, these μ-metal shields are composed of a ferromagnetic alloy composed of a Nickel–Iron mix of varying percentage.

3.2 The Set of Samples: Properties & Preparation

The set of specimens employed for the following investigations is composed of three elements – Aluminium, Carbon and Copper – in different allotropic forms and crystalline aggregations. Each of these elemental materials exhibits a sufficiently different electronic structure and has distinctive physical properties. For each of the mentioned materials, targets with a varying degree of long-range order were selected – single crystals and their poly-crystals or amorphous counterparts – and employed for several types of measurements, all aiming at the study of their SE-emission properties and reflectivity characteristics. In particular, comparative studies were performed among targets of a same elemental material, but different surface crystallography.

The aim for such an investigation is to separate contributions to the total electron yield (TEY) and to the SE-spectra associated only to the electronic structure from those additionally influenced by the geometrical arrangement of the target.

Aluminium was studied in the single crystalline form with a surface orientation along the (100) symmetry direction and was compared to measurements performed on a polycrystalline surface, which is composed of crystallite oriented along all available symmetry directions.

Two Carbon allotropes were measured: a Highly Oriented Pyrolytic Graphite (HOPG) and its amorphous counterpart in form of a technical surface; a Carbon coating (a-C) used to cover the beam pipes in the vacuum system of the LHC at CERN[7]. These two C allotropes possess the same microscopic structure, but manifest a completely different long-range and structural order. While HOPG exhibits a well-defined band structure, with given high-symmetry directions, for experiments performed on the a-C surface it is necessary to integrate over all crystalline directions, since the electron bands are randomly oriented.

Two different single crystalline Copper surfaces – Cu(100) and Cu(111) crystals – were used to highlight the importance of the role played by the (unoccupied) band structure in explaining the measured TEY at low impact energies (LE-regime). Also in case of Copper, measurements conducted on the polycrystalline surface were used for additional comparison.

[7]This a-C coating was prepared by means of magnetron sputtering in the laboratories at CERN [180].

3.2.1 Graphite, HOPG and a-C

Carbon (Z =6) is the forth most abundant element in the universe and the second most abundant element in the human body (after Oxigen). It's a polymorphic element capable of forming many allotropes. Well-known forms of Carbon include diamond, graphite, graphene and fullerenes. The physical properties of Carbon strongly vary with the allotropic form. For example, diamond is highly transparent, whereas graphite exhibits an opaque black appearance. The carbon-bonding in diamond involves sp^3 (tetrahedral) hybridisation, imposing a 3D-crystalline structure, whereas graphite consists of Carbon layers, also known as graphene layers, (displaying both covalent and metallic bonding in-between layers) stacked in an AB-sequence, linked by weak Van Der Waals force induced by the delocalised π-orbitals [181, 182, 183].

As suggested by its name, Highly Oriented Pyrolytic Graphite (HOPG) is a form of graphite with the highest degree of in-plane order extended over a 3D-crystalline structure, consisting of identical stacked graphitic planes with outstanding regularity and smoothness at nanoscale. The quality – associated to the degree of crystalline order along the $\hat{c}$-axis – of these specimens is generally defined by the so-called *mosaic spread* describing the angular spread in-between graphitic layers. The graphitic planes are, in turn, composed of a mixture of tiles oriented in all symmetry directions in-between the two main symmetry directions of graphite – ΓK and ΓM. In our laboratory at RM3, a HOPG specimen of the ZYA quality, with a nominal mosaic spread of $0.4^\circ \pm 0.1^\circ$, was employed. The same specimen was also used for the TEY-measurements performed at CERN.

Graphite and its highly ordered form (HOPG) have been subject of extensive investigations. Details on its band structures both in the occupied and unoccupied state can be read in Refs. [184, 185, 103, 186, 187, 188, 189] , to name a few. Electronic and structural properties of graphite studied by means of Electron-Energy-Loss and Secondary-Electron-Emission spectroscopy can be found in Refs. [190, 191, 192, 193, 140, 194, 195, 196]

The lamellar structure of graphite (and HOPG) is composed of graphitic planes exhibiting the characteristic honey-comb lattice and these stacked layers are weakly connected via Van der Waals bonds – which are responsible for the characterisitc cleaving behaviour. With its layered structure, this material is a prototype of highly-anisotropic, uniaxial crystals and gives an exemplary model for a layered electron gas (LEG) material [197, 198]. For this reason, it has been also subject of several (e,2e)-spectroscopy investigations [199, 200, 159, 201] among others.

The anisotropy of graphite manifests itself in its optical properties imparting this material a strongly differentiated dielectric response along its surface and along its crystal $\hat{c}$-axis. This anisotropy of its dielectric tensor, $\hat{\epsilon}$, can be brought in connection with excitations of valence band electrons, where distinct selection rules lead to the available inter-band transitions between the (occupied) valence band and the (empty) conduction band as well as collective excitations [202].

Panels in figure 3.2 show the Brillouin zones (BZ), both of the surface (b.) and over the three-dimensions (a.), and the band structure (BS) of graphite along the three main high-symmetry directions (panels (c.) (d.) and (e.)). Knowledge of the BS is needed to properly interpret the outcome of the experiments discussed in chapter 4. Panel (b.) of figure 3.2 represents the surface BZ of graphite where the two in-plane symmetry directions are highlighted by coloured arrows. The corresponding reciprocal lattice vectors along ΓM and ΓK can be calculated as shown in the inset.

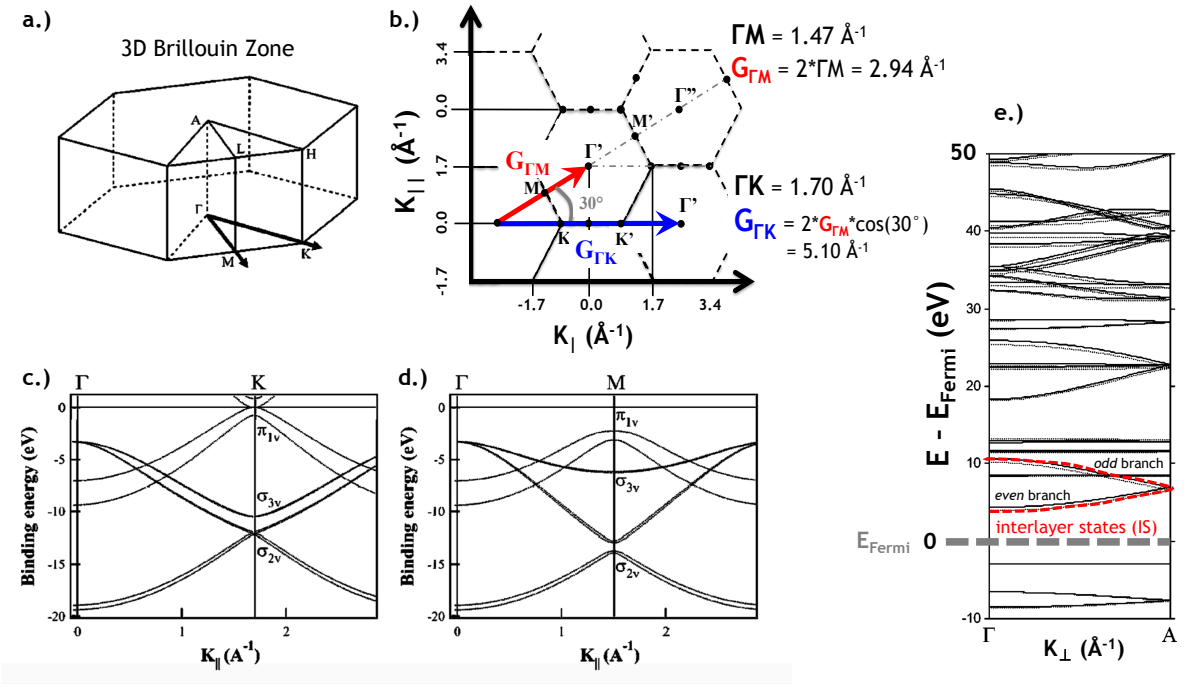

Figure 3.2: The band structure of Graphite: (a.) the three-dimensional Brillouin Zone (BZ), (b.) the two-dimensional first BZ along with neighbouring BZs. (c.) Occupied band structure (BS) given along the ΓK-direction with $\Gamma\bar{K} = 1.7031^{-1}$ and reciprocal lattice vector $G_{\Gamma K} = 5.10^{-1}$. (d.) Occupied BS along the ΓM-direction with $\Gamma\bar{M} = 1.4647^{-1}$ and reciprocal lattice vector $G_{\Gamma M} = 2.94^{-1}$. (e.) The ΓA-symmetry direction from -10 eV$\leq \varepsilon_{bin} \leq$ +50 eV, thus exhibiting both occupied and unoccupied states along the $\hat{c}$-axis. The bands highlighted in red represent the so-called "*interlayer states*" (IS) according to authors from Refs. [203, 204]. [Figures (a.), (c.) and (d.) were extracted from [183] whereas fig. (e.) was taken from [196] highlighting in red the interlayer states].

Fig. 3.2 (e.) shows mostly the unoccupied bands of graphite given along the perpendicular symmetry direction (ΓA) on an energy scale given w.r.t. the Fermi level. The bands highlighted in red represent the so-called "*interlayer states*" (IS), which according to Strocov *et al.* [196] (among others Pisarra *et al.* [204] and Bose *et al.* [203]) originate through a combination of even symmetry states in the unoccupied BS of graphite and are identifiable with regions of strongly localised higher DoS. While bands with odd symmetry can be responsible for the formation of *surface states*[8].

[8]Surface states are electronic states forming at the surface of a crystalline material induced by the sharp/abrupt transition from the bulk material terminated by the presence of a surface [205]. In 1932, Tamm [206] demonstrated the existence of such surface states by studying a model in which the surface atom was not equal to the bulk

HOPG or also the graphite(0001)-surface have been proven to be an inert surface at their basal plane [173]. Several LEED experiments have shown that there is no chemical adsorption of H_2O, CO, Oxygen, Iodine, or Bromine on the (0001) surface of graphite when kept in UHV at room temperature. A HOPG sample air-cleaved (or equivalently mechanically exfoliated in air), quickly inserted into a vacuum system and annealed (∼450°C for ca. 5 h) produces a clean surface as judged by authors of Ref. [173].

In the LASEC laboratory, the HOPG-surface was prepared by means of mechanical exfoliation followed by a cycle of annealing (up to a maximal temperature of 480°C, measured using an optical pyrometre). The annealing cycle generally lasted over a period of 2–3 hours. Exfoliation of the surface helps to expose a fresh uncontaminated surface. Annealing in a ultra-high vacuum (UHV) environment is necessary to get rid of adsorbed and intercalated water. Residual gas analysis during the annealing showed that the water was successfully removed.

At CERN, the maximal temperature achievable by the heating filament is of 300 °C, for this reason we preferred to anneal the specimen over night (for about ten hours). In either case, the maximal pressure reached during the annealing cycles was always kept below 3×10^{-8} mbar. Based on our experience, even if the annealing treatments were performed at temperatures well below the melting point of graphitic surfaces (with its sublimation point at 3825°C), a prolonged heat transfer seems to make the surface smoother and more uniform at macroscopic scale, which also helps to obtain a well-ordered surface at microscopic scale. This observation is in fact well-supported by the statements found in Ref. [173] concerning the preparation of this surface.

The cleanliness of the surfaces was verified by means of X-ray Photo-electron Spectroscopy (XPS). XPS is the most widely and routinely used spectroscopic tool for analysing the surface chemistry of a material. By means of XPS it is possible to measure the elemental composition, the chemical state and the electronic state of the elements within a material. The target is irradiated by a beam of X-rays while the kinetic energy and the distribution of the emitted electrons is measured. These ejected electrons originate roughly from the top 1–10 nm of the irradiated material, hence they carry characteristic information from the surface layers [48, 61]. Throughout this work XPS was only used to monitor the cleanliness of target surfaces prior and after the

atoms. Through such crystallographic cut of the material, the Fermi energy is shifted into a band gap for electrons propagating normal to the surface. These surface states – found only at the atom layers closest to the surface – have a discrete energy spectrum; their wave functions exponentially decay with distance from the surface in the directions toward both the crystal bulk and the vacuum. For such electrons, with wave functions of decaying amplitude in both directions, movement in the surface plane is still possible thus giving rise to a two-dimensional electron gas. They exhibit a large local Density-of-States (DoS) at the surface, thus additionally increasing the number of electrons per surface atoms. These types of surface states were identified by Shockley [207]. Such a Shockley surface state exists in a gap between an *s*- and a *p*-band, when the bands have crossed, when the gap is "inverted", when the state at the bottom of the gap has *p*-character and at the top of the gap has *s*-character. On the clean surface of semiconductors (HOPG), the density of surface states equals the density of surface atoms, whereas in NFE- and transition metals this can be additionally enhanced.

habitual cleaning procedure. The kinetic energy of the photo-emitted electron depends upon the photon energy ($h\nu$) and the binding energy (E_{bin}) of the electrons prior to their emission, required to remove the electron from its bound state. The minimum amount of energy required to remove an electron from a surface equals the workfunction (Φ) of the apparatus[9] Their energy relation is linked via Einstein's *photo-electric equation* ($E_{kin} = h\nu - E_{bin} - \Phi$).

In the LASEC laboratory, a monochromatic Al Kα X-ray source with a photon energy of 1486.7 eV is used and the analyser workfunction is ca. 4.2 eV. Oxygen, Carbon and Nitrogen are the most common contaminants present on a surface. For this reason, to determine their presence(absence) acquisition of the photo-electron spectrum is generally performed by scanning over kinetic energy ranges corresponding in turn to the characteristic binding energies of the core-level electrons of these elements. The characteristic binding energy of the core-level electrons in Oxygen (O_{1s}) is 529.5 eV, the core-level energy of a C_{1s} electron is 284.8 eV whereas the one of N_{1s} is 397 eV.

In case of HOPG, the intensity of the C_{1s} peak was measured (shown in panel (a.) of figure 3.3) and spectral portions shown in panels (b.) and (c.) demonstrate the complete absence of both Oxygen and Nitrogen. Red arrows indicate the binding energy (E_{bin}) and the corresponding kinetic energy, where one should expect the appearance of peaks corresponding to these elements.

To check the quality of the surface crystallographic order, we routinely employed Low-Energy Electron Diffraction (LEED). For a brief review on the principles of LEED see subsection 4.2.1. In the LASEC laboratory, the freshly prepared surface is bombarded by a monochromatic electron beam of a given excitation energy E_0. The elastically reflected electrons are collected by an electrostatic energy analyser tuned on the energy E_0, while the polar angle of incidence θ_{in} (and of emission θ_{out}) is varied by rotating the sample surface normal with respect to both electron source and analyser. The elastically scattered electrons were measured using the analyser "R66". More information concerning both electron gun and analyser are entailed in subsection 3.3.3. During such an angular scan the azimuthal angle of the sample is kept constant, $\varphi = const.$ The diffraction pattern shown in figure 3.4 was measured using 91.73 eV-primary electrons, while the sample was rotated on its polar axis in steps of 0.25°. The average width (measured at FWHM) of the diffraction peaks for this HOPG sample was found to be comprised between 0.5° and 1.3°.

The intrinsic beam width of our monochromatic electron source (in the LASEC laboratory; see also subsection 3.3.3) is of ca. 0.5°, hence in the case of HOPG it is very close to the value of the sample nominal mosaic spread. For this reason, it is not possible to unambiguously assign

[9]The "apparatus" is the measuring system, composed of target and analyser. Generally, both the target potential and the potential of the analyser involved in the experiment are connected to ground through the experimental chamber, hence their Fermi levels are aligned. The workfunction of the analyser is usually well known, since all of its elements are coated by a low-emitting layer of "aquadag" [178] which minimises the emission of additional SEs from the analysers' walls. This coating has the workfunction Φ = 4.2 eV. The kinetic energy scale of the photoemitted electrons is therefore referred to the workfunction of the analyser. If the workfunction of the material is higher than the one of the analyser detecting the photo-emitted electrons, then one considers the Φ in the photo-electric equation to be the one related to the sample. In case the workfunction of the target is lower than the workfunction of the analyser, then it is the latter that needs to be considered.

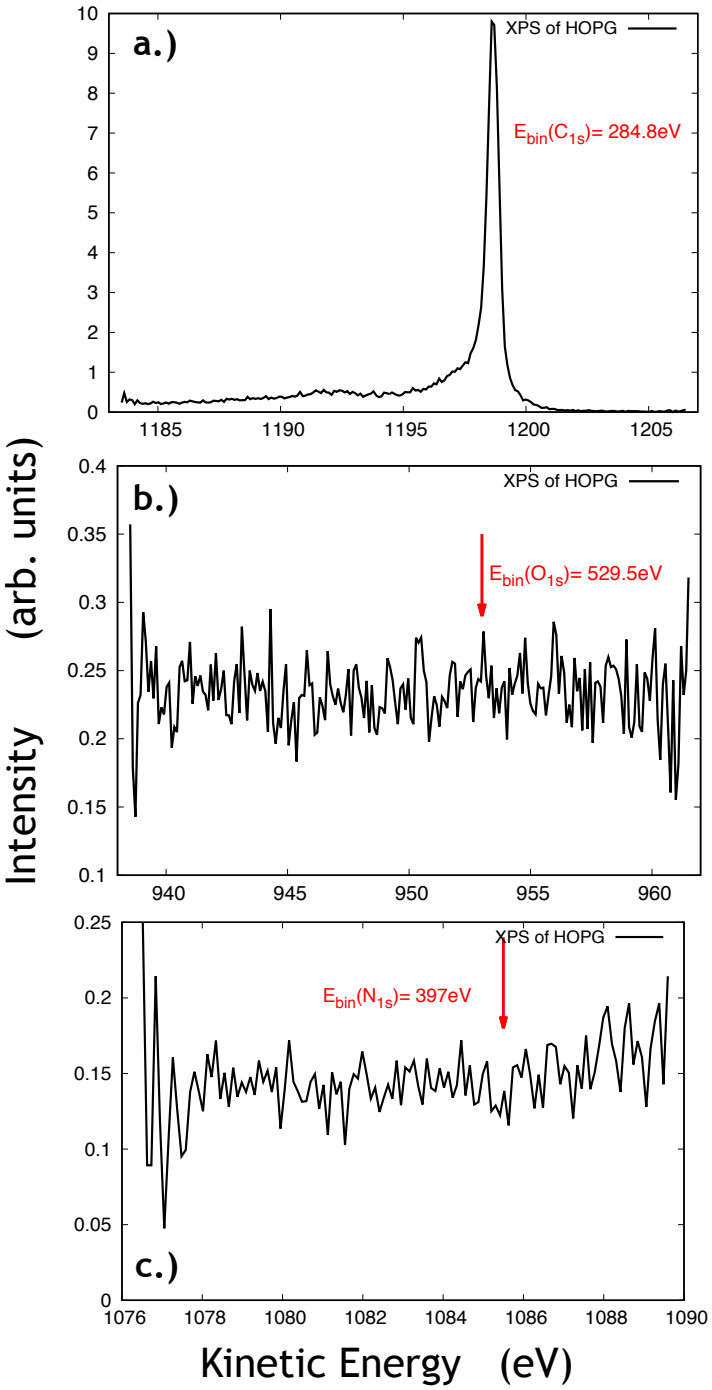

Figure 3.3: XPS spectra acquired after the annealing of HOPG and used to monitor the cleanliness of its surface. Panel (a.) shows the C_{1s} peak and panels (b.) and (c.) demonstrate the absence of both O_{1s} and N_{1s} peaks, exhibiting only a signal background.

the measured 0.5° to the mosaic spread of the ZYA HOPG sample.

The upper scale in fig. 3.4 indicates the real incidence angle, θ_{in}, given with respect to the $\hat{c}$-axis, during the experiment. Correspondingly, the bottom scale displays the angle of emission. The analysis of the diffraction pattern (explained in subsection 4.2.1) revealed that for this primary energy E_0 and kinematics, both symmetry directions contribute to the diffusion of scattered electrons. A first order diffraction peak along the ΓK-direction was measured (indicated

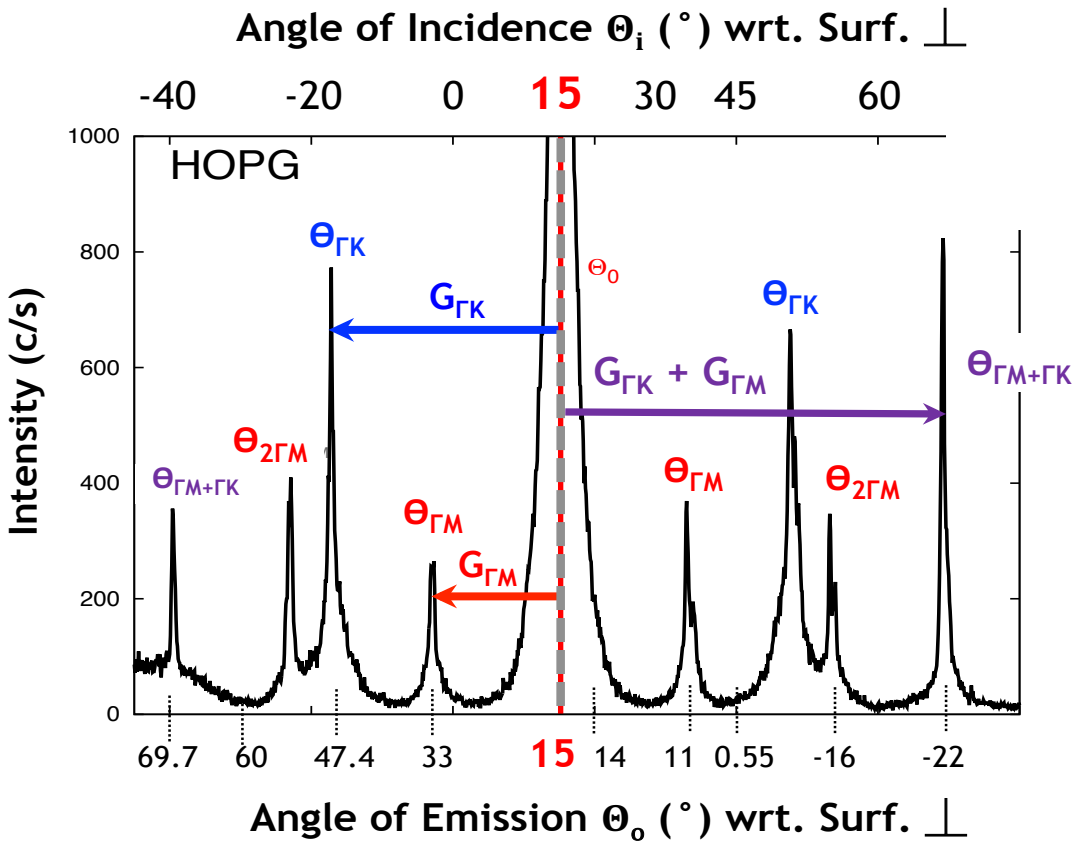

Figure 3.4: Diffraction pattern from HOPG of the elastically scattered electrons (E_0 = 91.73 eV). Specular reflection conditions of $\theta_{in} = \theta_{out} = 15°$. The specular peak has an angular width of 0.5° at FWHM, which corresponds to the intrinsic width of our monochromatic electron beam. Diffraction peaks given along the two main symmetry directions of ΓK and ΓM as well as intermediate ones are indicated by coloured arrows.

by the blue arrow) for which $\Delta K_{\parallel}$ yielded the reciprocal lattice vector $|\vec{G}_{\Gamma K}|$ =5.10 Å^{-1} for the ΓK-symmetry direction. Diffraction peaks along ΓM-direction were measured up to the second order Bragg-diffraction (with the first order diffraction peak indicated by the red arrow with $\Delta K_{\parallel} = |\vec{G}_{\Gamma M}| = 2.94$ Å^{-1}). The parallel component of the exchanged momentum $\Delta K_{\parallel}$ calculated for the two outermost diffraction peaks, yielded a mixed reciprocal lattice vector corresponding to the sum of $|\vec{G}_{\Gamma K} + \vec{G}_{\Gamma M}|$ (purple arrow).

The acquisition of such a diffraction pattern was routinely done after each sample preparation cycle and after running an (e,2e)-coincidence measurement for a few days. The regular acquisition of diffraction patterns was also used to monitor the status of the surface in between measurement cycles. Generally, the annealing of the sample was done on a weekly basis to preserve its cleanliness and order. A prolonged irradiation of the target, even if by means of electron beams of very low primary currents (in our experiments we use electron sources with currents of the order of 0.5–15 pA) ultimately leads to alteration and contamination of the surface, which therefore needs

to be re-cleaned.

By monitoring the shape, width and the intensity of peaks it is possible to check the quality and the crystalline order of the surface. The LEED pattern shown in figure 3.4 represents one of the various LEED-scans performed on this sample after a cycle of annealing. The diffraction peaks are sufficiently narrow and the Thermal Diffusion Scattering (TDS) background [166] is very low in comparison the the peak intensity, thus demonstrating the recovery of the surface crystallography. Nonetheless, a higher TDS background – generally associated to a lack of long-range order – is observable over a small angular region $\theta_{out} = (60° - 70°)$. This higher TDS contribution is caused by the fact that at those rotation angles the sample surface was no longer aligned along the manipulator rotation axis. Due to such a mismatch between the rotation axis and the surface axis, illumination of lateral (hence unordered) sample regions is induced, which in turn leads to a higher multiple scattering background.

An amorphous – hence lacking any crystalline order – Carbon coating (a-C) typically used to reduce the TEY in the beam-pipes of the vacuum system in the LHC [27] was prepared for the TEY-investigations. This sample was investigated at CERN, where TEY-measurements were performed along with those from HOPG. The a-C coating was sputtered with 3 keV Argon ions and the cleanliness of the surface was monitored by means of XPS during sputtering. The annealing cycle was performed for ca. two hours at a maximal temperature of 250° C. In this case a lower temperature was chosen to avoid detachment of the coating from the substrate.

Comparison between TEY-curves acquired on these two C allotropes was performed to study the dependence of the electron yield as well as of the SEE-behaviour on the electronic structure as well as on the long-range order of a sample.

3.2.2 Al(100) and its polycrystalline counterpart

Aluminium (Z=13) is the most abundant metal in the Earth's crust (8.1%) and since its discovery in 1825 by Oersted it has been one of the mostly investigated elements and not least for its exploitation in a huge variety of products. It has low density (with 2.7 g/cm^3) and high thermal and electrical conductivity. Moreover, this non-magnetic metal has an excellent corrosion resistance, is easily malleable and highly ductile. In technical applications, Al is mostly combined in alloys, since by itself it is not particularly strong, but in alloys with Copper, Manganese, Magnesium and Silicon it remains lightweight, but becomes stronger. Nowadays, these types of Al-alloys are routinely used in the construction of aeroplanes and other forms of means of transport.

Both the electrical and the magnetic properties of a metal strongly depend on its band structure, or its electronic dispersion $\varepsilon_{bin}(\vec{q})$, i.e. on how the binding energy of an electron varies as a function of the crystal wave-vector $\vec{k}$. The electronic structure of Aluminium has been firstly calculated by Heine in 1956 [94, 95, 96] on the basis of x-ray photon-spectroscopy measurements performed by Skinner in 1938 [208] which were used to determine both the lattice structure of the Al-crystal and the inner-shell structure of the Al atoms. Several authors after continued to investigate its electronic [209, 210, 211] and optical properties [212, 213, 214]. The occupied bands of Al display a dispersion which was found to be in qualitative agreement with the nearly-free-electron (NFE) model according to Sommerfeld and self-consistent band calculations. Figure 3.5 (a.) shows the bulk band structure of Al along all high-symmetry directions, which are also marked on the bulk Brillouin zone of a fcc-metal shown in panel (c.) of the same figure. This band structure extends from the occupied to the unoccupied states up to a binding energy of ca. 18 eV above Fermi level. Panel (b.) of figure 3.5 shows the surface symmetry direction of ΓX (whose reciprocal lattice vector is 1.1 Å^{-1}), along which most of the experiments shown in chapter 4 were performed. The Al(100) surface exhibits a sharp *surface state* of Shockley-type (indicated by open circles) within the energy gap (hatched area) around the X-symmetry point [210].

As visible from figure 3.6, this NFE-metal has a nearly continuous density of states (DoS) both in the occupied and unoccupied states. Therefore, for an electron originating from whichever occupied band below Fermi level it is highly probable for it to escape above E_{vac} for any kinetic energy value of its ejected SE, since availability of empty state is always granted. As mentioned in the introduction the secondary electron yield (SEY) of Al has been extensively studied by many authors, however the discrepancies found in these measured SEY-curves [71] emphasise that the need for accurate experimental data on secondary electron emission is still an important topic.

The energy loss region in the electron spectrum of Aluminium exhibits characteristic spectral features attributed to the typical collective excitations of surface ($\hbar\omega_s = 10.5$ eV) and bulk ($\hbar\omega_b = 15$ eV) plasmons. In Al the plasmon-losses are strongly pronounced due to the strong

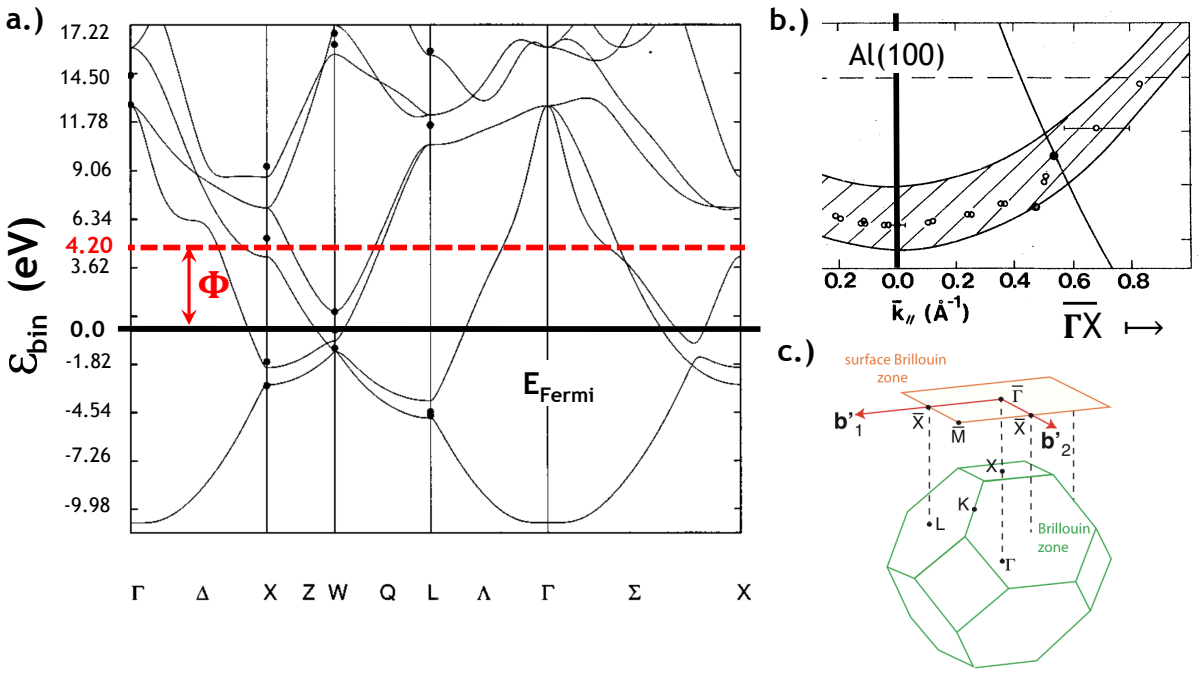

Figure 3.5: Panel (a.) shows the calculated band from Aluminium, according to Ehrenreich *et al.* in Ref. [212] with its high-symmetry points. The bands of Al have a free-electron-like character except in proximity of the Brillouin-zone boundary where degeneracy of electron bands are split by the weak periodic crystal potential. The binding energy scale ε_{bin} is given in eV (translated from Rydberg-energy scale). Panel (b.) gives the surface band structure given along the 2D-ΓX-symmetry direction. The hatched area marks the energy gap of Al wherein the surface states are given as open dots [Fig. extracted from Ref. [210]]. Panel (c.) displays the bulk Brillouin zone (green) for Aluminium (or for a *fcc* solid in general), where on the upper part the 2D-Brillouin zone (orange) is also shown. [This figure was extracted from Ref.[61]].

electron-plasmon coupling in this metal. Figure 3.7 shows the optical data [125] of Al. The dielectric function ϵ is linked to the polarisability of the material, thus it represents its efficiency to screen (or to respond) to the perturbing electric fields created e.g. by the impingement of electrons or photons. From the trend of $\mathfrak{Re}(\epsilon)$ it is possible to determine the phase lag between the driving and response frequency (ω) of the material to this external perturbation.

When the $\mathfrak{Re}(\epsilon)$ crosses zero a the collective mode of a plasmon excitation can be excited and sustained in the medium. If the frequency is lower than this zero-crossing, the real part is negative meaning that the light is completely reflected. In such a case, the electrons at the surface can screen the electric field of the light before this latter can penetrate into the bulk. If the frequency of the impinging photons (or the energy of the electrons) is higher than the plasmon frequency, the real part is positive and the metal behaves like a dielectric medium. The imaginary component of ϵ represents the damping factor with which this oscillator is damped and describes the loss of energy or absorption of light. In Al these characteristic collective modes of these plasmons are particularly pronounced features in the electron spectrum. For this reason, this NFE-metal represents an ideal candidate for the study of these collective modes.

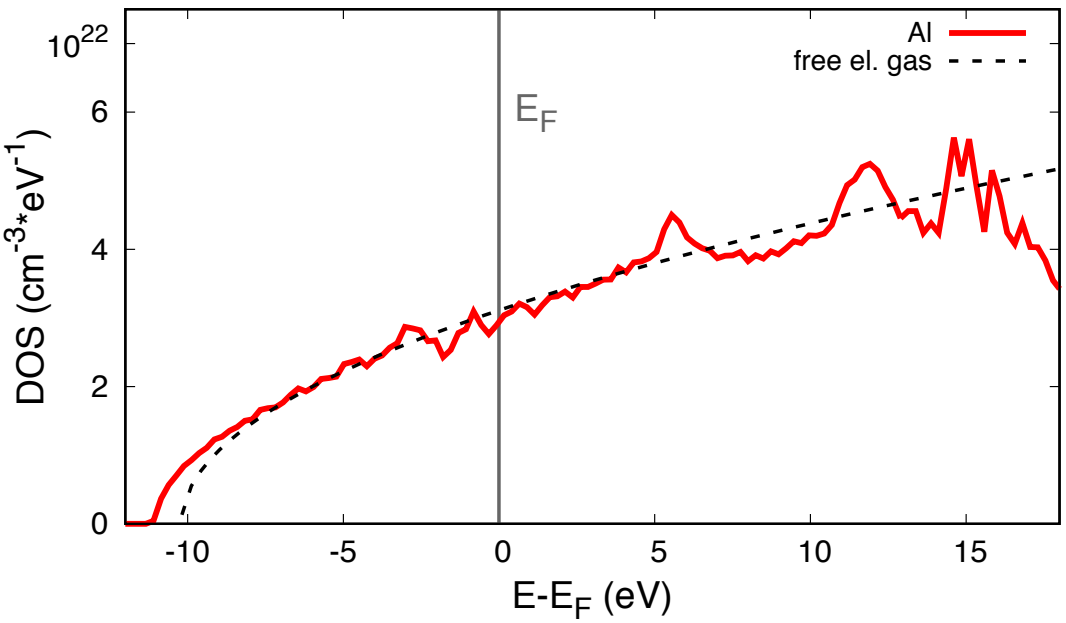

Figure 3.6: The DoS from Al (red) in three dimensions is displayed along with the 3D-DoS of a gas of fermions, proportional to the square root of the kinetic energy of the electrons. [This figure was produced using calculations from Ref.[214] which were performed up to an energy of ca. 20 eV above Fermi level and plotted up to 18 eV].

The Al(100)-surface was employed mostly for the acquisition of (e,2e)-coincidence spectra, which were measured in the LASEC experimental chamber. Prior to setting up each (e,2e)-coincidence measurement the surface of the sample needed to be freshly prepared on a daily basis, to avoid its oxidation. The preparation of the sample involved a sequence of sputter cycles alternated with annealing intervals. A first cycle of sputtering was conducted by means of 2.5 keV Ar^+-ions at room temperature. The duration of this first step varied according to the cleanliness of the surface, lasting approximately 3–4 hours if coming from air or about 20–30 min. if already in UHV. To ensure an integral etching of the surface, during the first sputter-cycle the sample was azimuthally rotated and its in-plane position varied in intervals of 5 minutes. Also the angle of incidence was regularly varied. A second cycle of sputtering followed at a decreased ion-beam energy of 2 keV, done in combination with a first cycle of annealing at ca. 280° C. This step lasted for ca. 30 min. A second combined sputter-annealing cycle of another half an hour was done at E_{ion} =1.5 keV and at an annealing temperature of 400° C. Finally, the sputtering unit was turned off and a "*flash-annealing*" of the surface was done for the exact duration of 3 minutes, during which the surface temperature is raised to 550° C. This temperature is about 100° below the melting point of Aluminium (T_m =660°C) [216]. Generally, the surface region of single crystals starts melting around 75° below the bulk melting temperature. During the whole procedure the maximal pressure reached in the preparation chamber was always kept in the low 10^{-6} mbar range. The overall duration of this procedure reached approximately 2–3 hours, when the sample was already inserted in the UHV-system. Even though comprehensive, this recipe was found to

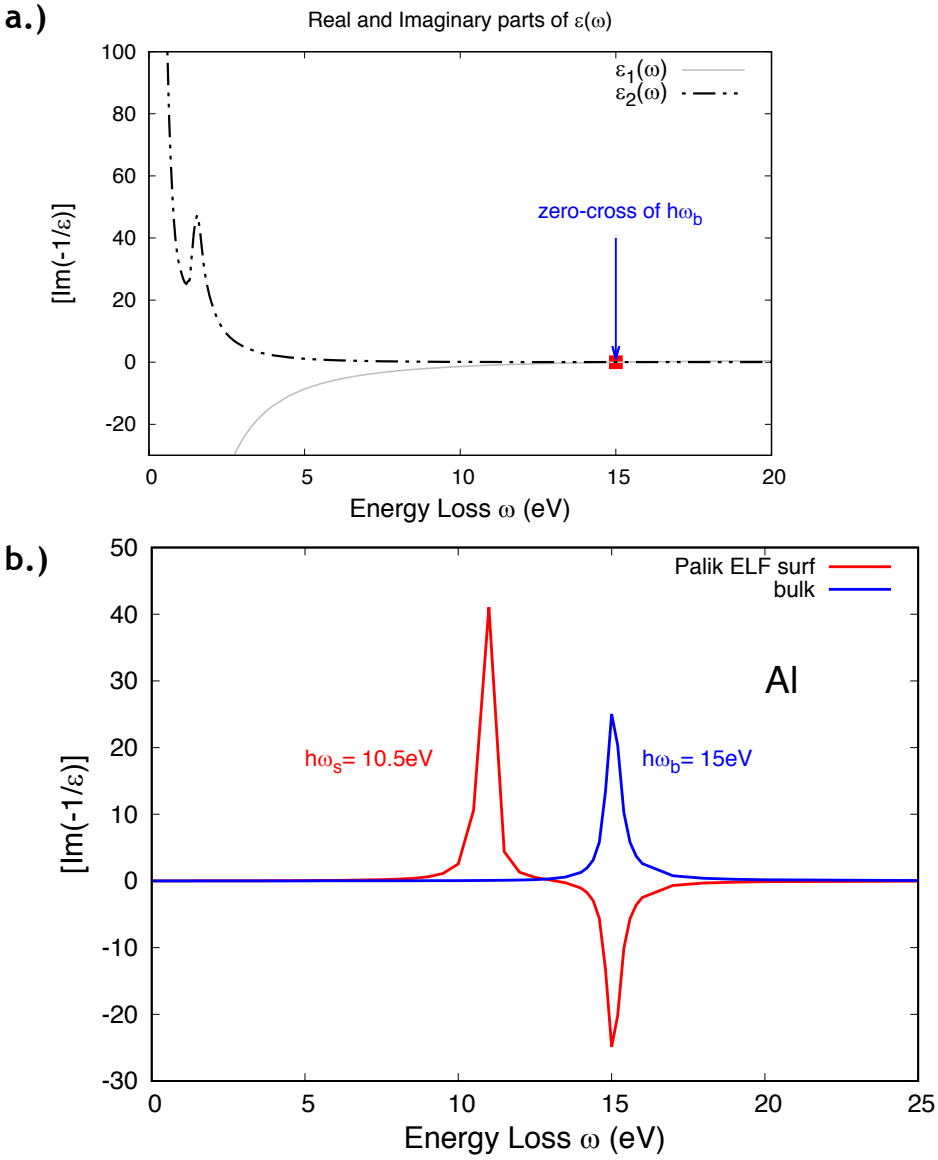

Figure 3.7: Optical data of Al (from Palik Ref. [125]): panel (a.) shows the real $[\mathfrak{Re}(\epsilon)]$ and imaginary $[\mathfrak{Im}(\epsilon)]$ parts of the dielectric function in Al. The zero-crossover of $\mathfrak{Re}(\epsilon)$ marks the energy loss ΔE – which in this case is labelled as ω – at which the longitudinal wave of these characteristic collective modes can be sustained in the bulk of the medium. This ΔE or 15 eV marks the characteristic excitation energy of the *volume plasmon* ($\hbar\omega_b$) in Al. Panel (b.) gives the Energy Loss Functions (ELF) of both the surface (red) and the bulk (blue) from which the energies of these characteristic plasmon losses can be read [215].

be successful in both cleaning and reordering the surface region of the crystal.

Since in the experimental chamber of the SPECS-SEY apparatus the maximal achievable temperature of annealing is of ca. 300° a slightly different procedure for the preparation of the single crystal was embraced. The sputter cycles were also done using 2.5 keV-energetic Ar^+-ions at the beginning of the cycle, however each cycle was kept of shorter duration than in the LASEC

laboratory and the cleanliness of the surface was checked by means of XPS at regular intervals (every 10–15 min.). The first step of annealing was done at 250° C, the second at 280° C and the final "flashing" – forcefully done at only 300° C – of the sample was done for the duration of ca. 10 min, after which the status of the freshly prepared surface was monitored by means of XPS.

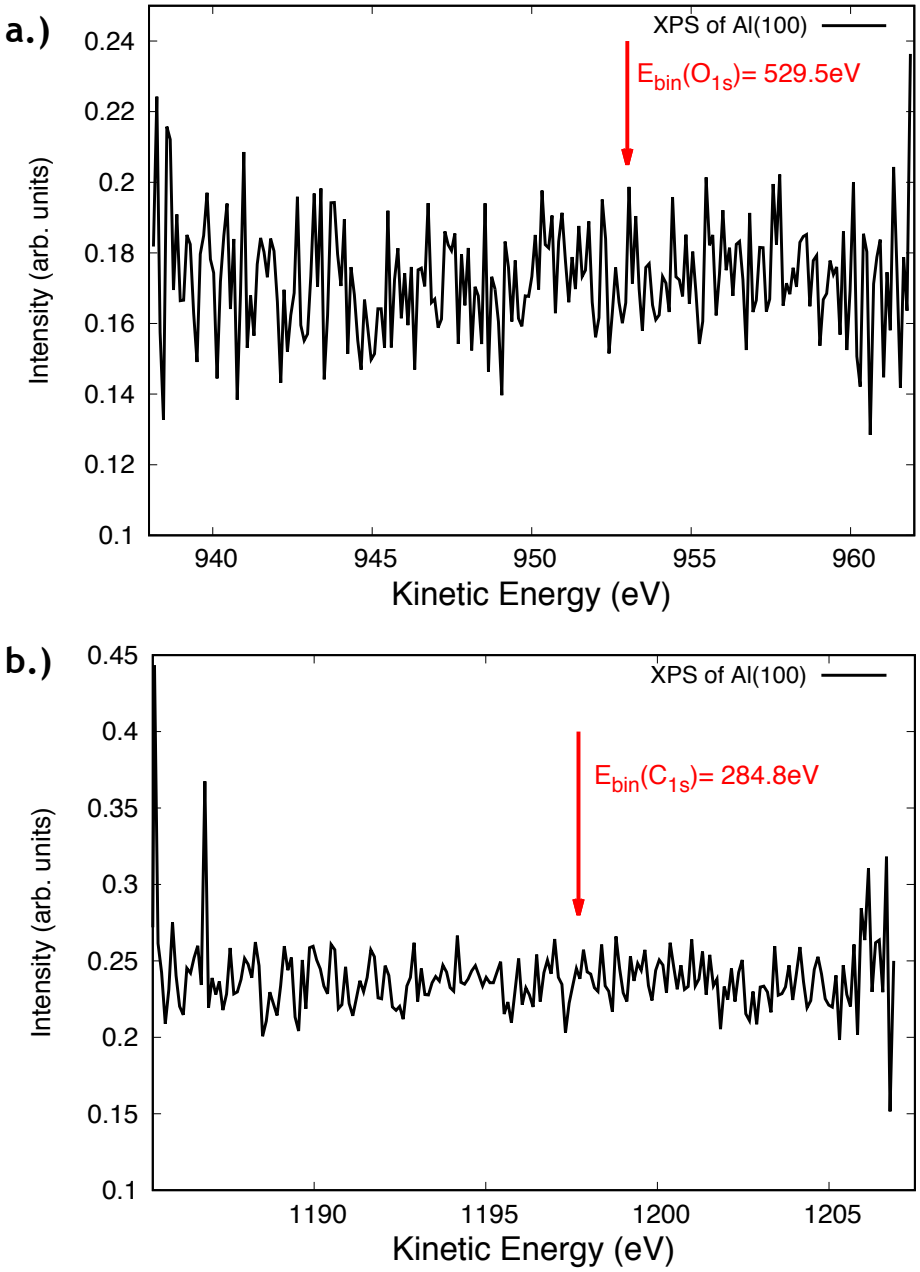

Figure 3.8: XPS spectral ranges acquired at the characteristic kinetic energies of the core levels of C_{1s} and O_{1s}. These XPS spectra were measured in the LASEC laboratory.

When neither Oxygen nor Carbon was revealed Low-Energy Electron Diffraction scans of the elastically reflected electrons was performed to monitor the crystallographic order of its surface.

The XPS spectra shown in figure 3.8 demonstrate the absence of contaminants on its surface. At the characteristic binding(kinetic) energies – indicated by red arrows in panels (a.) and (b.) of figure 3.8 – where to expect intensity linked to photo-emitted electrons of the core-levels of Oxygen and Carbon, no intensity could be revealed.

Just as previously explained for the case of HOPG (see subsection 3.2.1), the crystalline order of the clean Al(100) surface was routinely monitored by acquisition of a diffraction pattern, under variation of the polar angles of incidence and emission between source and analyser (R66). A typical LEED-scan measured on Al(100) is shown in figure 3.9, which shows the rocking curve of elastically scattered electrons (ELP) with a primary energy of E_0 =100.73 eV. The measurement was performed with a pass energy of 2 eV. The ordinate scale is given in degrees of the angle of incidence, θ_{in}, where 15° represents the angle of the specular reflected beam.

Normally, in electron diffraction, the 0^{th}-order Bragg peak is the one exhibiting the highest intensity. This is not the case for this diffraction pattern, probably do to a slight tilt of the sample surface with respect to the rotation axis normal (making them not precisely orthogonal to each other). A further indication for this slight misalignment is given by the intensity asymmetry of diffraction peaks of the same order (e.g. see 3^{rd}-order diffraction peaks). Despite

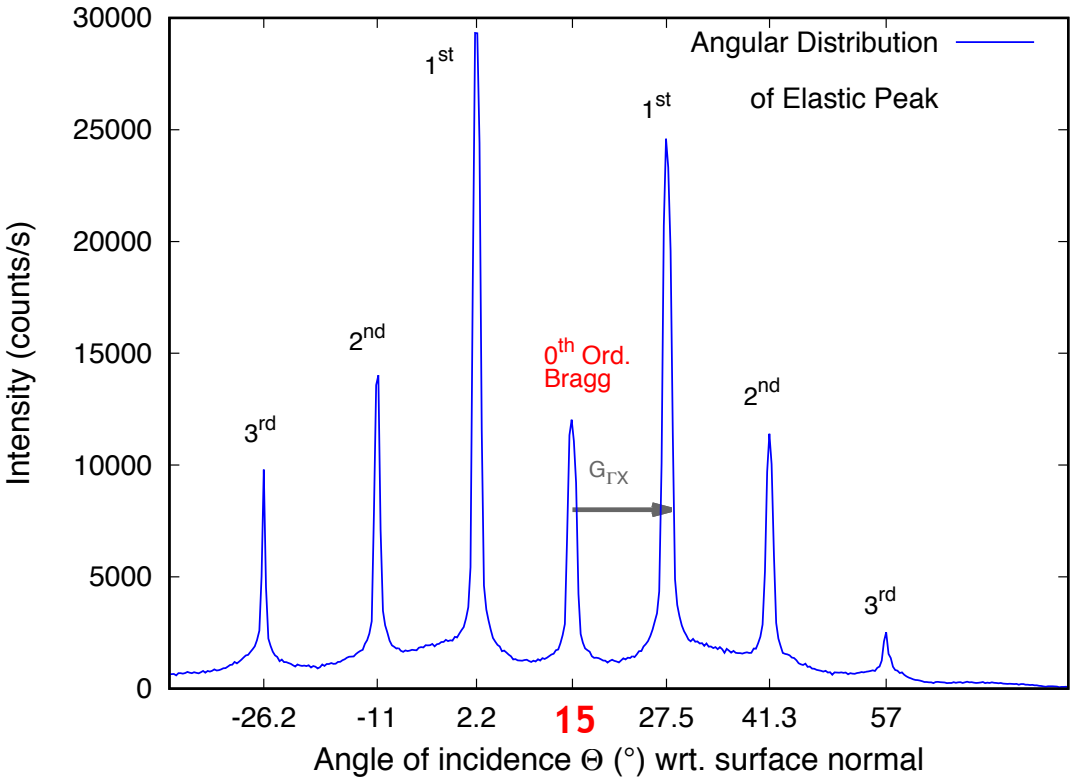

Figure 3.9: Diffraction pattern of the elastic peak (ELP) in Al(100) measured for primary beam energy of 100.7 eV and using a pass energy E_{pass} = 2 eV. This LEED-scan was acquired right after the preparation procedure to clean and re-order the surface of the single crystal.

the presumed misalignment, the diffraction pattern is relatively symmetric exhibiting a very low TDS background in between Bragg-peaks. This is an additional indication for its high crystalline order. The highest intensity is observed for first order diffraction peaks, which exhibit a $\mid \Delta\vec{K} \mid \equiv \mid \vec{G}_{\Gamma X} \mid \simeq 2.2\,\text{Å}^{-1}$. For this primary energy, E_0, and for the used scattering conditions it was possible to measure up to the third order diffraction.

Angular scans were performed also on the two prominent energy loss channels in Aluminium, on the *surface* – at $\Delta E = \hbar\omega_s = 10.5\,\text{eV}$ – and *bulk* – with $\Delta E = \hbar\omega_b = 15\,\text{eV}$ – *plasmons*. For the acquisition of these LEED-scans, the kinetic energy at R66 was tuned on either corresponding scattered electron energy. The results are shown in figure 3.10, where the blue line is the scan performed on the bulk plasmon and the red line the one on the surface plasmon. The measurement

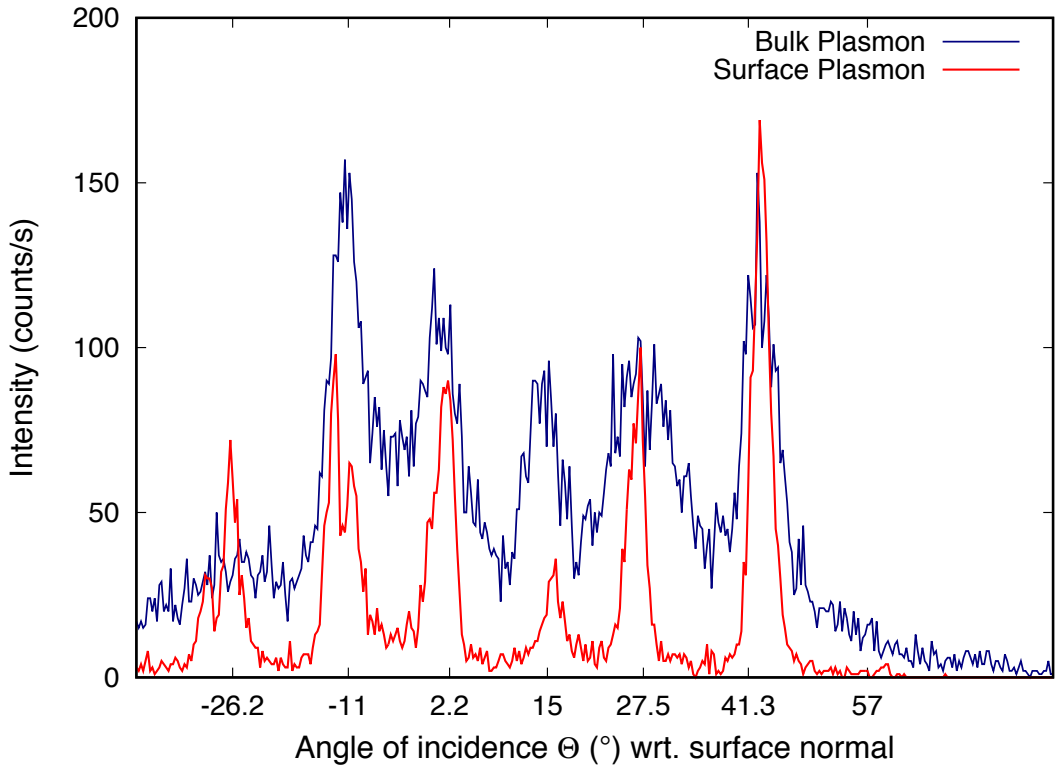

Figure 3.10: Diffraction patterns from the two characteristic plasmon losses of Al(100): bulk (blue) and surface plasmon (red). Both angular scans were performed in the exact same conditions as the rocking curve of the ELP shown in fig. 3.9.

was performed by varying the polar angle in 0.25°-steps and acquiring at each position for 1 s. The pass energy used was maintained constant (as for the acquisition of the ELP) at 2 eV, to compare intensities with the elastically scattered electrons. This low pass energy however lead to a rather poor statistics, as recognisable from the scans shown in fig. 3.10. Nonetheless, it is worth noticing that, both characteristic collective excitations exhibit a coherent scattering behaviour on the ordered surface. Furthermore, whereas in case of the bulk plasmon, some incoherent scattering contributions seem to exist, giving rise to a subtle TDS-background, in case of the angular scan

performed on the surface plasmon, no incoherent scattering contributions can be observed.

The fact that no incoherent scattering is observed during the excitation of a surface plasmon strongly suggests that this characteristic loss truly involves the sole top-most layers of the surface, essentially being an coherent inelastic collision confined in two dimensions.

In the course of this thesis work, the polycrystalline surface of Al was only used for the acquisition of electron yields. Its preparation was done in the vacuum chamber of the CERN-laboratory and due to its random crystalline order, involved much less effort. The surface was treated by a sputter-cycle at room temperature done employing 3 keV-energetic Ar^+-ions for the duration of ca. 20–40 min. (if the surface had been already inserted in the UHV-system and had been previously sputtered). Also in this case, the sample position was regularly (every 3 min.) varied to ensure homogeneous irradiation. Prior to the sputtering at room temperature, the sample was additionally heated up to 300° for ca. 10 min., to ensure the removal of residual water and hydrocarbons on the surface. In the apparatus at CERN, it is possible to acquire XPS-spectra on the very same spot irradiated by the ion-gun, thus enabling to perform also depth-profiles. During the sputtering procedure, several XPS-spectra were acquired to monitor the stage of cleanliness. When no Oxigen, no Carbon, nor other contaminants were visible in the survey XPS-spectrum the sputtering of the poly Al was terminated.

The comparisons of (e,2e)-coincidence spectra between the Al(100) and the poly Al shown in subsection 4.3.2 of chapter 4 were done between the actual data-set measured on the described Al(100)-sample and a poly Al specimen which was measured in the SE2ELCS laboratory of the University of Technology in Vienna during my diploma thesis project [217, 126]. There the poly Al surface underwent only Ar^+-sputtering cycles at room temperature and its status was checked by means of Auger electron spectroscopy (AES).

3.2.3 Cu(100), Cu(111) and Poly Cu

Copper (Z=29) is a malleable and ductile metal with very high thermal and electrical conductivity. Cu is one of the few metals available from Nature in a directly usable metallic form, however it also plays a relevant role in various metal alloys. One of the major applications of copper is still represented by the production of electrical wires (up to 60% of the extracted Cu). One further important technological application of the modern days for polycrystalline Cu is represented by its extensive employment in high-energy Physics facilities, e.g. in the beam-pipes wherein the proton beam travels or in other radio-frequency components of particle accelerators [218].

Copper belongs to the group of "transition metals", in which there is no sharp distinction between "free" conduction electrons and the "bound" (core) electrons resulting from the partially filled *d*-shells. Energy loss spectra measured on transition metals are mode difficult to interpret, since observed spectral features are not always unambiguously assignable either to collective modes or to direct single-electron excitations [219, 220, 221]. Furthermore, possible energy-shifts, where to expect these characteristic loss features can occur, due to strong influence induced by the available inter-band transitions. The crystal structure of Cu exhibits a fcc-lattice, as the one of Al (shown in panel (c.) of figure 3.5).

The band structure of *d*-band metals shows typical energy gaps in the *d*-band region due to the crossover of a *s*-band with a *d*-band of the same symmetry. In such a band gap the probability to find a surface state – generated when bulk-energy bands are projected onto the two-dimensional Brilllouin zone (2D-BZ) – at the energy of which scattering is generally strong, was found to be rather high [222].

In particular, for the case of the two Cu(100) and Cu(111) single crystals employed in this work, surface states were observed by authors of Refs. [223, 224] at the top of the bulk *d*-bands using angle-resolved photoemission spectroscopy. These dispersing surface states were found to fall in absolute energy gaps of the projected bulk band structure near the symmetry point M of the 2D-BZ for both faces [223].

Euceda *et al.* in Ref. [224] report on the projected charge (given in electrons per atom) onto basis functions of s, p, and d symmetry in each Cu(100) and (111) plane, together with the total planar-projected charge and the integrated-planar charge. They state that the number of electrons per atom in case of *s*-, *p*- and *d*-bands is about 0.4, 0.68 and ca. 9.7, respectively, thus yielding a total number of valence electrons per (surface) atom of ca. 11. Only a very small portion of these valence electrons make up the density of states of the surface-state electrons, ϱ_{surf}.

According to Fiete and Heller in Ref. [205] ϱ_{surf} in Cu(111) is of $n \approx 7 \times 10^{13}\,\mathrm{cm}^{-2}$ or equivalently it corresponds to approximately 4% electrons per surface atom (being the density of surface atoms of the order of $10^{15}\,\mathrm{cm}^{-2}$). The surface-state electron density can be brought in connection to the effective mass of these surface-state electrons (m^*) and with their energy (or

equivalently frequency/wavelength) through the following dispersion relation:

$$E_{surf}(k) - E_{Fermi} = \varepsilon_{surf} + \frac{\hbar^2 k^2}{2 m^*} \tag{3.1}$$

The average binding energy of a surface-state band minimum – $\varepsilon_{surf} < 0$ – in such crystals is of the order of few meV below Fermi level. Such small binding energies allow to regard the dispersion relation of these SS given in eq. (3.1) to be quadratic and isotropic. The isotropy of these surface-states dispersion relation allows one to disregard the crystal orientation of the irradiated crystalline lattice when considering only these surface-state contributions, i.e. these surface-states may affect (even if very marginally) the overall electron yield response (intimately linked to the available DoS in a target) of a Cu-crystal independently from its precise surface crystallography. The energy position of these surface states commonly coincides with a maximum in the density of states (DoS).

Knowledge on the presence of these surface states can therefore be important for the proper interpretation of spectral features in electron spectra as well as for the understanding of the energy structures in TEY-measurements.

However, in spite of this knowledge, it shall be noted that in the TEY-measurements performed within this work, it was not possible to exactly determine to which extent the presence of these surface states influences the TEY-structures observed. In case of the Cu(100) surface, a rise in the TEY could be nonetheless unambiguously correlated to the presence of an energy gap, as discussed further in sub-section 4.1.3.

Figure 3.11 (a.) shows the Cu band structure along the two symmetry directions, ΓX and ΓL [225] – relevant to the subsequent interpretation of the LE-TEY measurements. These band structures range from the bottom of the valence band (≈10 eV) up to ca. 28 eV above E_{Fermi}. The ΓX-direction exhibits an energy gap of ca. 3 eV-width right above vacuum level (highlighted in yellow), not present along the ΓL-symmetry. Panel (b.) shows a calculation of the electron bands in the Brillouin zone of Cu along with the DoS (displayed in grey on the right-hand side).

Two crystalline samples of Copper given along the (100) and (111) surface direction were employed along with a polycrystalline surface for Total Tlectron Yield (TEY) measurements in the LE-regime. These data were acquired in the "SPECS-SEY"- system in the laboratories at CERN. As previously stated, polycrystalline Cu represents an important material for the applications at CERN, where the cryogenic systems and vacuum chambers are predominantly made of this material. The measurement of LE-TEY curves represents an important mean of diagnostic and is employed to study how to limit the detrimental consequences of the electron cloud phenomenon on the beam stability, induced by the power deposited by this electron multipackting in the beam-pipes. To improve the understanding of the observed energy-dependent variations of the yield – also E-structures in the following – visible in the polycrystalline surface of Copper, it was

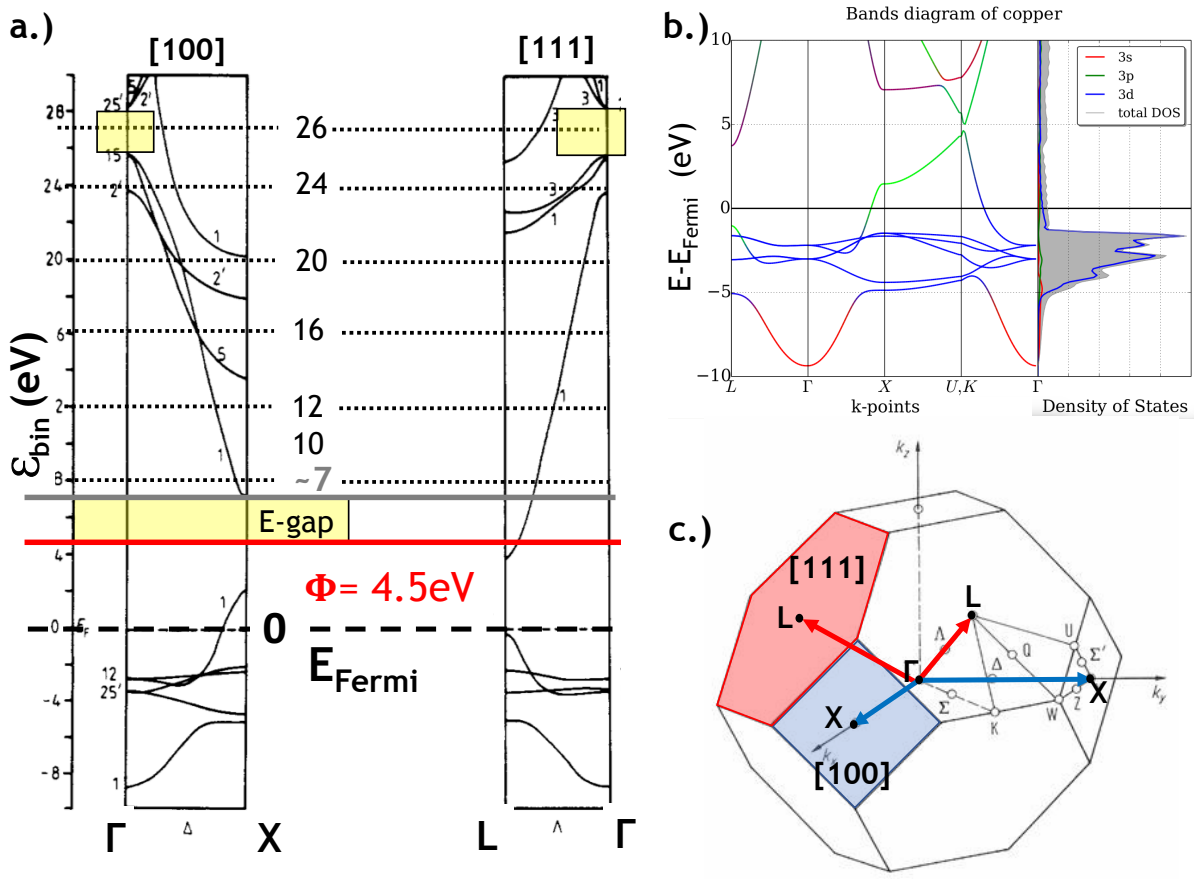

Figure 3.11: Panel (a.) shows the calculated band structure (BS) [225] of Cu given along the two high symmetry directions of [100] and [111]. These crystalline symmetry directions are those which were sampled during the series of Total Electron Yield (TEY)-measurements discussed in subsection 4.1.3 in the next chapter. The band structure regions shown in this panel are given for binding energies ε_{bin} (defined w.r.t. the Fermi level) ranging from -10 eV up to +28 eV, thus showing both the *occupied* and *unoccupied* bands. Regions highlighted in yellow indicate energy gaps. Panel (b.) shows another calculated BS accompanied by the Density of States (DoS) in the three dimensions. Highest electron densities are clearly visible in correspondence of the *d*-bands in Cu. Panel (c.) shows the polyhedron representing the first Brillouin zone (1.BZ) of the *fcc* crystal in the bulk. Surface Brillouin zones (SBZ) are highlighted in blue and red indicating the [100] and [111] SBZ respectively. During a LE-TEY scan performed in normal incidence, the perpendicular component of the momentum is aligned with the ΓX and ΓL symmetry directions, which are shown in panel (a.).

decided to measure LE-TEY curves also from the single-crystalline surfaces.

For the preparation of the two single crystals a similar procedure, as explained previously for the Al(100)-surface, was adopted and the cleanliness of the targets was checked via XPS-measurements (not shown) similarly as done for the case of HOPG and Al(100). In case of the polycrystalline surface only sputtering cycles was performed and its cleanliness was monitored during and after the sputtering.

3.3 Experimental Set-ups & Principles of Operation

This section is dedicated to the description of the principles and design of the experimental apparatus employed for the series of investigations. The main aspects of the measurement methods are explained along with the apparatus description.

At CERN there are two experimental chambers dedicated for the measurement of the TEY situated in the surface analysis laboratories of the Vacuum Surface and Coatings (VSC) group of the Technology Department (TE) at CERN. Both experiments are dedicated to the full characterisation of surfaces, to determine their elemental composition and chemical state. Therefore both set-ups are equipped with standard surface analysis tools like a monochromatised X-ray source, several electron guns and an Argon ion sputter gun for sample preparation.

Their set-up is different and consequently also the principles upon which the measurement method relies, imparting also distinct capabilities for measuring over different (but also similar) energy ranges. One of the experimental set-ups is equipped with a polarised collector surrounding the biassed sample. A sketch of this instrument can be found in Ref. [29]. By means of this set-up, TEY-curves are measured for primary electron beams ranging between 50 eV and 1800 eV. Due to the presence of the polarised collector, it is not possible to acquire TEY-curves below 50 eV, which, on the other hand, represents exactly the energy range of major interest for this work. Although, in the course of this thesis project a whole series of measurements was performed by means of this "collector-SEY" system, it is not treated in the remainder of this work.

In the second experimental chamber – the "SPECS-SEY" – instead, the (sample) currents for the determination of the TEY are measured at a picoamperometre directly connected to the specimen. The principles of this measurement method rely on Total Current Spectroscopy (TCS) [226]. By means of this set-up it is possible to measure the TEY of a target in the very low kinetic energy range down to 0 eV landing energy. This is the apparatus employed for the acquisition of all LE-TEY curves discussed in section 4.1.

The experimental chamber in the "LASEC" laboratory in the Università degli Studi di Roma Tre is designed for the performance of several surface analysis measurements and in particular it is equipped with two electrostatic energy analysers thus to enable the simultaneous acquisition of correlated electron pairs as it is needed in (e,2e)-spectroscopy. In this apparatus the sample surface can be cleaned via sputtering and its crystalline order can be restored by annealing and monitored using a Low Energy Electron Diffraction (LEED) unit or alternatively by acquisition of a linear diffraction scan (at fixed azimuthal angle) of the elastic peak.

Electron spectroscopic techniques such as Angle-Resolved Reflection Electron Energy Loss (Ar-REELS) and Photo-Electron Spectroscopies (in the UV-light and in the soft X-ray range) are routinely used in the LASEC laboratory to analyse the targets of interest. The two hemispherical

mirror analysers are positioned orthogonally with respect to each other within the detection plane. This arrangement allows to conduct (e,2e)-coincidences spectroscopy measurements for a variety of kinematics, when they are simultaneously operated.

3.3.1 The "SPECS-SEY" Experimental Chamber at CERN

Most of the TEY measurements shown in the next chapter were acquired in the very low-energy regime, with electrons of $E_0 \leq 50\,eV$ in the "SPECS-SEY" experimental chamber.

As previously emphasised (see section 3.1), to ensure the performance of electron spectroscopy and TEY measurements in the LE-range it is necessary to compensate the Earth's magnetic field in the scattering region. In the "SPECS-SEY"-apparatus (sketched in figure 3.12) this is solved by the presence of a μ-metal shielding of the vacuum vessel. The manipulator in this analysis

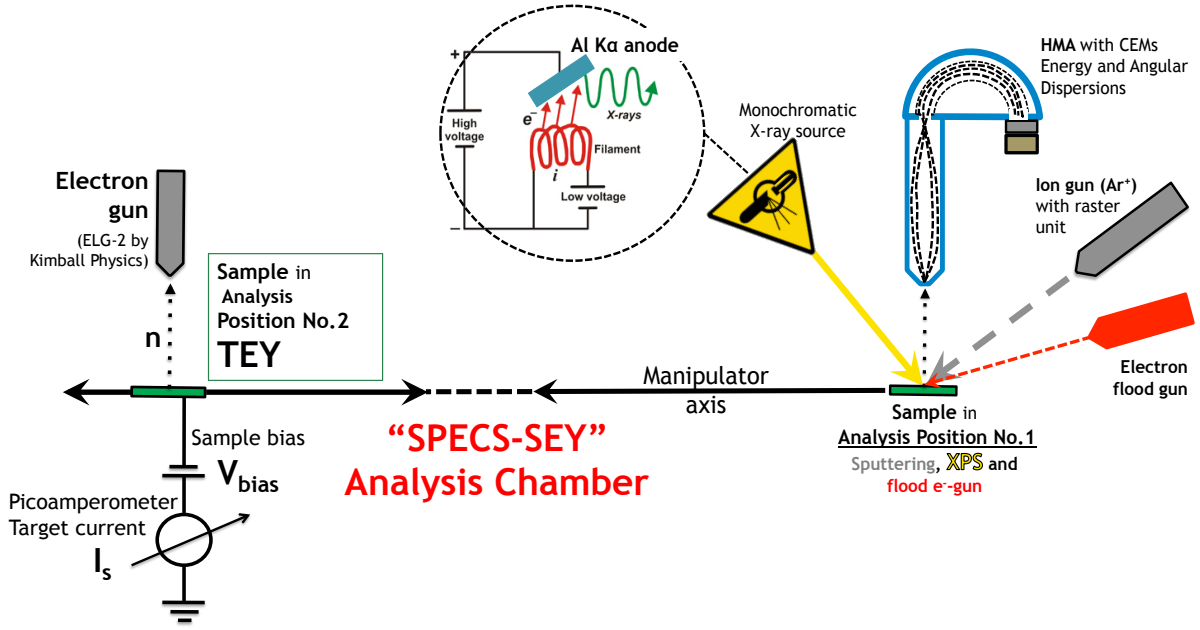

Figure 3.12: The "SPECS-SEY" experimental set-up used at CERN: schematic illustration of the equipment available in the analysis chamber. In the analysis position No. 1 it is possible to prepare the surface by means of Ar^+-ion sputtering and to analyse the chemical composition of the target via XPS analysis. The sample position No. 2 is used for TEY-measurements of samples achieved by bombarding the surface with a primary electron beam with an effective landing energy E_0 and current I_0.

chamber enables to move the specimen between two analysis positions. The large sample stage consents to accommodate samples of various dimensions, even of larger dimensions (e.g. 9–12 cm^2). The specimen can be azimuthally rotated for nearly 360° and variation of the polar angle can be meaningfully (thus to be aligned with the various available sources) done over a range of ca. ±45°.

Furthermore, it is possible to tilt the sample surface in the direction parallel to the manipulator axis over an a range of ca. $\pm 20°$. The manipulator stage is also furnished with a heating filament, by means of which annealing of the sample can be done up to a maximal temperature of ca. 300° C.

In the analysis position labelled as No. 1 in figure 3.12, it is possible to perform all standard surface analysis procedures normally used to prepare and to characterise a (clean) surface. Here the sample can be sputtered by using 3 keV Ar^+-ions and since the monochromatised Al Kα X-ray source is aligned in such a way thus to irradiate the sample on the very same spot as the ion gun, it is also possible to employ X-ray Photoelectron Spectroscopy (XPS) to obtain a "depth-profile" of the target.

In "*depth profiling*" the ion beam etches away surface layers and contaminants, revealing subsurface information. The surface is etched by rastering the ion beam over a defined area of the sample. By combining a sequence of ion gun sputter cycles with XPS analyses it is possible to access to quantified information on the surface chemistry as well as layer thickness and its characteristics. After each sputter cycle (of the average duration of the order of minutes) the ion beam is blanked and another set of XPS-spectra is recorded on the sputtered area. This sequence of etching and acquisition of photoelectron spectra is repeated until profiling has proceeded to the required depth. In the following investigations, X-ray photoelectron spectra from each sample were regularly acquired to monitor the cleanliness of the surface before, during and after sputtering.

In position No. 1 the sample can be also irradiated by an electron flood gun. This is useful when measuring insulating or semi-conducting materials. When such surfaces are irradiated either by photons or electrons, charging of the bombarded sample can be induced, thus leading to the formation of a positive (or negative) net charge on the irradiated area of the target. To avoid these surface charging effects, a flood electron gun can be used, where a steady flow of low-energy electrons is directed on the "flood area" of interest. Charge neutralisation is achieved when each impinging flood gun electron knocks out one SE from the target, thus preserving the net charge in the target area.

The analysis position No. 2 (shown in fig. 3.12) is dedicated to the acquisition of TEY-curves. It is furnished with an electron source by Kimball Physics Inc. (of the model type ELG-2 with the EGPS-1022 power supply) [227] capable to reliably generate electron beams over wide energy ranges. The thermionic emitter of this electron source is made of a Tantalum disc (type ES-042) yielding a nominal emission area of $5.5 \times 10^{-3}\,\mathrm{cm}^2$ ($\varnothing = 0.84\,\mathrm{mm}$) and exhibiting a low energy spread of $<0.7\,\mathrm{eV}$. The workfunction of the Ta-disc cathode is declared to be 4.1 eV. According to the manual of operation this electron source is capable of generating beams with kinetic energies ranging from $\sim$1 eV up to an energy of 2000 eV. Beam energy, beam current and spot size are independently adjustable over the whole range. The nominal working distance to be used for very low-energy operations is of ca. 20 mm. However, for the VLE-range used in the series of

LE-TEY acquisitions the optimal working distance (d_w) was found to be of 10 mm.

The base pressure of this analysis chamber is in the low 10^{-9} mbar range; even though it is at the upper limit of the UHV-range, it is sufficient to perform surface analysis experiments of brief durations (minutes to hours). At these pressures contamination of the surface is more rapid and demands for a more frequent cleaning procedure.

3.3.2 Measuring the Total Electron Yield (TEY) in the LE-regime

The total electron yield, σ, of a material is in general measured for perpendicular incidence (θ_{in} =0°) of electrons as a function of the impact energy, E_0, ranging up to several keV. The experimental method relies on Total Current Spectroscopy (TCS) [226], schematically shown in figure 3.13, where an electron beam impinges on a sample and σ is investigated by monitoring the target current. In TCS the target – with a given workfunction Φ_{sample} – is set to a potential V_{bias} (of arbitrary value) and the electron gun irradiates the sample with a source energy, E_{gun}, defined by $e \cdot U_{fil} + \Phi_{fil}$, where U_{fil} is the potential set at the gun given with respect to (w.r.t.) the common Fermi level of the apparatus and Φ_{fil} is the workfunction of the electron gun. The landing energy, E_{Land}, i.e. the electron energy with respect to the vacuum level of the sample is then obtained as follows:

$$E_{Land} = e \cdot (U_{fil} - V_{bias}) + \Phi_{fil} - \Phi_{sample} \tag{3.2}$$

Negative landing energies correspond to a situation where the electrons are repelled from the electric field between the biassed sample and the electron gun. For positive E_{Land} the electrons can penetrate the target.

Especially when operating with very low energy electrons, calibration of the electron energy scale represents an essential step prior to the actual measurement (see sub-subsection 3.3.2.1). Furthermore, from equation (3.2) it can be understood that once the electron energy scale has been calibrated, the V_{bias} for which E_{Land} becomes zero allows to determine, through eq. (3.2), the sample work function. Figure 3.13 gives a schematic representation of the instrumentation used in this work for the series of TEY-measurements presented in section (4.1). It displays the experimental set-up used in the analysis position No. 2 of the "SPECS-SEY"-experimental chamber. The TEY (already defined in terms of σ, η and δ in eq. (1.1)), as a function of E_0, is experimentally obtained by

$$\sigma = \frac{I_0 - I_s}{I_0} \tag{3.3}$$

where I_0 represents the total impinging (or primary) current and I_s is the sample current. In

either case, the current is measured as the current drained by the bombarded target via a pico-amperometre (as sketched in figure 3.13).

Depending on the sample bias, contributions to the ejected (or SEs) electron current, I_E, and to the reflected (I_R) current can be varied. However, these contributions are experimentally indistinguishable from one another and their variation results in an overall variation of I_s.

For sufficiently high V_{bias} >0 V (also $V_{bias} \gg U_{fil}$) the primary current, I_0 is obtained; since in this case all electrons are collected by the sample and transmitted towards the pico-amperometre – measuring the sample current.

Whereas for V_{bias} <0 V (the specific case represented in figure 3.13) the measured sample current, I_s, is equal to the current of absorbed electrons excluding contributions given by the ejected electrons, I_E, generated in the course of the electron beam–specimen interaction. By applying a negative bias on the target it is ensured that all SEs are repelled away from the surface, thus not contributing to the measured sample current, I_s.

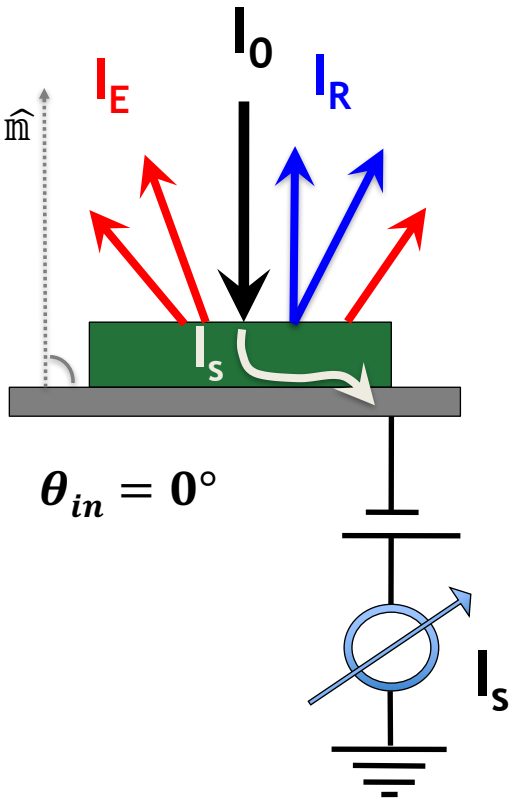

Figure 3.13: Experimental set up used at CERN to acquire the TEY-curves based on a retarding potential measurement layout. The sample is bombarded by a primary electron beam with effective landing energy E_0 and current I_0. The scheme represents the case when a negative bias (V_{bias} <0 V) is applied on the target. The current drained by the sample, also I_s, is given only by transmitted electrons which have an energy greater than the applied voltage, thus excluding current contributions both of the reflected (I_R) and the ejected (I_E). The experimental TEY-value is obtained for each landing energy, E_0, according to equation (3.3).

Thorough investigation on the distance-dependent primary-current-behaviour was performed to ensure that the best focussing distance was selected for *"all"* beam electrons to land on the target, thus contributing entirely to the measured current (I_0). The *"all"* in the previous sentence is highlighted for the following reasons: (i.) to be precise, it shall be noted that, a small fraction of elastically reflected electrons is always present. The current associated to these reflected electrons I_R is not definable in this experiment. However, it can be assumed that, when the target is

irradiated on the very same spot (as normally done for both the acquisitions of I_0 at $V_{bias} > 0\,V$ and of the subsequent I_s at $V_{bias} < 0\,V$) the probability for these electrons to be back-reflected does not change upon time, and will remain the same for a chosen polarity of the sample bias. Hence, this non-measurable current remains constant for all measurements performed for a same V_{bias} on the same sample area (source for *systematic error*).

Another factor that could prevent electrons of very low *landing* energies to hit the surface is given by the divergence of the beam. Electron beams always have a certain width which is determined by the level of focussing of the electrons departing from the emitter. The presence of a small divergence is inevitable. Also in this case, this beam divergence (which depends on the emission energy, E_{gun}, depending in turn on the focal lens settings) is always constant for all measurement and for a same E_{gun}. However, when the sample bias polarity switches to negative values, the additional retarding field may induce a reversal of the momentum of the incoming electron prior to its landing on the surface. If the sample is positively biassed, this problem is less probable to occur (due to the accelerating field). This aspect needs to be considered, since in this case the TEY-measurement yields a value which in the range close to 0 eV-landing energy could be compromised by an overestimation of the I_0 with respect to I_s. On the other hand, this kind of error is also classifiable as *systematic error*, since it will always affect the results of the experiments in the same predictable way.

Despite these sources of systematic errors, it could be assessed that for a working distance (d_w) of ∼10 mm the best achievable focus was obtained, thus to maximise the number of landing electrons onto the surface. In addition, I_0 was routinely compared to the primary current measured using a Faraday cup, to assure consistency. This FC is however positioned at 20 mm away from the source apex. Therefore to check the reliability of the I_0-measurement as done by biassing the target, this latter was also positioned at a d_w of 20 mm away from the source and the two I_0-measurements were compared, yielding the same result.

The calibration of the energy scale (given w.r.t. Fermi level of the target) is provided by measuring the low-energy (LE) TEY curve from a clean polycrystalline Gold surface, of which the workfunction, $\Phi_{Au} = 5.2\,eV$, is known [228, 48] and defines the energy scale in our following experiments (see figure 3.16 in sub-subsection 3.3.2.1).

A typical LE-TEY curve is shown in Fig. 3.14 for the case of a sputter-clean polycrystalline Aluminium foil. The curve is subdivided in three coloured rectangular regions, which are brought in connection with the energy level diagramme of the measurement (shown in figure 3.15). This LE-TEY curve was acquired for normal incident electrons by setting the poly Al sample to a negative bias of ca. -40 V and by scanning the E_{gun} energy from 38 eV up to 62 eV, hence the (effective) landing energy of the PEs reaching the target goes from a negative landing energy up to $E_{Land} - E_{Fermi}\,(Al) = 22\,eV$.

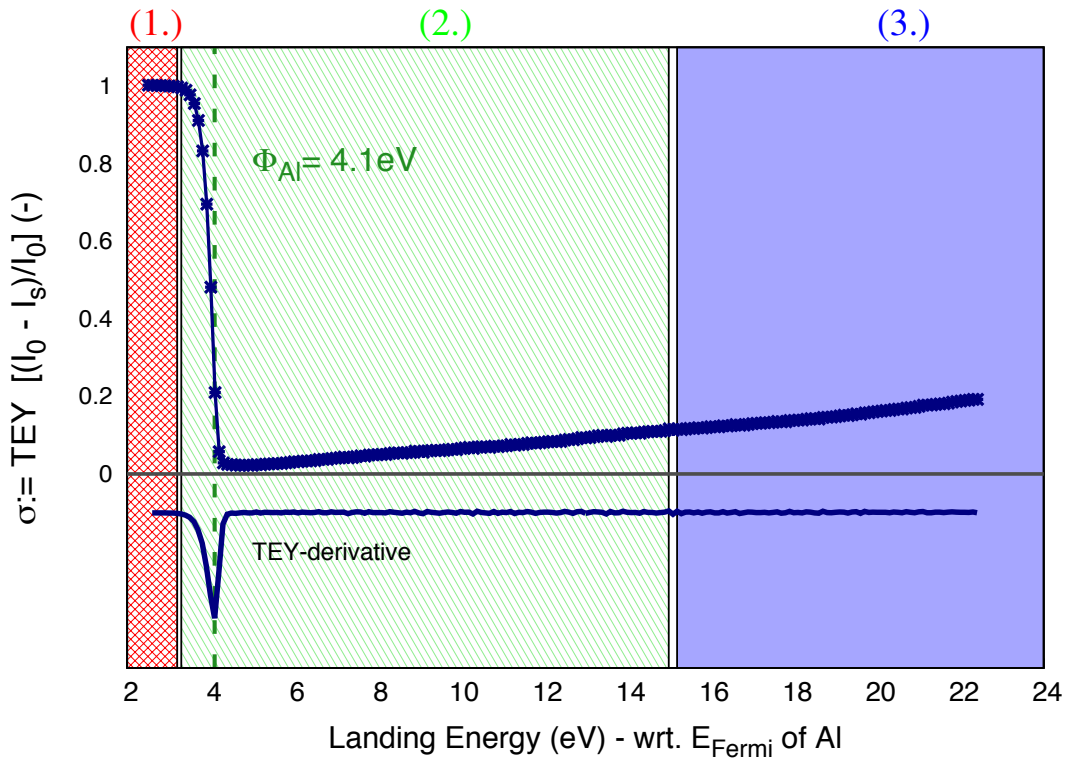

Figure 3.14: LE-TEY curve from a clean poly Al surface. Red region (1.) with σ =1 is given by total reflection of electrons as displayed by step 1.) in the E-diagramme of figure 3.15. Green region (2.) is associated to step 2.) in the same E-diagramme; same for the region highlighted in blue (3.).

The measurement of the total yield in the LE-range can be subdivided into three main steps, each one of which associated to a range of landing energy. The coloured numbered regions in figure 3.14 refer to the three experimental steps shown in the energy diagramme of fig. 3.15. The E-diagrammes in figure 3.15 show the path travelled by the free incoming electron from its point of generation (at the filament of the electron gun) to the surface of the biassed target, traversing different regions (indicated by Roman numbers) at different potentials. Regions (I) & (II) (coloured in grey) represent the potential set at the electron source. The electron gun energy is determined by the filament workfunction ($\Phi_{Ta} = 4.1\,\mathrm{eV}$ [227]) and by the accelerating voltage U_{fil}. Region (III) represents the electron path travelled in vacuum. The potential for this region is set to ground. The electrons emitted from the "snout" of the electron gun travel in vacuum towards the biassed target. At the target, illustrated as the blue region (IV) the potential is determined by the sample workfunction Φ_{sample} and by the applied (negative) bias V_{bias}.

As long as the landing energy is negative all impinging electrons are reflected by the surface sample, which acts as a barrier. This yields a σ of 1. This case of total reflection is displayed by the energy diagramme shown in panel (1.) of figure 3.15, where the incoming electron (highlighted in red) encounters the potential barrier at the biassed sample.

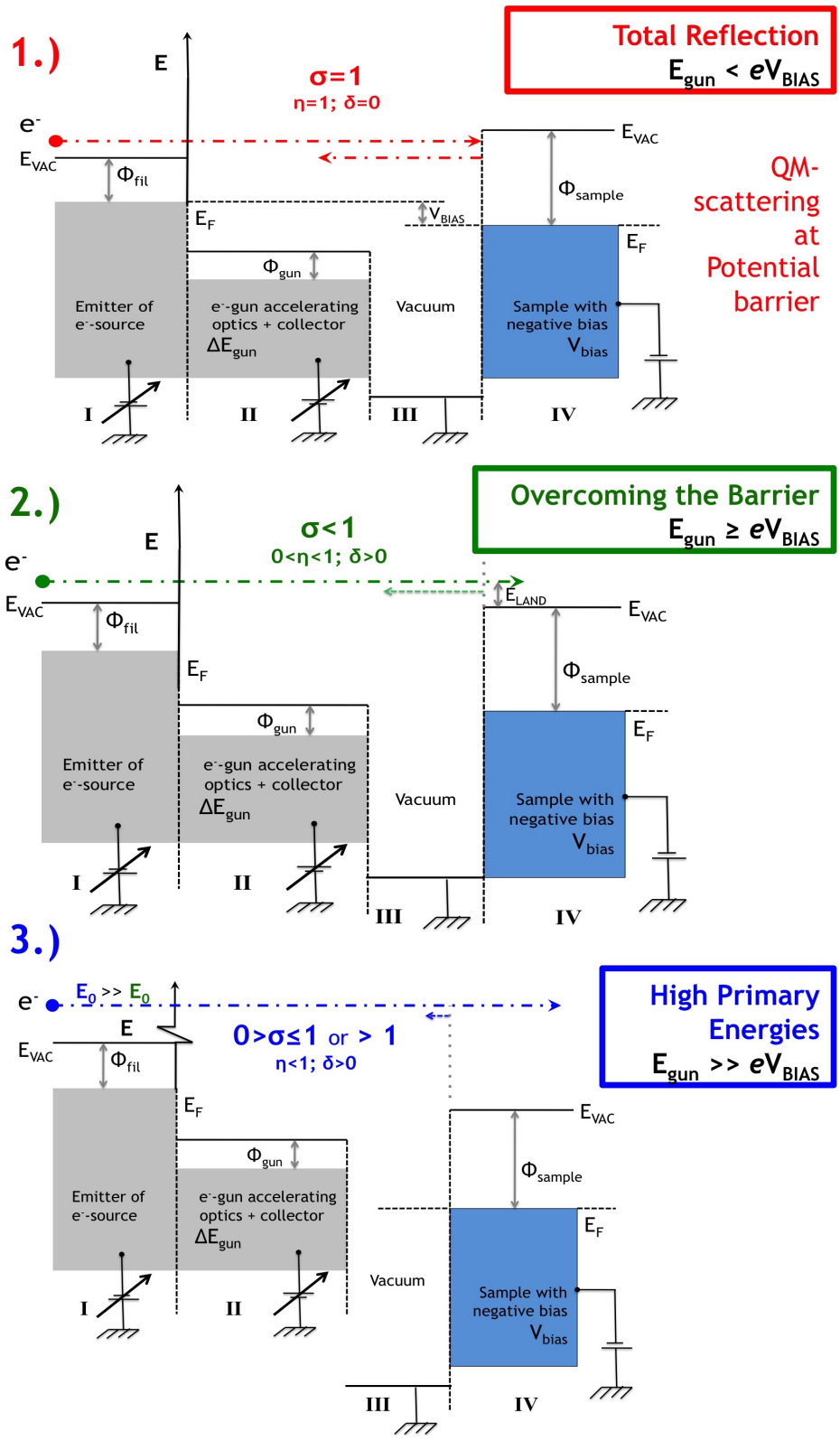

Figure 3.15: Energy diagram of an LE-TEY measurement: Step 1.) For $E_{gun} < e \cdot V_{bias}$ total reflection of electrons occurs at the potential barrier yielding a σ =1. Step 2.) depicts the case when the landing energy E_0 of the PEs starts to be greater than the workfunction of the target. Here, the incoming electrons can penetrate the surface barrier. The derivative of the slope yields the value of the sample workfunction. Step 3.) represents the case for electron energies much higher than the applied sample bias, $E_0 \gg e \cdot V_{bias}$.

When the electron landing energy is positive electrons can penetrate the target, provided that their wave functions can couple with matching Bloch waves inside the crystal [229] (see also section 4.1 in chapter 4).

Due to this penetration into the solid, σ exhibits a drop from 1 to nearly 0. This decrease in the LE-TEY is given by a decrease in reflectivity, η. This sudden drop of σ is expected to happen exactly at 0 eV landing energy, hence this energy w.r.t. Fermi level yields the sample workfunction (in this case of the poly Al with $\Phi_{Al} \simeq 4.1\,\text{eV}$). The sample workfunction of the material can be then conveniently obtained by making the derivative of σ at the inflection point of this slope.

Under the assumption of a sharp reflectivity step, at the workfunction one should expect a sharp step, but indetermination on the incident beam energy, given by the energy spread of the electron beam, turns the step-function into a descending slope of a given width obtained by the convolution of this step-function and the source energy spread of the beam, a Gaussian with a FWHM of $\sim$0.5 eV. This case is depicted in panel (2.) of the energy diagramme symbolised by the green electron path. For single crystals oriented along well-defined symmetry directions instead, the crystal potential and its energy bands need to be taken into account.

Region (3.) – highlighted in blue in both figures 3.14 and 3.15 – is reached by further increasing the electron landing energy, hence for electron beam energies much higher than the potential set at the biassed target.

Results presented in section 4.1 in chapter 4 demonstrate that the LE-TEY energy structures can be explained on the basis of the irradiated target band structure and can furthermore be brought in connection either with *emission* of SEs (with the SEY or δ) or with *reflectivity* of electrons (η or REY), this latter induced by the presence of E-gaps in the band structure of the target. The role played by the band structure of a solid is particularly evident when the LE-TEY is measured on single crystals.

The band structure of polycrystalline Al is represented by an average over all available symmetry directions for an Al crystal and it does not exhibit any remarkable E-gap. For this reason, the curve shown in figure 3.14 does not manifest any particular feature (i.e. E–structure induced by current modulations in the measurement).

3.3.2.1 Calibration of the Energy Scale & Measuring the Workfunction of Samples

Clean polycrystalline Au surfaces are routinely used as reference systems to perform energy calibration in electron spectrometers and instrumentation. One of the main sources of uncertainty in a LE-TEY measurement is primarily given by the indetermination of the energy scale, which therefore needs to be carefully calibrated.

The nominal energy value set at the controller of the electron source (E_{gun}) seldom delivers an electron beam of precisely the nominally set value, thus exhibiting an energy offset of ΔE_{gun}. This offset mainly depends on the variation of the emitting filament workfunction, Φ_{fil}, which can occur in dependence of the filament temperature or if the filament is contaminated by spurious material deposited on its surface. Since the status of the emitting filament can vary with time and with vacuum conditions, it is necessary to regularly perform a calibration of the energy scale using reference materials.

Furthermore, the electron beam itself is not an ideal point-like source, exhibiting a certain energy spread, ΔE_{spread}. This latter is generally known and declared in the manual of the manufacturer of the electron gun unit. In case of the Kimball Physics Inc. (ELG-2) electron gun the declared ΔE_{spread} is $\leq 0.7\,eV$; we found it to be approximately 0.5 eV.

For $E_{Land} = 0\,eV$ (given w.r.t. vacuum level as in equation (3.2)) convolution of the step-function at the potential barrier and the source energy spread of the beam, given by a Gaussian with a FWHM of $\Delta E_{spread} \sim 0.5\,eV$, leads to the observed slope, where the workfunction of the material (w.r.t. E_{Fermi}) can be determined. The primary purpose of this calibration procedure is to fix the absolute energy scale and – if present – to determine the energy offset, ΔE_{gun}.

The LE-TEY measurement is conducted (as explained in the previous paragraph) on the clean poly Au target with a known workfunction of 5.2 eV. This measurement is shown in figure 3.16. In case of this calibration measurement the inflection point of the slope is fixed at the value of 5.2 eV, thus to obtain the energy reference for the energy-scale calibration.

For $E_{Land} = 0\,eV$ equation (3.2) becomes:

$$e \cdot U_{fil} + \Phi_{fil} = e \cdot V_{bias} + \Phi_{Au} \tag{3.4}$$

Here the energy offset was considered to be zero ($\Delta E_{gun} = 0\,eV$). For $\Delta E_{gun} \neq 0\,eV$ instead, this offset can be determined as follows:

$$\Delta E_{gun} = \Phi_{Au} - \Phi_{fil} - e \cdot (U_{fil} - V_{bias}) \tag{3.5}$$

The herewith determined offset is used to properly re-adjust the energy scale in all LE-TEY measurements conducted on other materials. An example for the validity of this procedure is given in figure 3.17 showing a series of LE-TEY curves acquired on clean surfaces after calibration of the absolute energy scale. The measurements were performed up to a landing energy (given

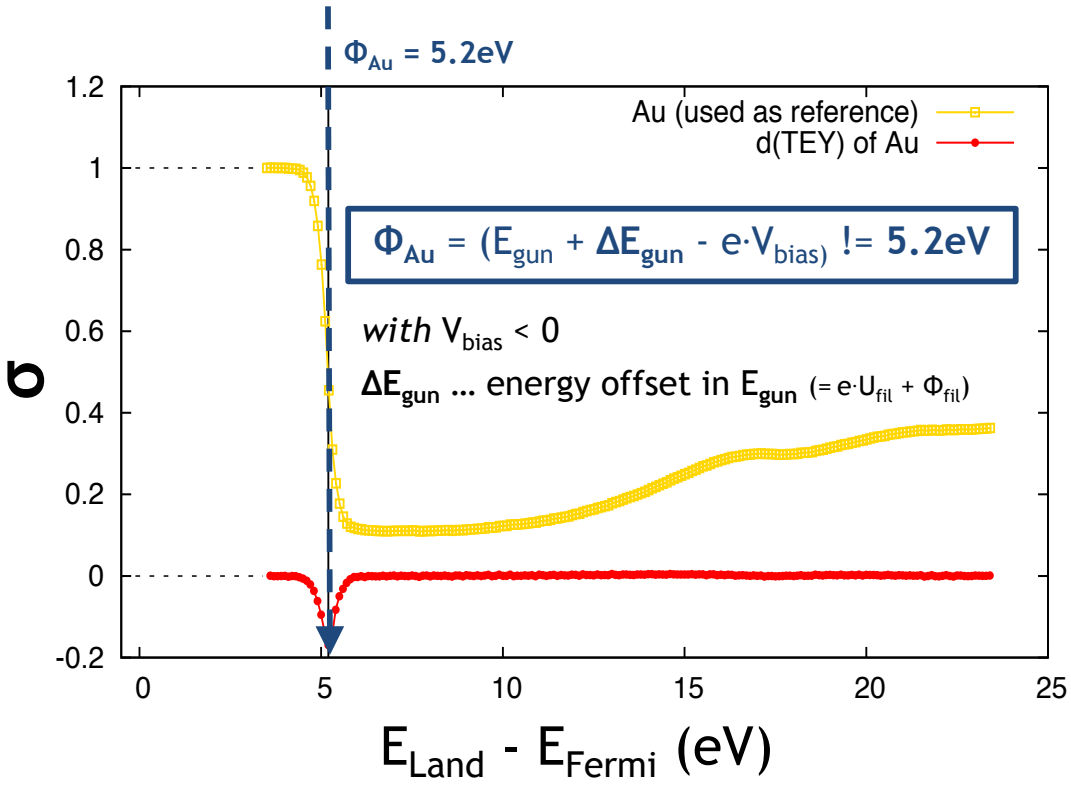

Figure 3.16: LE-TEY curve of polycrystalline Au measured for $E_{Land} - E_{Fermi}\,(Au)$ ranging from 0 eV up to 25 eV. At the inflection point of the LE-TEY curve the first derivative of this curve delivers the value of the workfunction of the target material. In case of the calibration measurement this inflection point is set to the value of the workfunction of Gold of 5.2 eV and herewith determines the energy scale. The energy offset ΔE_{gun} can be determined according to equation (3.5).

w.r.t. E_{Fermi} in this case) of ca. 20 eV.

The workfunction of each material can be conveniently obtained by making the first derivative of the LE-TEY curve and by "reading" the energy value at the inflection point. For polycrystalline Al (blue) Φ was found to be 4.1 eV, for polycrystalline Cu (orange) a value of 4.5 eV was obtained, whereas for HOPG (grey) Φ resulted being 4.4 eV, all with an estimated accuracy of ± 0.2 eV. The first two values were found to be well in accordance with literature data [228]. We additionally measured their workfunctions *in situ* by means of a Kelvin probe. Even though with a different measurement accuracy[10], we found good agreement between the workfunction values determined via the two experimental methods. In spite of the different level of accuracy, LE-TEY measurements can nonetheless represents a useful tool to establish the workfunction of materials. Foremost, being σ highly sensitive to the chemical state of the surface, its measurement in the LE-range offers an additional method to check the cleanliness of a specimen. In presence of a surface layer (oxide or contaminants) the TEY is immediately affected, often exhibiting an evident shift in the onset energy, which as previously demonstrated implies a variation in the

[10]The accuracy of Kelvin probe measurements is generally in the tens meV-range.

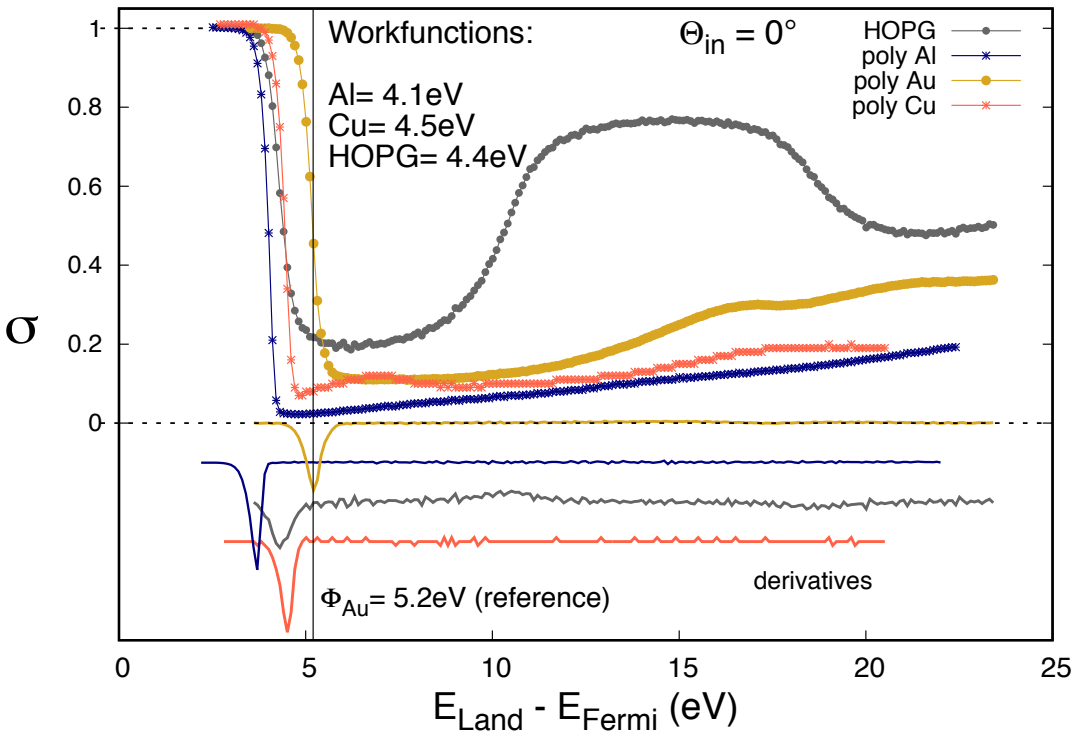

Figure 3.17: LE-TEY curves acquired under normal incidence on the clean surfaces of polycrystalline Au (gold dotted line – reference), polycrystalline Al (blue starred line), polycrystalline Cu (orange starred line) and HOPG (grey dotted line). The position of the minima in the first derivatives of each LE-TEY curve (given at the bottom for "σ <0") yields values for the workfunction of each target.

surface potential.

In the case of HOPG, with a Φ =4.4± 0.2 eV, it is lower than expected [230]. In further experiments, other strategies were adopted to perform the annealing of the sputter-cleaned HOPG surface. As the sample was baked under UHV at a constant temperature of 300° for about 10 hours the workfunction measured resembled more the expected value, exhibiting its onset-slope between 4.5–4.6 eV. In general, baking cycles of specimens performed in a UHV environment are adopted to remove water vapour adsorbed on the surface [7, 33].

This series of experiments demonstrated the reliability of the used instrumentation and of the performed energy calibration.

For the proper interpretation of the different trends in the LE-TEY-curves, visible as landing energy-dependent structures at higher landing energies, it will be demonstrated that knowledge of the (unoccupied) band structure of the target is necessary. This topic is discussed in further detail in section 4.1.

3.3.3 The "LASEC" (e,2e)-Coincidence Spectrometer at Roma Tre

The "LASEC" apparatus is composed of two communicating UHV-chambers one dedicated mostly to the preparation of the sample, the other for the characterisation of the target by means of multiple electron spectroscopy techniques. The preparation chamber is equipped with an Ar^+-ion gun for sputtering, an evaporation crucible (not used in this work) and a Low Energy Electron Diffraction (LEED) unit. The analysis chamber contains three excitation sources and two home-built hemispherical mirror analysers (HMAs); when operated simultaneously these analysers are employed for the acquisition of (e,2e)-coincidence spectra.

The sample can be moved between the two chambers by means of a manipulator (commercial VG model HPT-WX) which is also equipped with a heating filament for the annealing of (crystalline) targets. When in communication (standard conditions during measurements) the base pressure of these chambers ranges between $4.0–7.3\times10^{-10}$ mbar. In this apparatus, UHV-conditions are achieved by means of two membranes (one per chamber) establishing the primary pumping system, followed by a series of turbo-molecular pumps and in addition the analysis chamber is equipped with an ion pump. A getter pump additionally helps to maintain the pressure low in the preparation chamber.

Cleaning, i.e. sputtering and annealing, of the target surface is performed in the preparation chamber, when separated from the analysis chamber. To keep the chambers disconnected is relevant to avoid contamination of sources and detection systems induced e.g. by sputtered material, and also to keep the pressure in the analysis chamber low. Sample preparation procedures were already explained for each individual specimen in section 3.2 and subsections therein.

The analysis chamber is equipped with a monochromatised Al Kα X-ray source ($h\nu = 1486.7$ eV), a Ultra-Violet Photo-electron Source (UPS) consisting of a He I discharge lamp with a photon energy of 21.2 eV, with a home-built monochromatic electron source (Mono-gun). The XPS and UPS sources were utilised only for monitoring the cleanliness of a surface in the former case, and for determining the transmission function (χ_{trans}) of the electron optics of R66 in the latter case.

In Mono-gun, after its emission at the filament (made of a Tungsten wire) the electron beam gets monochromatised by its passage through an energy dispersive element, as the ones used in hemispherical analysers, with a mean radius of 33 mm operated at a pass energy $E_{pass} = 1.3$ eV. After its passage through the hemispheres the monochromatic electron beam is focussed onto the sample by an electron optical system, equipped with deflection plates for deflecting in the vertical and horizontal direction, reaching a spot dimension of 1–2 mm diameter. The limit energy resolution of Mono-gun, at the pass energy of 1.3 eV, is of about 60–90 meV.

For electron detection two home-built hemispherical analysers are used: "R66" & "TOF"[11].

[11]The naming of "TOF" for this hemispherical analyser may be misleading, since it is not a Time-of-Flight analyser. This naming was chosen years ahead since originally it was planned for it to be furnished with a Time-of-Flight detection unit.

Figure 3.18 illustrates the experimental chamber of the "LASEC" apparatus, showing the main elements of the experimental equipment employed for the acquisition of (e,2e)-coincidence spectra; representing the predominant spectroscopic tool used in this thesis project. Both HMAs and electron source are fixed and aligned in the scattering plane. The two analysers are perpendicular to one another and the electron source encloses an angle of 30° with R66. The target (black) can

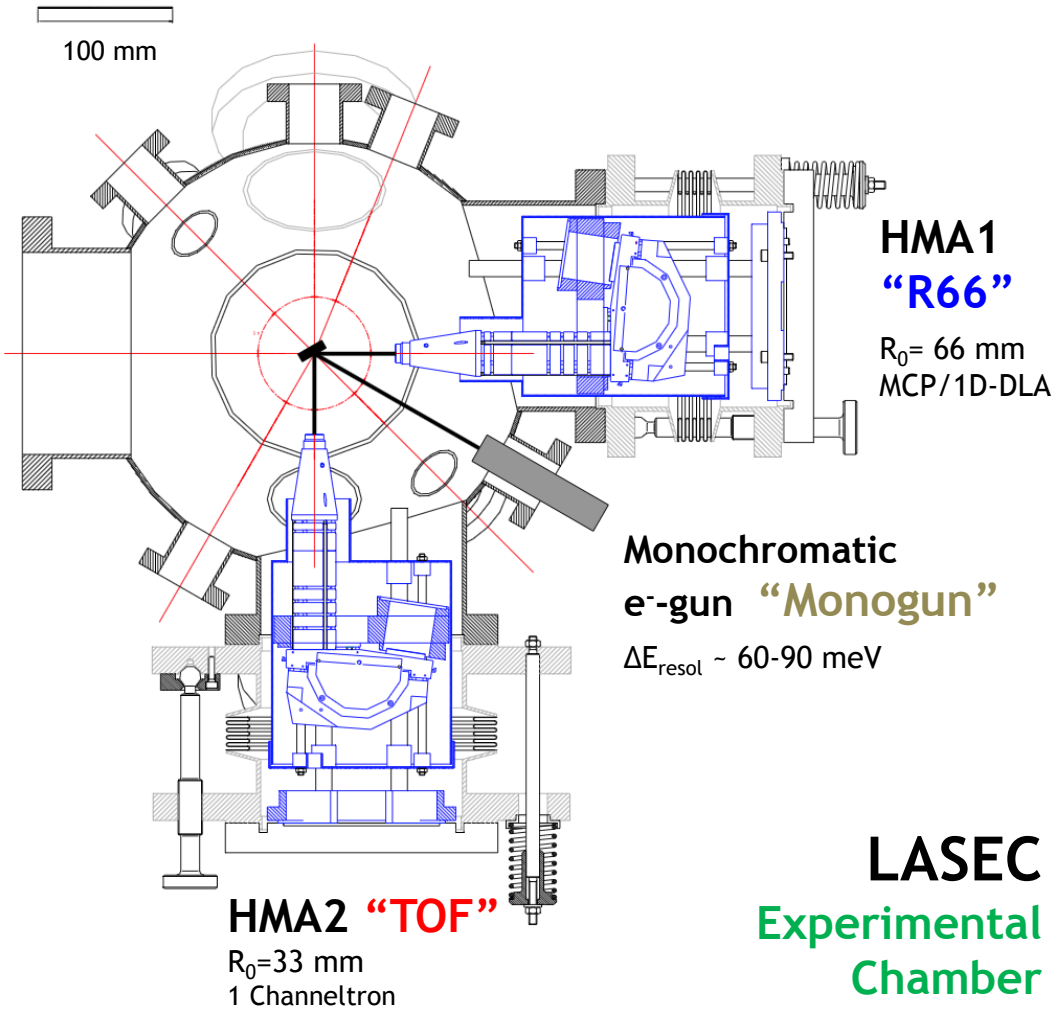

Figure 3.18: Experimental chamber of the LASEC spectrometer displaying the two HMAs and Mono-gun, which encloses an angle of 30° with R66. This latter is positioned at 90° from TOF within the detection plane. R66 is equipped with a MCP/1D-DLA detector, whereas TOF with a single channeltron (CEM). [Figure taken from Ref. [147] and modified according to the actual set-up.]

be rotated around the manipulator axis orthogonally to the scattering plane. By means of this rotation, the sample surface normal encloses different polar angles with respect to (w.r.t.) the electron source (θ_{in} . . .incidence angle) and both analysers ($\theta_{out1,2}$ . . .ejection angles w.r.t. either HMA), respectively. By varying the sample surface rotation w.r.t. the two analysers a large variety of kinematics can be accessed, ranging from specular reflection conditions to higher order Bragg diffracted beams, i.e. different components of the exchanged momentum are projected onto

the surface of the sample ($\Delta\vec{K}_{\parallel}$). Azimuthal rotation of the sample can be used to adjust the surface along a specific crystallographic direction of interest.

The mean radius (R_0) of the "TOF" analyser is of 33 mm and the width of the entrance slit (positioned on the Herzog-plate preceding the hemispheres) is of 3 mm. The detection unit of this HMA is furnished with a single channeltron, thus allowing to measure one energy-point (with a given energy resolution, ΔE_{resol}) at a time.

In a first approximation, the energy resolution in a hemispherical analyser is proportional to E_{pass} through a factor depending on the dimension W_{slit} (given by the average between the dimensions of the two slits), the mean radius R_0 (in between the two hemispheres) and the angle α (given in radians) w.r.t. the normal direction when entering the slit [48, 231]:

$$\frac{\Delta E_{resol}}{E_{pass}} \simeq \frac{W_{slit}}{2\,R_0} + \frac{\alpha^2}{4} \tag{3.6}$$

The angle α is the linear half-angle accepted at the Herzog-plate at the entrance of the analyser, whose maximum (α_{max}) was estimated to be $\pm$ $\sim$4° (for both HMAs). From eq. (3.6) it can be understood that ΔE_{resol} is mostly effected by the dimensions of R_0 and can be additionally improved by varying the acceptance angle α. Variations in α can be achieved by opportunely tuning the electron optical elements preceding the hemispheres, which determine the electron transport towards the energy-dispersive element.

Considering only the first term of eq. (3.6) the achievable energy resolution in TOF is of ca. $\Delta E_{resol}(TOF) = 4.5\% \times E_{pass}$.

This second home-built hemispherical analyser – "R66" – was assembled and implemented in the UHV-system during the first year of my PhD-project, which called for a long period of testing and calibration both of its hardware and software. The main characteristics of this new HMA are: (1.) larger mean radius R_0 of 66 mm to improve the energy resolution and (2.) a detection unit composed of a two-stage micro-channel plate (MCP) and a mono-dimensional delay line anode (1D-DLA) to allow the in-parallel acquisition of a larger energy window at a time.

In R66 the average dimension of all slits is 1 mm and being its mean radius of 66 mm, if one considers only the first term of equation (3.6) one should expect an energy resolution of $\Delta E_{resol}(R66) = 0.75\% \times E_{pass}$.

During a coincidence measurement, the electron optics of R66 was, in most of the cases, tuned for the acquisition of LEEs, when this analyser was employed to measure the SE-part of the electron spectrum. A paragraph dedicated to the tuning of the electron optical system of this analyser can be found in the following (paragraph 3.3.4.1). Further details on this novel HMA are discussed in a to it dedicated sub-subsection in the following (see sub-subsection 3.3.3.1).

All Angle-resolved (Ar) Reflection Electron Energy Loss and Secondary Electron Emission Spectra (Ar-REELS and Ar-SEES) as well as (e,2e)-coincidence spectra discussed in chapter 4 were acquired employing the monochromatic electron source (Mono-gun).

These double-differential spectra, both Ar-REELS, Ar-SEES and LEED-scans presented in section 4.2 and subsections therein were acquired employing either of the two HMAs.

Figure 3.19 shows the instrumentation used for the acquisition of LEED-scans, Ar-REELS and Ar-SEES with R66. While LEED and Ar-REELS measurements were performed employing the High-Resolution (HR) configuration of the electron optical system, for the acquisition of Ar-SEES, the lens system was adjusted in such a way to achieve High-Transmission (HT) of LEEs. For the acquisition of LEEs it is necessary to tune the electron optical element in such a way, thus to obtain a transmission function as constant as possible over the whole energy range of a SEES, to ensure that this latter is measured for all electron energies with a same efficiency (preventing a chromatic aberration of the detected LEEs). Details on the tuning of the electron optics for the LE-regime can be found in a dedicated paragraph in the following. Specular

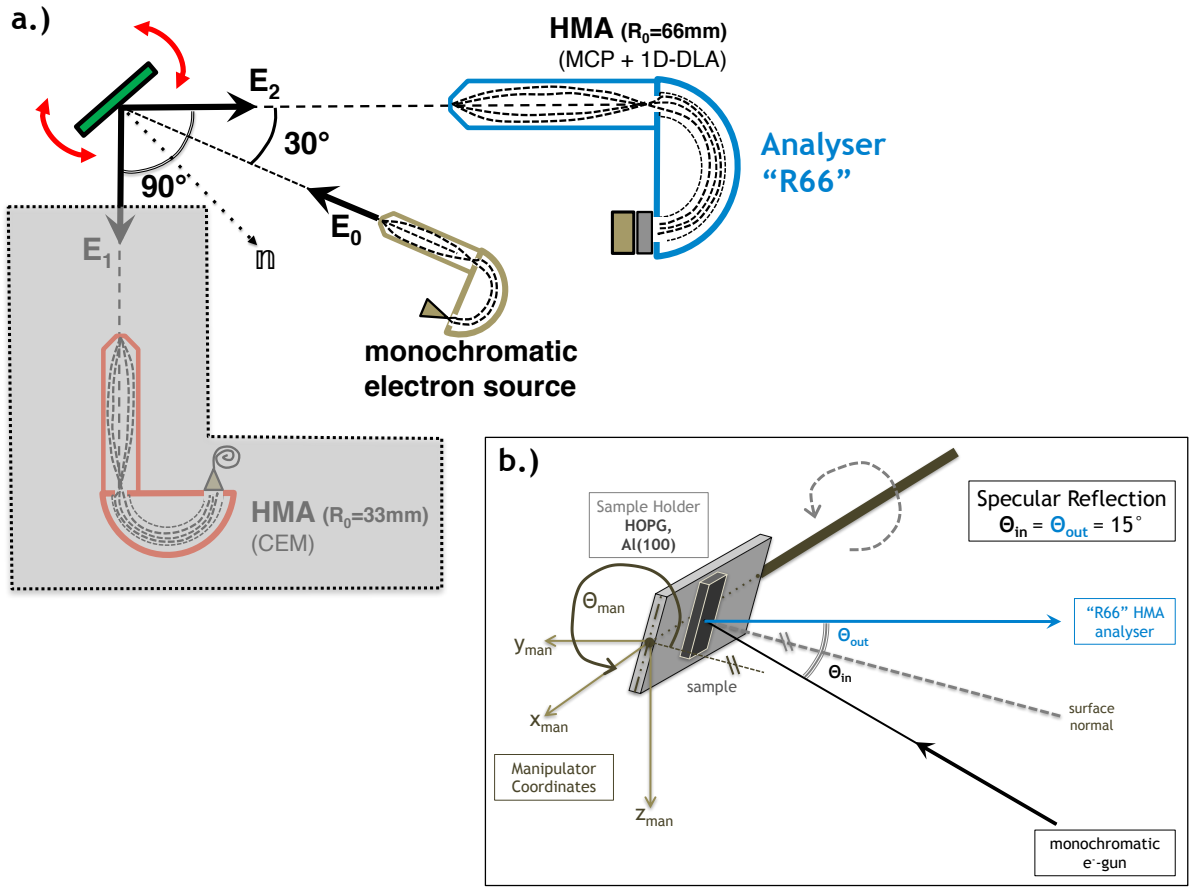

Figure 3.19: Instrumentation used in the LASEC laboratory to perform Ar-REELS and electron diffraction measurements with high-resolution is exposed. For these kind of measurements the electron optics of the R66-energy analyser is tuned achieving a high-energy resolution (ΔE_{resol}(HR)=0.9%×E_{pass}). Operated in HT-mode the electron optical configuration is optimised for the acquisition of Ar-SEES, with an energy resolution of ΔE_{resol}(HT)=1.85%×E_{pass}. Panel (b.) illustrates the case for specular reflection condition.

reflection in this configuration is given for $\theta_{in} = \theta_{out} = 15°$. In all experiments, the analyser was operated at a constant pass energy, E_{pass}, in order to maintain the same energy resolution in each spectrum. The width of the entrance slit in R66 (considered in the E-dispersive direction) is of $W_{slit} = 1$ mm. Herewith, the overall estimated energy resolution for the HR-configuration is of $\Delta E_{resol}(HR) \simeq 0.9\% \times E_{pass}$. For LEED-scans generally a pass energy, E_{pass}, of 2 eV or 5 eV was employed, depending on the electron beam current (I_0) setting. When I_0 was already adjusted for the acquisition of (e,2e)-coincidence spectra, thus being low, with 10–15 pA, a pass energy of 5 eV was chosen, otherwise for higher values of I_0 the scan could be performed at a lower pass energies. For Ar-REELS acquisition predominantly a pass energy of 5 eV was used. In these cases, the average energy resolution $\Delta E_{resol}(HR) \simeq 32$ meV was achieved. In case of Ar-SEES, the optics of

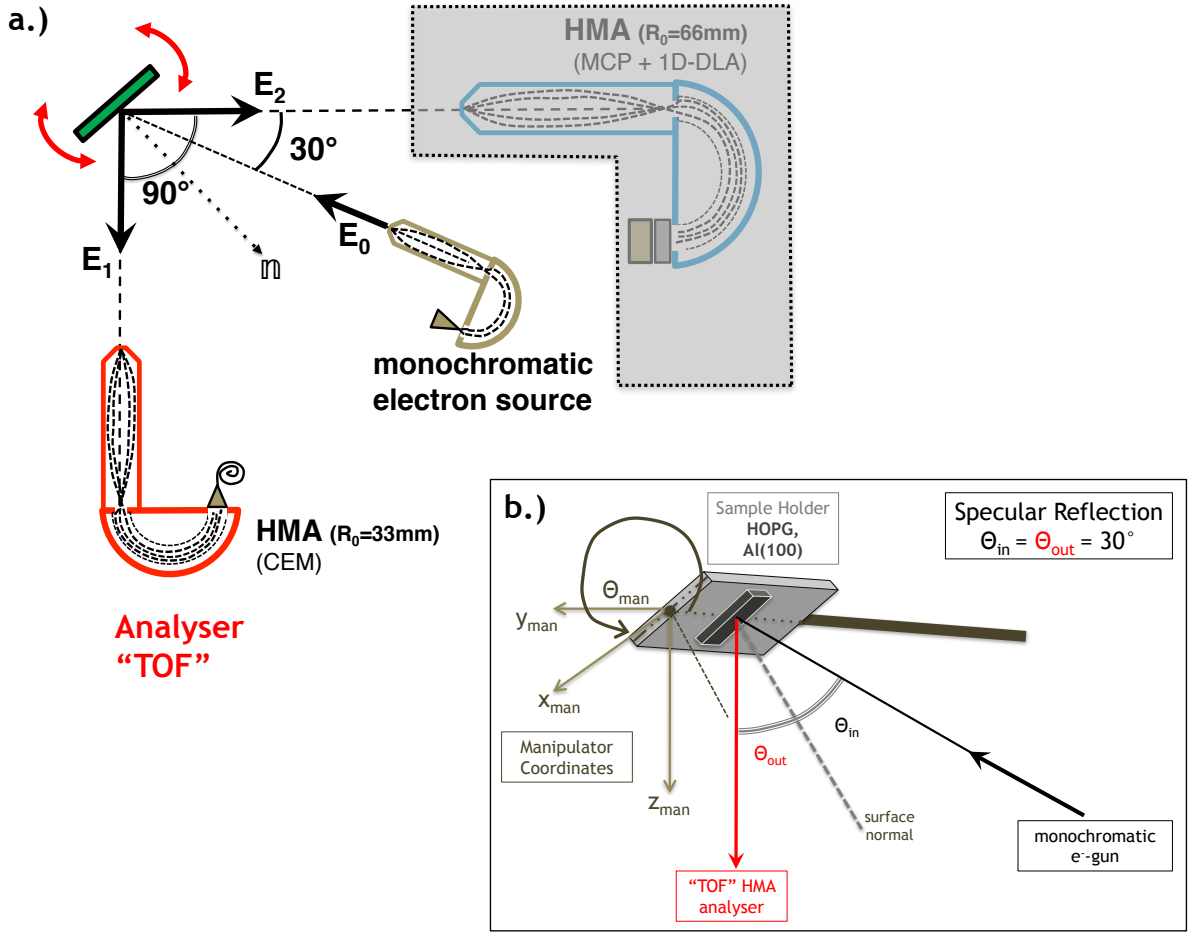

Figure 3.20: Instrumentation used in the LASEC laboratory to perform Ar-SEES, Ar-REELS and electron diffraction measurements with high-transmission is exposed. The electron optics of TOF is tuned to enhance detection of both the energy loss range and the LE-part of the electron spectrum ($\Delta E_{resol}(HT) = 4.5\% \times E_{pass}$). Panel (b.) illustrates the case for specular reflection condition.

R66 was tuned to the HT-mode and in this case the analyser was operated at a pass energy of 25 eV. In this case the achievable energy resolution was of $\Delta E_{resol}(HT) \simeq (0.9\% \times E_{pass}) \simeq 225$ meV.

Figure 3.20 displays the experimental instrumentation used for the acquisition of LEED-scans,

Ar-REELS and Ar-SEES using the TOF-analyser. In this case specular reflection conditions are reached for $\theta_{in} = \theta_{out} = 30°$. In TOF, the electron optics was (in most of the cases) tuned to maximise the accepted solid angle from which the electrons were emitted (or scattered) and its energy resolution was of ca. $\Delta E_{resol}(HT) = 4.5\% \times E_{pass}$. This very same configuration could be used to acquire the entire electron spectrum provided that the primary electron energy, E_0 was low, e.g. 50 eV.

3.3.3.1 The Hemispherical Analyser "R66"

As recognisable from eq. (3.6), two of the main parameters influencing the most the achievable energy resolution (ΔE_{resol}) of an electrostatic energy hemispherical mirror analyser (HMA) are the dimensions of the average of all slits (W_{slit}) and the mean radius (R_0) in between the two hemispheres. Hence, by decreasing the former and increasing the latter ΔE_{resol} can be additionally improved. To achieve a higher energy resolution the HMA of R66 was therefore planned with an R_0 of 66 mm and an entrance slit with a width in the energy dispersive direction of 1 mm and in the angular dispersive direction of 7 mm.

Another relevant physical parameter determining the achievable energy resolution is given by the range of angles ($-\alpha_{max} < \alpha < +\alpha_{max}$) the beam of electrons subtends at the entrance aperture (entrance slit at the Herzog plate). This angle spread, $\pm\alpha_{max}$ (defined with respect to the optical axis) is typically controlled by the angular magnification ($|M_\alpha|$) of the injection lens preceding the energy dispersive element. By convention, trajectories launched (at the entrance Herzog plate) with $\alpha > 0$ are defined as *outer* trajectories, while those with $\alpha < 0$ are *inner* trajectories.

A conservative choice for the maximal accepted angle α_{max} (calculated in radians) is given by following expression [232, 175, 233]:

$$\alpha_{max} \leq 0.8 \times \frac{W_{gap}}{\pi R_0} \tag{3.7}$$

where W_{gap} is the width of the gap in between the two concentric hemispheres (ca. 25 mm). In R66 the maximal accepted angle α_{max} is ca. 4° for which one expects the electrons to pass through the gap between the hemispheres without impacting on their walls. It is important to avoid an overfilling of this gap, which would indeed lead electrons to impact on the hemispheres' walls. To minimise the probability of an overfilling of the gap, it is also necessary to contain the ratio (X_{max}/R_0) between the maximal deviation (X_{max}) for an electron trajectory (considered w.r.t. the central trajectory), and the mean radius, R_0. In general, a reasonable choice for this ratio is given by a 20% margin; this is the reason why for the calculation of the α_{max} as given in equation (3.7) one assumes to fill only 80% of the gap (W_{gap}).

After their passage through the E-dispersive element, the electrons reach the exit Herzog plate on which a trapezoidal exit slit is mounted. This trapezoidal exit slit was shown previously in figure 3.1 and its shorter side is 7 mm long (corresponding to ca. 20% of the gap) whereas in the E-dispersive direction it is 20.1 mm long, which corresponds to ca. 80% of the analyser gap, W_{gap}. The pencil of electron trajectories passing through the hemispheres have therefore a width comprised between 20% and 80% of the gap between the hemispheres.

For the electron transport, this new HMA is equipped with an electron optical element composed of six electrodes whose polarisation can be adjusted according to the desired configuration of focussing lenses. The so-called high-resolution (HR) configuration of the lens-system is used to obtain high energy and angular resolutions needed for instance when performing Ar-REELS or XPS measurements. The high-transmission (HT or acceleration) modality is mainly used for the acquisition of LEEs, hence for SEES and for (e,2e)-coincidence experiments, where the highest transmission of electrons at a large acquisition angle is aimed. Also the electron optical element of the TOF-analyser can be set thus to perform both HR- and HT-measurements.

During the planning of this novel analyser, former group members dealt with the simulation of the electron optics for the electron transport in this analyser [234] and with the first experimental performances of this analyser in the gas phase [235]. According to these simulations and first test measurements (performed in 2002), expected energy resolutions for this analyser were comprised between 0.77% and 2.0% of the used pass energy. After implementation into our UHV-system, R66 was tested and calibrated, delivering an average energy resolution of ca. $1\% \times \mathrm{E}_{pass}$, which corresponds fairly to the expected one.

In the following, the characteristics of R66 and its detection system are discussed focussing mainly when operating in the HT-modality, hence when tuned for the acquisition of SEES and (e,2e)-coincidence spectra. For the majority of the measurements presented in this work, R66's electron optical elements were tuned in such a HT-mode aiming at maximising the transport of LEEs and at enlarging the accepted elevation (from the target) angle of these LEEs towards the detector. In sub-subsection 3.3.4.1 the procedure of fine-tuning of this electron lens system for the LE-regime is discussed in more detail.

R66 is equipped with a detection unit composed of a two-stage micro-channel plate (MCP) [19, 236] and a mono-dimensional delay line anode (1D-DLA) [237]. MCPs are two-dimensional sensors detecting electrons, ions and photons (of various frequencies) in a HV or UHV environment, and they amplify these detected signals. A MCP is usually composed of an array of $10^4 - 10^7$ miniature electron multipliers oriented parallel to one another with typical channel diameters in the range 10–100 μm. The pair of MCPs used in R66 are stacked in chevron configuration and each channel has a diameter of 27 μm. The linear diameter of the whole MCP-surface is 40 mm. Operation requires two DC voltages for MCP "front" and "back" contacts and one voltage for the anode wire array ("dla"). In our instrumentation, optimal operation conditions for the MCP/1D-DLA

detector were found when the voltage of the MCP "front" is kept at ground potential and the MCP "back" is set at +1750 V w.r.t. to its front. The 1D-DLA consists of a wire array passing right behind the MCP and its optimal voltage depends on the distance between the MCP carrier plate and the anode wires. In our case we found this optimal voltage to be +150 V higher than the voltage set at the MCP "back". The detection-unit is upended on the retarding voltage of the analyser.

This detection unit was conceived and assembled at ELETTRA Sincrotrone in Trieste and its electronics is operated by the THR-02-ST unit [238], which is a 4-channel advanced Time-to-Digital Converter (TDC) of which only two channels are used in our case. Every channel is equipped with a Constant Fraction Discriminator (CFD) that allows very low jitter measurements on a wide input of pulse amplitude range. The achievable time resolution is of ca. 100 ps (and below). The spatial resolution is limited only by the channel dimensions and their spacings. The THR-02-ST is configured with a 1D-DLA, enabling computing of position and arrival times (with respect to the used trigger signal) of the detected electrons. After the electrons travel through the energy dispersive element of R66 they reach the MCP-detector, which registers its signal and amplifies it producing an electron cloud. The electron cloud emerging from the MCP is collected by the the 1D-DLA and its signal travels towards both ends of the wire array. This signal get therefore split into a pair of signals (labelled as "CH#1" and "CH#3" in the THR- 02-TS electronics). A typical MCP-signal is shown in figure 3.21. This negative pulse is collected directly after its attenuation by the pre-amplifier. Each one of these signals is fed

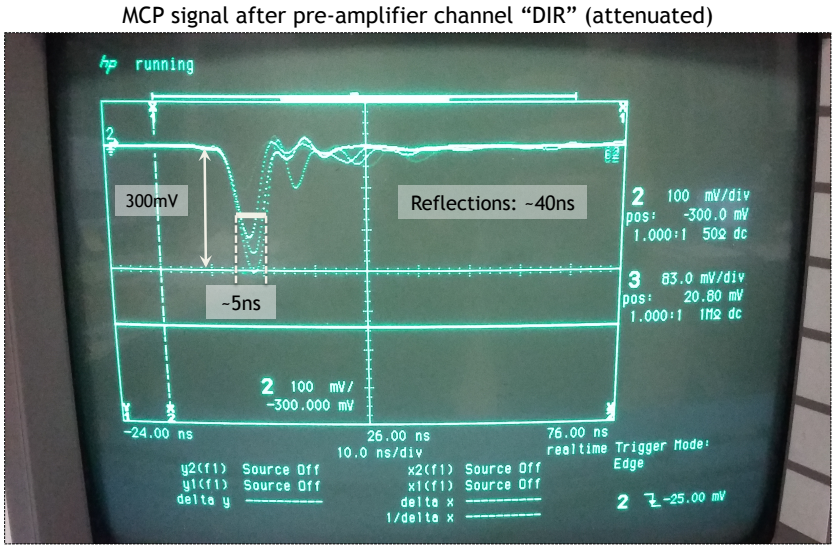

Figure 3.21: MCP signal (from the "direct" channel) observed at the oscilloscope after its passage through the pre-amplifier. Typically, an attenuated MCP-signal has an amplitude of ca. 300 mV and a width (at FWHM) of ca. 5 ns. The main signal can be accompanied by some reflections, which in this case are about 40 ns long. These reflected signals are cut off from the actual signal by imposing a "dead time" of 40 ns at the THR- 02-TS electronics.

to an internal Constant-Fraction Discriminator (CFD) and is split into a "direct" (DIR) and a "delayed" (DEL) signal. The internal CFD extracts the time-information, by overlapping the 2 signals, having an "ideal crossing" condition independently from the pulse shape and height. The position of the detected electron is encoded by the signal arrival time difference at both ends of the delay-line. The difference between the signal arrival times at the adjacent ends of the

delay-line is proportional to the position on the MCP in the same direction. The sum of these arrival times is fairly constant with few ns for each event.

Differently from a single Channel Electron Multiplier (CEM or channeltron) the MCP-detector is capable to perform the *in-parallel* acquisition of a larger energy window at a time, E_{win}. The width of this energy window is dependent on the pass energy set at the hemispheres. This results advantageous especially when performing (e,2e)-coincidence measurements, by means of which the acquisition times can be decisively reduced, enabling to reach a same signal statistics in hours instead of days.

The electrons exiting the exit slit, at the exit Herzog-plate, are projected onto the MCP, whose active illuminated area corresponds to 500 $channels$. Each of these MCP channels has a corresponding time-width of 27 ps, which in turn also corresponds to the time resolution of the DLA, i.e the minimum difference in time resolved by the DLA-detector. The arrival position of an electron (registered at the MCP) is encoded on the basis of the arrival time of its signal at the two extreme of the delay line. The software written for handling the (e,2e)-coincidence acquisition chain (written by Sbroscia [239]) was step-wise adapted along with the calibration of this analyser.

The nominal kinetic energy set at the R66-analyser corresponds to the central energy of $E_e(cx)$ which coincides with the central bin-channel illuminated on the MCP-detector. Correspondingly, the extremal MCP channels centred around this central bin (with $\pm 250\, channels$) define the detectable energy range of this energy window with extremal values of $E_e(lx)$ and $E_e(rx)$, being the minimal and maximal kinetic energies, respectively.

Through calibration of the energy scale, a conversion factor fixing the relation between kinetic energy, E_{kin} and MCP-channels was determined, according to which: the kinetic energy of 1 eV measured at an $E_{pass} = 1$ eV corresponds to 4700 $channels$. Hence, for a pass energy of 25 eV, the energy window of acquisition corresponding to these 500 active channels on the MCP is of ca. ± 1.35 eV around the chosen central kinetic energy of the SE, E_e. This energy window, ΔE_{win}, is obtained by multiplying the $E_{pass} = 25$ eV with the conversion factor $\zeta = {}^{500}/_{4700}$ between channels. The higher the pass energy the larger the energy window. The main advantage of having an MCP-detector instead of a single channeltron is represented exactly by this in-parallel acquisition capability over a larger energy range centred around a kinetic energy of choice.

However, it shall be noted that, as long as the pass energy is of $\leq$30 eV the extremal energies (at $E_e \pm ({}^1/_2) \times \Delta E_{win}$ respectively) do not differ more than 1.6 eV from the central energy, whereas if one sets $E_{pass} = 50$ eV this energy window becomes of ca. ± 2.65 eV which in the LE-range makes a great difference between the two extremal E-points.

For example, if the central energy at R66 is set at $E_e(cx) = 4.5$ eV, for a pass energy of 50 eV the low extreme is given by $E_e(lx) = 1.84$ eV and the high extreme by $E_e(rx) = 7.15$ eV. These are very different kinetic energies, for which *chromatic aberration* effects could easily arise, if the χ_{trans} is not sufficiently uniform over this kinetic energy range. This is a further aspect that

needs to be considered when planning an (e,2e)-coincidence measurement in which one wants to employ such higher E_{pass}-values.

This was done for the series of (e,2e)-measurements from HOPG at $E_0 = 50\,eV$. However in this occasion the electron optics of both analysers were re-optimised in order to minimise these chromatic aberration effects. In this series of measurements R66 and TOF were both capable of acquiring the entire electron spectrum and their role could be switched at any time. For doing so their electron optical elements were opportunely tuned, thus to achieve a sufficiently uniform χ_{trans} down to ca. 3 eV. In such an experiment it no longer makes sense to label electrons as ${e_s}^-$ and ${e_e}^-$.

Through the predetermined scattering kinematics and by virtue of knowing of the exact arrival time (see subsection 3.3.4 for more details), and hence position, of the detected electron signal on the MCP/DLA-detector unit, it then becomes possible to reconstruct the complete kinematics of the underlying scattering process.

When R66 is employed for single-electron spectroscopy, hence for the acquisition of REELS, XPS, SEES, etc. measurements the "start" signal for opening the time-window (of max. $2\,\mu s$) where the incoming electron event represents the "stop" signal, is provided by an internal trigger of THR-02-ST.

As explained in more details in subsection 3.3.4, to measure an (e,2e)-spectrum the arrival times of the scattered (${e_s}^-$) and on the ejected (${e_e}^-$) must be determined. This also requires knowledge on the transit-time of both electrons with their respective kinetic energies inside R66's and TOF's optics and hemispheres. Variations in the transit-time influence the arrival time of these electrons at their respective detection units.

In an (e,2e)-coincidence experiment, R66 was mainly tuned on the *slow* secondary electrons, whereas the energy at the TOF-analyser was tuned to collect the inelastically scattered electrons (*fast*). The slow secondary electrons, collected by R66, therefore automatically deliver the "stop" signal in such a coincidence-logic acquisition chain. Whereas the "start" signal, opening up the $2\,\mu s$-time-window, needs to be fed externally into the THR-02-ST unit. This "start" signal is determined by the fast inelastically scattered electron signal coming from the TOF-analyser. Once that this $2\,\mu s$-time-window is opened, all signals collected at the MCP/DLA-detector, each one provided with an own time-stamp (created by the CFD) are then registered as "stop" signals falling within this time-window. Once that such an electron event is registered the time-window is closed. During this "closing" time, the collected data are elaborated and a new window can be opened as soon as a new starting signal from TOF arrives. If, by any chance, during the period that the time-window is still open an additional "start" signal from TOF arrives, this latter will be ignored, since it can not trigger the opening of an additional $2\,\mu s$-time-window, while the former being still active. In this case, a coincident electron pair falling within this window would be lost. Nonetheless, we do not expect this to happen too often, since our truly *correlated*-event frequency is low.

3.3.4 (e,2e)-Coincidence Spectroscopy

Figure 3.22 shows the instrumentation as wired for the acquisition of (e,2e)-coincidence spectra. The sample (green) is rotated wrt. the TOF-analyser in such a way for its surface normal, $\hat{n}$, to enclose with this analyser an emission angle, $\theta_{out}(TOF)$, at which the parallel component of the exchanged momentum $\Delta\vec{K}_{\parallel}$ is equal to the reciprocal lattice vector in a given symmetry direction. In this case TOF is tuned to collect the energy loss part of the electron spectrum (ELS). Whereas

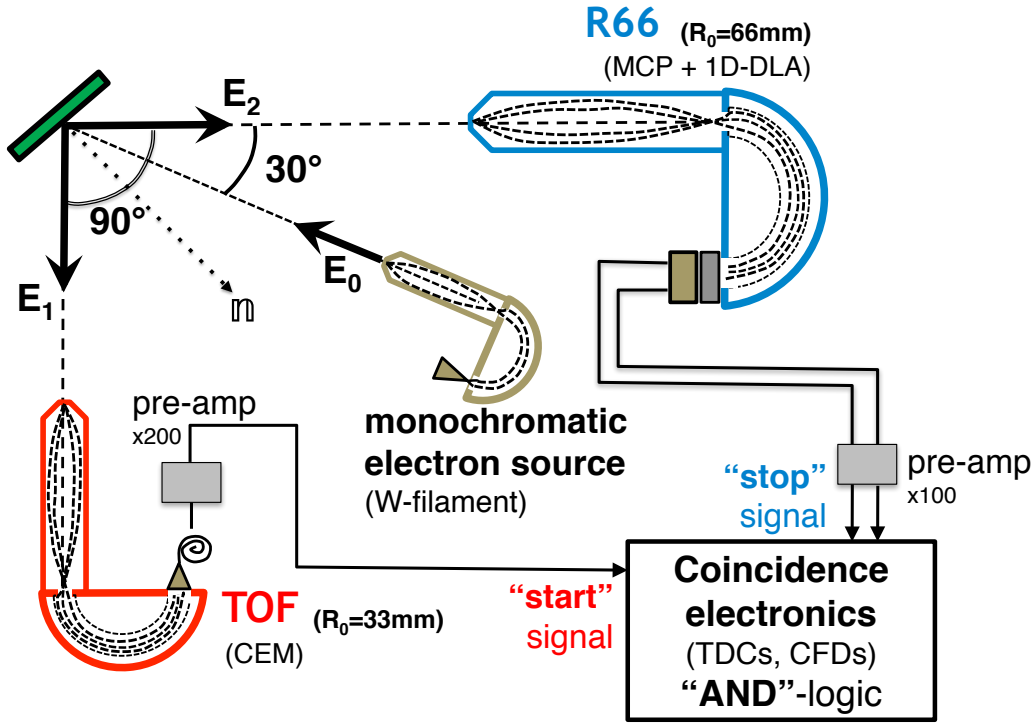

Figure 3.22: The configuration of the LASEC apparatus as wired for an (e,2e)-coincidence experiment depicted with a simplified scheme for the acquisition chain.

R66, tuned on the kinetic energy range of the SE-spectrum, is operated at a constant pass energy for the whole series of an (e,2e)-measurement campaign[12]. When TOF is aligned on the specular beam, R66 collects the SEs under an emission angle, $\theta_{out}(R66)$ of 60°. The target is bombarded by a continuous electron beam produced by Mono-gun.

The electron beam interacting with the target induces the inelastic scattering event in the

[12]Under the definition of a measurement campaign, it is meant the acquisition of a series of (e,2e)-coincidence spectra from the same sample under the same kinematical conditions for different correlated electron pairs. Such a series of measurement is subsequently opportunely merged yielding what we define to be an entire (e,2e)-spectrum. Such an (e,2e)-measurement campaign generally lasts for about 3–4 months

course of which SEs are generated. The inelastically back-scattered and the ejected SE electrons ($e_s{}^-$ and $e_e{}^-$) are then detected at each analysers respectively, each one of which is tuned on the expected kinetic energy for the correlated electron pair. Considering that electrons are indistinguishable fermions, thus making a distinction between *"scattered"* and *"ejected"* electrons seems rather inappropriate, nonetheless depending on the tuning of the electron transport system employed in an analyser we can enhance the acquisition of electrons with a selected kinetic energy range, pertinent to distinct electron spectral regions. Such a tuning of the electron optics justifies a distinction between scattered and emitted secondary electrons.

The acquisition of coincidence events (i.e. their frequency) is performed in terms of arrival times of these two electrons, which are then gathered in a time histogram displaying the arrival time difference of the electron pair. Additional details on the acquisition and on the evaluation of such coincidence spectrum can be found in sub-subsection 3.3.4.3.

In an (e,2e)-coincidence measurement, when the target is bombarded, the inelastically scattered (faster) electron arriving at the TOF analyser sets the beginning of the acquisition providing the THR-02-ST electronics with a *"start"* signal. At this point the electronics opens up a time window and awaits for the maximal duration of 2 μs the arrival of a signal detected at the second analyser, R66. If a SE (slow) electron of a given energy (the nominal kinetic energy set at R66) is detected at the MCP/1D-DLA detector a *"stop"* signal is produced which closes the previously opened time window. Hence, a so-called coincidence event is detected and registered to disk. After detection of this event the electronics is subject to a so-called *dead-time* – corresponding to the lapse of time after the detection of an event during which the detector is not able to record another event. Our MCP/1D-DLA detector has a dead-time of 40 ns. In case no stop signal is detected within the maximal time of 2 μs, THR-02-ST closes this time window and awaits for a new start signal, at which this same sequence is re-initiated.

For a pair of kinetic energies – of the electrons $e_s{}^-$ and $e_e{}^-$, respectively – it is possible to predict/calculate their total flight-times from the target to the electronics, hence the arrival times for the start- and stop-signals are known.

Their flight-times can be subdivided into two different intervals. One is essentially determined by the lapse time of their transport inside the lens-system and the hemispheres of each analyser till they reach the detectors; in the following defined as $\mathbb{T}_{HMA_{s,e}}$. The second interval of time corresponds to a time delay (t_{delay}) accumulated during the transfer of the detected electron signal to the coincidence electronics THR-02-ST and the time needed by all pieces of electronics to process this signal. Hence, this t_{delay} is composed of the lapse time spent in the (delay) cables, in the pre-amplifiers, the TDCs and the intrinsic delay of the THR-02-ST electronics which is essentially determined by its CFDs. The propagation delay of a coaxial cable (type RG 58) is of ca. 5 ns/1 m. This time-length-ratio was also applicable to all connection cables; hence knowing the cable lengths an equivalent time value is easy to obtain. More precisely, we determined the

exact overall t_{delay} of the (e,2e)-coincidence chain by sending a signal through each channel of the chain and monitoring this signal by means of an oscilloscope with respect to a reference signal. By doing so, we could also determine the intrinsic delays of each single piece of electronics. This t_{delay} is constant for all experiments, provided that a same delay cable length is maintained. Knowing all potentials set at the electrodes and at the spheres of an analyser, the flight-time of $\mathbb{T}_{HMA_S}$ for each travelled segment L_S – e.g. the length of an electrode or the path within the hemispheres – of the considered analyser, is easily determined for each electron of a given kinetic energy by the following relation:

$$\mathbb{T}_{HMA_S} = \sqrt{\frac{m_e}{2\,\alpha}} \cdot \frac{L_S}{\sqrt{(E_{s,e} + V_S)}} \tag{3.8}$$

where α is such that $\mathbb{T}_{HMA_S}$ delivers a time in ns when L_s is given in mm and $E_{s,e}$ in eV, this latter being the kinetic energy of the scattered(ejected) electron at its passage through the considered segment and finally V_S is the applied voltage at the segment. Remaining symbols stand for their usual meaning. A custom-made FORTRAN code [240] was used to calculate the complete time-of-flight for each E_e and E_s travelling through all segments of either HMA.

For a selected correlated electron pair – whose energies are determined by means of conservation law given in equation (2.3) – after determining their individual flight-times it is possible to assess also their arrival time difference or delay ($\Delta\tau$) at the counting unit. The intensity, i.e. the frequency of appearance, of all registered coincidence events is then displayed as a function of this $\Delta\tau$-scale.

The key parameter of a coincidence experiment is represented by its capability of discriminating *"true"* from *"false"* coincidences, which ultimately sets the limit for the feasibility of such an experiment. A so-called *"true"* coincidence event is given by a truly correlated electron pair, composed of the inelastically back-scattered and the ejected SE electron that have participated to the same collision event. The rate of probability for such a truly correlated event can be obtained as follows [241]:

$$R_{true} = \kappa \cdot I_0 \cdot \left(\frac{d^3\sigma_{(e,2e)}}{d\Omega_s\, d\Omega_e\, dE} \right) \Delta\Omega_s \Delta\Omega_e\, \Delta E_{(e,2e)} \tag{3.9}$$

where the $(d^3\sigma_{(e,2e)}/(d\Omega_s\, d\Omega_e\, dE))$ is the TDCS as defined already in eq. (2.9). The $\kappa = ((\varrho\, l) \cdot \Xi_s\, \Xi_e)$ in the front of the equation is a (nearly) constant factor determined by the density of the target $(\varrho\, l)$ and the detection efficiencies of each analyser $(\Xi_{s,e})$. "Nearly" constant because, whereas the target density remains unchanged, the detector efficiency – which also entails the transmission function χ_{trans} of an analyser – may vary in dependence of the detected kinetic energy. Nonetheless, in a first approximation this efficiency can be regarded as constant, since we verified that the transmission function and the collection efficiency of the analysers was fairly uniform at all considered energies.

The $\Delta\Omega_{s,e}$ are the solid angles of either analyser and the $\Delta E_{(e,2e)}$ is the "effective" overall

energy resolution of coincidences. In eq. (3.9) the main factors influencing the true count rate are given by the primary current I_0 and the shared detection volume of the two analysers, determined by the product of the individual angular resolutions.

"False" coincidences, instead, occur between uncorrelated electron events, i.e. between electron signals generated in randomly distributed scattering processes, detected however within a same time-window, t_w. Such events are always present and constitute a continuous background of signal in the time distribution of the delayed (by $\Delta\tau$) electron pair. The probability rate for these events is then given by:

$$R_{false} = \kappa_s\ \kappa_e \cdot I_0^2 \cdot \left(\frac{d^2\sigma_s}{d\Omega_s\, dE}\right) \cdot \left(\frac{d^2\sigma_e}{d\Omega_e\, dE}\right) \Delta\Omega_s\, \Delta\Omega_e\, \Delta E_s\, \Delta E_e \cdot t_w \tag{3.10}$$

Differently from the true rate, R_{false} is proportional to the square of the incident current, I_0^2, and to the "singles" cross-sections of the single electron events counted at either analyser, given by the the double-differential expressions and their respective angular and energy resolutions. The time t_w defines the minimal delay time (between two pulses), i.e. the time window within which true coincidence events are expected to be distributed.

For clarity, it shall be emphasised that it is not possible to distinguish whether an individual coincidence event is a false or a true one, however the accumulated intensity of truly correlated electron pairs can be indeed distinguished in such time histograms, since their accumulation leads to the formation of a peak superimposed over the background of false coincidences (as shown in figure 3.31).

In order to enhance the performance of an (e,2e)-coincidence experiment, a large True-to-False ratio – (T/F) = (R_{true}/R_{false}) – of these events is aimed. As recognisable from the formulae defined in equations (3.9) and (3.10), the main factors influencing these rates are the primary current I_0 and the shared detection volume, since all remaining factors, such as $(\varrho\, l)$, Ξ_s and Ξ_e and the energy resolutions ΔE_s and ΔE_e are nearly constant at a given kinetic energy.

An increase of the primary current does not help to ameliorate the (T/F)-ratio, since false coincidences are proportional to the squared current, whereas the true events relate linearly to it, which implies that choosing a minimal low current value would yield an ideal (T/F)-ratio. On the other hand, setting this current to a vanishing low value would demand infinitely long acquisition times, therefore a compromise for the choice of I_0 needs to be made between these two factors, when planning an experiment.

In fact, for the optimal planning of a coincidence measurement it is more convenient to estimate the acquisition time τ_{acq} needed to obtain an (e,2e)-spectrum with an acceptable (selected) statistical error, $Err(\%)$, expressed as the percentage of "true" coincidences for the

selected experimental condition. This τ_{acq} can be calculated as follows [241]:

$$\tau_{acq}[Err(\%)] = \frac{\sqrt{2}}{\Xi_s\,\Xi_e\,\Delta\Omega_s\,\Delta\Omega_e\left(\frac{T}{F}\right)Err(\%)^2}\cdot\frac{1}{\sigma_{(e,2e)}}\times \times\left[\frac{1}{I_0\,(\varrho l)\,\Delta E_{(e,2e)}}+t_w\cdot\frac{\sigma_s{}^{(2)}\cdot\sigma_e{}^{(2)}}{\sigma_{(e,2e)}}\right] \tag{3.11}$$

in this expression $\sigma_{(e,2e)}, \sigma_s{}^{(2)}$ and $\sigma_e{}^{(2)}$ are the abbreviations for the TDCS and the double-differential cross-sections (2DCS) of the single electron spectra, respectively. From equation (3.11) one would expect that with an increase of I_0 the acquisition time reduces, however this τ_{acq} is also inversely proportional to the (T/F)-ratio, thus emphasising once again that the choice of the incident flux must be carefully weighted between these two factors. Furthermore, this acquisition time will eventually saturate, reaching a limit, for which any further increase of the primary current does not lead to any additional diminished τ_{acq}. Also, from eq. (3.11) it is recognisable that the acquisition time, being inversely proportional to the accepted solid angles $\Omega_{s,e}$, can be decisively enhanced by maximising these individual solid angles. In addition, it is desirable for these solid angles to be brought to maximal superposition, thus to maximise their shared volume of detection by means of which the (e,2e)-coincidence rate can be further enhanced. To achieve the maximal overlap of the individual solid angles, both analysers need to be carefully aligned in such a way that their individual Fields-of-View (FoVs) are well superimposed. In sub-subsection 3.3.4.2 a more detailed description of this experimental aspect is delivered.

Let us assume that a certain (e,2e)-experiment is running already for some time, e.g. for one hour, and that in the acquiring time histogram a coincidence peak starts to appear, then it is possible by means of eq. (3.11) to make a rough estimation of the overall acquisition time needed to achieve a certain statistical error.

For this experiment most of the settings are already known, since they have been fixed prior to its launching. Hence, the I_0 is known, all other contributions, intrinsic to the kinematics of the experiment (e.g. the two 2DCS, the solid angles $\Omega_{s,e}$) as well as the detection efficiencies will remain constant for the whole duration of this (e,2e)-measurement and can be therefore regarded as a constant factor. At this point, by making a first rough approximation of the experimental count rates R_{true} and R_{false}, it is possible to use a simplified version of eq. (3.11) to estimate for how long this measurement needs to run in order to achieve a given statistical error, for instance an $Err(\%)\,!=10\%$. In this case, the $\tau_{acq}[Err(\%)]$–formula simplifies to:

$$\tau_{acq}[Err(\%)] = \frac{R_{true}+R_{false}}{R_{false}\cdot Err(\%)^2} \tag{3.12}$$

from which it can be understood that a good (T/F)-ratio contributes to maintaining this acquisition time as short as possible. Such estimations were routinely done, which also helped in the scheduling of the (e,2e)-coincidence measurements campaign. This is advantageous since one single acquisition, i.e. one single (e,2e)-spectrum (time histogram) can run for the duration of

some days to reach such percentage of error.

In average, for measurements in which the 2DCS were reasonably high – e.g. when tuned on relevant characteristic spectral features such as plasmon peaks – the singles count rates were higher, thus τ_{acq} shorter and it was possible to reach percentage errors between 6–10%. When the scattering conditions were such to yield lower 2DCS and lower count rates, then the average accepted $Err(\%)$ ranged between 15–26%.

The (e,2e)-experiments discussed in section 4.3 of chapter 4 were acquired for three primary energies of $E_0 \simeq (50; 90; 100)$ eV. During these series of coincidence measurement the primary current, I_0, of the electron beam varied between 10 pA to a maximum of 22 pA. The primary current was monitored nearly on a daily basis to ensure that the acquired (e,2e)-yields were properly normalised each to their own incidence current.

The series of measurements performed on the Al(100) single crystal were conducted at a primary energy of ca. 100 eV. Whereas for the HOPG sample two different series of (e,2e)-acquisitions were conducted at $E_0 \simeq (50; 90)$ eV, respectively. When the two higher excitation energies were employed, the TOF-analyser was always tuned on the ELS under specular reflection conditions ($\theta_{in} = \theta_{out} = 30°$) and its pass energy was of set to 40–45 eV and with an average resolution of ΔE_{resol} of ca. 2 eV.

The SE-spectrum was collected by R66 at a constant $E_{pass} = 25$ eV. Being equipped with an MCP/1D-DLA this analyser is capable to collect a wider energy window than in a single channel detector case (e.g. channeltron) in parallel, the width of which depends on the chosen pass energy.

3.3.4.1 Optimisation of the Electron Optics for Electron Transport in the LE-range & Transmission Function

As previously explained, on the basis of equations (3.9) and (3.10) for the acquisition of (e,2e)-coincidence measurements it desirable to maximise the solid angles (Ω_s and Ω_e) detectable by the two analysers. To obtain an enhanced electron yield during SEES or (e,2e)-coincidence experiments the electron optics of the analyser is tuned thus to achieve a high-transmission of LEEs. To this end, it is important to optimise the electrostatic lenses of the optical element used for electron transport (and their focussing) from the target to the entrance slit of the energy dispersive element, which in our case is represented by the hemispherical analyser. Such electron optical elements are relevant to transport and to focus the beam onto this entrance slit, on the one hand, and to tune the kinetic energy of the electrons adjusting it to the pass energy of the analyser, on the other hand.

For the newly implemented analyser "R66" the electron optical element preceding the energy analyser's hemispheres needed to be optimised to find a suitable configuration for the operation in the LE-regime. The electron optics of R66 is composed of six axially symmetric electrodes that can be independently polarised. When a bias is applied on these electrodes, they produce equipotential surfaces similarly shaped as the surfaces of physical optical lenses. The electron beam passing through these surfaces can then be either accelerated or decelerated, focussed or defocussed, in accordance to the applied voltage. The entrance electrode is kept to ground whereas the exit electrode (the one preceding the HMA-entrance slit) is set to the retarding (or accelerating) potential.

To maximise the detected solid angle requires that even electrons generated (or scattered) at the target exiting under large elevation angles (w.r.t. the surface normal) are transported and focussed onto the entrance slit at the Herzog-plate. To this end, an accelerating and demagnifying (in angle) 3-cylinder-lens system (whose scheme is shown in fig. 3.23) was designed and tested for the acquisition of LEEs. For the tuning of this 3-cylinder-lens system the retarding potential V_{rit} was chosen to be positive, thus to accelerate slow electrons towards the entrance slit of the analyser. Both electrodes placed at the entrance, $E1$ and $E2$, are connected and set to ground potential, whereas electrodes $E4$ and $E5$ were set to the same potential as V_{rit}. Hence, the only electrode potential that needed to be accordingly adjusted and tuned was electrode $E3$ (red) where the focussing of the electron trajectories occurs. Furthermore, this double-lens system has an angular magnification of $M_\alpha < 1$ (demagnifying effect), for which it was possible to detect even LE-electrons, whose (maximal) linear elevation half-angle at the target was $\pm 12°$. This system of demagnifying lenses permitted to reduce this linear emission half-angle to $\pm 4°$ (which corresponds to the maximum accepted linear angle at the Herzog-plate) at the entrance slit of the analyser, thus enhancing the overall luminosity of this electron optical element. The *luminosity* $\mathbb{L}$ of a lens system is basically determined by the product of the target area A_{target} – i.e. Field-of-View

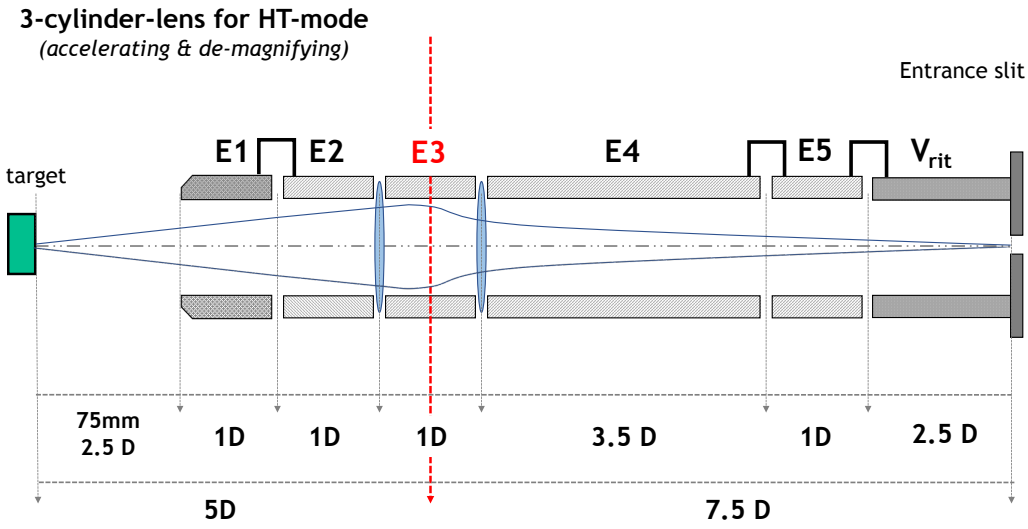

Figure 3.23: The 3-cylinder-lens system used for the acquisition of LEEs. This electron optical system exhibits a high-transmission in the LE-range; accelerating and focussing electrons towards the entrance slit of the analyser emitted from a larger solid angle. Polarisation of electrodes: $E1 = E2 = 0\,\mathrm{V}$; $E3 > 0\,\mathrm{V}$; $E4 = E5 = V_{rit} > 0\,\mathrm{V}$. "1D" stands for 1 diameter; in electron optics lengths are given in units of the electrode diameter.

(FoV) – and the solid angle Ω, therefore it is clear, that high luminosity corresponds to a large solid angle and to a large FoV ($\mathbb{L} = A_{target} \times \Omega$).

The 3-element-optics was designed according to Harting and Read [242] to provide an angular magnification $\mathrm{M}_L \lesssim 1$ at a linear magnification $\mathrm{M}_L \approxeq 1.5$ in a range of accelerating ratios from $\mathrm{R}_{acc} = (1.0 - 7.0)$ (equivalent retard ratio RR from 1.0 to 0.14) to enhance its luminosity.

The working points (wp) of this lens were tested sweeping the voltage of the focussing electrode ($E3$) in function of a fixed retarding ratio RR. This way two wp_s were found (as expected) one belonging to an upper branch and one to a lower branch of the acceleration in the focussing element $E3$ versus the overall lens acceleration ratio. These experimental wp_s were found to be in fairly good agreement with the calculated ones. As already decided during the design of the lens, only the working points belonging to the upper branch were used. The lens was designed as to minimise variations in the lens overall transmission due to chromatic aberration. This requirement is particularly strict especially when performing (e,2e)-experiments in which the RR spans from ca. 0.05 to 0.5.

In some cases, an enhanced transmission of LEEs is obtained at expenses of the uniformity of the χ_{trans} in the LE-range. This may lead to a deformation of the shape or to a diminished intensity in the measured SE-spectrum.

The transmission function of the electron optical element of the R66-analyser was determined by a series of voltage-dependent SEE-measurements conducted on the HOPG surface (shown

in figure 3.24). The clean HOPG surface was bombarded by 91.7 eV-primary electrons under

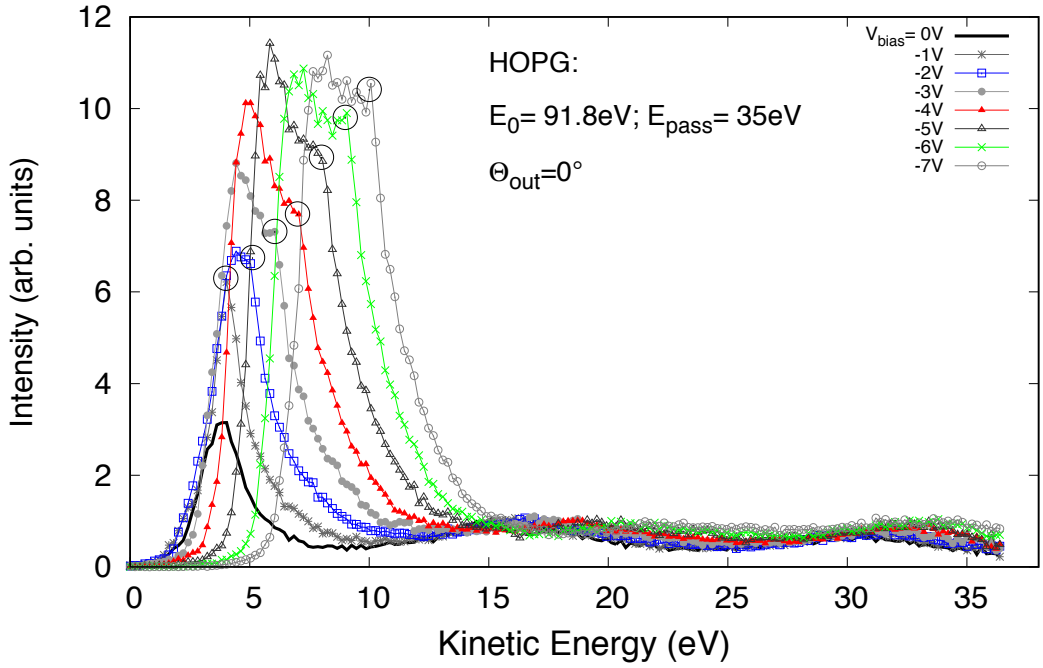

Figure 3.24: Series of SEES from HOPG acquired with R66 at various negative sample bias (V_{bias} <0 V) using 91 eV-primary electrons and under normal emission. Energy position and intensity of the spectral feature spotted by the circle was used to determine χ_{trans} of the 3-cylinder-lens system.

30°-incidence. SEES were measured under normal emission (i.e. the sample surface normal was aligned with the analyser axis as sketched in figure 3.23). The sample was progressively set to a negative bias V_{bias} ranging from 0 V down to -7 V. The intensity and energy position of characteristic spectral features, intrinsic to HOPG, were monitored for the increasing negative sample bias. Such a spectral feature is highlighted by an open circle in figure 3.24.

Considering that for an increasing negative V_{bias} the emission cone of LEEs squeezes accordingly – i.e. more and more electrons are ejected closer to the surface normal – and after having checked that the shift in the energy position of the spectrum corresponded to an expected shift due to the applied negative bias, it was possible to assess that the observed increase in intensity was related to the varying emission cone dimension. By analysing the spectral intensity variation in dependence of V_{bias} it was possible to determine χ_{trans}, by means of which all subsequent (non-biassed SEES) were re-normalised. Out of this measurement the calibration has shown a constant transmission of the lens for an energy range spanning between 10 eV and 25 eV, whereas decreased for lower kinetic energies. The herewith determined transmission function was routinely used to correct the shape and intensity of SEES.

Using this transmission function which was determined for the energy range of ∼2.5–20 eV, it was possible to correct further SE-spectra for the real transmission, thus recovering their shape and intensity.

Figure 3.25 gives an example for the successful application of this correction procedure. The

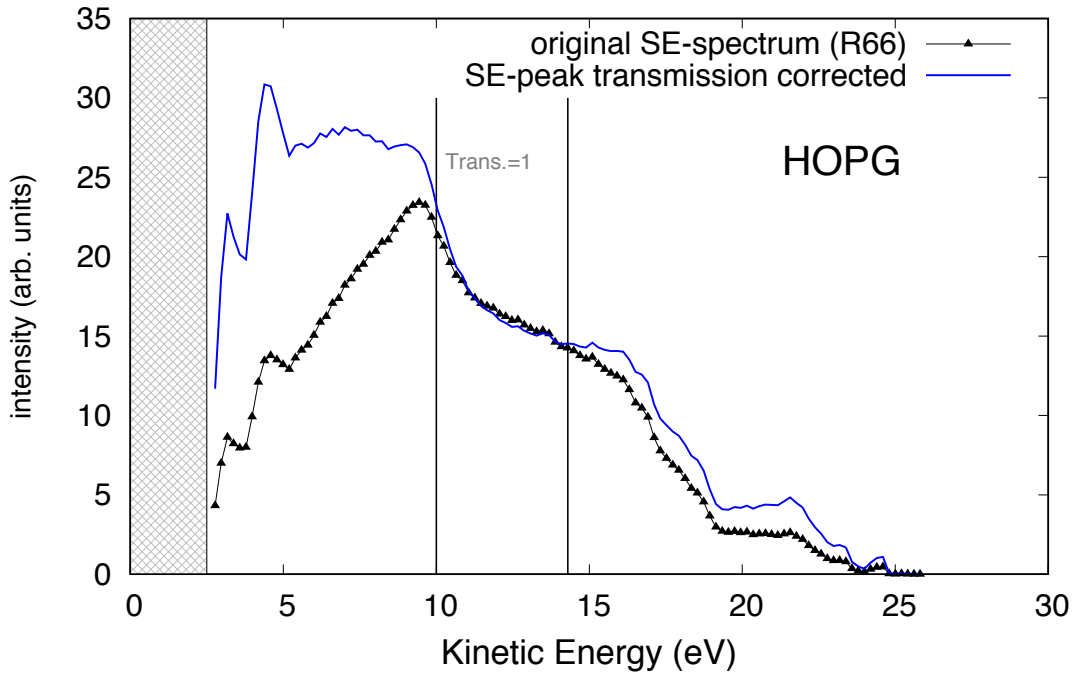

Figure 3.25: SEES from HOPG: comparison between the original (black line with triangles) and transmission-corrected (blue line) SE-spectra. Spectral features superimposed over the SE-peak correspond to well-known features reported also in literature [190, 191, 186, 103, 194].

SE-spectrum plotted with black triangles is the spectrum as directly measured by R66 as tuned for the HT-mode. It was assessed that spectral features observed in the SEES before and after the application of the transmission correction correspond to known features from literature [103, 186]. The SEES shown in fig. 3.25 was measured for an incident angle, θ_{in} =30°, and under normal emission, with θ_{out} =0° with the sample on ground potential. The corrected SEES is shown in blue. The energy range enclosed in the two grey vertical lines marks the energy range wherein $\chi_{trans} = 1$.

During the (e,2e)-measurements performed on Al(100) another set of lenses was employed for the acquisition in the LE-range. Acquisition of SEES from Al(100) was habitually done always before setting an (e,2e)-coincidence measurement by means of the R66-analyser, the one employed for the collection of the SE-spectrum. All (e,2e)-experiments on Al(100) were conducted by tuning the TOF-analyser on the energy range of the scattered electrons, which were detected under specular reflection. The SEs were therefore measured by the R66-analyser under an angle of emission of 60° wrt. surface normal. In this scattering geometry, it was noticed that the shape of the SE-spectrum exhibited an unusual diminished intensity in the very low kinetic energy range, between 2 eV and ∼10 eV. This SE-spectrum from Al(100) is shown in red in figure 3.26. The electron optical element used during this series of (e,2e)-coincidence measurement was tuned specifically for the transport of LEEs ranging between 3.5–24 eV. However, the transmission in the very LE-range was not uniform and needed to be re-corrected, for which a dedicated experiment was conducted to determine the transmission function for this lens system.

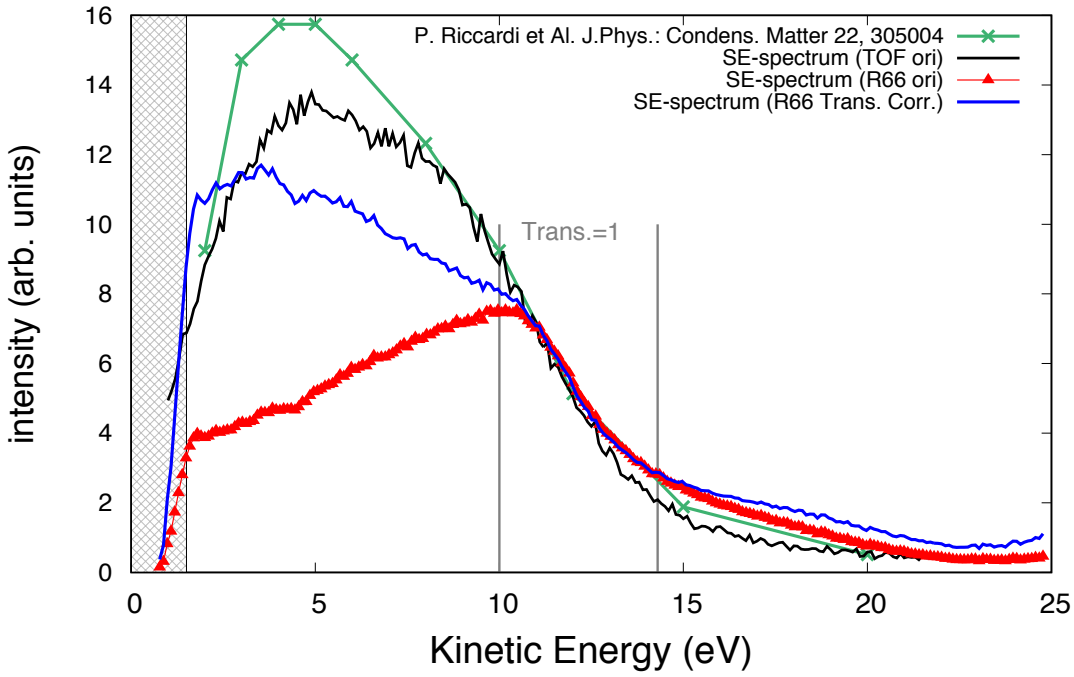

Figure 3.26: SEES from Al(100): (red) spectrum acquired employing the set of lenses used for the acquisition of (e,2e)-spectra under 60° emission angle, exhibiting a diminished intensity for $E_e < 10\,eV$; (black) SE-peak measured with the TOF-analyser; (green) SEES measured by Riccardi *et al.* [243] and (blue) same spectrum as the red one corrected for the determined χ_{trans}, by means of UPS-measurements.

The transmission function χ_{trans} in this case was determined by a series of ultraviolet-photoelectron spectroscopy (UPS) experiments done in dependence of the sample bias. The UPS spectra of Al(100) display the kinetic energy distribution of photoelectrons, which have absorbed UV-light emitted by a $He_{1\alpha}$ gas discharge lamp, with a source energy of 21.22 eV. In Al(100), the noticeable spectral feature of the surface state [210] – visible at $E_{kin} \simeq 14\,eV$ – was exploited for the monitoring of the intensity and energy variation, in the same way as discussed above.

Figure 3.26 also displays a SE-spectrum acquired by means of the TOF-analyser (black) under a different scattering geometry as used for the R66's SEES shown in red. The transmission of this analyser is known to be nearly constant down to ca. 2 eV. In addition, the shape of the black SE-spectrum resembles the most another (independent) experimental result obtained by Riccardi *et al.* in their work [243] (green spectrum in fig. 3.26). Also other authors report in their experiments that the energy position of their SE-peaks from Al are expected to fall between 3 eV and ca. 6 eV. By re-correcting the red SE-spectrum by the transmission function, it was possible to obtain a relatively similar shape and intensity as measured in the TOF analyser ((blue spectrum in fig. 3.27)) The residual difference between the blue (R66 corrected) and black (TOF original) appearing in the figure is due to the different acquisition geometry. This strategy for the correction of the SE-peak shape and intensity was applied to a series of SE-spectra measured under different scattering geometries, thus to ensure the validity of this procedure.

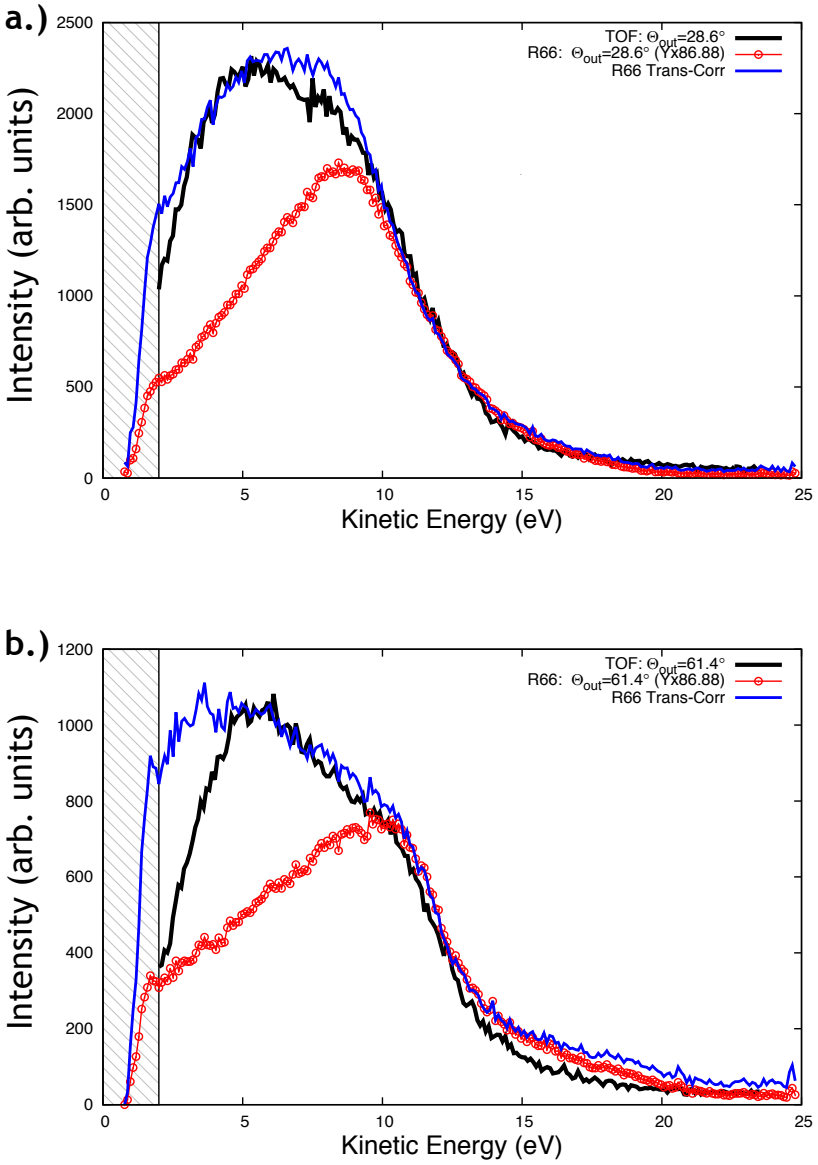

Figure 3.27: SEES from Al(100). In both panels the (red) spectrum was acquired using R66, the (black) spectrum was measured using TOF under the same scattering geometry as for R66 and the (blue) spectrum is the SEES by R66 corrected for the χ_{trans}. The emission angles θ_{out} are indicated in each legend respectively.

In figure 3.27 two further examples for this transmission correction procedure are shown. Also in this case, the original SE-spectrum acquired by means of R66 is plotted in red. The SEES measured by TOF is used as a reference, since it was asserted that the transmission in this analyser is uniform down to ca. 2 eV. Both spectra were measured under exactly the same scattering geometries. The blue spectrum is the one obtained by multiplying the original R66's SEES with the transmission function of its electron optical elements.

Both panels (a.) and (b.) show two measured spectra (by R66 and TOF) under the same emission angles (θ_{out}) respectively and one re-corrected spectrum (in blue). In either case, the re-corrected spectrum of R66 strongly resembles the original one measured by TOF, thus reconfirming that the strategy applied is valid.

3.3.4.2 Optimisation of the shared Field-of-View (FoV) for (e,2e)-coincidence experiments

As previously discussed, a strong enhancement in the performance of an (e,2e)-coincidence measurement is obtained by maximising the accepted solid angles $\Omega_i(\theta_i, \varphi_i)$ with $i = (s, e)$ for both analysers. Apart from maximising the luminosity of the electron optical element of an analyser, it seems obvious that for a coincidence measurement it is essential for these two Fields-of-View (FoVs) to overlap as much as possible, so that both analysers "observe" the same spot area on the sample from where the electron pairs depart.

In spite of the fact that, the source and both analysers are mechanically aligned within the scattering plane, it is not self-evident that the mechanical alignment of the two analysers' axes also corresponds to the optical axes of the analysers for all kinetic energies. The area on the sample

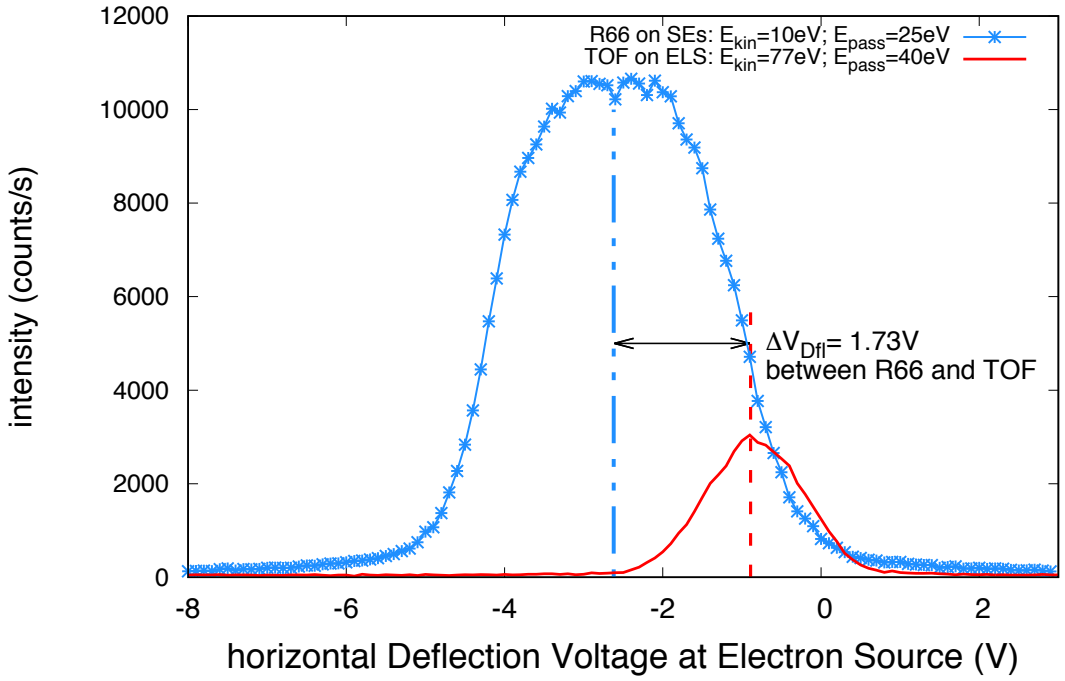

Figure 3.28: Misalignment of the horizontal FoVs for R66 (blue) and TOF (red). Each analyser is tuned the the kinetic energy of interest; R66 on the slow SE electron and TOF on the fast scattered. The mismatch between these Fields-of-Views was caused by a poor compensation of the Earth's magnetic field, which caused the a deflection in the slow electron trajectory.

which is seen by an analyser is defined as Field-of-View (FoV). This FoV can be determined by scanning the electron source across the sample, while this latter is moved along with the electron beam, thus to ensure that the electron beam always impinges onto the very same spot of the target. By means of this type of scan, the intensity measured at the analyser is representative for the sole observed area, i.e. the sample does not contribute to the intensity, since it is bombarded

in the same spot.

Deflection of electrons is achieved by tunable deflection plates that apply an electric field perpendicular to the electron trajectory. By modifying step-wise these deflection voltages ($D_{Defl}(H)\ldots$ for the horizontal deflection and $D_{Defl}(V)\ldots$ for the vertical deflection) the electron beam can be scanned across the target area. This $D_{Defl}(i)$ (with $i = H, V$) translates to an energy-dependent distance Δx (or Δy) in mm projected onto the sample surface in both the horizontal and vertical directions. Knowing this translation factor it is possible to move the sample beneath the deflecting electron beam thus irradiating (nearly) the same spot for the whole scan. The intensity monitored at the analysers then yields the shape corresponding to the FoV of the analyser along the horizontal (or vertical) direction. For a fix sample position and for the two fixed kinetic energies at which each analyser is tuned – e.g. $E_s = 77\,eV$ and $E_e = 10\,eV$ – the deflection voltages at Mono-gun shall be opportunely set for both analysers to be aligned thus to detect the same FoV-regions, i.e. their respective FoVs shall be aligned. The main source of

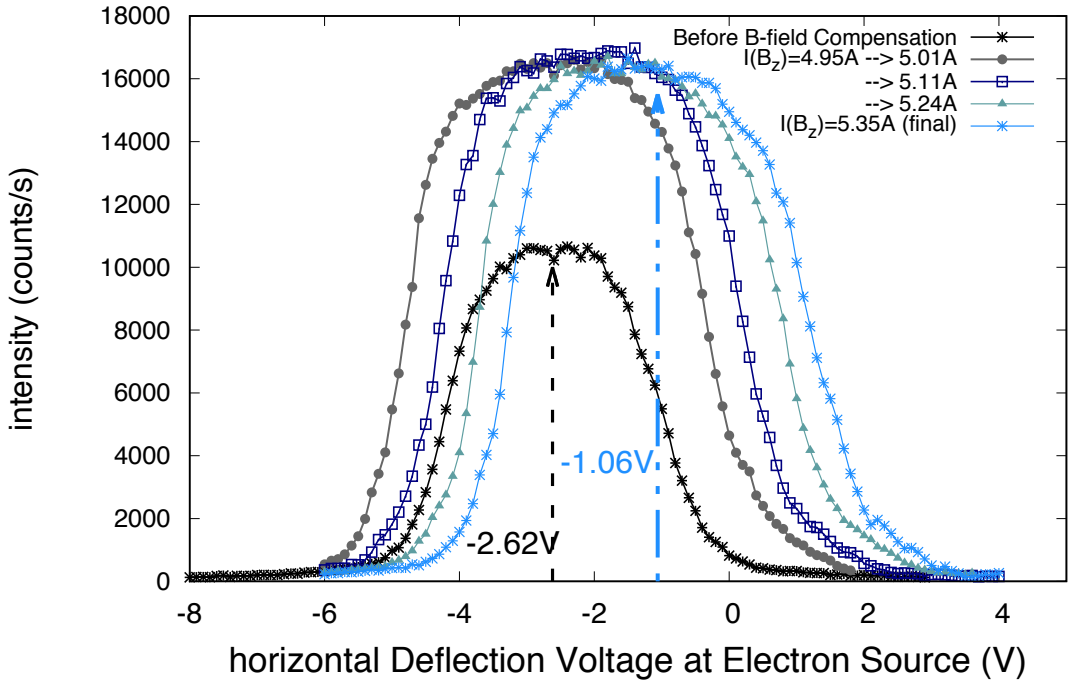

Figure 3.29: Each scan in this figure shows the position shift of the horizontal FoV for the 10 eV-electrons detected by R66 in dependence of the re-adjusted Helmholtz-coil current I(B_z). At the end of this procedure R66's FoV was completely overlapped with TOF's.

misalignment between these FoVs is given by a bad compensation of the remnant $\vec{B}$-field in the centre of scattering, which can severely affect the trajectory of a slow electron.

While the 77 eV-electron is not significantly deflected, the 10 eV-electron can be indeed deviated from its original trajectory, thus the FoVs of the analysers exhibit a bad overlap. Such an example is shown in figure 3.28. The blue-starred curve represents the horizontal FoV as seen by R66 for the 10 eV-electron, whereas the red curve is the horizontal FoV of TOF for the fast electron. The

mismatch between these two curves is non-negligible and disadvantageous for the performance of an (e,2e)-experiment.

To cure such mismatch, which arose due to a poor compensation of the remnant Earth's $\vec{B}$-field, it was necessary to re-adjust the Helmholtz-coil currents thus to re-shift the central point of R66's FoV (blue) on top of the FoV seen by TOF (red). Since the shift in deflection was present only in the horizontal direction, to re-shift the FoV area back towards the other, only the current flowing in the perpendicular direction (I(B_z)) needed to be re-optimised. The various steps of this procedure are displayed in fig. 3.29, where in the end the central position of R66's FoV was shifted by $\Delta D_{Defl}(H) = 1.56\,V$. Figure 3.30 shows the optimal conditions for which TOF's and

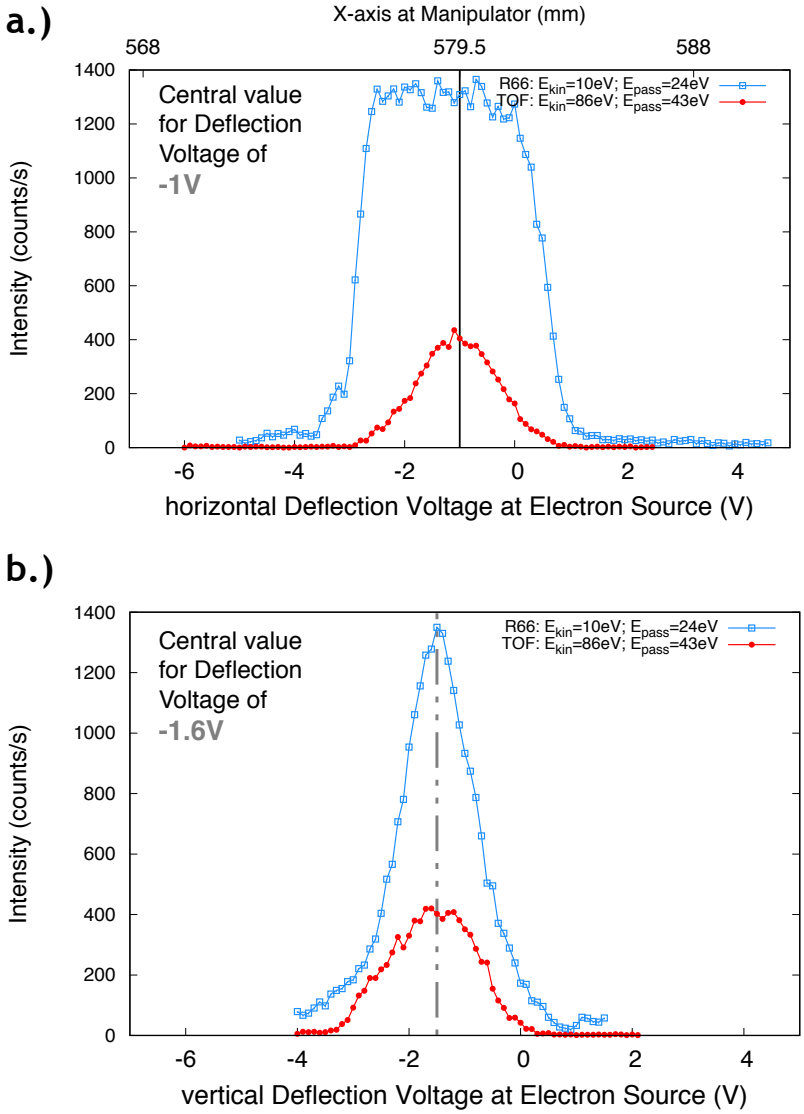

Figure 3.30: Example of ideal overlap for both Fields-of-View given in either direction: (a.) horizontal FoV and (b.) vertical FoV, each one acquired for the indicated energies. The suitable deflection voltages for for analysers were adjusted at the source for the subsequent (e,2e)-coincidence measurement.

R66's FoV are completely overlapping for both directions. These are the ideal conditions for performing an (e,2e)-coincidence measurement. Prior to setting up a coincidence measurement to monitor the quality of these "shared FoVs" is mandatory.

3.3.4.3 Acquisition & Evaluation of an (e,2e)-Spectrum

Figure 3.31 shows a typical time histogram displaying the intensity of all coincidence events as a function of the delay time $\Delta\tau$ between the arrival times of the two electrons registered at either detector end – or also *"(e,2e)-spectrum"*. For this specific experiment (performed on the Al(100) surface with a primary energy of $\sim 99\,\mathrm{eV}$) the TOF-analyser was tuned to collect scattered electrons of $\mathrm{E}_s = 85\,\mathrm{eV}$, with a correspondent $\Delta\mathrm{E} = 14\,\mathrm{eV}$, which is in proximity of the characteristic energy loss of a bulk plasmon ($\hbar\omega_b = 15\,\mathrm{eV}$). The detected SE at R66 was of 9 eV (see the legend in the plot).

The background of accidental (false) coincidences is represented as red-hatched area. The peak superimposed over this background of uncorrelated electron pairs corresponds to the frequency of the truly correlated electron events. The $\Delta\tau$-range in correspondence of this peak is highlighted in blue.

In order to determine the number of true coincidence counts it is useful to subdivide this time spectrum into three regions: (a.) from T_1 to T_2 related to R_{false}; (b.) The $\mathrm{T}_2 < \Delta\tau < \mathrm{T}_3$ where the coincidence peak is included and (c.) which similarly to the interval (a.) is associated only to accidental events and stretches from T_3 to T_4. Both R_{true} and R_{false} contribute to the intensity given by the area of the blue peak, which can then be obtained as follows:

$$A_{peak} = \sum_{\Delta\tau_i = T_2}^{T_3} c_i \tag{3.13}$$

Here c_i is the number of coincidences evaluated at a given $\Delta\tau_i$ comprised within the given interval. The uncertainty on the determination of this number is given by Poisson's statistics with

$$\delta A_{peak} = \sqrt{\sum_{\Delta\tau_i = T_2}^{T_3} c_i} \tag{3.14}$$

In order to obtain the contribution of the sole true events, associated to the area of the peak above the accidental background it is necessary to perform a subtraction of this background. The number of events within to the red-hatched areas (at both sides of the peak) gives the total number of false coincidences, which can be obtained by making the sum over these areas and its uncertainty is given by the square root of their sum:

$$A_{false}{}^{(bgd)} = \sum_{\Delta\tau_i = T_1}^{T_2} c_i + \sum_{\Delta\tau_i = T_3}^{T_4} c_i \quad , \quad \delta A_{false}{}^{(bgd)} = \sqrt{\sum_{\Delta\tau_i = T_1}^{T_2} c_i + \sum_{\Delta\tau_i = T_3}^{T_4} c_i} \tag{3.15}$$

$A_{false}{}^{(bgd)}$ is then associated to the whole (red-hatched) range for a $\Delta\tau$-interval comprising the ranges (a.) and (c.) yielding a large $\Delta\tau_{bgd}$. Owing to the fact that the uncorrelated coincidence

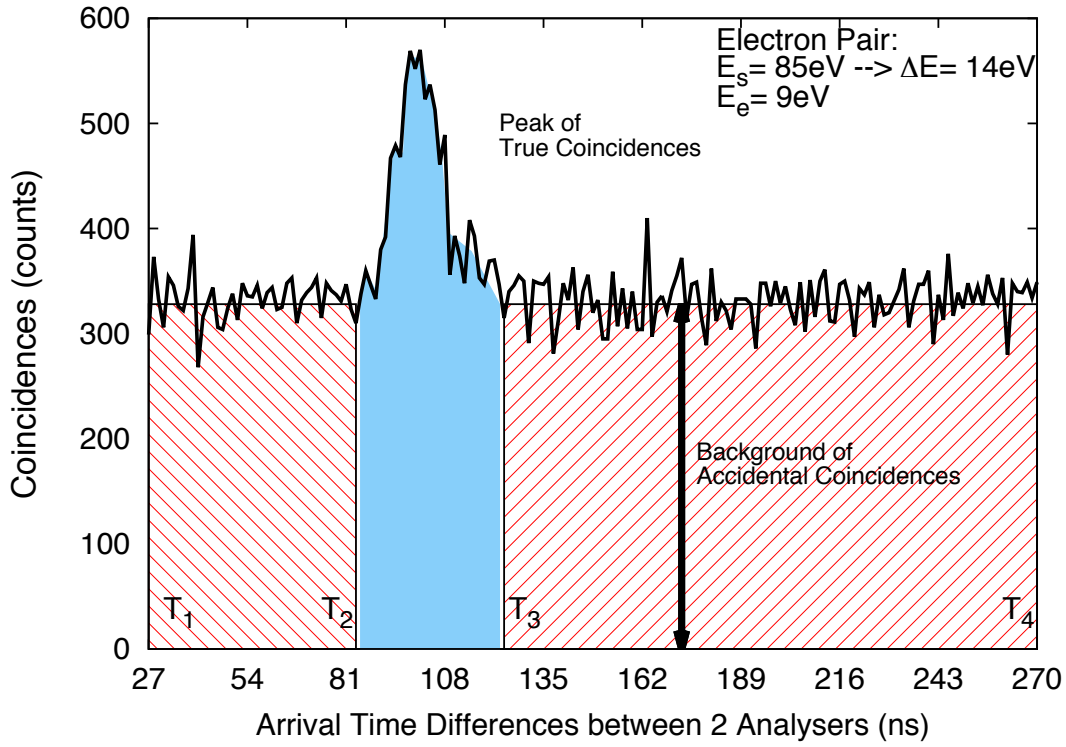

Figure 3.31: This time histogram represents the frequency of appearance for the correlated electron pair having a specific delay time $\Delta\tau$ between them, i.e. it represents the yield of coincidences given on a scale of flight-time differences. The hatched red area defines the sole background of false coincidences given over the whole time scale. The blue area at the peak position, where true coincidences appear superimposed over the false-events-background is identified with the area of the whole coincidence peak. After performing a background subtraction the sole peak area is obtained yielding the number of true coincidence events.

events are evenly distributed over the whole background (*bgd*), to obtain the number of the only accidental coincidences within the blue area, hence beneath the coincidence peak, it is possible to relate the two portions of background (blue and red) to their respective time intervals, thus extracting a proportional factor, $\beta = (\Delta\tau_{peak}/\Delta\tau_{bgd})$ by means of which the false coincidences beneath the peak can be extracted by:

$$A_{false}{}^{(peak)} = \left(\frac{\Delta\tau_{peak}}{\Delta\tau_{bgd}}\right) \cdot A_{false}{}^{(bgd)} \quad , \quad \delta A_{false}{}^{(peak)} = \beta\, \delta A_{false}{}^{(bgd)} \tag{3.16}$$

The bare number of true coincidences N_{true} can be simply determined by the difference between the total peak area A_{peak} and this $A_{false}{}^{(peak)}$ below the peak, yielding:

$$N_{true} = \sum_{\Delta\tau_i=T_2}^{T_3} c_i - \beta \left(\sum_{\Delta\tau_i=T_1}^{T_2} c_i + \sum_{\Delta\tau_i=T_3}^{T_4} c_i \right) \tag{3.17}$$

$$\delta N_{true} = \sqrt{\sum_{\Delta\tau_i=T_2}^{T_3} c_i + \beta^2 \left(\sum_{\Delta\tau_i=T_1}^{T_2} c_i + \sum_{\Delta\tau_i=T_3}^{T_4} c_i \right)} \tag{3.18}$$

To minimise the error δN_{true} it is advantageous to evaluate the background of false coincidence events over a large $\Delta\tau_{bgd}$, which then renders the proportional factor β small.

Such evaluation procedure was adopted for all acquired time histograms of all (e,2e)-measurements by means of a dedicated custom-written FORTRAN code [240] performing this algorithm over each acquired time spectrum. After having determined by means of this software (SW) the true and false coincidence yields with their associated errors another piece of SW processes further these data, thus to eventually determine the experimental TDCS given in eq. (3.9). An expression for the calculation of this empirical TDCS can be extracted from the (T/F)-ratio:

$$\left(\frac{T}{F}\right) = \left(\frac{R_{true}}{R_{false}}\right) = \left(\frac{\sigma_{(e,2e)}}{{\sigma_s}^{(2)}\,{\sigma_e}^{(2)}}\right) \cdot \frac{\Delta E_{(e,2e)}}{I_0\ (\varrho\, l)\ \Delta E_s\, \Delta E_e\, t_w} \tag{3.19}$$

The 2DCS are known, since prior to setting up any coincidence measurement both REELS and SE-spectrum are routinely acquired under the very same conditions (for the same scattering angles and I_0) as the subsequent coincidence measurement.

Examples for these 2DCS obtained by "singles" electron experiments are given in figures 3.32 and 3.33, displaying the scattered electron energy of interest and the SE-spectrum, respectively. These spectra were acquired from the Al(100) single crystal under specular reflection conditions for TOF ($\theta_{in} = \theta_{out} = 30°$) and for a primary energy of 100 eV.

The crystalline order of the target was formerly determined by performing LEED-scans, through which proper alignment of the sample in the above-mentioned scattering conditions could be achieved. Examples for such diffraction patterns were shown in section 3.2, where the preparation of the sample surfaces was discussed.

The coloured arrows, in figure 3.32 indicate the energy position of the characteristic energy losses of the singly- and doubly-excited plasmons. In this ELS, the 2DCS for a doubly excited plasmon is about a factor of 6 lower that the 2DCS in correspondence of the surface plasmon peak. If an (e,2e)-experiment is tuned on this loss, then longer acquisition times can be expected than when measuring in correspondence of a single plasmon instead, as previously explained on the basis of the formula given in eq. (3.11). The SEES shown in fig. 3.33 was acquired by R66 under $\theta_{out} = 60°$. The red and blue rectangles highlight the SE-energy interval sampled by the E_{win} measured in parallel by the analyser, for kinetic energies of the SEs corresponding to an ejected electron from the Fermi level, hence with $E_e = (\Delta E - \Phi) = (\hbar\omega_{pl} - \Phi)$. During this series of (e,2e)-measurements, the energy of the ejected electrons was varied thus to scan over the whole kinetic energy range of the shown SE-peak.

These two 2DCS are used to re-normalise the measured (e,2e)-yield, as shown in the following.

The t_w is also known, since this represents the interval given by the region (b.) of the time histogram. The primary current is routinely monitored (by means of a Faraday cup (FC) aligned with the sample surface, hence at the same distance from the source [13]) prior to launching the

[13]Being aligned in this way the electron current measured in the FC corresponds to the effective total current

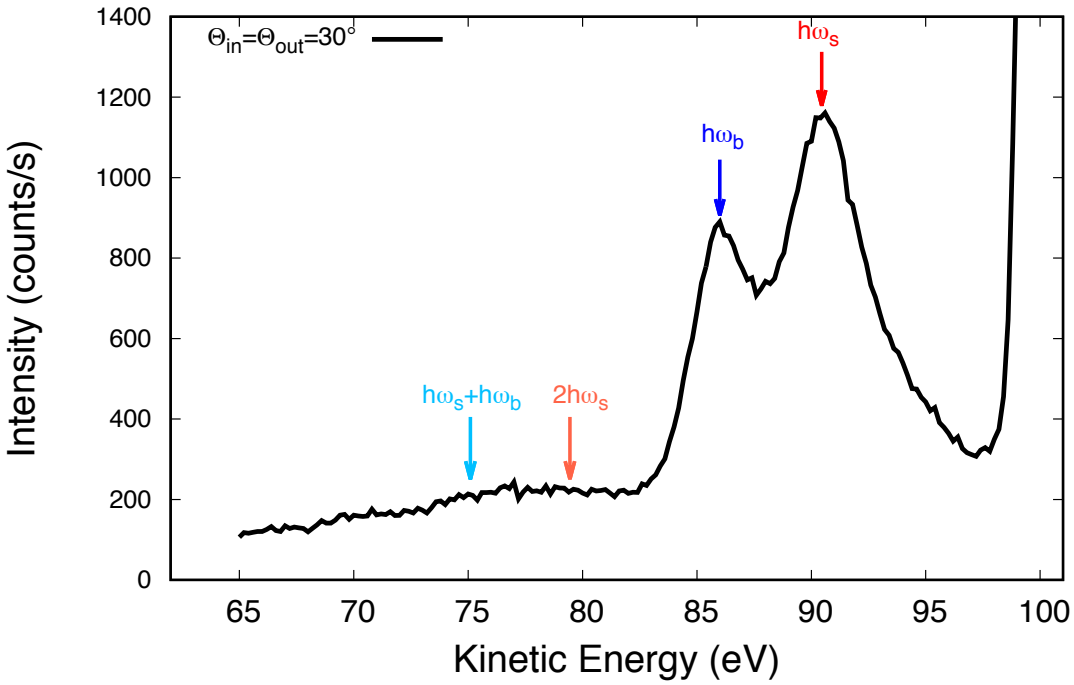

Figure 3.32: REELS from Al(100) acquired using the TOF-analyser in specular reflection under the same conditions as the (e,2e)-coincidence measurement. Coloured arrows indicate characteristic energy losses of interest corresponding to the excitation energies of singly- and doubly-excited plasmons.

(e,2e)-experiment. The target density ($\varrho\, l$) is a known constant value. Finally, the three energy resolutions are determined by the experimental settings.

The product of ${\sigma_s}^{(2)}$ and ${\sigma_e}^{(2)}$ as given by the experiment reads as follows:

$$ {\sigma_s}^{(2)} \cdot {\sigma_e}^{(2)} = \frac{R_s \cdot R_e}{(\varrho\, l)^2\, {I_0}^2 \Delta\Omega_s\, \Delta\Omega_e \Delta E_s\, \Delta E_e\, \Xi_s\, \Xi_e} \tag{3.20} $$

where R_s and R_e are the singles count rates measured at TOF and R66 respectively at a specific kinetic energy for the scattered and ejected electrons. By inserting these experimental 2DCS in equation (3.19), the experimental TDCS ($\sigma_{(e,2e)}$) is then calculated as follows:

$$ \sigma_{(e,2e)} = \left(\frac{d^3\sigma_{(e,2e)}}{d\Omega_s\, d\Omega_e\, dE} \right) = \left(\frac{T}{F} \right) \cdot \frac{R_s\, R_e\, t_w}{\Delta E_{(e,2e)}\, (\varrho\, l)\, I_0\, \Delta\Omega_s\, \Delta\Omega_e\, \Xi_s\, \Xi_e} \tag{3.21} $$

By means of eq. (3.21) the experimental (e,2e)-cross-section is then opportunely normalised to the incident current, to the 2DCS evaluated at their specific kinetic energies (E_s and E_e) of the correlated electron pair and for the efficiencies and solid angles of each analyser. This measured TDCS can be then interpreted by means of the theoretical expressions discussed in the previous chapter 2.

impinging on the target within the given spot size, thus making the I_0-measurement very reliable.

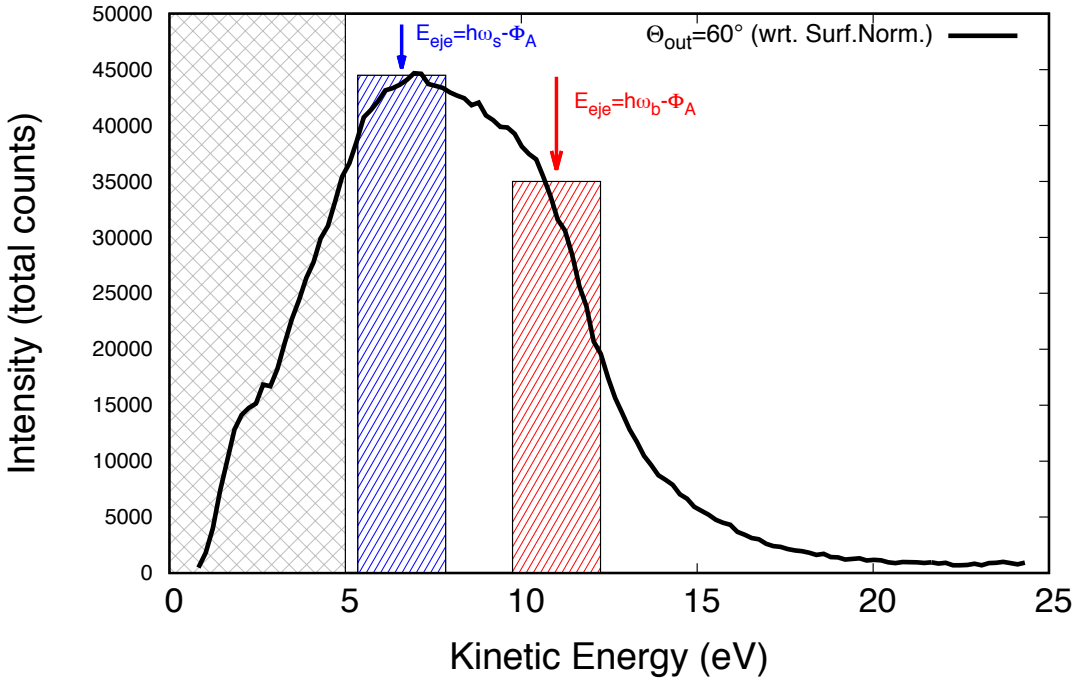

Figure 3.33: SEES from Al(100) acquired with R66 in (e,2e)-configuration. Coloured hatched areas correspond to the E-range (defined by E_{win}) acquired during a coincidence experiment for a SE escaping from the Fermi level, hence with the entire energy loss of the scattered PE after overcoming the workfunction. The grey crossed area at lower kinetic energy represents the region in the SE-spectrum where the transmission function χ_{trans} was no longer uniform, reason for which we re-corrected the SE-spectrum by this χ_{trans}; restoring intensity and shape for this LE-range.

3.3.4.3.1 Calibration of the (e,2e) Frequency Scale by Determination of the "Experimental Zero" In order to determine the sensitivity limit in an (e,2e)-coincidence experiment, a coincidence measurement is set up to collect only uncorrelated electron events, i.e. acquiring a time spectrum of *accidental* (false) coincidences. By means of such a time histogram, it becomes possible to determine the default frequency of the false coincidence background; which in turn delivers the real "*experimental zero*" of our intensity scale.

To ensure the measurement of solely false coincidences there are two possibilities: (1.) either to purposely violate energy conservation law or (2.) by selecting a specific kinematics for which one knows a priori that either no initial (bound) or final (unbound) electron state is available.

In the first case, this can be easily done, by tuning the kinetic energies at either analyser in such a way, thus to force them to collect uncorrelated scattered and ejected electrons. Such an example of a *"null time histogram"*, hence one displaying the frequency of events related only to the accidental background of coincidences, is shown in figure 3.34.

This experiment was performed on Al(100) (whose workfunction is 4.2 eV) employing primary electrons with $E_0 = 100.73$ eV. The TOF-analyser was tuned on the energy of an inelastically scattered electron with $E_s \simeq 85$ eV. Hence, it was set to monitor the characteristic energy loss corresponding to the excitation energy of the bulk plasmon in Al (with $\Delta E = \hbar\omega_b = 15$ eV). The

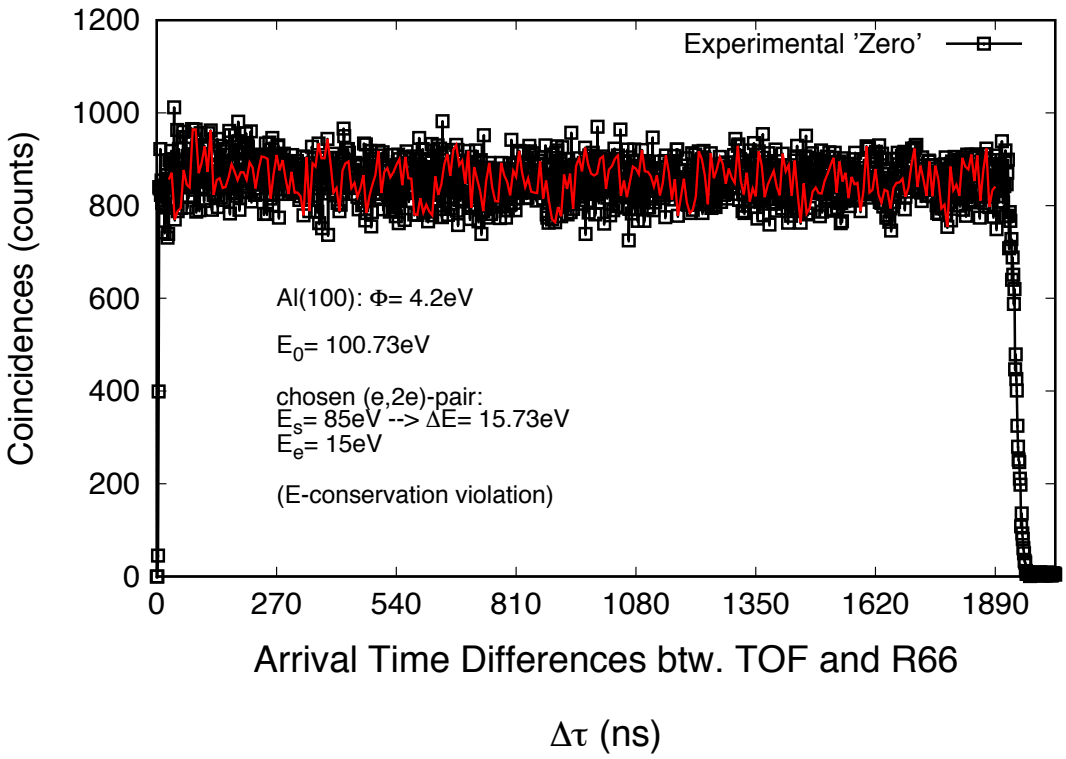

Figure 3.34: Time histogram representing the frequency of appearance for the *uncorrelated* electron pair, i.e. it gives the yield of accidental coincidences given on a scale of flight-time differences. For the pair of kinetic energies, at which each analyser is tuned, no true coincidence even is expected, thus also no peak of true events is supposed to appear superimposed on this background of accidental events.

analyser tuned on the SE-spectrum, R66, was set to collect electrons with a kinetic energy of 15 eV.

Owing to energy conservation law – see eq. (2.3) – it is clear that no electron can be emitted from the target with the full amount of the energy lost by the primary electron, since in order to be promoted above vacuum level a bound electron always has to overcome the surface barrier and herewith the workfunction, Φ of the material. Thus, the maximal kinetic energy for such an ejected electron would correspond to $E_e = \Delta E - \Phi = 10.8\,eV$ and not 15 eV.

As expected, the time histogram shown in fig. 3.34 is completely flat. By performing the same analysis of this time spectrum as done in the case of the time histogram shown in fig. 3.31, we obtain a frequency of "true" events of the order of $6.0 \times 10^{-5} - 6.0 \times 10^{-4}\,(counts/s)$. This intensity defines our experimental sensitivity and sets the "*absolute zero*" of our intensity scale to be $3{\times}10^{-4} \pm 3{\times}10^{-4}\,(counts/s)$.

For the case (2.) mentioned previously, one can be sure to measure such a *"null time histogram"* also by opportunely choosing a kinematics, by means of which it is known that no available energy bands are accessible either to consent the extraction, nor the transmission of electrons

for the chosen collision event. When the kinematics of the (e,2e)-experiment is such thus the initial state of the bound electron, defined through a pair of ($\vec{q}_{\parallel}$, ε_{bin}) in phase-space, happens to coincide with a region in the band structure where no energy bands are available, no electron can be promoted above vacuum level.

On the other hand, in spite of the availability of an occupied initial state, if the kinematics of the experiment is such that the ejected electron, characterised by a pair of ($\vec{k}_e, \mathrm{E}_e$) coincides with an energy gap in the conduction band, this electron cannot escape above vacuum, since no available final state is accessible.

For either case, the measured time histogram would resemble the one shown in fig. 3.34. An example for such an experiment, where the kinematics was purposely chosen thus to prove the absence of coincidence events in absence of available energy bands, will be shown in subsection 4.3.1 where (e,2e)-experiments from HOPG are discussed.

CHAPTER 4

Results & Discussion

Section 4.1 contains a series of Total Electron Yield measurements performed in the Low-Energy regime ($E_0 \leq 50$ eV) which in the following will be referred to as LE-TEY. Measuring the σ of a material is needed to obtain a quantitative answer to *how many* electrons are effectively scattered and/or generated when one incoming electron approaches the surface of a solid. These measurements are performed as a function of the primary energy E_0 and in some cases also in dependence of the angle of incidence, θ_{in}. The TEY then measured corresponds to the *total* number of electrons – elastically and inelastically scattered and of ejected electrons – emitted from the solid into the vacuum per incident electron, in all directions entailed with the hemisphere above the target. Therefore, at a given incident flux (determined by I_0) $\sigma(E_0)$ yields a integral result over all emission angles.

Even though TEY-meauserements were performed up to incident energies of 1800 eV, in section 4.1 the focus is set on the low-energy range 0-50 eV, energy domain of election for the thesis at stake in this work. It is noteworthy that σ is always dictated by an interplay between emissivity (δ or SEY) and reflectivity (η or REY). Furthermore, it will be shown that in this LE-range, σ is dictated by the (unoccupied) band structure of the irradiated target, which precepts both reflection and emission processes of LEEs. The measurements were performed on the set of samples presented in section 3.2 and inter-comparison of LE-TEY acquired for a same material, but from surfaces exhibiting different degrees of long-range order is discussed. The aim of such inter-comparisons is to separate contributions to σ induced by the sole electronic structure from those additionally dictated by the crystalline order.

The spectroscopic techniques based on measurements differential in energy and angle of the electrons emitted from the surface are presented in more detail in subsequent sections; they are employed to obtain a doubly-differential information on the scattering of electrons in solids in dependence of these two parameters. The measured double-differential cross section (2DCS) expresses the flux-density of scattered (or ejected) electrons given as a function of the energy loss, ΔE, observed within a given direction, defined by the detected solid angle, $\Omega(\theta, \varphi)$. This 2DCS

can be expressed as follows:

$$\frac{d^2\sigma}{d\Omega\, d(\Delta E)} \tag{4.1}$$

where the energy loss corresponds to $\Delta E = (E_0 - E_s) = (E_e - \varepsilon_{bin} + \Phi)$ according to E-conservation applied to the entire system, composed of probe and target. Here, E_s and E_e represent the energies of the scattered and ejected electrons respectively, $\varepsilon_{bin} < 0\,\text{eV}$ is the energy of the bound electron prior to emission and Φ is the workfunction of the target. From the experimental point of view, the analyser is tuned to collect electrons emitted from the surface within a specific energy range. For the investigation of the energy loss range, the analysers scans over an energy interval characteristic for primaries that have undergone small energy losses. For the acquisition of SEE-spectra, the analyser collects electrons ejected from the target with kinetic energies, E_e, typically comprised within the SE-peak.

Depending on the tuning of the electron optics used for the transport, collection and analysis of the electrons, the dimensions of the detection cone and herewith of the solid angle $\Omega(\theta, \varphi)$ can be opportunely varied to achieve the desired energy and momentum resolutions (consult sub-subsection 3.3.4.1 for more details).

In Low-Energy Electron Diffraction measurements, generally, the elastically scattered electrons (the zero-loss peak, ZLP) are detected. LEED scans are performed at a fixed azimuthal direction, $\varphi = const$, for a varying polar angle, θ. In this case, the 2DCS corresponds to an angular distribution of the scattered electron for a fix energy and can be written as follows:

$$\left.\frac{d^2\sigma}{d\Omega\, d(\Delta E)}\right|_{\Delta E} \tag{4.2}$$

Diffraction patterns of the elastically reflected electrons enable to investigate the long-range order of the target crystalline surface giving information on the symmetry directions entailed in its unit cell and, if present, on the different domains [61, 62]. Furthermore, such a rocking curve represents a useful tool to monitor the quality of the prepared surface, since it is strictly linked to the rearrangement of surface atoms on the clean surface. Well-ordered surfaces generally exhibit singly- and narrow-peaked elastic peaks superimposed over a moderate bland thermal-diffusion scattering (TDS) background.

In case of Angle-resolved Reflection Electron Energy Loss Spectroscopy (Ar-REELS) the information obtained concerns the excitation channels available in a solid. Also in this case, the electron spectrum measured is given as a function of the energy loss (ΔE) observed within a given direction, defined by the detected solid angle, $\Omega(\theta_{out}, \varphi)$. Each REEL spectrum is acquired for a fixed combination of incidence and emission angles (θ_{in}; θ_{out}) while scanning the electron energy at the analyser.

$$\left.\frac{d^2\sigma}{d\Omega\, d(\Delta E)}\right|_{\Omega(\theta_{out},\varphi)} \tag{4.3}$$

By means of Ar-REELS we focus our attention on the Energy Loss part of the electron spectrum (see section 1.1), therefore the ΔE considered are rather small and generally reach a maximal energy of the order of 1 Hartree ($\sim$27.22 eV)[1].

In REELS the energy deposited by the primary electron is distributed over the degrees of freedom accessible in a target; these are characteristic for the elemental composition, which is in turn intimately connected to the electronic structure of the specimen. With angle-resolved measurements, it is possible to investigate how the variation of the scattering conditions (imposed by a change of θ_{in} and θ_{out}) – i.e. the variation of the transferred momentum projected onto the surface, $\Delta\vec{K}_{\parallel}$ – can lead, for a very same energy loss ΔE, to evidently different spectral shapes exhibiting a large variety of features. These changes in the shape and intensity of spectral features in Ar-REELS can be assigned to changes in the accessible excitation channels – inter-band transitions, plasmon excitations, or else vibrational modes. A proper interpretation of detected spectral features requires knowledge on the electronic structure (both in the occupied and unoccupied states) of the sample. The REELS cross-section reflects the so-called joint density of states (JDOS) – between valence and conduction band DOS [49].

To study the angular distribution of characteristic energy losses, e.g. plasmon resonances and inter-band transitions, diffraction patterns can be acquired by setting the electron energy analyser tuned to an energy for scattered electrons, that have suffered a specific energy loss corresponding to the chosen (plasmon) frequency, thus ΔE in eq. (4.2) is kept fixed at $\Delta\mathrm{E} = \hbar\omega_{pl}$.

Angle-resolved Secondary Electron Emission Spectroscopy represents another spectroscopic tool yielding a 2DCS entailing information on the emission process. Just like in Ar-REELS, the 2DCS of the ejected electrons is measured for a fix pair of incidence and emission angles, while the energy of the detected electrons is scanned over the LE-range corresponding to the SE-spectral region.

Ar-SEES is routinely exploited to map the unoccupied bands of a target, since they deliver momentum-resolved information on unoccupied states [103, 186]. By means of measurements resolved in the momentum, such a band-mapping of the conduction band can be performed, since these detected SEs exhibit a given momentum $\vec{k}_e$ for which it is possible to reconstruct from where in the conduction band they originated after their escape over vacuum level.

Angular distributions of the SEs can be obtained by considering much larger energy losses, for which the detected electron has a kinetic energy of $\mathrm{E}_e = (\Delta\mathrm{E} + \varepsilon_{bin} - \Phi)$, with a magnitude of the order of the SE-peak.

In section 4.2 results obtained by means of the single-particle electron spectroscopies are presented and discussed for HOPG and Al(100).

HOPG and different Al-surfaces were additionally investigated by means of (e,2e)-coincidence

[1] One Hartree is mentioned in this context, because in solids, this amount of energy characterises the average binging energy of the loosely-bound solid-state electrons, which makes the usage of this unit additionally convenient in connection with inelastic scattering processes involving valence electrons.

spectroscopy, a technique which enables to directly link the Energy Loss Spectrum (ELS) to the Secondary Electron Emission Spectrum (SEES). In an (e,2e)-experiment both electrons ($e_1{}^-$ and $e_2{}^-$) participating to the collision are detected coincident in time, their energy ($E_{1,2}$) and momentum ($\vec{k}_{1,2}$) are measured and by means of E- and K-conservation the complete kinematics and energy transfer of the process are reconstructed. Their acquisition is resolved in energy and momentum, since their probability of detection is given for the defined solid angles $\Omega_1(\theta_1, \varphi_1)$ and $\Omega_2(\theta_2, \varphi_2)$ of the two analysers, each one of which is tuned on the energy of one of the electrons. By selecting the kinematics of the scattering process and by choosing both the energy and momentum transfers (ΔE and $\Delta\vec{K}$) occurring during the collision, the measured (e,2e)-yield corresponds to a triple-differential cross-section (TDCS), which is sensitive to the ionisation mechanism and to the initial and final states (for more details, please consult sections 2.3 and 2.4 and subsection 3.3.4 and Refs. therein).

In the series of measurements discussed in section 4.3, connection between the ejection mechanism of SEs is made with the energy- and momentum-transfers occurring during the selected loss process. The measured probability-flux – also (e,2e)-coincidence yield – therefore corresponds to a SE-yield obtained for each ejected electron energy (E_e) chosen at a selected energy loss process (E_0-E_s).

$$\frac{d^3\sigma_{(e,2e)}}{d\Omega_1\, d\Omega_2\, dE} \tag{4.4}$$

In equation (4.4) the energy-dependence dE is determined by the overall energy balance of the process. The measured TDCS is interpreted as a differential SE-yield, which is specific to a given energy loss ΔE undergone by the incident electron – differential in both energy and momentum.

Section 4.3 discusses (e,2e) results measured employing two different coincidence set-ups: (1.) the (e,2e)-spectrometer of the LASEC laboratory at the Università degli Studi Roma Tre (RM3) described in section 3.3.3 and (2.) the Secondary Electron-Electron Energy Loss Coincidence Spectrometer (SE2ELCS) at the Technical University of Vienna (TUV) described in Refs. [244, 217, 106]. By means of these experimental set-ups it was possible to perform (e,2e)-measurements under two different kinematics. Inter-comparison between these datasets is discussed in subsection 4.3.1, for the HOPG surface and in 4.3.2 for the case of Aluminium. In this latter case, the inter-comparison was done between data acquired from a single crystal with surface orientation in the (100) symmetry direction and its polycrystalline counterpart (data from Ref. [126]). Additional coparison is performed with the theoretical model presented by K. Kouzakov and J. Berakdar in Ref. [164].

The overall goal of these investigations aims at achieving a better insight on the fundamental mechanisms involved in the scattering, generation and ejection processes of SEs. By combining the gathered information delivered by these electron spectroscopic techniques, each one with its own individual degree of differentiability, we want to identify which are the essential ingredients that need to be accounted for obtaining the full-picture on SEE in the LE-regime.

4.1 Fully Integral Information via LE-TEY Measurements

Total Electron Yields (TEY) in the very low kinetic energy range (for primary electrons with $E_0 \leq 50\,eV$) were measured as a function of the primary energy (E_0) and in some cases these were also investigated in dependence of the impact angle, θ_{in}. The set of specimens (presented in section 3.2) was examined as introduced in the ultra-high vacuum chamber (UHV) and after having been cleaned by Ar^+-ion sputtering. In case of single crystals, the sputter-cleaned surface was subsequently annealed to restore the crystalline structure of their surfaces (as explained in section 3.1).

As mentioned in the introduction (in chapter 1), the measurement of the TEY is nowadays widely used, representing a crucial mean of diagnostics to probe the quality of technical surfaces in many technological fields. These *technical surfaces* generally lack of long-range order and are in most of the cases either amorphous or polycrystalline. Besides, it is relevant to mention that cleanliness in case of these technical surfaces is not at all mandatory, since they have to endure and perform also in non-perfectly clean environment. In fact, for these materials particular interest is devoted to the study of the "*as received*" (contaminated) samples. Most of these studies are therefore driven by aspects mainly linked to the ultimate technological application of the investigated targets.

In this work, on the other hand, the focus is set on the elementary processes governing the TEY-behaviour of a material. Therefore, the choice of the investigated targets comprehends allotropes of a same element exhibiting similar microscopic electronic structure, but different long-range orders, thus also including single crystalline surfaces, which otherwise would seldom find a technological application. The Density-of-States (DoS) can vary among different allotropes. The aim for such an investigation is to separate contributions to the TEY and to the SE-spectrum associated only to the electronic structure from those additionally influenced by the atomic structure of the target.

In the following, it will be shown that the high surface sensitivity of TEY-measurement becomes particularly evident especially when comparing the σ measured on an *"as received"* surface (contaminated) with the σ obtained on the (same but) clean target. As already demonstrated in several other works [29, 71, 72, 73] (to name a few) the TEY behaviour is strongly influenced by the presence of contaminants, e.g. water, oxigen, CO. Presence of such contaminants on the surface is known to induce a strong change of the elastic scattering at low energy [170] and for this very same reason it is often difficult to establish a *de facto standard* value for the TEY – more commonly referred to as Secondary Electron Yield (SEY).

Figure 4.1 (a.) shows once more the basilar set-up used to perform LE-TEY measurement

under normal impingement. The electron beam of (nearly) energy-independent intensity is directed onto the sample surface in a retarding electrostatic field and the total sample current (I_s) is monitored as a function of the electron landing energy. As explained in more detail in sub-subsection 3.3.2, the total primary current, I_0 is measured at the picoamperometre as sample current, when the target is set at a positive potential. In most of the experiments, this positive V_{bias} was set to $\sim +40$ V. Hence, the source energy E_{gun} could be scanned starting from a higher energy value (of ca. 38 eV in this case) for which the emission characteristics of the electron source [227] are more reliable both in its stability and w.r.t. the nominal energy scale. The electron beam current for all measurements performed in this low kinetic energy range was of the order of 3 nA.

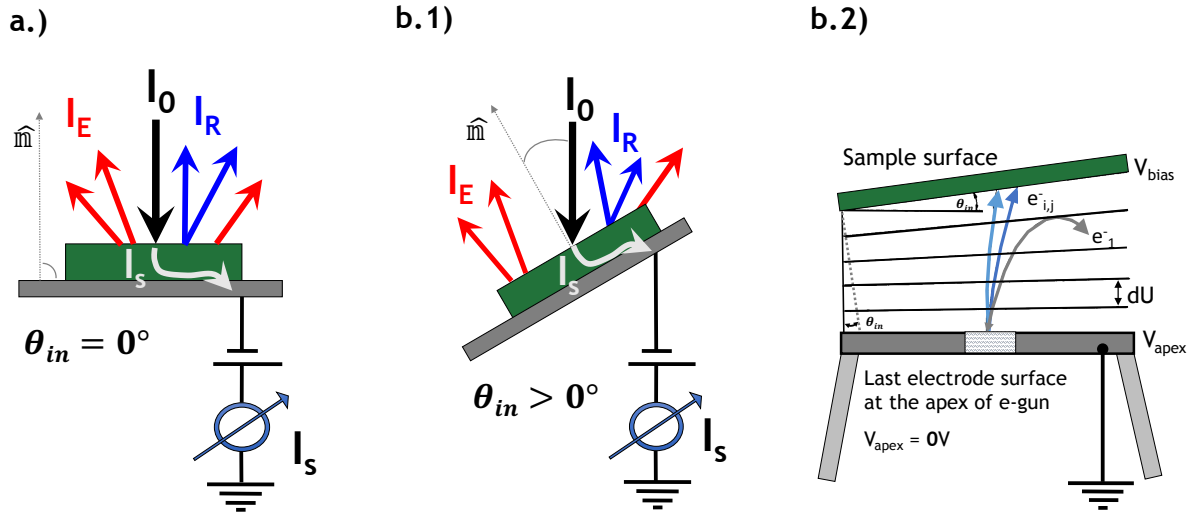

Figure 4.1: Scheme of the experimental set up used at CERN to acquire the TEY-curves based on a retarding potential measurement layout. (a.) Current circuit (as shown in Fig. 3.13) displayed for experiments performed under normal incidence. (b.1) experimental set up for acquisition of LE-TEY curves under *off-normal* incidence (with $\theta_{in} > 0°$). (b.2) shows the trajectories of electrons in a distorted retarding electric field based on the applied potential model explained in Ref. [245]. V_{bias} is the potential applied on the sample and V_{apex} =0 V represents the ground potential at the apex of the electron gun. θ_{in} is the angle of incidence determined by the sample tilt. Electron deflections are exaggerated with respect to what we consider being the real case. Equipotential planes differing by *dU* are slightly bent in the distorted electrostatic retarding field.

The current circuits shown in panels (a.) and (b.1) of figure 4.1 depict the case, when a negative bias ($V_{bias} < 0$ V) is applied on the target. The current drained by the sample – called I_s in this case – is given only by transmitted electrons which have an energy greater than the applied negative voltage. To continue with the same example: if the I_0-measurement was done with a V_{bias} of +40 V the subsequent measurement of I_s is performed with a sample bias of -40 V. This voltage is applied to the sample by a battery box and is maintained constant for the whole experimental scan, during which the source energy is step-wise increased starting from a value of the order of $e\,V_{bias}$. Thus, the measured I_s excludes current contributions of both the ejected (I_E) electrons – which for $E_{kin} \lesssim 40$ eV are repelled from the surface – and the reflected (I_R) electrons – which at this point can be categorised in two types: those which are omnipresently

reflected (inducing the systematic error) and those which do not manage to penetrate the target for reasons that are explained in the following on the basis of experiments discussed in the next sections. The experimental σ is obtained as a function of the landing energy, E_{Land}, according to equation (3.3).

When the target is irradiated under normal incidence (as depicted in panel (a.) of figure 4.1), its surface is parallel[2] to the surface of the last electrode at the apex of the electron source. By applying a negative bias on the target a (uniform) retarding electric field is established. This electric field, $\vec{E}$, is determined by the potential difference

$$\Delta U = (V_{apex} - V_{bias}) = \vec{E} \cdot \vec{d_w} \tag{4.5}$$

between the biassed sample surface (with $V_{bias} < 0\,V$) and the potential at apex of the last electrode of the electron gun ($V_{apex} = 0\,V$). The distance between these surfaces is the so-called *working distance* d_w. The effective energy of an electron reaching the surface travelling through this retarding field is the *"landing"* energy, E_{Land} (as already defined in eq. (3.2) w.r.t. vacuum level).

Figure 4.1 (b.1) depicts the case for measurements done in off-normal geometry. The surface of the sample is tilted with respect to the apex of the electron gun. The electric field established in between is not any more reducible to a uniform one and consequently primary electrons trajectories are distorted while travelling towards the target [245]. Figure 4.1 (b.2) gives a sketch of the (non-uniform) E-field between electron gun apex and sample surface and it shows (in an exaggerated way) the distorted electron trajectories through the non-uniform retarding E-field. This leads to an apparent shift of the σ onset-slope – due to a shift of the perpendicular momentum at which the electrons effectively land onto the target surface. Incident-angle dependent LE-TEY measurements shown in figure 4.5 clearly exhibit such an apparent energy shift, when θ_{in} is increased.

Under the assumption of a uniform retarding electric field, electrons start from the aperture centred at the apex of the electron gun with the initial velocity v_0. As they travel towards the sample surface, their perpendicular velocity-component $v(z)$ yields

$$\vec{v}^{\,2}(z) = \vec{v_0}^{\,2}(z) + \frac{2\,\vec{a} \cdot \vec{z}}{e} \tag{4.6}$$

with $\vec{a} = \left(\frac{e\,\vec{E}}{m_e}\right)$ being the acceleration in the retarding electric field $\vec{E}$.

As the electron travels towards the surface in this retarding $\vec{E}$ it gets uniformly decelerated, hence the potential between gun and target appears as a constant increasing inclined slope of potential. If the electron landing energy is smaller than the sample bias, total reflection occurs,

[2]Disregarding the microscopic surface morphology of the sample, it is consented to assume that the topmost surface planes of sample and gun electrode are parallel to a sufficient degree on the macroscopic scale.

thus yielding a σ =1. Otherwise, for positive E_{Land} values, hence when the electron manages to overcome the surface barrier, it undergoes refraction at the surface due to the mean inner potential U_{in} of the solid. The incident landing energy of the electron can be expressed as

$$E_{Land} = \frac{\hbar^2}{2m}\left({k_\parallel}^2 + {k_\perp}^2\right) \tag{4.7}$$

in dependence of the squared momentum given in its perpendicular and parallel components, which can be calculated as follows:

$$\begin{aligned} k_\perp &= \tfrac{1}{a_0}\cdot\sqrt{\tfrac{2\,E_{Land}}{E_H}}\cdot\cos(\theta_{in}) \\ k_\parallel &= \tfrac{1}{a_0}\cdot\sqrt{\tfrac{2\,E_{Land}}{E_H}}\cdot\sin(\theta_{in}) \end{aligned} \tag{4.8}$$

Their result is given in units of reciprocal Å with a_0 representing the Bohr-radius (0.5291 Å) and E_H is one Hartree of energy expressed in eV. The angle θ_{in} is the angle of incidence enclosed by the source and the sample surface normal (i.e. the incidence angle at the electron landing).

When the primary electron (PE) lands on the target surface, after having travelled through the retarding potential ΔU – defined in eq. (4.5) – for a path z equal to the working distance d_w, the equation of motion in the perpendicular direction becomes

$$\begin{aligned} v^2(d_w) &= \tfrac{2\,e\,\Delta U}{(m_e\,d_w)}\cdot d_w + {v_0}^2 \qquad if \quad \Delta U < 0 \\ \tfrac{m_e\,v^2(d_w)}{2} &= e\,\Delta U + \tfrac{1}{2}\,m\,{v_0}^2 \end{aligned} \tag{4.9}$$

In these conditions, the electron *lands* on the surface of the target, where the landing energy E_{Land} at z =d_w and at θ_{in} =0° represents the minimal energy for which the electron overcomes the retarding field, ΔU. When $E_{Land} \gtrsim \Delta U$, which in turn means that its landing energy is greater than V_{bias} (see eq. (4.5)), the electron electron beam manages to overcome the energy barrier of the target (which is defined by its workfunction Φ). At θ_{in} =0° the impinging electron has only a perpendicular component of the momentum ($\vec{k}_\parallel$ =0 Å) and the entire kinetic energy is invested to overcome the surface barrier and start to penetrate the target. For E_{Land} = 0 eV (w.r.t E_{vac}) the inflection point observed in the TEY-curve delivers the real value of the sample workfunction, Φ (consult sub-subsection 3.3.2.1 for more details). This value defines the "zero-point" of the kinetic energy of electrons landing on the specimen. This zero-point remains as a reference also for experiments performed at off-normal incidence. Owing to the fact that energy depends on the squared momentum, for simplicity we can re-write eq. (4.10) as incident-angle dependent landing energy – given on an energy scale with respect to the Fermi level – as follows:

$$E_{Land}\,(\theta_{in}) = \Phi + \cos^2\theta_{in}\cdot\left(\frac{1}{2}\,m\,{v_0}^2 + \Delta U\right) \qquad if \quad \Delta U < 0 \tag{4.10}$$

For θ_{in} =0°, the "zero-point" of the landing energy scale, the real workfunction value of the target is obtained. Hence, for an electron to overcome the surface potential barrier, it requires for the perpendicular component of the momentum to fulfil equation (4.10). It is the modulus of $k_\perp$, that determines whether or not the incoming electron manages to penetrate the target or not.

For off-normal incidence, the momentum of the impinging electron no longer possesses only a perpendicular component, $k_\perp$, but also a parallel component, $k_\parallel$ and the E_{Land} (of equation (4.10)) associated to the sole perpendicular component will increase for incrementing θ_{in}-values.

While in normal-incidence the total landing energy is associated to the sole perpendicular component of the momentum, in off-normal conditions a same landing energy is subdivided over both momentum components, thus, the magnitude of $k_\perp$ shrinks in favour of a growing $k_\parallel$-component. Thus, for the electron to overcome the same surface potential barrier a greater landing energy is required, so that the modulus of the perpendicular component of the momentum obtains the suitable value (as had in perpendicular incidence).

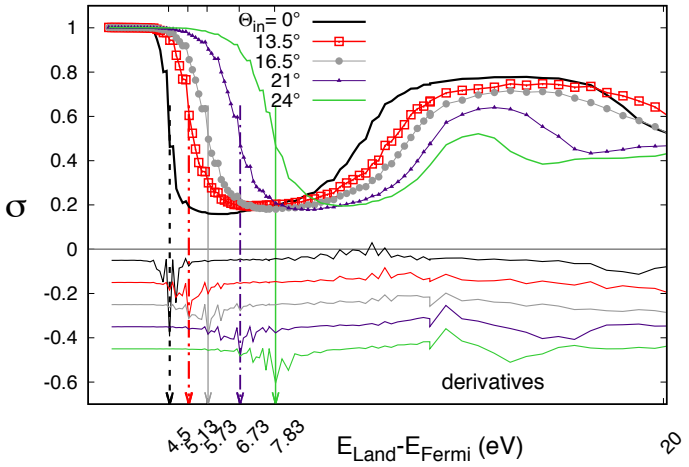

Figure 4.2: Increment of E_{Land} observed at the onset-slope measured in dependence of the impact angle θ_{in}. The increase in energy is induced by the electrostatic shift caused by the distorted retarding electric field. The series of angle-dependent measurements was performed on HOPG (also shown in figure 4.5 and further discussed in subsection 4.1.1).

θ_{in} [°]	E_{land} (calc.)	E_{land} (exp.)
0	4.50	4.50
13.5	5.37	5.13
16.5	5.82	5.73
21	6.70	6.73
24	7.42	7.83

Table 4.1: Comparison between the expected E-shift for the onset-slope (calculated according to formula in eq. (4.10) by setting $e\,V_{bias}$ =30.81 eV as used in the experiments) and the actual shift experimentally measured and shown in fig. 4.2.

Applying the formula given in eq. (4.10), it is possible to reliably predict at which which sample bias and consequently at which E_{Land} one can expect to observe the inflection point of the onset-slope, when performing LE-TEY measurements in off-normal geometry.

Figure 4.2 shows five LE-TEY curves measured on HOPG at different impact angles (reported in the legend). For each θ_{in}, in Table 4.1 the predicted E_{Land} of the onset-slope, calculated according to equation (4.10), is compared with the one experimentally measured. Both the calculation and the measurement were performed for $e\,\Delta U = (V_{apex} - V_{bias}) = 30.81$ V, hence for V_{bias} of -30.81 V. Reasonable accordance within the estimated accuracy of ±0.2 eV was found

between the expected and the actually measured values (consult table 4.1).

As demonstrated by the LE-TEY series in figure 4.2, the increase in impact angle induces the slope to shift towards higher landing energies.

As recognisable from LE-TEY curves shown previously in figure 3.17 the E-dependent structures measured on the various targets display evidently different features. As it will be shown, the presence (or the absence) of energy-dependent structures in the measured LE-TEY curves observed at higher landing energies (e.g. for $E_{Land}-E_{Fermi} \in (10-20)\,eV$) strongly depends on the material and its band structure.

Total Current Spectroscopy (TCS) and other TEY-data from literature [190, 246, 193, 247, 196] confirm that materials exhibiting the strongest current modulations are layered structures, of which graphite (and HOPG) represents a prominent prototype.

For landing energies between 0–50 eV, the TEY is dominated by elastically reflected and inelastically backscattered electrons [7, 33, 190]. Features corresponding to enhanced reflectivity η of electrons are directly linked to the band structure above the vacuum level [248, 229], in particular to the presence of energy gaps or to strongly-localised (non-dispersing) bands. Further modulations in the TEY of a material are associated to inelastic scattering processes, such as an interband transition and to collective modes, e.g. plasmon excitations [190, 196, 226].

To properly interpret the appearance of these structures, knowledge about the (unoccupied) electronic structure of the irradiated target is necessary and the wave-nature of electrons must be taken into account. In Ref. [229] the physical principles of the *matching formalism* for electron scattering at surfaces are given by means of which reflectivity of electrons at the surface-vacuum interface is explained. A (free) electron approaching the surface of a solid has an incident energy E_{Land} as given in equation (4.7) and its wave-function is given as follows

$$\varphi_0 = \exp\left(i\,\vec{k}_{\parallel}\cdot\vec{r}_{\parallel} + i\,k_{\perp}\cdot z\right) \tag{4.11}$$

The complete wave function (WF) ψ_0 in vacuum is given by the superposition of the incoming free electron WF as given in eq. (4.11) and the outgoing diffracted electron waves. The surface potential has a two-dimensional periodicity, therefore during scattering the parallel component of the electron momentum, $k_{\parallel}$ is conserved and matches the parallel component of the momentum inside of the crystal. The parallel component inside the crystal is determined by the 2D reciprocal lattice vector $\vec{G}_{\parallel}$. Hence, the complete WF outside is given by:

$$\Psi_0 = \varphi_0 + \sum_{\parallel} A_{\parallel}\,\exp\left[i\,\left(\vec{k}_{\parallel}+\vec{G}_{\parallel}\right)\cdot\vec{r}_{\parallel} - i\,k_{\perp}\cdot z\right] \tag{4.12}$$

Where the sum is performed over the in-plane components and where $A_{\parallel}$ is the parallel component of the scattered waves amplitude. The electron wave-functions inside the solid are described by

Bloch waves exhibiting the periodicity of a three-dimensional lattice, with a 3D reciprocal lattice vector $\vec{G}$.

$$\Psi_{in} = \sum_{\vec{G}} c_{\vec{G}}\left(\vec{k}\right) \exp\left[i\left(\vec{k}+\vec{G}\right)\cdot\vec{r}\right] \tag{4.13}$$

Also inside, for the Bloch wave-functions, the momentum of the electrons can be split in a parallel and perpendicular component. The matching conditions require that both $\vec{k}_{\|}$ components of the wave-function of the free impinging electron and of the Bloch electrons must be equal inside and outside the solid and that the total energy must coincide. These requirements imply that for a given E_{land} of the e-beam there must be available electronic states inside the crystal in order to have a flux of probability propagating inside. For the case the electron manages to propagate in the inside of the crystal, then refraction must be taken into account, therefore the effective kinetic energy of the electron penetrating the solid will be increased by the value of the target inner potential, U_{in}, yielding , $E_{eff} = (E_{Land}+U_{in})$. Otherwise, in the case E_{land} coincides with an energy gap in the target band structure (BS), its wave-function cannot couple with any Bloch wave in the crystal, since at the given energy there are no states available. In presence of such an E-gap – the incoming electron is totally reflected. This results in a higher value for the TEY, which in this case is associated to electron reflection. These reflected electrons do not contribute to the measured sample current, I_s, since they are not absorbed by the sample and are those associated to the (non-directly measurable) reflected current, I_R, previously mentioned and symbolised as blue arrows in figure 4.1 (a.) and (b.1). This reflected current is associated to the flux of all outgoing LEED beams and to the so-called REY, or reflection/back-scattering coefficient (η). It is this contribution of the reflected electrons associated to η that is essentially the reason for the crystallographic contrast in the SE-Microscope [249, 7]. In fact, when contamination layers are on the object surface, the image contrasts are a consequence of the variation in reflectivity rather then in δ. These crystallographic contrasts effects are explainable by excitation of Bloch waves, as previously mentioned.

Hence, the electronic band structure of the target, with its allowed and forbidden bands, is of considerable importance for the proper interpretation of the TEY-intensity observed at the corresponding E-structures. The experiments shown in the upcoming sections will demonstrate that the energy-dependent modulation of the absorbed target current, by means of which the LE-TEY curves are determined, are strongest in case of materials exhibiting many and large energy gaps. In these cases, the TEY is mostly determined by an elastic reflection phenomenon.

The general notions and considerations presented in this preamble form the basis for the interpretation of the experimental results presented in the next sections.

For a material exhibiting a long-range order, distribution and density of its energy levels above vacuum level varies in dependence of the symmetry direction, this strongly affects the E-structure of σ which then depends on the considered surface symmetry. Although polycrystalline

and amorphous surfaces of a same material have the same electronic structure as the single crystalline exemplars, the distribution of energy bands must be averaged over all possible symmetry directions available in the target. This affects the E-structure of the TEY, which in polycrystalline/amorphous targets is generally smoothened out wrt. the σ measured along a specific crystalline direction. Hence, the interplay of η and δ is what ultimately dictates the intensity of σ in the LE-range.

4.1.1 HOPG vs. a-C: LE-TEY

Analysis and inter-comparison of LE-TEY curves acquired on two C allotropes are discussed. A first comparison is performed on the σ measured under normal impingement of LEEs on the highly-ordered form of Graphite (HOPG) and its amorphous counterpart. During experiments the electron landing energy was scanned from 0 eV up to 50 eV in steps of 0.1–0.5 eV. In case of normal incidence, the perpendicular component of the momentum of the incident electron, $\vec{k}_{\perp}$ coincides with the total momentum and is directed parallel to the $\hat{c}$-axis of the target or in the specific case of HOPG, along the ΓA-direction in reciprocal space. Figure 4.3 is subdivided in three panels. Panel (c.) schematically shows the first Brillouin zone (BZ) of Graphite entailing all symmetry points and arrows highlighting crystallographic directions. Panel (b.) contains three LE-TEY curves acquired for landing energies ranging from 0 to 50 eV. Panel (a.) shows the BS of Graphite above vacuum level given along the perpendicular symmetry direction of ΓA in the BZ. Energy scales of panels (b.) and (c.) are given with respect to the Fermi level.

All LE-TEY curves shown in fig. 4.3 (b.) exhibits a σ of 1 as long as total reflection occurs, for $E_{land} < V_{bias}$, as explained in sub-subsection (3.3.2). The minima of their first derivatives yield the value for their respective workfunctions. In case of HOPG, the value for Φ measured at the onset-slope, for both the dirty (black line) and clean (red line) surfaces, is of ca. $4.54\,\text{eV} \pm 0.2\,\text{eV}$. An enlarged plot showing a comparison between these σ onset-slopes is given along with their first derivatives in figure 4.4.

For the clean HOPG surface, the workfunction was additionally measured in situ by means of a Kelvin probe. Even though, with a different measurement accuracy, good agreement within the respective uncertainties could be assessed. The blue dashed curve (in panel (b.) of fig. 4.3) is the yield measured on a clean amorphous C-coating and serves as a comparison to the ordered allotrope. This a-C sample represents as so-called "technical surface" [27] , which is generally produced to be used in an "as received"-state, without undergoing any (cleaning) treatment. For this series of measurements instead, the a-C sample was both sputter-cleaned and annealed, to ensure surface cleanliness.

For the a-C coating the workfunction determined at the onset-slope exhibits a value of ca. $5.1 \pm 0.2\,\text{eV}$. This value is well in accordance with the one reported in Ref. [228], where a Φ of 5 eV is assigned to Carbon.

After having excluded the presence of contaminants, alleged reasons for measuring different workfunction values for a same material can be ascribed to several aspects: (1.) to a different crystalline direction of the surface, which is known to influence Φ in a same material; (2.) to an electrostatic shift, due to a non-parallel arrangement of source apex and sample surface as previously explained; (3.) surface roughness, which may induce a non-parallel alignment at

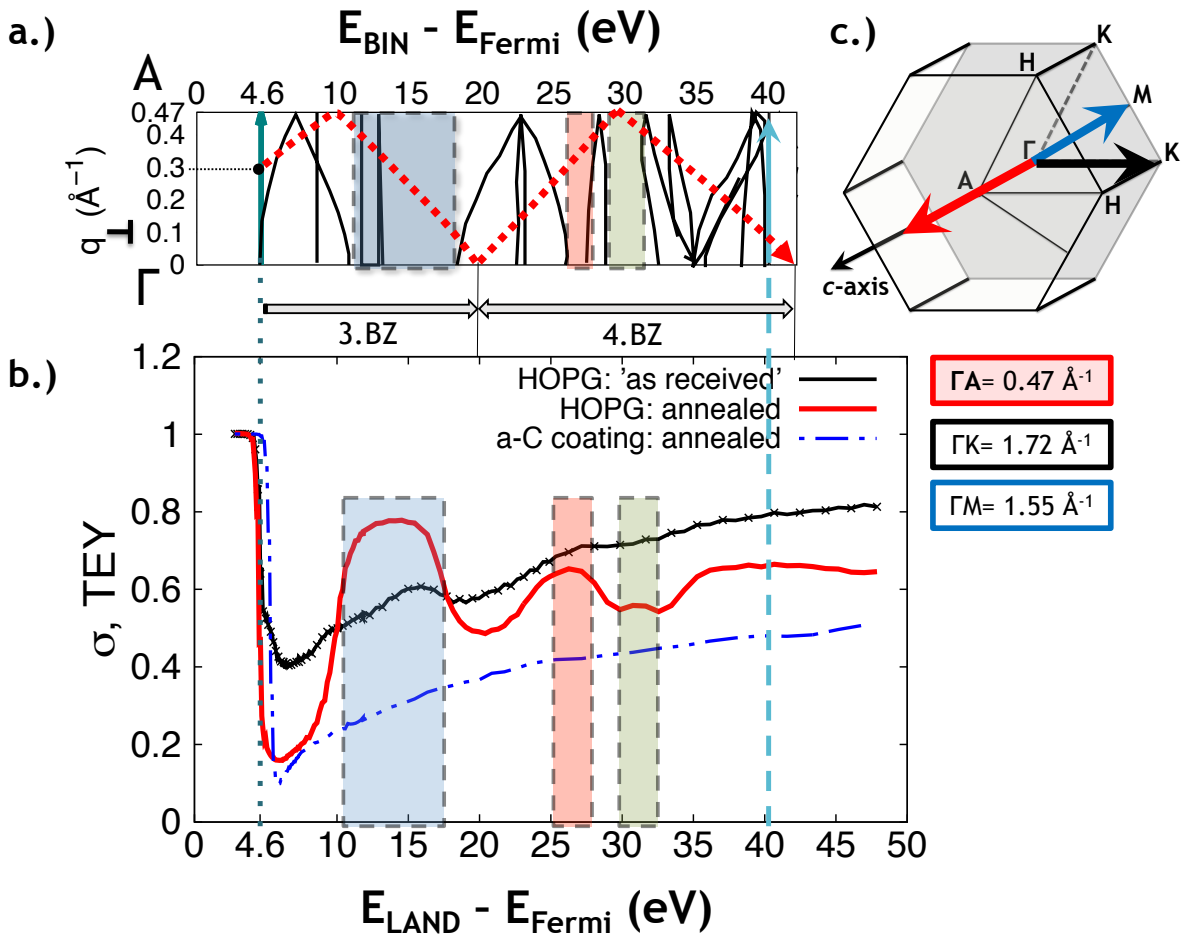

Figure 4.3: Interpretation of LE-TEY measurements from C allotropes in connection with the unoccupied band structure of Graphite. Panel (b.) shows LE-TEY curves from a dirty HOPG (black line), of a clean HOPG (red line) surfaces and of the clean a-C coating (blue dashed line). Three coloured rectangular areas highlight regions in the E-structure of HOPG, exhibiting a higher TEY-value. These regions relate to zones in the unoccupied band structure (a.) with energy gaps (marked in the same colour code). The calculated band structure (BS) of HOPG shown in (a.) is given along the ΓA-symmetry direction (BS-data taken from Ref.[196]). The red dashed curve superimposed on the BS of HOPG represents regions in phase-space sampled during the acquisition (consult Table 4.2), displayed in the reduced zone scheme via Umklapp-processes. At each landing energy the modulus of the perpendicular momentum ($k_\perp$) of the incoming electron is calculated under consideration of refraction, hence accounting for the inner potential U_{in}. For the given initial landing energy the incoming electron starts to sample from the 3^{rd} Brillouin zone (BZ). Panel (c.) illustrates the Brillouin zone of graphite with all main symmetry directions, with the critical-point notation.

micrometre scale, thus also leading to a small E-shift. In the specific case of this sample, it is difficult to exactly assess which of these effects is the one provoking this increased workfunction; it is rather believed to be a combined effect of all three.

In panel (b.) of fig. 4.3 the LE-TEY displaying an appreciable richness of E-dependent features is the red curve, which was acquired from the clean and ordered HOPG surface. After insertion into UHV of the mechanically exfoliated sample-surface, the target was annealed at a temperature of 300° C for the duration of ca. 10 hours. This baking procedure helps to remove foremost residual water and Hydro-Carbons. The cleanliness of the surface was confirmed by means of X-ray Photo-Electron Spectroscopy.

Unlike in the case of XPS, where it is possible to identify and quantify all elemental components of (and on) a specimen, if no exact quantification is required, LE-TEY measurements can be nonetheless exploited to qualitatively monitor the presence of contaminants and, in case of single crystals, to assess the long-range order of these latter. The LE-TEY measurement offers a useful method to check the quality of a surface. As previously mentioned, the σ of a material is particularly sensitive to the surface chemical state of the target, thus any variation in workfunction, any adsorbed contaminant, or any surface effect – e.g. a band-bending induced by the presence of an Oxide layer – can be immediately pinpointed by the acquisition of a LE-TEY, albeit not quantifiable.

The black curve of fig. 4.3 (b.) gives a good example for the effects caused by the presence of

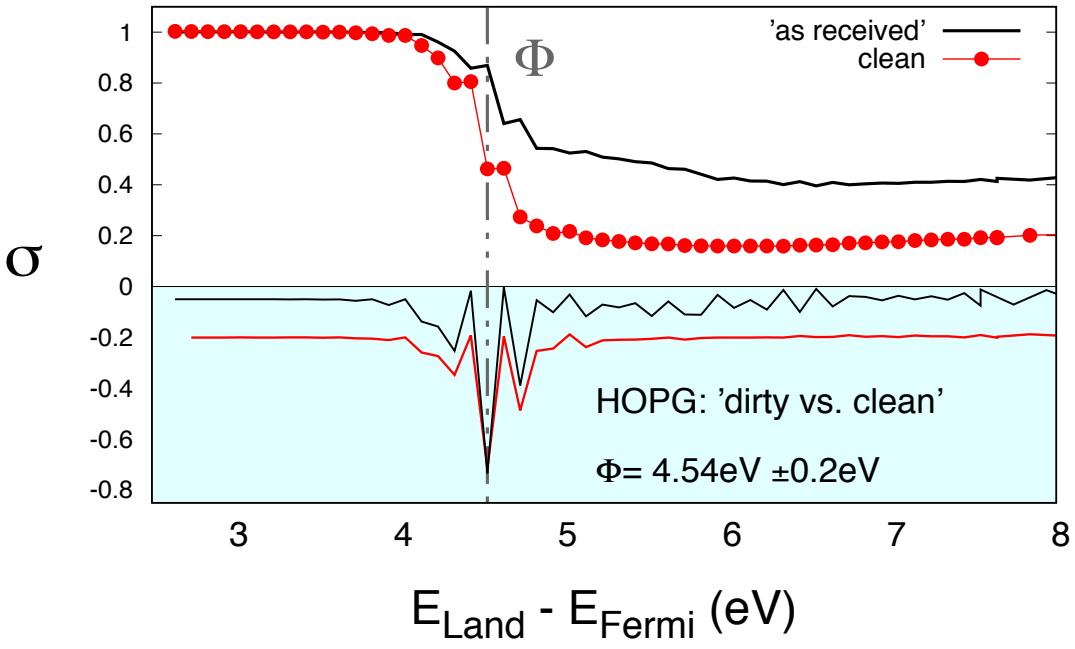

Figure 4.4: Enlarged onset-slopes for HOPG at two stages of cleanliness, indicated in the legend. First derivatives of the TEY-curves (entailed in the light-blue area below zero) exhibit their minima, where the inflection point, i.e. the "zero-point" of the electron landing energy is determined, in either case at a value of 4.54 eV.

impurities on the surface of HOPG. This E-structure, labelled "as received", was obtained from the HOPG sample, which underwent only mechanical exfoliation prior to its insertion into UHV. The E-dependent total yield exhibits some mild structures, which may recall those observed on the clean surface, however these features are only faintly pronounced, since they are intermixed with (and/or covered by) the TEY-signal induced by the extraneous elements. Over the whole E_{Land}-range the average TEY-value is higher than otherwise measured on clean C-surfaces, this is due to the presence of contaminants, such as the presence of water or of an oxide layer, which by covering the surface induce an increment of the SE-yield. If the contaminants give rise to an insulating oxide layer, a higher σ is often the consequence. Higher SEY-values for insulators are generally explained by a larger escape depth of the secondaries [7, 33]. This is due to the presence of large energy gaps wherein the escaping SE extracted from the conduction band does not undergo further inelastic collisions, thus a larger number of SEs manage to overcome the barrier.

The E-structure measured for normal incidence on the clean HOPG surface (red line of fig. 4.3 (b.)) exhibits features with an increased σ, which are highlighted by shaded rectangles. These rectangular areas relate to regions in phase-space shown along the ΓA-symmetry direction exhibiting energy gaps (see panel (a.) of the same figure). Here, rectangular shaded regions indicated with the same colour code as in panel (b.) highlight regions in this symmetry direction entailing E-gaps. Since the measurement was conducted in normal incidence, the incident electron possesses only a non-zero perpendicular component of its momentum, thus only the ΓA-symmetry direction in reciprocal space is sampled by the electron beam. For each electron landing energy (between $0 - 50\,\mathrm{eV}$) the perpendicular component of the momentum of the incoming electron is calculated according to formula (4.9), wherein E_{Land} is substituted by the effective energy ($E_{eff} = E_{Land} + U_{in}$) of the impinging electron. The incoming electron undergoes refraction at the surface (Snell's law) and its energy inside the target is increased by the inner potential, U_{in}, which in graphite is ca. 16 eV [195]. The result of these calculations is displayed as red dashed curve superimposed on the unoccupied band structure of HOPG in fig. 4.3 (a.) and it represents the values for E_{eff} and its related $k_\perp$-component as sampled during the experimental energy scan performed during the acquisition of the LE-TEY curve of HOPG shown in panel (b.).

Table 4.2 contains some salient values for this sampling, where for certain landing energies both the real $k_\perp$-value and the correspondent $q_\perp$ value, given in reduced zone scheme (RZS) after consideration of Umklapp-processes, are reported. As previously explained, for effective energies of the incident electron, with a $k_\perp$ falling in a region in phase-space coinciding with an energy gap, the electron is back-reflected since there are no Bloch states available inside the crystal for matching the outside wave function, thus resulting in a higher σ. The rise in yield is therefore related to an increase in the reflectivity, or η. For such a case, one would expect the σ to go back to unity. However, due to the formation of surface states or to the presence of the interlayer states – discussed previously in subsection 3.2.1 and shown in fig. 3.2 (e.) – the external

E_{eff} [eV]	$k_\perp$ (real) [Å^{-1}]	$q_\perp$ (RZS) [Å^{-1}]	BZ [#]
16	2.05	0.30	3
21	2.35	0.47(A)	4
30.5	2.82	0 (Γ)	4
41	3.29	0.47 (A)	5
54	3.76	0 (Γ)	5

Table 4.2: $k_\perp$-values calculated for the red LE-TEY curve shown in panel (b.) of figure 4.3 matching the correspondent $q_\perp$-value in the RZS given along the ΓA-direction of HOPG. Same values are displayed as red dashed curve in panel (a.) of the same figure.

wave-function matching with these states decay exponentially into the interior of the crystal at energies where Bloch states are forbidden. This is the reason why σ does not return back to one [167].

A complete counteracting trend, shown in figure 4.3 (b.), is given by the LE-TEY curve measured on the amorphous C (blue dashed line). What immediately stands out for this LE-TEY is the complete absence of any E-structure. For the amorphous target, σ monotonously increases from 0.1 after the onset-slope up to ca. 0.5 around 50 eV. The lack of features for the amorphous surface is not surprising, since in this case the impinging electron irradiates a surface that still exhibits the electronic structure of graphite, however it is averaged over all possible crystalline directions and coincidence with an empty band of the sample is possible at any E_{land}.

The total yield of HOPG was additionally investigated as a function of the angle on incidence, θ_{in}. Figure 4.5 (a.) shows a series of LE-TEY curves acquired from the clean HOPG surface in off-normal geometry for increasing θ_{in} up to 24°. As previously stated, in off-normal geometry the impinging electron has both $k_\parallel$ and $k_\perp$ components. Once that the electron reaches a landing energy for which its perpendicular component of the momentum is sufficient to overcome the surface potential barrier, it penetrates into the crystal and undergoes refraction.

However, at a given θ_{in} >0° the electron no longer samples only along the ΓA-symmetry direction, but accounting also for its parallel momentum, it probes in-plane directions in phase-space – thus also the symmetry directions of ΓK and ΓM (and intermediate ones) should be considered. For increasing incident angle, the the E-structure of the different LE-TEY curves

E_{eff} [eV]	$k_\perp$ (real) [Å^{-1}]	$q_\perp$ (RZS) [Å^{-1}]	BZ [#]
20	1.69	0.28	3
23	1.87	0.47 (A)	3
32	2.35	0 (Γ)	4
43	2.82	0.47 (A)	4
56	3.27	0 (Γ)	5

Table 4.3: $k_\perp$-values calculated for the green LE-TEY curve acquired at θ_{in} =24° in panel (a.) of figure 4.5. The correspondent $q_\perp$-value expressed in the RZS along the ΓA-direction of HOPG yields the green dashed curve in panel (b.) displaying the region sampled during the E-scan.

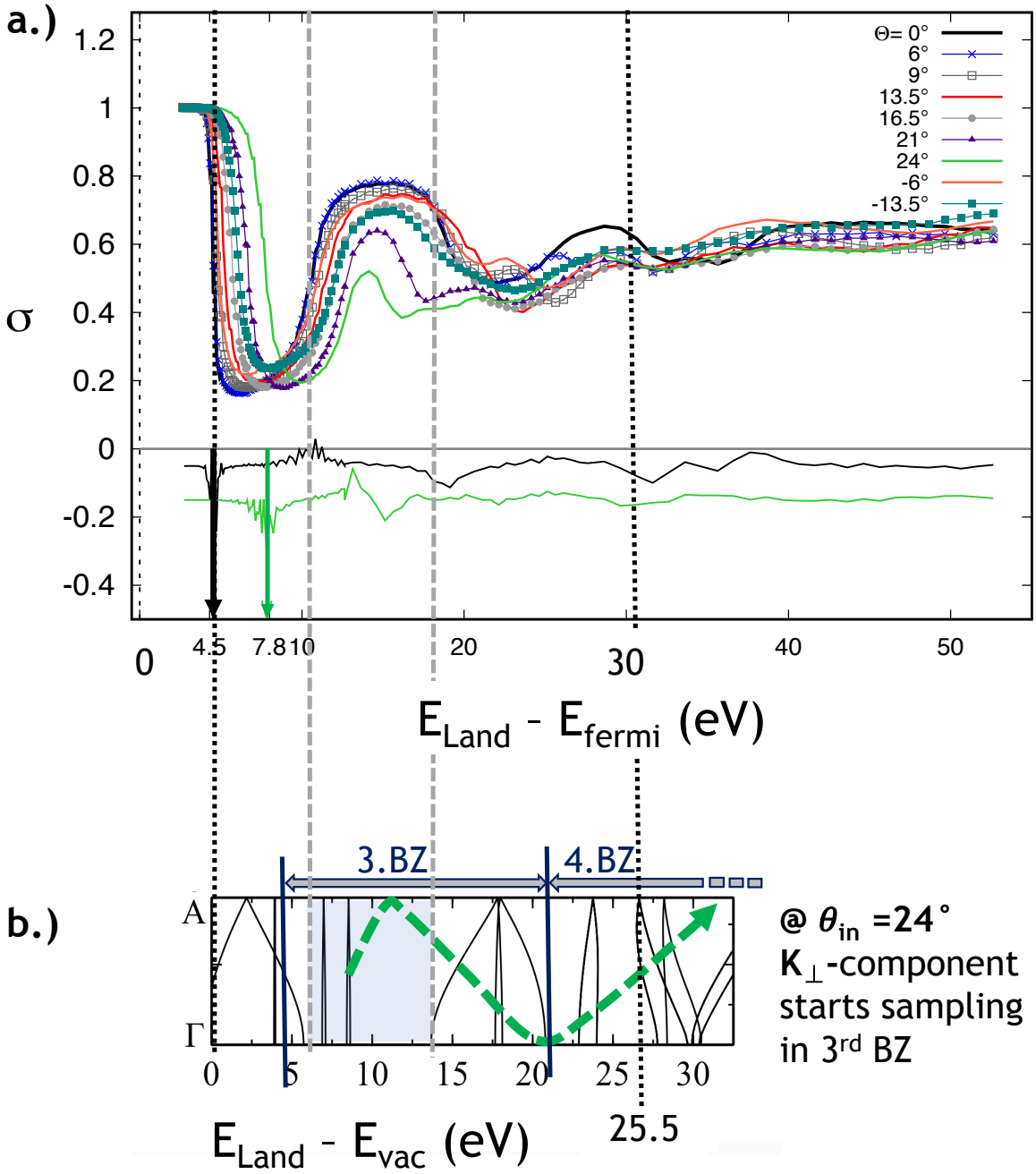

Figure 4.5: (a.) shows a series of impact-angle-dependent LE-TEY measurements from HOPG obtained by tilting the sample surface with respect to the impinging electron beam (as shown in Fig. 4.1 (b.1) and (b.2)). Variation of the impact-angle (θ_{in} as indicated in the legend) induces variations of both the shape and intensity in the measured E-structure. Derivatives of the extremal LE-TEY curves measured at θ_{in} =0° *(black)* and θ_{in} =24° *(green)* are plotted below the zero line. These correspond to the same curves discussed in fig. 4.2. The dashed green curve in (b.) shows the region sampled along the ΓA-crystalline direction corresponding to the experiment performed at θ_{in} =24° incidence angle.

exhibits evident variations, both in their intensity and shape. This is related to the fact that in off-normal incidence the electron samples a different region in the conduction band. Equivalently to table 4.2, values for $k_\perp$ (and the correspondent $q_\perp$ given in reduced zone scheme) calculated for the maximal incident-angle of 24° are given in table 4.3. These values are depicted as green dashed line in panel (b.) of figure 4.5, showing the region in phase-space sampled in the perpendicular direction.

Even if disregarding the parallel component of the momentum, it is possible to interpret the changes in shape and intensity observed in the LE-TEY curves of figure 4.5 by solely considering the perpendicular component. The decrease in intensity and the modified shape of the σ-feature comprised between 10 – 20 eV landing energy (given wrt. Fermi level) measured at 24° (green curve in panel (a.)) is well in accordance with the green dashed curve plotted in panel (b.) showing the regions probed by the electron during the correspondent E-scan.

4.1.2 Al(100) vs. Poly Al: LE-TEY

Inter-comparison of three LE-TEY curves acquired from Al-surfaces is shown in figure 4.6. The curve with purple triangles was acquired on the still contaminated single crystalline Al(100) surface. Apart from exhibiting a complete different trend with respect to both clean surfaces, with a σ which is higher by a factor of 2 over the whole landing energy range, it also has a higher workfunction (of 4.45 eV). This rise in the workfunction for the dirty sample can be assigned to the presence of an oxide layer, which was confirmed by XPS.

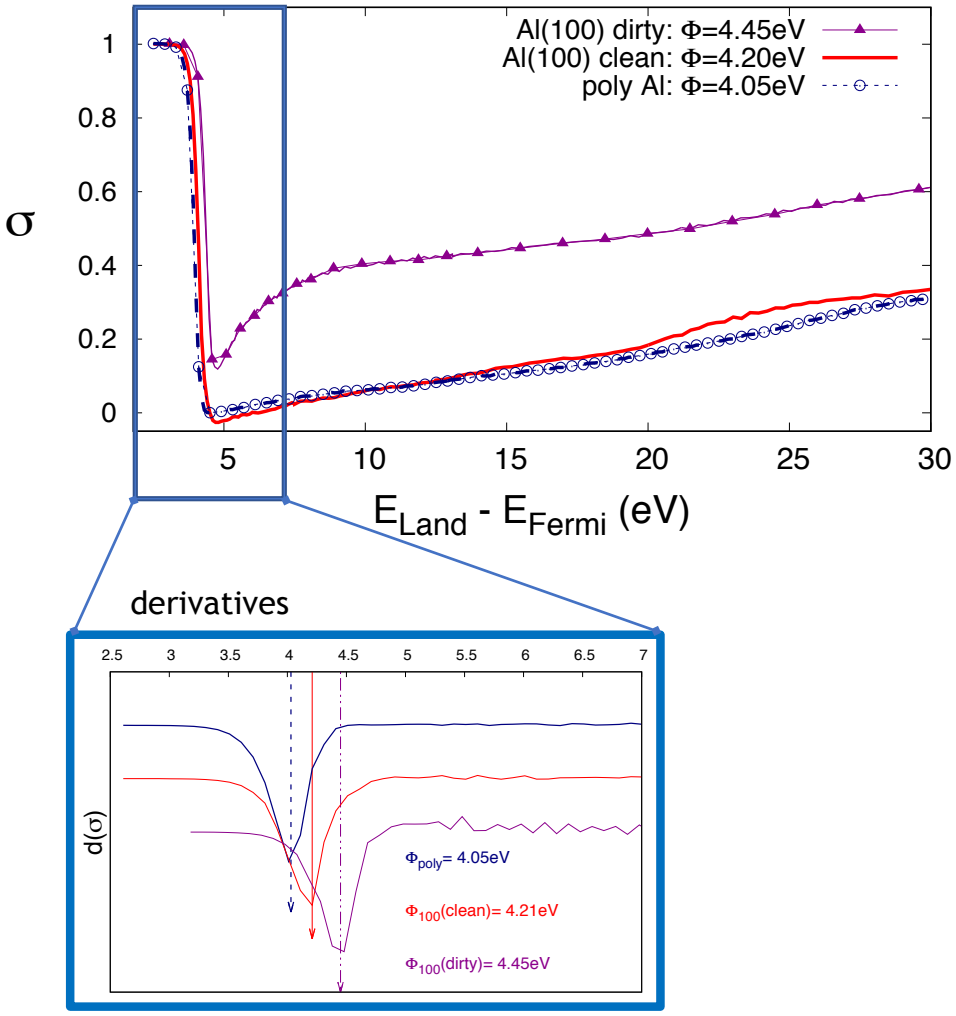

Figure 4.6: Inter-comparison of LE-TEY curves from various Aluminium surface acquired under normal incidence. For the area highlighted by the blue rectangle, first derivatives and the correspondent Φ are shown in the plot below. TEY-curves from the clean polycrystalline Al sample (dashed blue) and its clean single crystalline counterpart, Al(100) (red line) exhibit nearly identical E-structures. They are both substantially different from the LE-TEY measured on the contaminated Al(100) surface (purple line with triangles).

The pronounced rise of the σ in correspondence of the evident bulge forming between 5 – 10 eV landing energy is a feature often observed when the bombarded surface is contaminated by an oxide layer. Experience has shown that such a behaviour is independent from the underlying material.

The LE-TEY curves measured on both clean surfaces resemble one another nearly over the whole energy range. Subtle deviations can be found for $E_{Land} - E_{Fermi}$ between 20 –30 eV; here the σ measured on the single crystal is slightly higher. Derivatives of these two curves, yield – as expected – two different values for the workfunction. For the polycrystalline surface Φ is about 4.0 eV, whereas for the Al(100) crystalline surface it is 4.2 eV. Within the experimental accuracy of ± 0.2 eV, these values are well in accordance with those reported in Ref. [228].

The smoothness of the σ energy structure observed for both clean surfaces is not too surprising, since the density of states in Al is nearly constant exhibiting a quasi free-electron gas distribution (see figure 3.6). This is valid for all symmetry directions in the Aluminium crystal (see subsection 3.2.2 for more details) [212]. Rise in the σ due to reflectivity η is not expected, since in no symmetry direction of the Al crystal E-gaps are present in the conduction band. The monotonic and nearly smooth rise of the DoS above E_{vac} guarantees a continuous availability of empty states, hence there are always available electronic states to which the free impinging electron can couple and through which a SE can escape.

4.1.3 Cu(100) vs. Cu(111) vs. Poly Cu: LE-TEY

A further example of the relevance of the unoccupied BS of solids to the TEY is shown in this section, by the inter-comparison of LE-TEY curves acquired from two single crystalline surfaces of Cu and their polycrystalline equivalent.

Panels (a.) and (b.) of figure 4.7 show two LE-TEY curves acquired on the Cu(100) and Cu(111) surfaces, respectively. Measurements were carried out under normal impingement of electrons up to a landing energy of 50 eV. The E-structure shown in panel (a.) exhibits a high

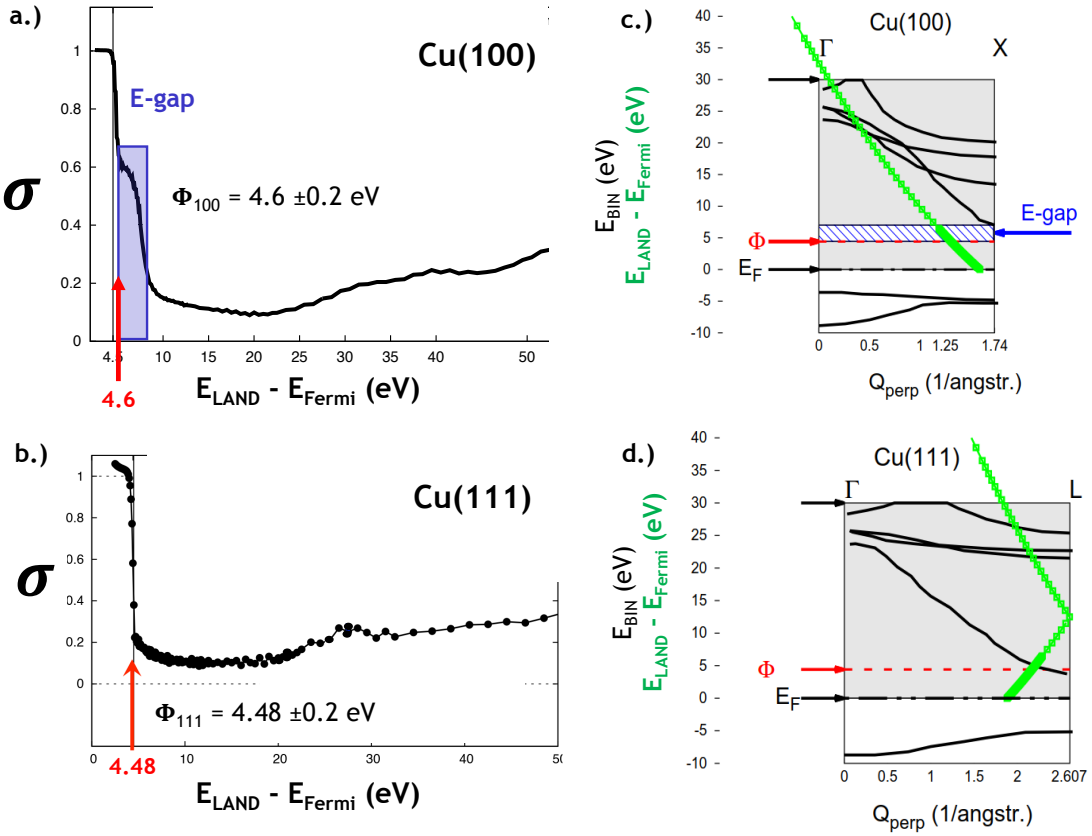

Figure 4.7: Panels (a.) and (b.) : LE-TEY curves acquired under normal incidence from Cu(100) and Cu(111), respectively. Panels (c.) and (d.) display the crystalline symmetry directions of ΓX for Cu(100) and ΓL for the Cu(111)-surface. For Cu(100), the rise in σ just above the Fermi level (highlighted in blue) is linked to the presence of an E-gap right above Φ along the ΓX-direction. Green curves in panels (c.) and (d.) represent regions in phase-space sampled during the respective measurements.

σ-value reaching 0.8 for a landing energy range going from 4.6 eV up to ca. 8 eV (highlighted by the blue rectangle). This rise in σ is linked to the presence of a small E-gap opening right above the vacuum level along the ΓX-crystallographic direction. Panel (c.) of figure 4.7 displays the unoccupied BS of Cu(100) where the mentioned forbidden region is equivalently marked in

blue. Whereas, in the conduction bands for the Cu(111)-surface, given along the correspondent ΓL-direction in panel (d.) an E-gap at opens up at Fermi and extends up to Φ. This gap is situated below vacuum level in the ΓL-direction, hence it does not affect σ as it does in the case of the ΓX-direction. A further narrow E-gap is visible around 25 – 27 eV (highlighted also in panel (c.) in fig.4.8). The LE-TEY curve measured on this crystalline direction exhibits only some mild E-structure coinciding with the mentioned energy range, corresponding to the gap.

The first derivative of the σ measured along this crystalline direction yields a value for the workfunction of ca. 4.48 eV, which according to the Handbook of Chemistry and Physics [228] is closer to the value assessed for the (112)-symmetry direction (with 4.53 eV) than to the one given for Cu(111), which would be 4.94 eV. For the case of the Cu(100)-surface, due to the presence

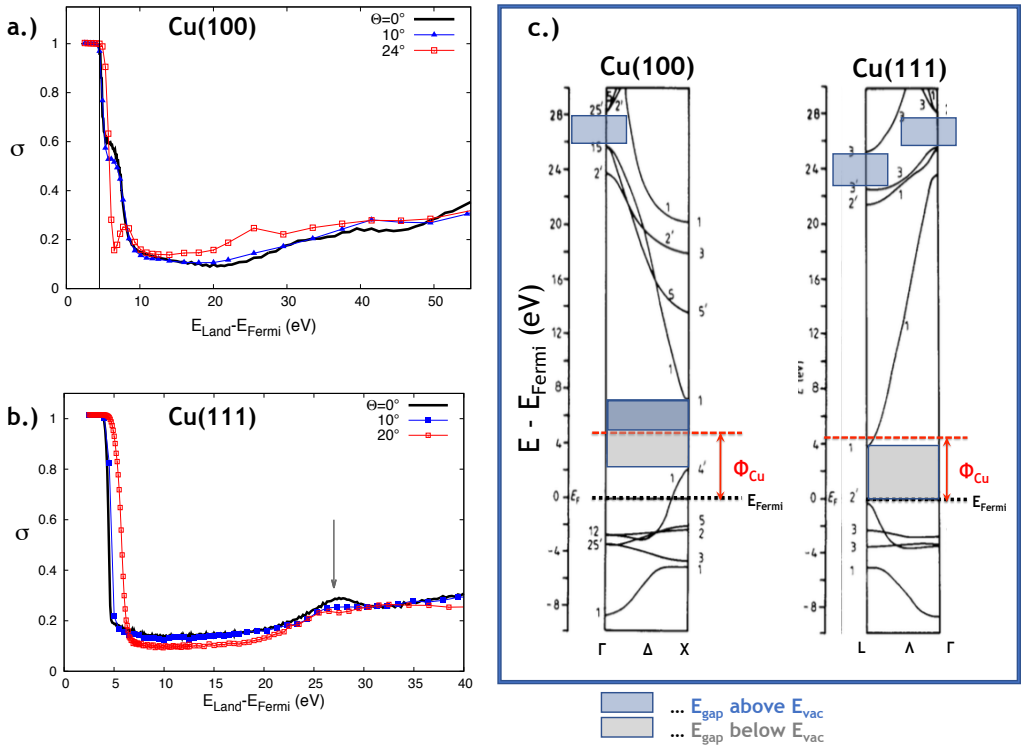

Figure 4.8: (a.) and (b.) : incidence angle-dependent LE-TEY measurements from Cu(100) and Cu(111). Panel (c.) depicts the band structures along the two relevant symmetry directions (extracted from Ref.[250]). Regions in phase-space highlighting E-gaps are shown as blue rectangles.

of the E-gap opening up just above E_{vac}, it is more difficult to measure Φ using the derivative method. On the other hand, by means of this method, we found for this surface a Φ of ca. 4.6 eV which in this case corresponds exactly to the value reported in Ref. [228]. This may confirm the validity of the procedure adopted for the "reading" of the workfunction.

Green curves plotted on top of both BS of panels (c.) and (d.) represent the calculated (E_{eff}; $k_{\perp}$) for the landing energy scans shown in panels (a.) and (b.) of the same figure. These green curves highlight the sampled regions in phase-space along pertinent symmetry directions, as explained for the case of HOPG in subsection 4.1.1).

Both LE-TEY exhibit some further mild features at E_{Land} - E_{Fermi} of ca. 27 eV. This subtle rise in yield can be understood when looking at the green curves in panels (c.) and (d.) of fig. 4.7. At these landing energies the impinging electron assumes $k_{\perp}$-values that correspond to regions in the given crystalline directions exhibiting some small gaps (highlighted by blue rectangles in panel (c.) of figure 4.8, where it is easier to recognise them). Therefore, in this case the rise of σ visible for both curves around 27 eV is given again by a rise in η.

The variation in shape and intensity of the above-mentioned E-structures observed in angle-dependent LE-TEY curves, shown in figure 4.8 (a.) and (b.), offer additional support for the validity of this interpretation. Panels (a.) and (b.) show for each single crystalline surface three LE-TEY curves acquired at increasing incident angle θ_{in}. Similarly to panel (c.) and (d.) of figure 4.7, panel (c.) in this figure reports once more BS in the the symmetry directions of ΓX and ΓL as extracted from Ref. [250].

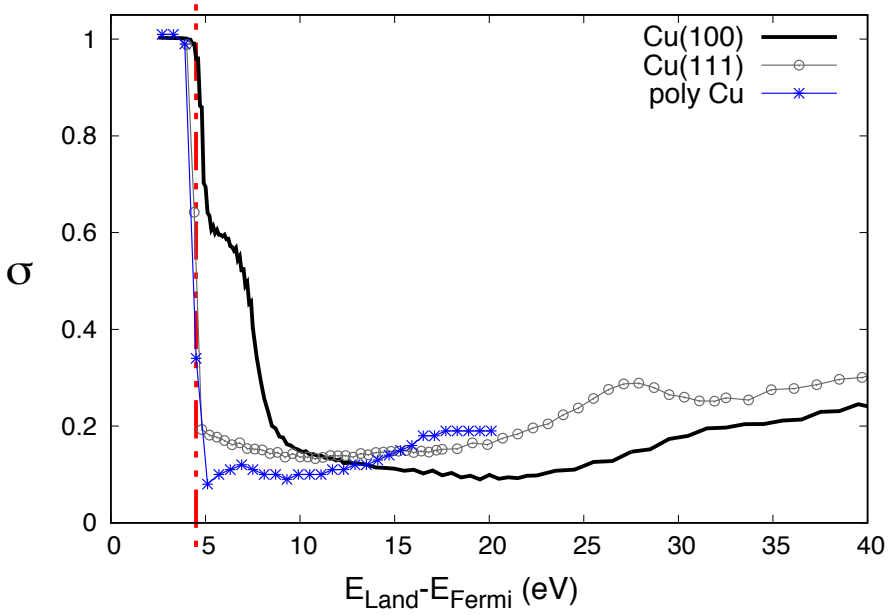

Figure 4.9: LE-TEY curves from three Copper surfaces exhibiting different long-range orders: Cu(100) given as black solid line, Cu(111) (grey line with open circles) and polycrystalline Cu (blue starred line). Apart from the expected different structures observed between the two single crystalline surfaces, also the polycrystalline surface exhibits slight modulations.

Some of the E-structure are diminished in intensity as the perpendicular component of the momentum varies (shrinks at expenses of an increasing $k_{\parallel}$). This is the case for the feature in Cu(100) associated to the E-gap above vacuum level. While for increasing θ_{in}, the red LE-TEY curve measured at 24° on the (100) surface exhibits the appearance of a new E-structure around 22 eV.

For the Cu(111) sample instead, in spite of mild intensity variations, the structure at 27 eV ca. persists at all angles. This is still associated to the presence of the small E-gap (around 27 eV) along the ΓL-direction.

One last inter-comparison is shown for normal incidence in fig. 4.9, where the σ from both

single crystalline Copper surfaces is plotted along with the one measured on the polycrystalline exemplar (blue starred curve). In spite of the fact that the polycrystalline surface exhibit a band structure averaged over all available crystalline directions, subtle features appearing in the LE-TEY curve nonetheless suggest the presence of a preferential crystalline direction.

In fact, the blue poly Cu LE-TEY curve displays a mild rise in σ in correspondence of the landing energy interval comprised between 5 eV and 10 eV. The presence of such small feature in the energy structure could be connected with the E-gap opening above E_{vac} observed for the Cu(100)-crystal.

4.2 Double-Differential Information via LEED, Ar-REELS and Ar-SEES

Electron spectroscopy techniques that employ electrons as well as probe as scattered signal are routinely employed to obtain information on the elemental composition, on the geometric structure of solid surfaces and to investigate electronic and optical properties of materials. In particular, owing to their short inelastic mean free path (IMFP) low energy electrons are ideally suited to sample near-surface regions in a solid. For example, 50 eV-primary electrons can travel only over very short distances ($\sim$ 5–10Å) in a solid before undergoing an inelastic collision. For this reason,in this LE-range, electron scattering measurements of the elastically scattered electrons are highly surface sensitive and permit to investigate the 2D-crystalline structure of a target. Moreover, for low kinetic energies, the de Broglie wavelength of electrons becomes of the same order of typical inter-atomic distances in crystals, thus diffraction phenomena are expected and routinely exploited to determine the crystalline order.

As already mentioned at the beginning of this chapter, these electron spectroscopy techniques deliver a doubly-differential information on electron scattering in solid surfaces. The measured flux-density is given as a function of the electron energy and of the detection angle. Depending on the choice of the energy range, the measured electron signal can yield different types of information on the same target. If the electron signal is composed of the sole elastically back-scattered electrons, as done in Low Energy Electron Diffraction (LEED), it is possible to obtain information on the geometrical arrangement of the target. If the detected electron energy is in the energy loss range of an electron spectrum, as done in Reflection Electron Energy Loss Spectroscopy (REELS), it is possible to investigate the electronic structure of a specimen and information on the available excitation channels (e.g. JDoS, plasmons, phonons, etc..) can be gathered. While to study the distribution of the low energetic ejected electrons, Secondary Electron Emission Spectroscopy (SEES) delivers the 2DCS of choice.

4.2.1 Low-Energy Electron Diffraction (LEED)

Owing to their surface sensitivity and to their de Broglie wave length, LEEs are exploited in surface crystallography. The "classical" LEED experiment is performed by bombarding the target under normal incidence with a monochromatic electron beam and detecting only the elastically scattered electrons. The main purpose of such a measurement is to learn about the crystalline structure of the target from the inspection of the surface diffraction pattern. These LEED patterns give information about the surface symmetry and periodicities and about the surface quality.

In this work, the acquisition of diffraction patterns was principally done to inspect the quality of the surface preparation and to determine the crystalline order and the accessible symmetry directions. The main purpose of this analysis was intended to assess the optimal target position in order to obtain the desired scattering conditions for subsequent electron spectroscopy measurements, e.g. Ar-REELS and (e,2e)-coincidence measurements. For this purpose, LEED-scans were performed (e.g. tuned on the ELP or alternatively to a kinetic energy corresponding to a characteristic ΔE such as a plasmon), for an unvaried azimuthal rotation (with $\varphi = const.$) while the scattered electrons were detected under a varying polar angle, θ (achieved by rotating the manipulator axis during the measurements). This type of LEED-scans are also known in short as *"rocking curves"*. Analysis of these LEED-scans is performed in exactly the same way as in a "classical" LEED experiment. The Bragg conditions dictate the diffraction conditions for a two-dimensional lattice.

$$\Delta\vec{K}_{\parallel} = \left(\vec{k}_{s,\parallel} - \vec{k}_{0,\parallel}\right) = \vec{G}_{\parallel} \tag{4.14}$$

Here $\vec{k}_{0,\parallel}$ and $\vec{k}_{s,\parallel}$ are the in-plane components of the momenta of the incoming (subscript "0") and scattered (subscript "s") electrons, respectively and $\vec{G}_{\parallel}$ is the surface reciprocal lattice vector. In elastic scattering (i.e. for the ELP with $E_0 = E_s$) the magnitude of the incident and scattered wave vectors must be equal, $|\vec{k}_{0,\parallel}| = |\vec{k}_{s,\parallel}|$ and they can be obtained as follows:

$$|\vec{k}_{0,s}| = \frac{1}{a_0} \cdot \sqrt{\frac{2\,E_{0,s}}{E_h}} \tag{4.15}$$

with a_0 being the Bohr-radius expressed in Å and E_h the Hartree energy in eV. Hence, the momentum vector in eq. (4.15) is given in units of reciprocal Ångstroms. Knowing the incident and emission angles θ_{in} and θ_{out} of the experimental scan, it is possible to calculate $\Delta\vec{K}_{\parallel}$ and thus to determine the crystalline direction (associated to a specific $\vec{G}_{\parallel}$) contributing to the diffusion of the scattered electrons. This is easily obtained by:

$$|\Delta\vec{K}_{\parallel}| = |\vec{k}_{0,s}| \cdot \{\sin\theta_{in} - \sin\theta_{out}\} = |\vec{G}_{\parallel}| \tag{4.16}$$

Another widely used application of LEED consists in the quantitative structure determination.

This is done by measuring the diffraction intensities as a function of the primary energy, while keeping the incident/outgoing polar angles unvaried.

Measurements like this are knowns as "I-V-curves", where the intensity is plotted vs. the kinetic energy (or equivalently the accelerating voltage) of the source electrons. In this case, by varying the primary electron energy, impinging electrons undergo refraction and have to fulfil the third Bragg condition, $k_{s,\perp} - k_{0,\perp} = G_\perp$ for the perpendicular component of the electron momentum. Differently from LEED, where the exchanged momentum $\Delta\vec{K}_\parallel$ is conserved, in an I-V-curve the considered perpendicular component of the momentum is *not* conserved when the electron travels from vacuum to the solid and vice versa. Such I-V-curves are composed of a series of Bragg-diffraction peaks exhibiting very strong intensity variations as a function of the primary energy, E_0. To explain the position of these intensity maxima it is necessary to account for refraction due to the barrier potential encountered at the surface-vacuum interface.

This potential barrier, known as inner potential, U_{in} – generally of the order 10–16 eV – make the kinetic energy of impinging electrons systematically higher inside the solid than outside. This also induce electrons to have a different direction (and angle wrt. surf. norm.) inside the crystal from the one they had outside.

In order to maximise the intensity during a measurement, it is useful to select a primary energy for which, at the chosen scattering geometry, the Bragg-peak intensity is maximal. In this work, after having selected the desired scattering conditions, the primary energy of the electron source was always tuned according to this Bragg law (also explained in Ref. [195]). After having determined at which primary energy the subsequent measurements were to be performed a series of LEED-scans (as explained previously) were conducted to determine the surface orientation. In the following a couple of examples for such LEED-scans are discussed for the case of HOPG and Al(100).

4.2.2 Angle-Resolved Reflection Electron Energy Loss Spectroscopy (Ar-REELS)

Exposing a specimen to a nearly monochromatic electron source, due to the Coulomb interaction with the ionic and electronic subsystems in the target, some electrons will undergo inelastic scattering, loosing a certain amount of energy to the electronic subsystem (and to the lattice, via phonons) and in the former case their trajectories are generally deflected in a forward direction (enclosing a small scattering angle with its original direction). Due to energy conservation, the energy lost during the beam-specimen-interaction is redistributed over the available degrees of freedom of the target thus yielding a characteristic energy distribution of the irradiated material. After each inelastic event the scattered electrons are detected by a spectrometer under a given direction and their kinetic energy, or equivalently the energy loss undergone by the primary electron, is recorded. The complete energy distribution of all these inelastically scattered electrons yields the Electron Energy Loss Spectrum (EELS).

EELS can be performed either in transmission (T) or in reflection (R) mode. In this work, only the latter was used. R-EELS contains characteristic spectral features corresponding to discrete energy losses of the reflected electrons due to excitation of plasmons[3] and provides information on the electronic and crystal structures of a specimen.

Plasmon peaks dominate the low-loss region in an energy loss spectrum. In materials with free valence electrons, plasmon excitations represent the most frequent scattering process. These characteristic spectral features arise as the valence electrons absorb energy (of the order between 5 eV and 30 eV, i.e. approximately 1 Hartree) from the incident electrons, where the energy transferred during the collision resonates at the frequency of these charge oscillation, i.e. plasmon wake. Generally, the plasmon-lifetime is very short (of the order of femtoseconds) and its inversely proportional to their line-width. The narrower the plasmon peak, hence its line-width, the longer lived its excitation. De-excitation mostly occurs in form of inter-band transitions ultimately leading to the ejection of a solid-state electron, provided that their energy suffice to overcome the surface barrier, or alternatively via heat. In the low-loss region of an EELS, in addition to the characteristic plasmon resonances, inter-band transitions may appear as additional peaks, which can also superimpose on the plasmon peaks. These additional loss channel represents a single electron excitation, wherein the electron undergoes a direct transition from the valence band to a discrete energy level in the unoccupied conduction band. Hence the differential cross section describing the scattering probability in EELS must be differentiated upon the energy (loss), thus

[3] Vibrational modes and phonons can be also excited, however the energy resolutions achieved in our experiments do not suffice to resolve these latter mentioned features. Furthermore, these are not of the general interest for the remainder of this thesis project.

becoming a double-differential cross section, as previously defined in (4.3) [50].

$$\frac{d^2\,\sigma}{d\Omega\,d(\Delta E)} = \frac{k_s}{k_0}\left(\frac{2\,m\,e^2}{\hbar\,\Delta K^2}\right)^2 \sum_s \mid \langle \Psi_s \mid \sum_{i=1}^{N} \exp\left[i\,\Delta\vec{K}\cdot\vec{r}_i\right] \mid \Psi_0\rangle \mid^2 \delta\left(E_0 + \Delta E - E_s\right) \quad (4.17)$$

As usual the subscripts "0" and "s" stand for "incident" and "scattered", respectively. $\Delta\vec{K} = (\vec{k}_0 - \vec{k}_s)$ is the momentum transfer and the square of the magnitude of the transition-matrix – containing the density-fluctuation operator, $e^{i\,\Delta\vec{K}\cdot\vec{r}_i}$, acting on the initial state $\mid \Psi_0\rangle$ leading to the final state $\mid \Psi_s\rangle$ – is also known as form factor. The delta-function incorporates energy conservation. Other symbols have their usual meaning.

An alternative way to derive the 2DCS is to use the wave vector and frequency dependent dielectric constant of the material, $\epsilon(\vec{q},\omega)$. All optical properties of a material are included in the dielectric function, thus, in this semi-classical picture, the 2DCS becomes [50]:

$$\frac{d^2\,\sigma}{d\Omega\,d(\Delta E)} \approx \frac{1}{\pi\,a_0\,m_e\,v^2\,N}\,Im\left[\frac{-1}{\epsilon(\vec{q},\omega)}\right]\frac{1}{\theta^2 + {\theta_E}^2} \quad (4.18)$$

where N represents the density of the specific element in the target and $Im\left[{}^{-1}/_{\epsilon(\vec{q},\omega)}\right]$ is the imaginary part of the dielectric function, also known as Energy Loss Function (ELF), which completely describes the response of a material during an inelastic collision.

During the acquisition of an energy loss spectrum, the target is bombarded by a primary beam of E_0 energy under a given scattering geometry – which determines both the incident and emission angles, (θ_{in}, θ_{out}) and consequently the momentum transfer, $\Delta\vec{K}$, occurring during the collision. The energy at the spectrometer scans over the E_s energy range of interest collecting all scattered electrons, which have undergone a certain energy loss, ΔE.

The electron spectrum reflects the energy distribution of all electrons that have suffered a given number of energy losses under a specific kinematics. For a specific pair of $(\Delta E, \Delta\vec{K})$ a multitude of single electron excitation (inter-band transitions) and collective modes can occur from the valence band to the unoccupied conduction band, where initial and final states are discrete. Therefore the EELS cross section reflects the so-called Joint Density of States (JDoS).

Figure 4.10 illustrates in essence which type of information is accessible by means of (R)EELS. Panels (a.) and (b.) are REELS from HOPG acquired along the two main in-plane symmetry direction of ΓM and ΓK. All spectra exhibit the characteristic energy losses associated to the $(\pi - \pi^*)$-transition (also known as π-plasmon) at ΔE=6 eV ca. and to the so-called $(\pi + \sigma)$-plasmon with ΔE≈24-28 eV. However, their shapes and intensities strongly differ depending on the scattering geometry, which is selective in the crystalline direction and differs also depending on the overall kinematics. This strong variation in shape and intensity is an indication for the fact that for a very same ΔE, but for different kinematics, also different inter-band transitions will be accessible, thus reflecting the variations in shape and intensity. For example, for the energy

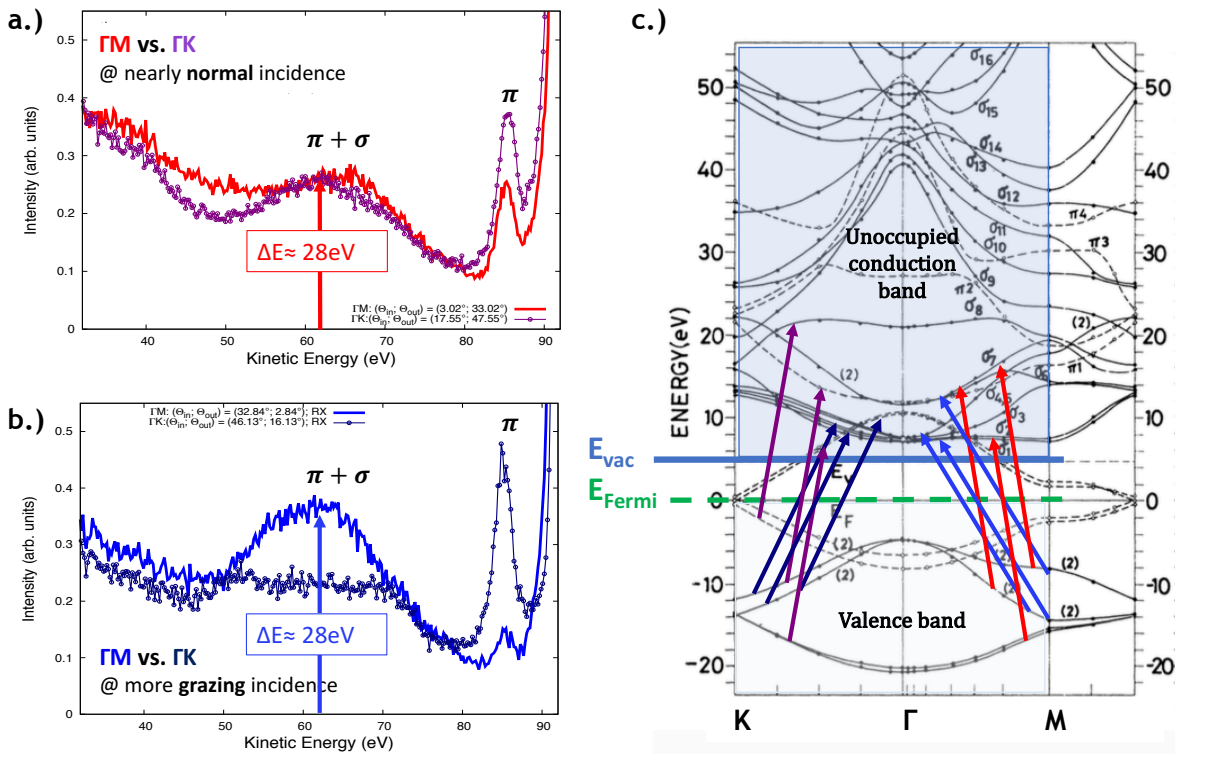

Figure 4.10: (a.) and (b.) : REELS from HOPG acquired along the two main crystallographic directions of ΓM and ΓK. The scattering conditions are indicated by the pair of incidence-emission angles given in each panel. REELS in (a.) were obtained at more normal incidence with respect to those shown in panel (b.). Characteristic π- and $(\pi + \sigma)$-plasmon peaks in graphite are indicated. The observed variation of both shape and intensity in all four REELS spectra is not only to be assigned to the anisotropy in the optical transitions of graphite [202], but can be due to interband transitions, which can appear (disappear) superimposed on the plasmon peaks. These interband transitions are a consequence of single particle excitations from the valence band to the unoccupied conduction band (shown in panel (c.) taken from Ref.[185]). Accordingly, features in REELS spectra reflect the so-called joint density of states (JDOS).

loss of ca. 28 eV, indicated by a red and blue arrow in panels (a.) and (b.), respectively, due to the different kinematics (determined by different pairs of incident-emission angles) a different manifold of inter-band transitions will be accessible.

Panel (c.) shows the occupied and unoccupied bands of Graphite along both crystalline symmetry directions. The differently coloured arrows are representative for some of the allowed inter-band transitions, which are accessible for the selected energy loss of 28 eV. Their colours recall the same colour code of the REELS in panels (a.) and (b.). The length of all arrows reflects the magnitude of the energy loss. The inclination of each arrow reflects the momentum transfer occurring during the transition. The spectral intensity measured at a selected energy loss is composed of all possible combinations for inter-band transitions occurring between the valence and conduction band, as illustrated by the arrows.

In this work, the series of Ar-REELS shown in the next sections were primarily acquired with the sole aim to determine the optimal scattering conditions for setting up an (e,2e)-coincidence

measurement. Especially in case of HOPG a rather extensive acquisition of REELS is presented, however no detailed analysis of the spectra was undertaken since this was not the principal aim within the framework of this thesis.

4.2.3 Angle-Resolved Secondary Electron Emission Spectroscopy (Ar-SEES)

It is well accepted that for polycrystalline and amorphous targets the angular distribution of SEs follows approximately a cosine distribution and is nearly independent of the incidence angle of the primary electrons [88]. Under the assumption that excited electrons are herewith isotropically distributed, the number of effectively emitted SEs depends on what fraction of the internally excited electrons are directed in such a way thus to be able to surmount the surface barrier. The potential barrier at a solid-vacuum interface controls the final shape of the SE energy distribution [251].

This is determined by the so-called *"escape cone"* which defines a conical region inside the sample from which the generated SEs can escape into vacuum. Only then when the perpendicular component of their momentum ($\vec{k}_{\perp}$) is greater that the momentum corresponding to the barrier height, which is this case given by the inner potential, U_{in} these electrons can overcome the surface barrier and escape over E_{vac} [252].

The typical shape of a SEES (in a polycrystalline material) is given by a smooth featureless asymmetric peak, exhibiting its maximum in an energy range generally comprised between 3-7 eV. The cut-off at its low-energy side is determined by the escape cone. In these cases, the band structure of the target is generally neglected, or better to say it is averaged out over all possible symmetry directions, since the material is polycrystalline.

In single-crystalline surfaces the angular distribution of SEs can exhibit anisotropy [7], since the unoccupied energy bands of the crystal manifest a well-defined structure comprehending allowed and forbidden regions (E-gaps). Only when the availability of an energy band is granted a SE can escape via this band, otherwise, in presence of an energy gap, there is no escape channel at disposal. In such a material, of which e.g. HOPG is a representative candidate, the typical bland shape of a SE-spectrum is instead superimposed with a multitude of distinct peaks, which are characteristic for these available unoccupied bands through which a SE – with a given pair of well-defined energy, E_e and momentum $\vec{k}_e$ – manages to escape. This means that when the secondary electron escapes via such unoccupied band, its energy and momentum will correspond exactly to the binding energy ε_{bin} and associated momentum $\vec{q}$ for the empty electron band in the unoccupied state. Hence, these SEs deliver information on these unoccupied bands. In such cases, the unoccupied band structure additionally modulates the SE-peak leading to the formation of a fine structure, which superimposes on the smooth background of the SEES.

This is for instance the case in Graphite and HOPG, of which an example is shown in panel (a.) of figure 4.11. The series of SEES was acquired at different emission angles (θ_{out}, as indicated in the legend). Shape and intensity strongly vary in dependence of the emission angle. A series of rather sharp peaks superimposed on the typical bland SE-peak are visible at specific kinetic energies. These distinct spectral features are interconnected to specific unoccupied bands in the conduction band of HOPG which are accessible under a given emission angle.

In fact, angle-resolved secondary-electron emission spectroscopy (Ar-SEES) represents a way to obtain direct information on the unoccupied band structure of solids. Alternative techniques exploited for the same purpose are inverse photo-emission spectroscopy (IPES) and target current spectroscopy (TCS) [193, 186, 103].

In order to reach a full understanding of the electronic properties of solids it is also mandatory to study the unoccupied band structure of materials. Therefore Ar-SEES represent a useful tool for their investigation. In Ar-SEES the energy of electrons emitted from the surface with certain energy and angle relative to the sample surface are measured. Direct information on the unoccupied band structure is obtained, because these SEs are supposed to have been situated on the conduction (unoccupied) band just before they escape from the surface into vacuum. Thus, Ar-SEES gives momentum-resolved information on unoccupied states. However, by means of

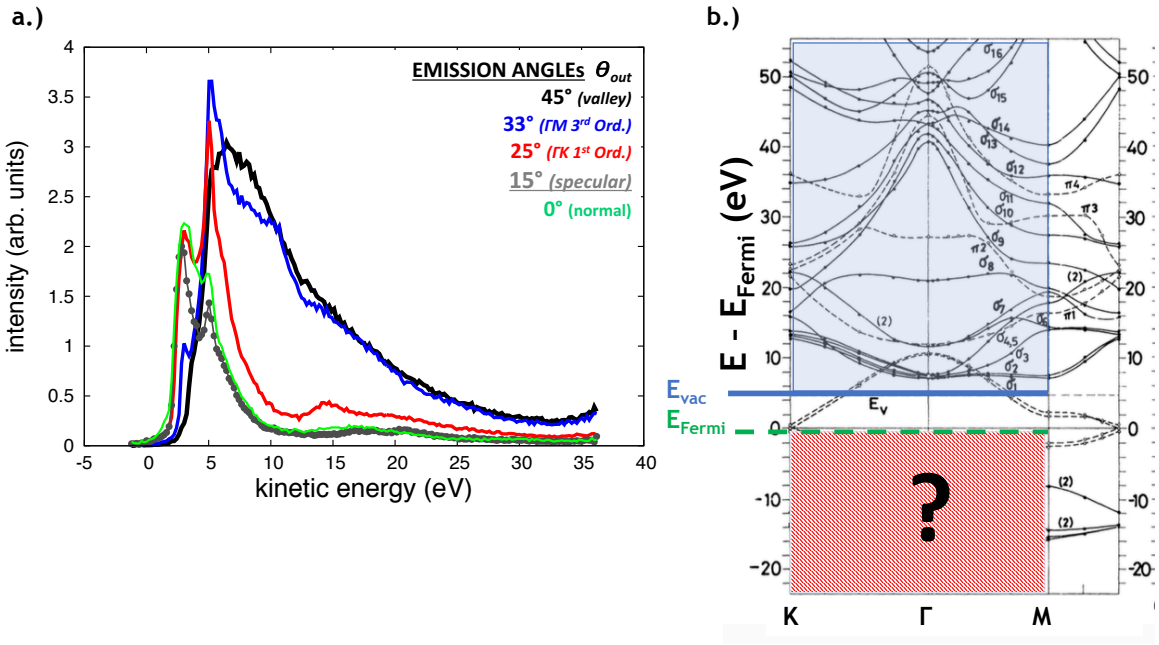

Figure 4.11: (a.) Series of Ar-SEES from HOPG acquired with the R66-analyser (equipped with the electron optical elements tuned for the high-transmission mode). panel (b.) serves to illustrate the obtainable information by this spectroscopic technique. Knowledge on the unoccupied BS is accessible, however no information on the initial state can be directly retrieved by Ar-SEES.

Ar-SEES no information on the origin, i.e. on the initial state, of the ejected electron prior to its excitation to the empty band can be obtained. This is symbolised by panel (b.) in figure 4.11, where the valence band region is obscured by a question mark.

Most of the SE-spectra presented in the following were acquired with the sole scope to determine the transmission of SEs under a given kinematics during a coincidence experiment. In some cases the SEES were re-corrected for the transmission function and their shape was compared to SE-spectra from literature and to other experimental spectra acquired with different settings for the electron optical element. Hence, also in case of Ar-SEES detailed analysis was neither aimed nor performed within the framework of this thesis.

4.2.4 HOPG: Ar-REELS

A series of Angle-resolved Reflection Electron Energy Loss Spectra (Ar-REELS) of HOPG were acquired using 91.7 eV-primary electrons and scanning the kinetic energy of the scattered electron from 30 eV up to the elastic peak (ELP). The series of measurements was conducted using the R66-analyser operated in the HR-mode and for which specular reflection conditions are obtained at 15°. All Ar-REELS from this series are documented in the appendix A.

It is a well-known fact that pyrolytic Graphite exhibits a strong anisotropy in its dielectric function $\epsilon(\omega, \vec{q})$ [202, 188]. This anisotropy manifests itself in electron spectra associated with excitation of the occupied (valence) band, when transitions between this bonding band and the unoccupied conduction band occur according to distinct selection rules. Depending on the orientation of the electric field polarisation vector ($\vec{E}$) – if the experiments are done using photons – or alternatively, depending on the orientation of the momentum transfer ($\Delta\vec{K}$) – in electron scattering experiments – with respect to the $\hat{c}$-axis, only certain inter-band transitions are allowed. For example, if ($\vec{E} \parallel \hat{c}$) then only $\pi \rightarrow \sigma^*$ and $\sigma \rightarrow \pi^*$ are allowed transitions, whereas for the case ($\vec{E} \perp \hat{c}$) only transitions of symmetric type are allowed, meaning that π-electrons can only escape over π^*-bands and that further only ($\sigma \rightarrow \sigma^*$)-transitions are allowed. When the orientation of the polarisation vector or of the momentum transfer are in-between these two orientations, a mixture of possible transitions is then accessible. Due to these selection rules, the shape and intensity of electron energy loss spectra (EELS) may strongly vary upon the orientation of the momentum transfer, $\Delta\vec{K}$ with respect to the crystalline $\hat{c}$-axis. Therefore, to quantitatively interpret the various spectral features appearing in Ar-REELS it is necessary to account for the anisotropy of ϵ and to properly associate these oscillator strengths to specific (allowed) inter-band transitions, whose probability varies with the orientation of the transferred momentum (wrt. the $\hat{c}$-axis). One example for the variation of intensity and shape of the relevant spectral features in a Ar-REELS is given in figure A.8b, which shows a pair of REELS each one acquired on the first order diffraction peaks given along the ΓK (navy blue with circles) and along the ΓM symmetry direction (blue thick line). Their pair of $(\theta_{in}, \theta_{out})$ angles is shown in the legend. The most prominent spectral features visible in these two spectra are likely to be linked to well-known plasmon losses in Graphite and HOPG. The characteristic energy loss of a so-called π-plasmon (alternatively known also as $(\pi - \pi^*)$-transition) can be identified at the kinetic energies of ca. 86 eV (corresponding to a $\Delta\mathrm{E} \simeq 6\,\mathrm{eV}$). Whereas, a broad peak centred around 62 eV is presumably linked to the characteristic loss of the $(\pi + \sigma)$-plasmon. Both peaks drastically vary in shape and intensity when the parallel component of the momentum transfer projected onto the surface is changed by the scattering geometry. This behaviour strongly suggests that when the $\Delta\vec{K}_{\parallel}$ component is changed, different electronic bands contribute to the REELS cross-section, which is modulated by the JDoS and the selection rules allowing or forbidding certain transitions.

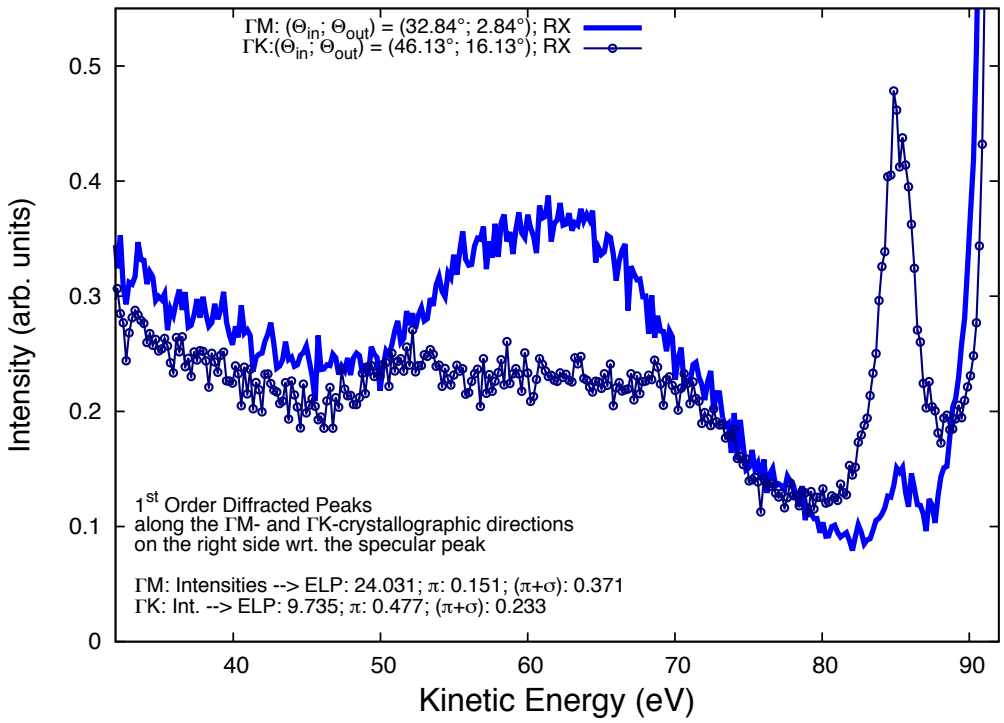

Figure 4.12: Comparison btw. REELS acquired on the RX-sided first order diffraction peaks along ΓK (ID No. 19) andΓM (ID No. 17) directions.

4.2.5 HOPG: Ar-SEES

The secondary electron spectrum of Graphite and its highly-oriented surface exhibits a richness of characteristic spectral features. This has been already observed in the past by many authors [190, 191, 186, 103, 194]. The incident electrons undergo a series of inelastic scattering processes and the electrons falling in the conduction band (above vacuum level) are emitted from the surface with unvaried energy and momentum. Hence, the characteristic features seen in SEES reflect the DoS of the unoccupied (conduction) electronic bands. For this reason, in case of Graphite, the acquisition of SEES has been exploited in the past to map the conduction band as alternative method to inverse photo-emission spectroscopy (IPES) or target current spectroscopy (TCS).

The peaks and shoulders visible at ca. 4–5 eV and 9 eV as well as the shoulder around 17 eV and 22 eV correspond to spectral features, which were also observed by the above-mentioned authors. The presence of these features confirms the reliability of our SE-spectra (automatically excluding any possible instrumental artefacts) and it also demonstrates the effectiveness of the adopted strategy applied to correct the shape and intensity of SEES, by means of which relevant spectral features of HOPG become evidently recognisable. Furthermore, in their works, all the mentioned authors also report on a very sharp peak somewhere around 2–3 eV, which does not

show any angular dependence in its energy position. This peak is also recognisable in most of the spectra (also independently from the scattering geometry) presented in this section. Pisarra *et al.* [204] (among others [203]) state that through a combination of even symmetry states in the unoccupied BS of graphite so-the called *interlayer* band (identifiable with regions of strongly localised higher DoS) can be generated, while odd symmetry states are responsible for the formation of *surface* states[4]. The low-lying peak in the SEES of figure 4.13 (a.) and (b.) appears around 2–3 eV, which would match fairly well with the calculation performed by Pisarra *et al.* of the nearly non-dispersing empty band corresponding to the *interlayer* states in the ΓKM-symmetry direction (see also sub-section 3.2.1).

The acquisition of the series of SEES at varying sample bias demonstrated that to be able to observe all real spectral features of the HOPG spectrum it is advisable to apply a small negative bias of -2 V. This helps to shift the whole SE-spectrum towards higher kinetic energies, without distorting its original shape (which is kept nearly constant also at higher negative potentials), but ensuring that all relevant real spectral features are detected.

A series of Ar-SEES from HOPG was acquired for 91.7 eV-primary electrons, at a constant sample bias of -2 V, under the same geometrical settings (pairs of incidence-emission angles) as those used to measure the corresponding Ar-REELS series presented in the previous subsection 4.2.4. Some of the acquired spectra are shown in panels (a.) and (b.) of figure 4.13. All spectra were plotted with their original intensities (no normalisation procedure was undertaken) to monitor its variation in dependence of the scattering geometry. Also in this case, no detailed analysis of any spectral feature was performed, since it did not represent the main aim of this work.

Numerous structures superimposed over the "typical" SE-peak appear (and disappear) at specific angular combinations. Panel (b.) contains several Ar-SEES in which a small peak appears around 12 eV. The energy position of this peak exhibits a relatively evident angular dependence. Changes in energy and intensity are expected in dependence of variation of the polar angle, since these spectral changes directly reflect the unoccupied band structure. By varying the angle of incidence and emission under which the SEES is acquired, different inter-band transitions and herewith different unoccupied bands will be inquired during the experiment. The background of the SE-peak can also vary in dependence of the angles since this background is linked directly to SEs populating the unoccupied electronic bands.

Other authors [186, 103], who conducted a series of Ar-SEES to map the unoccupied band structure of HOPG not only report on the strong angular dependence of the energy positions and intensity of some spectral features, but also report on prominent energy dispersions in dependence of specific electronic bands of different characters (π or σ).

[4]Presumably these surface states are the ones responsible for the fact that in the LE-TEY measurement of HOPG, shown previously in fig. 4.3, the TEY-value within the large E-gap around 10 eV above E_{Fermi} does not go back to unity. Due to the existence of surface states the wave-function of the free impinging electron then manages to couple with the Bloch-waves of these high-density surface states, thus penetrating into the solid.

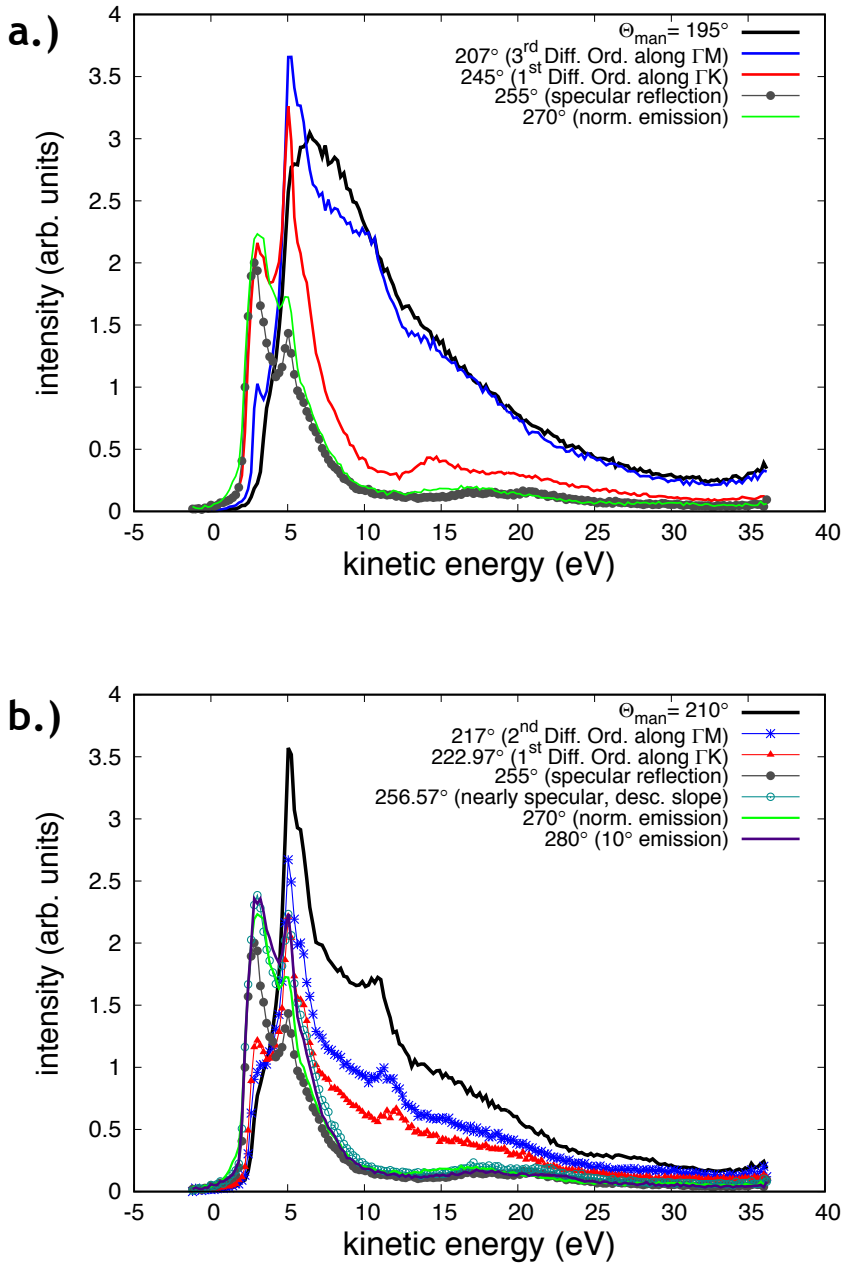

Figure 4.13: Series of Ar-SEES from HOPG acquired with R66 at various scattering geometries (see legend) using 91 eV-primary electrons. Small structures around 10–20 eV in these ARSEES spectra exhibit some angular dependence in the energy positions and intensities, probably due to the effect of the energy dispersions in unoccupied states. The spectral peak around 2 eV is nearly independent from the scattering angle, which suggests that this ejected SE might escape through a strongly localised (non-dispersing) energy band, which leads to believe that his peak might be connected to the so-called *interlayer* state of graphite [204].

4.3 Triple-Differential Information via (e,2e) Coincidence Spectroscopy

Triple-differential cross-sections from HOPG and Aluminium are discussed in the following. These (e,2e)-coincidence measurements have been conceived to investigate the mechanisms underlying the excitation-ejection process of SEs in the LE-regime. Therefore, experiments were conducted for low incident energies ranging between 50 – 100 eV ca.

To guide the reader through the sequence of experimental results, a summarising preamble entailing all relevant notions to (e,2e)-coincidence spectroscopy is given here below. For a more comprehensive picture and for further details, please refer to sections 2.3 and 2.4 for the theoretical fundamentals, and to subsections 3.3.3 and 3.3.4 for the experimental details.

One of the main objective of this series of experiments is to make connection between features in the ELS to those measured in the SE-peak.

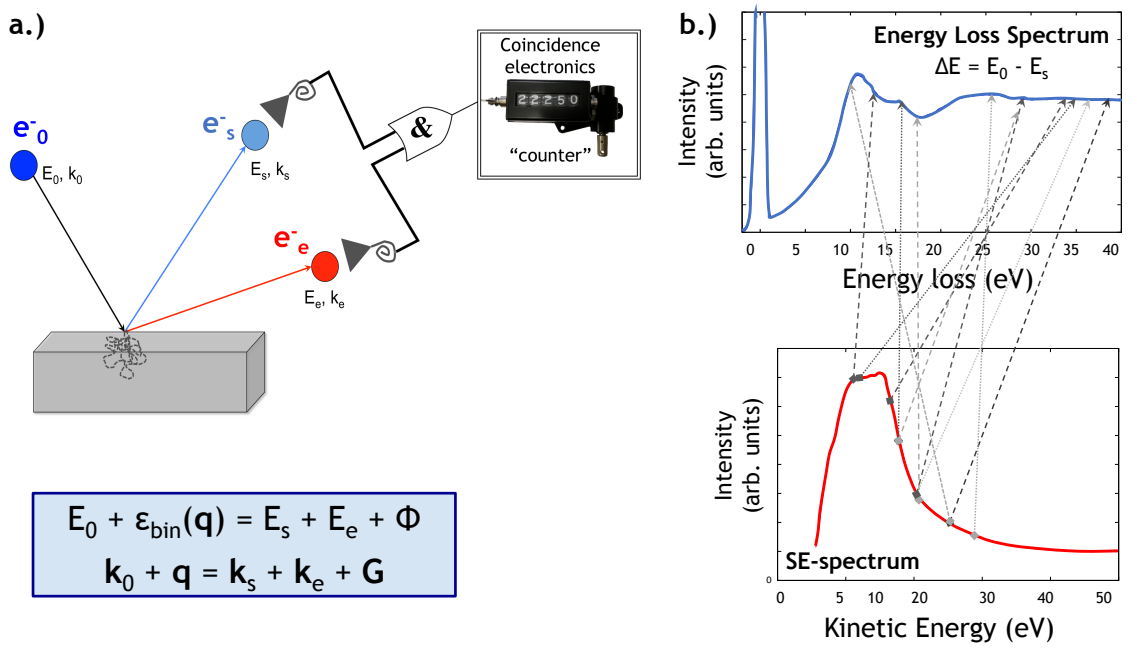

Figure 4.14: Scheme of principle of an (e,2e)-coincidence measurement. Panel (a.) depicts in a simplified way this *"one electron in–two electrons out"*- technique accompanied by energy and momentum conservation laws (blue box). Panel (b.) shows two double-differential electron spectra from poly Al: the ELS (blue on top) and the SEES (red at the bottom). Grey arrows connecting the SEES to the ELS shall symbolise, that a multitude of inelastic scattering processes occurring within the E-loss-range can give rise to a same secondary with a given and same kinetic energy.

Figure 4.14 schematically shows the principles upon which the (e,2e)-data acquired within this thesis are based. Panel (b.) of this figure shows two regions of the electron spectrum from a

polycrystalline Al sample. The plot on the top, gives in blue the energy loss range (ELS) of the spectrum extending from the elastic peak down to a ΔE of 40 eV. Noticeable spectral features in this ELS can be identified as two peaks in the single-scattering region, which correspond to the characteristic energy losses of a surface (at $\Delta E = \hbar\omega_s = 10.5\,eV$) and bulk (at $\Delta E = \hbar\omega_b = 15\,eV$) plasmons, respectively. For energy losses above ∼21 eV the plural and multiple scattering regimes are entered, wherein a plenitude of different scattering combinations can occur. The spectrum in red below is the SE-spectrum of poly Al, which extends from the workfunction up to 50 eV. Differently from the SE-spectra acquired from HOPG shown in subsection 4.2.5, the SE-peak of poly-crystalline Al is rather dull and exhibits only few mild features. A SE with a given kinetic energy, E_e, can be ejected as the result of a plenitude of inelastic scattering events and therefore it can be linked to any available energy loss process occurring in the ELS shown on the top. Or equivalently, a whole set of different inelastic scattering processes can give rise to a SE within the very same LE-range. The grey arrows connecting the two double-differential spectra serve to highlight this allegation.

By the sole study of the ELS or of the SEES, it is very difficult to assess to which extent a specific energy loss process contributes to the intensity in the SE-spectrum at a given kinetic energy. To investigate the underlying process linking these two electrons, it seems obvious that information from *both* scattering partners needs to be retrieved. To obtain the full picture of this collision dynamics, (e,2e)-coincidence experiments in reflection geometry are performed [253, 127] .

By collecting both electrons participating to a same collision – at the same side of the target and in coincidence – it becomes possible to correlate the excitation with the ejection event through the collision after accumulation of statistics for this electron pair (time histogram). The cartoon given in panel (a.) of figure 4.14 illustrates the principles of the scattering process. The incident primary (labelled ${e_0}^-$) impinges onto the target and as a result of its interaction with the solid-state electrons, it gets inelastically scattered, thus becoming ${e_s}^-$. Information on both the transferred energy and momentum during the collision can be retrieved by fixing both the initial and final states in the very same experiment. This transferred energy ($\Delta E = E_0 - E_s$) and momentum ($\Delta\vec{K} = \vec{k}_0 - \vec{k}_s$) are given to a bound electron, which is eventually emitted (labelled in red as ${e_e}^-$) if it acquires a kinetic energy sufficient to overcome the surface barrier (Φ). The selected electron pair is detected by a pair of energy analysers, each one of which is specifically tuned to the energy of either electron. Details on the instrumentation and measurement strategy employed for the acquisition of these TDCS are given in subsection 3.3.3. Upon selection of both the kinetic energy of the electron pair and of the scattering geometry under which the collision event is monitored, by means of energy and momentum balance, it is possible to reconstruct the complete ionisation process obtaining the full information on both initial and final states. Energy and momentum conservation were given in equations (2.3) and (2.4) of section 2.3 (as well as highlighted in the light-blue box at the bottom of panel (a.) in fig. 4.14). There momentum

conservation was separated into its components ($\parallel$ and $\perp$). In the following, energies are referred to the Fermi level.

The binding energy, ε_{bin}, as given here, is negative; subscripts 0, s, and e stand for the *"incident"*, *"scattered"* and *"ejected"* electrons. At the solid-vacuum interface, momentum conservation holds for its parallel components, whereas for the perpendicular component both refraction and the solid inner potential (U_{in}) must be taken into account.

The measured (e,2e)-yield represents the intensity distribution of selected correlated electron pairs. Since in the following experiments the aim is to link the generated secondary electron to the initiating scattering process, this (e,2e)-cross section describes the probability for a SE to be emitted in correspondence of a specific energy loss undergone by the PE under well-defined kinematics.

Precise selection of the kinematics can be achieved by planning experiments on well-ordered surfaces, where the coherent superposition of reflections via Bragg-scattering permits to investigate the crystalline structure of the target and to select a scattering geometry at which the component of the exchanged momentum ($\Delta\vec{K}_{\parallel}$) projected onto the surface matches specific crystalline symmetry directions. Owing to momentum conservation, determining the parallel component of the momentum transfer occurring during the interaction (where initial and final states are fixed) yields the in-plane momentum component of the bound electron ($\vec{q}_{\parallel}$) prior to its emission. Thus, for the recoil electron it is possible to fully determine from which band in the occupied DoS to which energy band in the unoccupied DoS it gets promoted in the course of this collision.

This tuning permits to explore specific regions within the Brillouin zone of the specimen. Hence, for different E_0 and a different scattering process, wherein ΔE and $\Delta\vec{K}$ are fixed, diverse regions in the BZ can be sampled, thus investigating the interaction-emission process also in dependence of the sampled band structure, i.e. as a function of the initial and final state of the recoil electron. This is demonstrated by experimental results discussed in the next sections.

The measured density-flux of coincident SEs can be therefore represented in different ways, depending on the aspect that is intended to be highlighted. (e,2e)-yields can be given as a function of ΔE and E_e or equivalently in dependence of the scattered and ejected electron energies, hence of E_s and E_e. To obtain the full picture of the electron-solid interaction measured during a coincidence experiment it is advantageous to indicate the resulting (e,2e)-yield as a function of the initial state of the bound electron prior to its emission above the vacuum level (as shown for HOPG in the next section). It is possible to represent the intensity of correlated electron-pairs as a function of the initial state, given in terms of the parallel component of the momentum of the bound electron ($\vec{q}_{\parallel}$) and its associated binging energy (ε_{bin}). Each pair of correlated electrons is then associated to a ($\vec{q}_{\parallel}$, ε_{bin}) calculated on the basis of conservation laws. By means of this representation it is possible to highlight the role played by the electronic structure of the target in the SEE-process.

Subsections 4.3.1 and 4.3.2 present (e,2e) results measured employing two different coincidence set-ups: (1.) the (e,2e)-spectrometer of the LASEC laboratory at the Università degli Studi Roma Tre (RM3) described in section 3.3.3 and (2.) the Secondary Electron-Electron Energy Loss Coincidence Spectrometer (SE2ELCS) at the Technical University of Vienna (TUV) described in Refs. [244, 217, 106]. Both data-sets were acquired in parallel at RM3 – by me – and TUV, by my colleague Vytautas Astašauskas, during a 3-year-period of collaboration within the ITN EU project of SIMDALEE2[5].

In the following, inter-comparison between TDCS from two HOPG, measured by means of both experimental set-ups under two different kinematics is discussed. Combination of both data-sets permitted to investigate this TDCS obtained by sampling regions in the $(\varepsilon_{bin}, q_{\|})$-phase-space covering nearly the complete first BZ. Further (e,2e)-coincidence measurements performed on HOPG at RM3 investigate the coincident SE-yield in dependence of specific crystalline directions. These experiments were conducted at excitation energy of 50 eV and by keeping the final state (the energy level in the conduction band where the ejected SE is promoted when escaping above vacuum level) constant. The TDCS obtained in this case, reflects the coincident SE-yield given as a function of the binding energy of the electron prior to its promotion to the fixed energy band above E_{vac}.

Additional inter-comparison of (e,2e)-data is discussed in subsection 4.3.2 for two Aluminium surfaces: a single crystal with surface orientation in the (100) symmetry direction and its polycrystalline counterpart. The TDCS of coincidences measured on Al(100) is compared to (e,2e)-data of polycrystalline Al acquired by SE2ELCS in 2013 [126]. Additional inter-coparison is performed with the theoretical model presented by K. Kouzakov and J. Berakdar in Ref. [164]. For this series of (e,2e)-measurements it was possible to investigate the role played by the characteristic energy losses of the surface and bulk plasmons in the SEE-mechanism. At these plasma frequencies, it was demonstrated that the coincident SE-yield is strongly enhanced. This finding was observed also in other works [147, 148, 126, 150, 149].

[5]SIMDALEE2 is a research and training network dedicated to the investigation of Low Energy Electrons near solid surfaces. The acronym of SIMDALEE2 stands for Sources, Interaction with Matter, Detection and Analysis of Low Energy Electrons. It is a Marie Curie Initial Training Network (ITN) financed by the European Commission (grant number 606988 under the FP7-PEOPLE-2013-ITN action of the EC). One of the main objectives for our common work within the IT-network is to investigate the elementary mechanisms inducing the SEE-process and to establish a set of "benchmark" SEE-spectra for which the spectroscopic technique of (e,2e)-coincidence spectroscopy is ideally suited. Such a set of data is inter-compared with simulated SEE-spectra relying on different models, with the scope to refine these models on the basis of experimental evidence.

4.3.1 HOPG: (e,2e)

Being Graphite and HOPG exemplar prototypes for layered electron gas (LEG) structures [197, 193], they have been often subject of (e,2e) studies [200, 159, 201, 154, 217], since they represent ideal candidates for the investigation of elementary energy transfer mechanisms, both from the theoretical and the experimental point of view.

Before presenting the results obtained within this thesis project, a short overview on some of the aspects investigated by previous experiments is given and used for comparison in the following.

Previous experiments [201, 154] investigated the TDCS from HOPG at grazing angle reflection geometry for intermediate energies, with $E_0 \simeq 300\,eV$. In these experiments, Rioual, Liscio and co-workers shed light on binding energy and momentum density of solid surfaces by doing a mapping of the target valence band. In their experiments, the TDCS was investigated for fixed ejected electron energies given as a function of the binding energy of the recoil electron in its initial state. These ε_{bin}-spectra were measured by scanning E_0 between 300 – 340 eV, while maintaining fixed E_s and E_e. Hence, their (e,2e)-yield was measured for constant final states while scanning through the initial states with different ε_{bin}, or equivalently, for different energy transfers. The slower (or ejected) electrons were collected by means of a CMA with rather large angular acceptance, good q-resolution and with a wide detection range in phase-space on the other. By fixing their final state, its influence on the (e,2e)-cross-section was minimised, thus for the constant sum of (E_s + E_e) chosen, they always measured an intensity contribution to the TDCS, provided that an initial state (in the occupied BS) was available.

Furthermore, it shall be noted that, while for secondaries with sufficiently high kinetic energies ($> 20\,eV$ and more) – no matter under which kinematics the (e,2e)-experiment is conducted – it is likely for them to be ejected, for SEs with kinetic energies less than $\approx 20\,eV$ emission is only possible when unoccupied bands are accessible. In the limit of large E_e ($> 20\,eV$) an ionised electron, which gets promoted by the energy and momentum transferred in the collision towards one of these unoccupied energy bands, the probability to find an accessible state is high, since the unoccupied DoS – given by the term $\varrho_{unocc}(\vec{k}_e)$ in eq. (2.12) – monotonously increases towards the continuum, resembling more and more a continuum of empty bands. In this limit it becomes admissible to describe the ejected electron wave-function as a plane wave.

Whereas in the LE-range, the DoS of the unoccupied bands cannot be disregarded and its structure modulates the (e,2e)-yield. The probability for the allowed transition is determined by the joint initial-final state momentum density and is modulated by the dielectric function, or alternatively by the screening length (see section 2.4 for more details). Strictly speaking the wave-function of these LE-SEs cannot longer be approximated by a simple plane-wave, but rather

by distorted one-electron Bloch waves.

What clearly came out from their experiments [201, 159, 154] is the relevance of the role played by the *initial state* – and the BS of the target in its occupied state – in the emission process. However, since in these former experiments the energy of the collected secondaries where rather high (with $E_e \gtrapprox 20\,eV$), the role of the unoccupied band structure was disregarded.

On the other hand, results obtained in the framework of this thesis will demonstrate that for a comprehensive interpretation of the measured (e,2e)-cross sections, and herewith for the understanding of the underlying SEE-processes involved, it is necessary to consider the electronic structure of the target both in the *occupied* as well as in the *unoccupied* states.

Panel (b.) of figure 4.15 shows a Secondary Electron-Electron Energy Loss Coincidence Spectrum (or SE2ELCS) from HOPG measured in Vienna some years ago for 50 eV-primary electrons. These data are described in detail in Ref. [217] and show the (e,2e)-yield obtained for correlated electron pairs given as a function of ΔE and the Time-of-Flight[6] of the ejected electron (which corresponds to a given kinetic energy). Events of the correlated electron pair along the white parabola (in fig. 4.15) would correspond to a SE escaping from the Fermi-level carrying the full energy loss undergone by the primary electron after having overcome the workfunction. If there were intensity along this parabola, it would correspond to correlated electron pairs, of which the ejected electron escapes from the target, after having overcome the surface barrier, with the entire energy contribution lost by the primary electron (PE) during the collision. Hence, its energy would correspond to $E_e = \Delta E - \Phi$. In coincidence spectra no intensity can be observed above Fermi level, since no electrons can be ejected with kinetic energies exceeding the energy lost by the impinging electron (this would violate energy conservation).

Onset for the (e,2e)-intensity in the SE2ELCS of fig. 4.15 (b.) is observed for energy losses around 9 eV where a ridge-like spectral feature starts to form extending up ΔE of ca. 25 eV. The energy correlation for electron pairs along this spectral feature is readily explained on the basis of equation (2.3) and implies that these events are due to single scattering processes in which the whole energy transfer is invested to promote one single electron above vacuum level (to accessible empty states). This single-scattering spectral feature is associated to secondaries emitted in correspondence of the $(\pi + \sigma)$-plasmon of HOPG. However, it is noticeable that no intensity in SE2ELCS is observed for $\Phi < \Delta E < 9\,eV$.

On the other hand, the REELS shown in black in panel (a.) of the same figure, exhibits sharp loss features, due to single inelastic scattering events, at $\Delta E \sim 6\,eV$ and around $\Delta E = 15\,eV$. The former of these energies corresponds to a ΔE generally attributed to a π plasmon excitation or to the inter-band (π–π^*)-transition, the second spectral feature is usually linked to the excitation of

[6]Since in SE2ELCS detection is performed by a combination of a HMA and a Time-of-Flight analysers, results are often displayed with respect to this combined energy-time-scale. In some cases, it is preferable to display SE2ELCS with respect to this combined scale, to facilitate indistinguishability of spectral features which could be smeared out if the Time-of-Flight scale is transformed into ($E_e - E_{vac}$)-scale – otherwise routinely used.

a $(\pi + \sigma)$-plasmon (see Refs. [192, 140] and references therein).

Nonetheless, in correspondence of the characteristic π-plasmon loss (or $(\pi$–$\pi^*)$-transition) no intensity is observed in the SE2ELCS. Clearly – in this experiment – the excitation of the π-plasmon leads to no SE-emission. This is particularly evident by looking at the coincident loss spectrum given in red in panel (a.), which displays the total number of coincidences summed over the whole range of TOF-scale, of the secondary electrons. By comparing the singles ELS with the coincident loss spectrum, the complete lack of intensity in the coincident line-spectrum is evidently visible exactly in correspondence of the π-plasmon loss, which is otherwise present in the 2DCS of the REELS. Spectral intensity at higher losses (with $\Delta E \gtrsim 25$,eV) arises mostly due

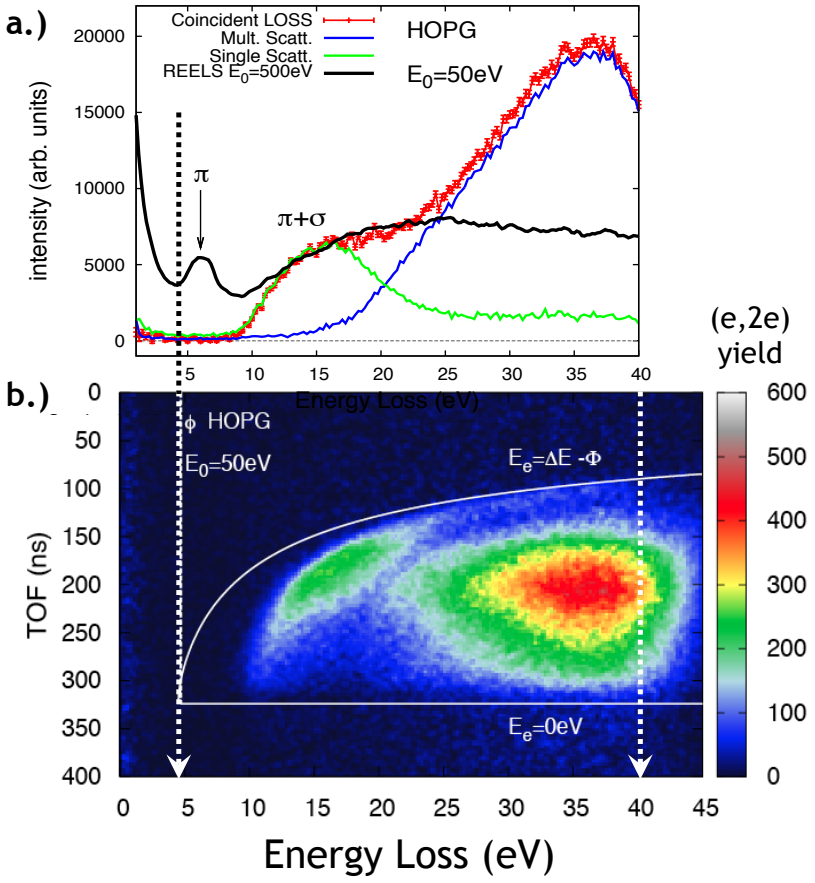

Figure 4.15: (a.) Comparison between the double-differential REELS (black) of HOPG measured for 500 eV-primary electrons with the coincident energy loss spectrum (red) obtained by integrating the SE2ELCS given in (b.) over all Time-of-Flights. (The REELS with different excitation energy was used to highlight the presence of the characteristic loss spectral features of a π- and $(\pi + \sigma)$-plasmons, which were also visible, though less intense, in the REELS measured at E_0 =50 eV.) The green and blue curves in (a.) represents the experimental separation of singles and multiple scattering contributions to the (e,2e)-yield. Panel (b.) is the SE2ELCS form HOPG measured for E_0 =50 eV in 2014. Data are extracted from Ref. [217].

to electrons participating in multiple inelastic collisions. The green and blue lines in fig. 4.15 (a.) represent the experimentally separated contribution to the intensity in SE2ELCS obtained for the single and multiple scattering regions, respectively (see Ref. [217] for further details).

In order to explain the complete absence of (e,2e)-events in correspondence of the π-plasmon excitation, it does not suffice to account only for energy conservation, but also momentum conservation needs to be considered, as given in equation (2.4). Owing to momentum conservation, determining the parallel component of the momentum transfer ($\Delta\vec{K}_{\parallel}$) occurring during the interaction yields the in-plane momentum component of the bound electron ($\vec{q}_{\parallel}$) prior to its emission.

Hence, for a given ΔE and a given $\Delta\vec{K}_{\parallel}$ there must be an available initial state with a suitable pair of ε_{bin} and $\vec{q}_{\parallel}$ for which the bound electron can be potentially extracted and promoted to the conduction band. In addition, it will be shown, that for this electron to be emitted an available empty state, characterised by $(E_e, \vec{k}_e)$ needs to be available as well. Only if this is the case, transition from the occupied to the empty energy level contributes to the intensity of the (e,2e)-spectrum.

Recent experiments performed in parallel at both institutions of RM3 and TUV, indeed demonstrated that the lack on intensity observed in SE2ELCS is to be assigned to the kinematics of the experiment, which does not permit to explore regions in phase-space, where for the π-plasmon energy an electron could be promoted from the valence to the conduction band. In fact, for a $\Delta E = \hbar\omega_\pi$ of ca. 6 eV, the maximal ε_{bin} for the initial state is given by $\Delta E - \Phi$ which equals -1.4 eV. In the BS of Graphite (see subsection 3.2.1 and [181, 200, 188]) given along the ΓK and ΓM symmetry directions, the only bands available at this binding energy are the $\pi_{1,2}$-bands for values of $\vec{q}_{\parallel}$ in proximity of the K-point. Firstly, it is well-known that in Graphite the DoS at the K-point approaches zero, secondly if the kinematics of the experiment does not permit any sampling in that specific region in phase-space, no electrons can be extracted from the solid. This was indeed the reason for which in the SE2ELCS experiment (shown in fig. 4.15) no intensity was measured.

To highlight the importance of the role played by the electronic structure of HOPG in the SEE-mechanisms, the upcoming (e,2e)-coincidence measurements are displayed as a function of the initial state of the recoil electron (additional details on these can be found in my colleagues Astašauskas' thesis [106] and in an upcoming publication [79]).

Figure 4.16 displays the (e,2e)-yield measured from HOPG for 91.7 eV-primary electrons, and the (e,2e)-cross section is given in false colour scale within the sampled region in the BZ of HOPG. The (e,2e)-intensity map (indicated by the colour scale) was superimposed over the in-plane band structure calculated for the symmetry directions ΓM and ΓK. The $\pi_{1,2}$-bands are given as dashed black lines whereas the $\sigma_{2,3}$-bands as continuous grey lines. Since these experiments were performed in specular reflection geometry, both in-plane symmetry directions of ΓM, ΓK and all in between crystalline directions in the electronic structure of graphite contribute to the diffusion of electrons during a collision and therefore energy bands in all directions need to be considered as available initial states.

After preparation of the surface (consult subsection 3.2.1) and after its characterisation done employing single-electron spectroscopic techniques as explained in the experimental chapter (see sub-subsection 3.3.4.3 and with greater detail also in section 4.2) measurements have been performed in asymmetric kinematics and under specular reflection conditions for the scattered electron, which impinged onto the target under 30° polar angle with respect to the sample surface normal (see figure 3.18). These faster electrons were detected by TOF equipped with a single

channeltron. The spectrum of SEs was measured using the HMA R66 under 60° emission angle wrt. to the surface normal at an azimuthal rotation of 180° away from the scattered electron. At either analyser the pass energies were maintained constant for the whole acquisition ranges. At TOF, tuned on the kinetic energy range of the ELS, the pass energy was of 40 eV, whereas at R66 the optics was optimised at a pass energy of 25 eV. The energy resolution of the SEs together with the uncertainty in determining E_0 and E_s yield a binding energy ε_{bin} resolution of ca. 2.65 eV. Whereas the momentum resolution in $\vec{q}_{\parallel}$ is determined by the combination of the energy window E_{win} detected by R66 and the accepted solid angles ($\Delta\Omega_{s,e}$), giving the uncertainty on the electron momentum vectors, $\vec{k}_{0,s,e}$, of all three electron involved in the (e,2e)-process. The average momentum resolution Δq obtained for the sampled regions shown in fig. 4.16 is of ca. 0.165 $Å^{-1}$. The (e,2e)-spectrum shown in fig. 4.16 is the result of a series of acquisitions

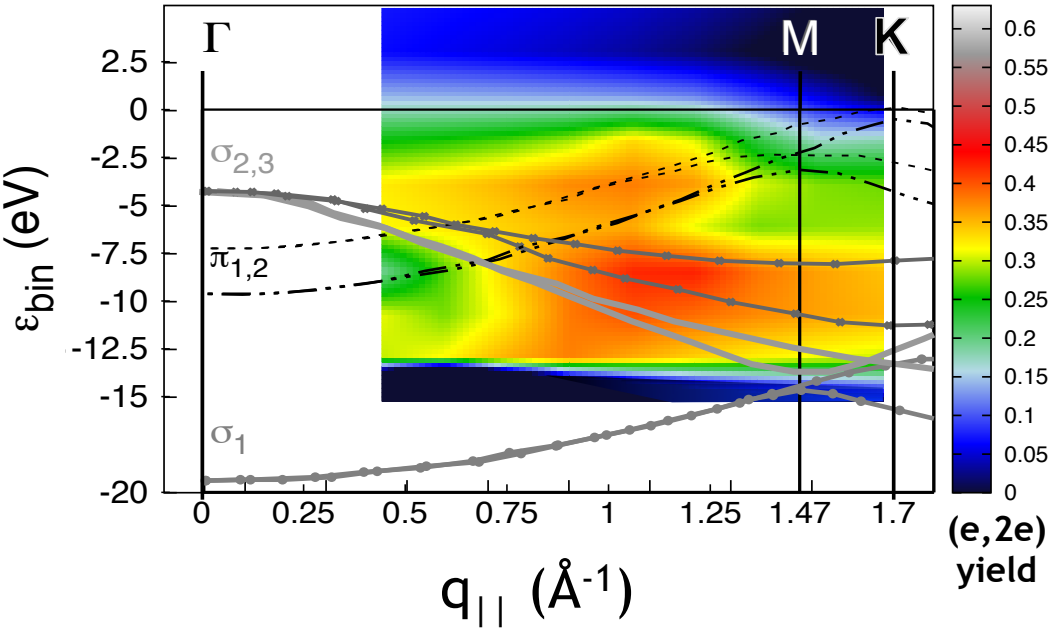

Figure 4.16: TDCS from HOPG measured at RM3 for 91.7 eV-incident electrons and for specular reflection geometry. The (e,2e)-yield (indicated by the colour scale) is represented as a function of the initial state of the bound electron prior to its emission. The region in phase-space probed during the experiment is superimposed on the ($q_{\parallel}, \varepsilon_{bin}$)-phase-space given for the in-plane symmetry directions of ΓM and ΓK.

conducted over the duration of ca. 4 months. During each measurement, acquisition at both energy analysers was kept fixed on the same pair of energies of E_s (or ΔE) and E_e, respectively. For each experiment, time-histograms were evaluated and analysed independently and after proper normalisation they were merged yielding the intensity map of figure 4.16. More details of the acquisition and the data analysis are explained in subsection 3.3.4 and sub-subsections therein, e.g. in sub-subsection 3.3.4.3.

The (e,2e)-yield shown in fig. 4.16, represents the probability for a SE to be ejected, given as a function of its initial state – characterised by a pair of $q_{\parallel}$ and ε_{bin} in the valence band – which

in turn is intrinsically correlated (and fully determined by) to the E-transfer which had occurred in the interaction.

In general, high (e,2e)-yield is found in correspondence of (occupied) energy bands. Highest intensity (indicated in arbitrary units by the colour box) was obtained in correspondence of $\sigma_{2,3}$-bands for $\varepsilon_{bin} \in (-12; -6)$ eV. For the kinematics chosen in this experiment it was possible to probe regions in phase-space close to the Brillouin zone boundary in proximity of the K-point (with $\vec{q}_{\parallel}$ =1.703 $^{-1}$). The (e,2e)-cross section drops by a factor of 3.5 when moving from the σ-bands (exhibiting highest intensity) towards the K-point, for binding energies in the range of the Fermi level. This drop in intensity reflects what is expected on the basis of the fact that at the K-point in HOPG, the so-called Dirac singularity exhibits nearly zero DoS.

It shall be pointed out that the low intensity observable slightly above the Fermi level is due to the experimental energy resolution, which was about 2.65 eV in this experiment and is in no case linked to any scattering events occurring with unbound electrons, which indeed would violate energy conservation.

Furthermore, for regions in the valence band where no bands are available – e.g. at $q_{\parallel}$ =0.5Å^{-1} with ε_{bin} =-15 eV – given the experimental energy and momentum resolutions, it is possible to observe a decisive drop (going towards zero) in the (e,2e)-cross section.

These observations demonstrate that the measured TDCS is substantially modulated by the DoS of the initial state. Results shown in fig. 4.16 reflect what was observed in Refs. [201, 154], thus re-confirming the relevance of the occupied BS in the SEE-process.

The different kinematics in SE2ELCS allows to sample regions in the $(\vec{q}_{\parallel}, \varepsilon_{bin})$-phase-space which are closer to the Γ-point in the BZ. Figure 4.17 shows the combined (e,2e)-cross sections from HOPG resulting from experiments acquired by means of the SE2ELCS and the LASEC spectrometers. Also these (e,2e)-coincidence spectra are overlaid with the in-plane symmetry directions of ΓM and ΓK (in this case given as white lines). Identical investigations were conducted by the two apparatus in complementary kinematics. Hence, a common ($\vec{q}_{\parallel}$,ε)-phase-space can be used to plot in false colour scale the coincidence rates arbitrarily normalised to a common relative intensity scale. The regions in phase-space sampled by the SE2ELCS spectrometer range from values of $\vec{q}_{\parallel}$ for the bound electron going from Γ =0 Å^{-1} to ca. 0.5 Å^{-1}, whereas in the (e,2e) experiments performed in the LASEC laboratory the sampled region ranges from ca. 0.5 Å^{-1} to the K-point. The combination of the two measurements allows to obtain the coincident SE-yield for the complete first Brillouin zone down to a maximal binding energy of ca. -12 eV. Additional details on these (e,2e)-measurements are entailed in Ref. [79].

Highest intensity of correlated electron pairs can be observed in correspondence of occupied bands, which is not surprising, on the basis of the argumentations discussed previously. The energy and momentum transferred occurring during the collision induce the promotion of a bound electron above the vacuum level, whose ($\vec{q}_{\parallel}$,ε)-values correspond to an occupied energy band. The intensity for this coincident SEE-yield, observed in correspondence of a given occupied

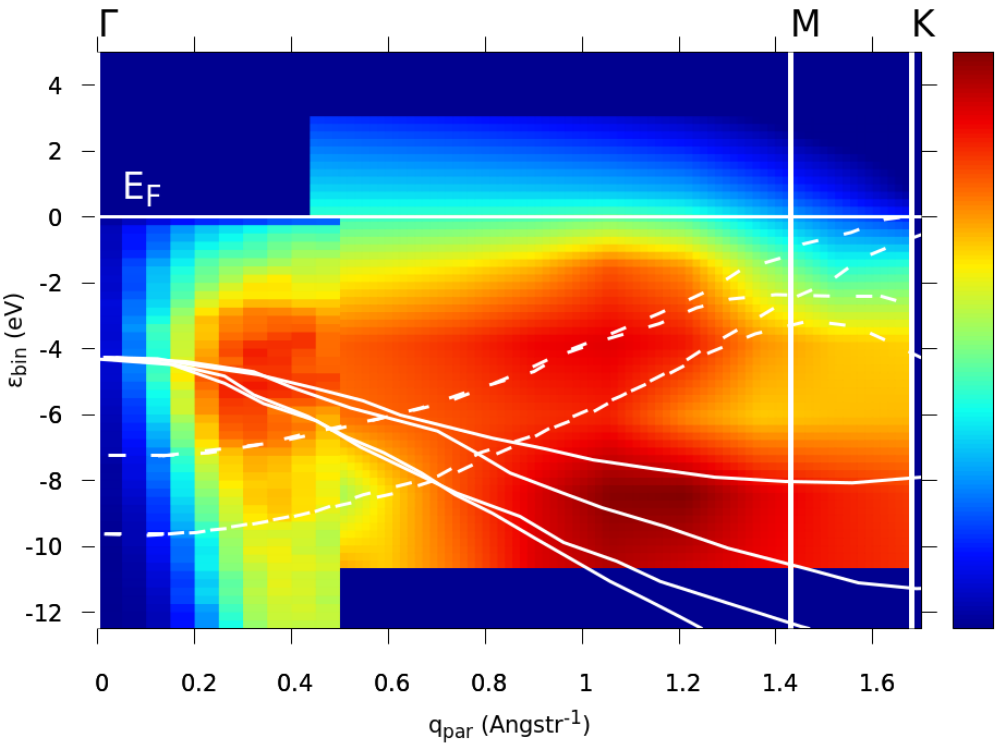

Figure 4.17: The combined (e,2e)-yield measured from HOPG using both experimental set-ups (LASEC and SE2ELCS). The (e,2e)-cross section is given as a function of the initial state – or of the bound electron prior to its emission – and its intensity represents the probability for an electron with a given $(\vec{q}_{\parallel}, \varepsilon_{bin})$-pair to be promoted above vacuum level. The kinematics used in both experiments allow to cover nearly the complete first Brillouin zone of graphite, which is given here along the two main in-plane symmetry directions. By means of SE2ELCS it was possible to sample from $\vec{q}_{\parallel}$-values ranging from Γ up to ca. $0.5\,^{-1}$, whereas at RM3 it was possible to sample up to the BZ boundary (at $\vec{q}_{\parallel} \approx 1.70\,^{-1}$).

band, is proportional to the density-of-states (DoS) and to the probability for an electronic inter-band-transition to occur as stated by the ingredients provided in the TDCS equation (2.12).

By combining both experiments it was possible to investigate the (e,2e)-yield for nearly the whole first Brillouin zone. As shown in fig. 4.17, the regions in the $(q_{\parallel}, \varepsilon_{bin})$-phase-space reach a maximal value for $q_{\parallel}$ of $0.5\,\text{Å}^{-1}$. At this $q_{\parallel}$-value no occupied bands are available in correspondence of the small binding energy of ca. -1.5 eV, which would be to the maximal ε_{bin} for a bound electron extractable from the valence band as a consequence of a π plasmon loss. Hence, it is not surprising that also in this SE2ELC spectrum (just like in the one shown in fig. 4.15) no (e,2e)-yield could be observed in correspondence of the typical π-plasmon loss (see [106] and [79] for more details).

Up to now only the role of the initial state, i.e. of the occupied band structure, was examined. For the planning, but also for interpreting an (e,2e)-experiment it is essential to determine,

which region in the occupied $(q_{\parallel}, \varepsilon_{bin})$-phase-space is probed for a given energy loss at a specific kinematics. For this reason, simulations were routinely run [240], on the basis of which, tuning of the experimental settings was optimised to enable the sampling of specific regions in the BS, on one hand, and interpretation of the measured (e,2e)-spectra was performed.

Panel (a.) in figure 4.18 gives an example for such a simulation, where potentially sampled areas are highlighted in red and orange tones in dependence of the considered energy transfer indicated in the legend. This simulation was run using a self-developed FORTRAN [240] code conceived for calculating the kinematics of an (e,2e)-experiments (further details on the simulation software are mentioned in the sub-subsection dealing with the evaluation of a coincidence measurement 3.3.4.3.).

Let us now consider two measurements having an identical initial state, which is equivalent to say that the bound electron is characterised by a same pair of $(q_{\parallel}, \varepsilon_{bin})$ in phase-space. The right-hand panel in figure 4.18 shows a simulation for two experiments, where the ejected

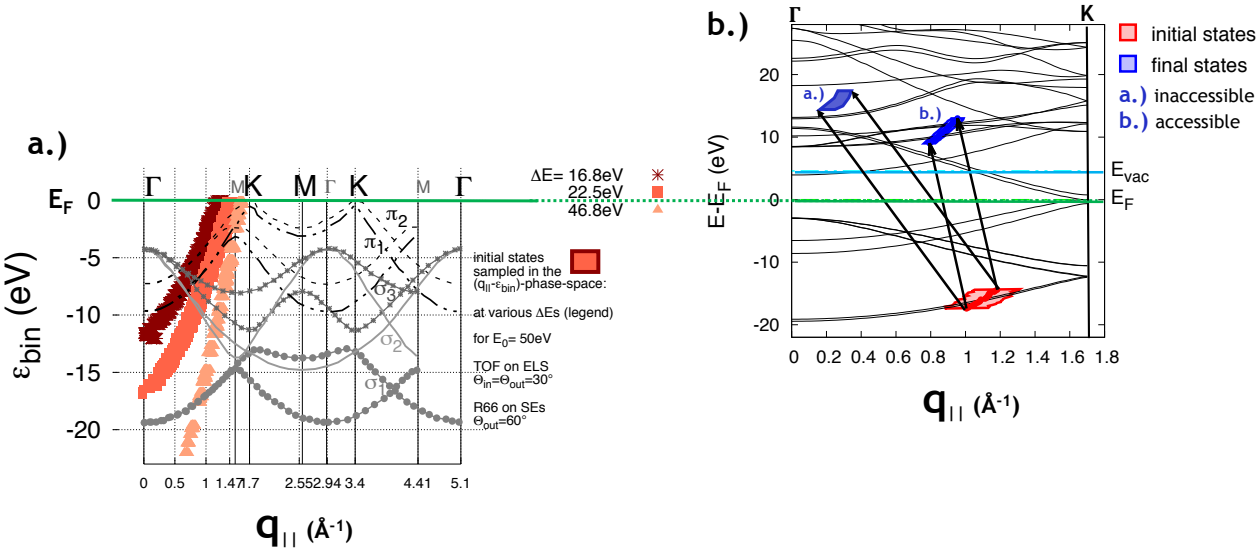

Figure 4.18: Simulations for planning (e,2e)-coincidence experiments on HOPG. Panel (a.) shows in red and orange, regions in phase-space which are sampled at a fixed kinematics for the energy losses indicated in the legend. For pairs of $(q_{\parallel}, \varepsilon_{bin})$ coinciding with occupied bands, availability of initial states is granted. Panel (b.) shows a simulation for two different experiments. The initial state (indicated by the red polygon) is fixed and identical for both experiments. By means of different momentum transfers, hence due to different energy loss processes and kinematical conditions, different final states (blue polygons) are reached. The final state labelled as **(a.)** leads to no contribution to the (e,2e)-yield, due to the presence of an energy gap. For the case labelled as **(b.)** instead, availability of unoccupied energy bands makes the interband transition from the occupied σ_1-band possible. The FORTRAN code from Ref. [240] was also embedded in an existing SW-package (BRUCE by Werner *et al.* [63]), by means of which this figure was produced.

electron originates from an identical initial state (highlighted as red polygon). Depending on the energy loss, ΔE and momentum transfer $\Delta\vec{K}_{\parallel}$ occurring during these two experiments a multitude of different final states, characterised by $(E_e, \vec{k}_{e,\parallel})$ for the ejected electron, can be reached. In figure 4.18 (b.) the final states are represented by blue polygons, labelled with

the letters **(a.)** and **(b.)**. The simulation shown in panel (b.) was performed using the same FORTRAN code from Ref. [240] which in this case was embedded in a pre-existing simulation SW-package named BRUCE [63]. If the considered electronic transition is allowed – this implies availability of unoccupied energy bands in correspondence of the considered fixed final state – electrons can be ejected and promoted to the empty energy band. This case is depicted by the simulation labelled with the letter **(b.)**. Electrons from the σ_1-energy band can access to several empty bands above E_{vac} for $(q_{||}, \varepsilon_{bin})$-values comprised within the blue polygon **(b.)**. In the case, labelled as **(a.)** instead, due to the presence of an energy gap, there is no accessible final state and the cross section for the SEE vanishes. In other words, in spite of the availability of an initial state, if the momentum transfer is such that no available unoccupied energy band can be reached, no electron will be promoted above vacuum level and the given pair of initial and final states does not contribute to the intensity in the (e,2e)-cross section, hence of SEE.

Correct interpretation of measured (e,2e)-cross sections can be only performed if the electronic structure of the irradiated target is considered both in the occupied and unoccupied states. This is particularly important when working within the LE-regime and when the energy of the ejected (or also incident) electron is very low. As also proven by the series of LE-TEY measurements, in fact, the unoccupied BS plays a relevant role in the reflectivity and the emissivity of a material. The BS above E_{vac} dictates, on the one hand, the behaviour of a low-energy incident electron, which depending on the availability of empty bands can penetrate the target (as demonstrated by the LE-TEY curves), but, on the other hand, it also determines whether a LE-SE can effectively escape from its initial state (in the occupied BS). Hence, the electronic structure below and above E_{vac} modulate the emission of LE-SEs.

This is particularly evident in Graphite, since its BS exhibits large forbidden regions, both in the valence and in the conduction bands. The empty BS region just above vacuum level (e.g for energies up to max. 30 eV) contains several zones with energy gaps, where neither incident electrons can enter nor SEs can exist.

At higher energies ($E-E_{vac} \gtrapprox 25$ eV) the density of empty bands increases, while forbidden gaps rapidly diminish. For this reason, if in an (e,2e)-experiment it involves high energetic secondary electrons, these latter can easily escape from the surface, since availability of accessible final states is more probable at these energies.

Furthermore, as explained in section 2.4, the intensity for such an event is additionally modulated by the density of momentum ($\rho(\vec{q})$) of the considered initial and final states and is ultimately moulded by the joint density of these momenta [199, 200, 159]. This was demonstrated on the basis of two more (e,2e)-coincidence experiments performed at RM3, of which the results are shown in figures 4.20 and 4.22.

In these (e,2e)-experiments, the HOPG specimen was bombarded by a monochromatic beam of 50.8 eV-primary electrons. The source energy, E_0, was maintained constant for the whole

duration of the experiment series. The energy set at R66 was adjusted to scan over a large energy loss range, whereas the energy monitored by TOF was kept fix monitoring LEEs with $E_e \simeq 4\,eV$, hence it was tuned on the SE-peak.

The optical elements for the electron transport were optimised in both analysers and their lenses were tuned to provide optimal and almost uniform transmission of electrons over the entire kinetic energy range of interest (going from the SE-spectrum up to the ELP). This allowed the role of the two analysers to be interchangeable, meaning that either energy range was measurable by both HMAs with similar efficiency and transmission.

After surface preparation, diffraction patterns were acquired employing both analysers. These served to monitor the quality of the surface preparation and to determine the symmetry directions which contributed to the diffusion at these scattering conditions.

For this lower excitation energy, other kinematics can be accessed, thus consenting to sample also different regions in the $(q_{\parallel}, \varepsilon_{bin})$-phase-space. The accessible in-plane projections of the exchanged momentum, $\Delta\vec{K}_{\parallel}$, for this primary energy can be monitored by acquiring a LEED-scan of the elastically scattered electrons. Such diffraction patterns of the elastic peak (ELP) are shown in figure 4.19 and were measured with a monochromatic electron beam of ca. 51 eV employing both analysers.

The LEED-scan in black was measured using R66 whereas the red one was measured with TOF. In R66, for this combination of primary energy and scattering geometry, first order diffraction peaks are seen for both symmetry directions. Whereas in TOF, the LEED-scan exhibits only the first order diffraction peak along the ΓM-direction. The ordinate scale indicates the angle at the manipulator axis, θ_{man}. This manipulator scale is used to display the relative angular differences between the two rocking curves. Its angle can be transformed in a pair of incidence-emission angles for each analyser respectively. Analysis of the two diffraction patterns permitted to identify the various in-plane crystalline directions. For example, for the diffracted peak seen at θ_{man} =208.9°, the in-plane component of the reciprocal lattice vector yielded a value of $5.1 Å^{-1}$, which corresponds to the lattice vector $\vec{G}_{\parallel}$ for the ΓK-symmetry direction. The rocking curve acquired by means of the R66-analyser (shown in black) exhibits first order diffraction peaks for both in-plane symmetry directions of ΓK and ΓM at manipulator angles θ_{man} of 208.9° and of 231.39°, respectively . Whereas in case of the TOF-analyser (red curve in fig. 4.19) only the first order diffraction along ΓM was measured.

Acquisition of these two LEED-scans was performed to decide under which scattering conditions the (e,2e)-coincidence measurements were to be conducted. It is worth noticing, that for this primary energy the first order diffracted peak along ΓK, measured with R66, falls together with the specular peak measured in TOF (with $\theta_{in} = \theta_{out} = 30°$). This particular scattering condition, at $\theta_{man} \approx 210°$, was selected to perform an (e,2e)-coincidence experiment, in which R66 was tuned on the energy loss spectrum, thus detecting only scattered electrons which were inelastically deflected along the sole ΓK-direction, whereas the TOF-analyser was tuned on the SE-peak. The fact that TOF was aligned w.r.t. source and sample surface normal in such a way

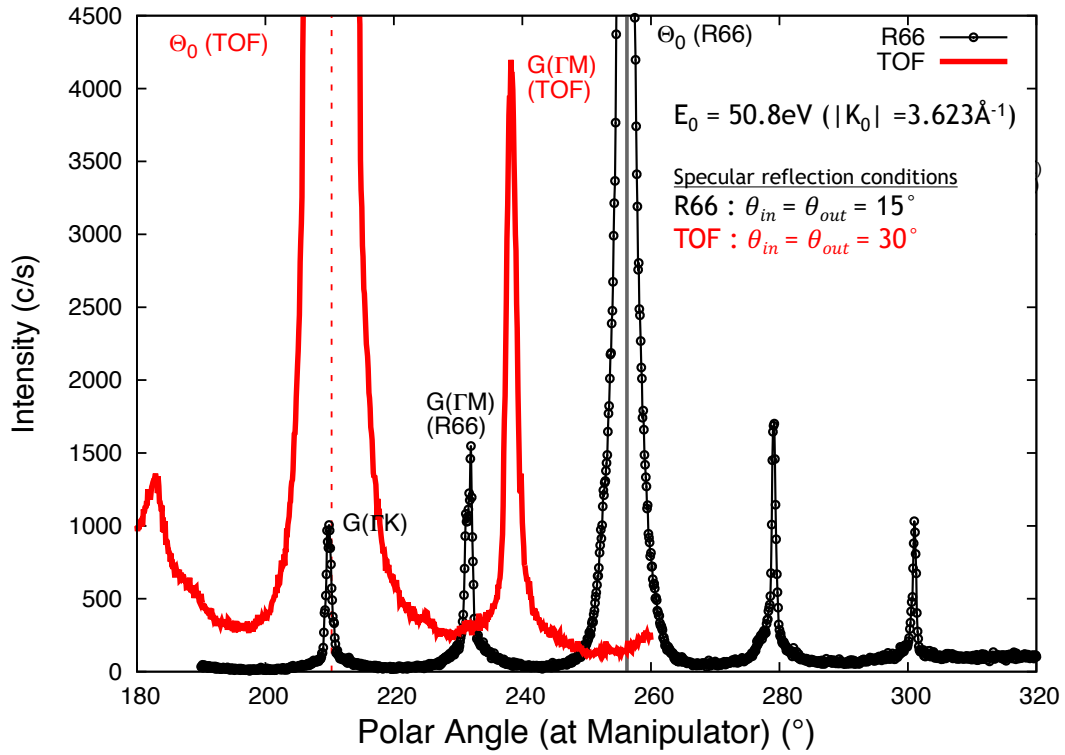

Figure 4.19: Diffraction patterns from HOPG measured for 50.8 eV PEs with both analysers are compared. At this primary energy, R66's rocking curve (black) exhibits first order diffraction peaks for both symmetry directions, whereas for TOF (red) – having specular reflection conditions for $\theta_{in} = \theta_{out}$ =30° only the first order diffracted peaks along ΓM are measured. The position of the first order diffracted peak along the ΓK-symmetry direction (in R66) coincides with the specular peak measured in TOF.

thus to correspond to specular reflection conditions can be disregarded.

In general, the angular distribution of SEs is rather broad and in our measurements it was found to be isotropic over a large angular interval. Therefore, even if Bragg scattering conditions are such to correspond either to a maximum or to a minimum in intensity for the elastically reflected electrons, the overall (intensity) distribution of SEs is rather unaffected, thus remaining (nearly) unchanged over large angular ranges covering different scattering conditions.

The degree of discrimination in such an (e,2e)-coincidence experiment is additionally increased, since in this case only the SEY of secondaries ejected in coincidence with a scattered electron from the ΓK-direction, will be detected and registered as true coincidences. For such an experiment, lower count rates are to be expected and consequently also longer acquisition times.

The first order diffraction peak measured by R66 at ca. 231° falls together with a minimum in the intensity of the LEED-scan acquired with TOF. A further (e,2e)-experiment was done under this scattering kinematics, where in this case the correlated electron pair is composed of

the inelastically scattered electron, which was re-diffused along the ΓM-direction only, whereas the SE was collected by TOF under an angle at which the rocking curve of the ELP exhibits a low intensity, within the so-called thermal diffusion scattering background (TDS). Also in this case, the orientation of the sample with respect to the TOF analyser plays no major role, since the angular distribution of SEs is broad and featureless.

For the first (e,2e)-experiment – the one performed for the polar angle θ_{man} =208.9° at the manipulator – of which results are displayed in figure 4.20, the sample surface was rotated in such a way for both the incident electron (characterised by E_0 and $\vec{k}_0$) and the faster (or *"scattered"* [7]) electron (with E_s and $\vec{k}_s$) to impinge onto the target and to be ejected from the target along the ΓK-symmetry direction only. For this alignment, both the momentum-reversed incident electron with ($\vec{k}_0'$) and the scattered electron (in this case $\vec{k}_s$) are practically oriented in the same direction, according to the dual-step scattering process of the "DL"-scattering (see section 2.3). Such an selective alignment consents to discriminate scattering events occurring along a well-defined crystallographic direction (in this case ΓK) – consequently minimising all other events occurring along concurring symmetries (e.g. along ΓM). Upon selection of only one crystalline direction (among all possible in-plane symmetries in between ΓK and ΓM for HOPG) all other directions are excluded from the scattering event and therefore only those inter-band transitions are allowed according to the electronic structure sampled in that specific direction. Electron e_s was collected by R66, whose energy was scanned on an energy range corresponding to the kinetic energies of scattered electrons. Consequently, the TOF-analyser was tuned to collect the slower electron of the two – labelled with index "e" – for a polar angle coinciding with its specular reflection conditions.

During the experiment, the final state was kept constant. For doing so, the TOF analyser was tuned to a fixed energy of $E_e - E_{vac} = 5 \pm 1.5\,\text{eV}$. In fig. 4.20 (a.) this final state is highlighted by a green hatched box in the conduction band. Width and height of this box are representative for the obtained energy and momentum resolutions ($\Delta E \sim 3\,\text{eV}$ and the mean $\Delta q \sim 0.45 \text{Å}^{-1}$). Whereas, the energy at R66 was scanned from $E_s - E_{Fermi} \in (24 - 42.5)\,\text{eV}$ in 2.5 eV-steps, thus covering a large range of initial states. Variation of the kinetic energy of electron e_s is equivalent to a changing of the energy loss ΔE undergone by the PE, which in turn is identical to a correspondent variation in binding energy, ε_{bin} of the secondary electron in its initial state (according to eq. (2.3)). Herewith, the binding energy was varied between -22.2 eV to +3.7 eV (wrt. Fermi level). Scanning through the mentioned energy range is equivalent to perform a "cut" along a series of initial states given in a certain direction in the $(q_{\parallel}, \varepsilon_{bin})$-phase-space. This experimental cut is displayed by red squares in fig. 4.20 (a.). Horizontal bars indicate the average Δq of ca. 0.45Å^{-1} whereas the

[7] It should be emphasised that being electrons indistinguishable fermions, to make distinction between *"scattered"* (high energy) and *"ejected"* (low energy) becomes rather irrelevant especially if the excitation energy is around 50 eV or even lower. Nonetheless, the tuning of the electron optics can optimise either the high energy or the low energy ranges of the electron energy spectrum. Such a specialised tuning allows for associating each analyser to detection of either "scattered" or "ejected" electrons.

vertical bars give the experimental step size of 2.5 eV (the energy resolution in this experiment was about 3 eV).

Owing to momentum conservation, as given in equation (2.4), and to the kinematics of this experiment, the parallel component of the momentum of each initial state can be projected over the sole ΓK in-plane direction. Therefore panel (a.) displays the experimental scan superimposed on the BS (from Ref. [185]) given along ΓK only. Since in this experiment, the TDCS was measured for a constant final state while scanning through the initial state, it is advantageous to display the measured (e,2e)-yield as a function of the (scanned) binding energy. This is shown as line spectrum in panel (b.) of fig. 4.20. The experimental data (black squares with error bars) were acquired for the duration of three days achieving an average statistical error on the measured points of ca. 16% [8]. The experimental data in plot (b.) are guided by a red curve which merely serves to highlight the trend of the measured TDCS.

In order to interpret the measured trend for the (e,2e)-cross-section, it is relied upon several ingredients and notions, which at this point deserve to be recalled to our attention. Based on the elastically-assisted inelastic scattering model (also "DL"-scattering) – according to which the (e,2e)-coincidence experiments presented in this work are interpreted – the TDCS (from equation 2.12) is essentially modulated by the kinematical factor, by the selection rules defining the possibility for a given inter-band transition to occur as a result of the inelastic scattering event and ultimately by the form factor, which is in essence given by the density of momentum for the considered initial and final states.

In addition, the experiments discussed up to now, have brought evidence for the fact that proper interpretation of TDCS can be only performed if the electronic structure of the irradiated target is considered, both in its occupied and unoccupied state.

Similarly to the experiments performed by Rioual *et al.* [201], the measured TDCS in this experiment is essentially modulated by the density of momentum, $\varrho(\vec{q})$, of the initial states only, since the final state was kept fix. Before explaining any further features in figure 4.20 (b.), it is necessary to mention that for the kinematics in our experiment (see figure 4.19), the direction of the momentum transfer $\Delta\vec{K} = (\vec{k}_0 - \vec{k}_1)$ with respect to the $\hat{c}$-axis of the 2D-crystal encloses a polar angle of ca. 60°. Hence, $\Delta\vec{K}$ possesses both a parallel and a perpendicular component. Strictly speaking the experiment was performed along an "in-between"-crystalline direction, which is neither ΓK nor ΓA only, but intermediate one. Therefore to project results merely along these high-symmetry directions shall be regarded as a first order approximation. Provided that this method represents a rather crude approach, it nonetheless helps to the interpretation of the acquired data, as it will be demonstrated in the following.

To get the proper $\Delta\vec{K}_{\parallel}$, the "DL"-model is to be used. $\Delta\vec{K}_{\parallel}$ fulfils equation (2.4) wherein

[8] Generally, the average error achieved during our (e,2e)-experiments was comprised between 6–10% at the very most. Exceptional cases exhibiting higher errors were either due to shorter acquisition times or linked to a very low cross-section for that particular correlated electron pair

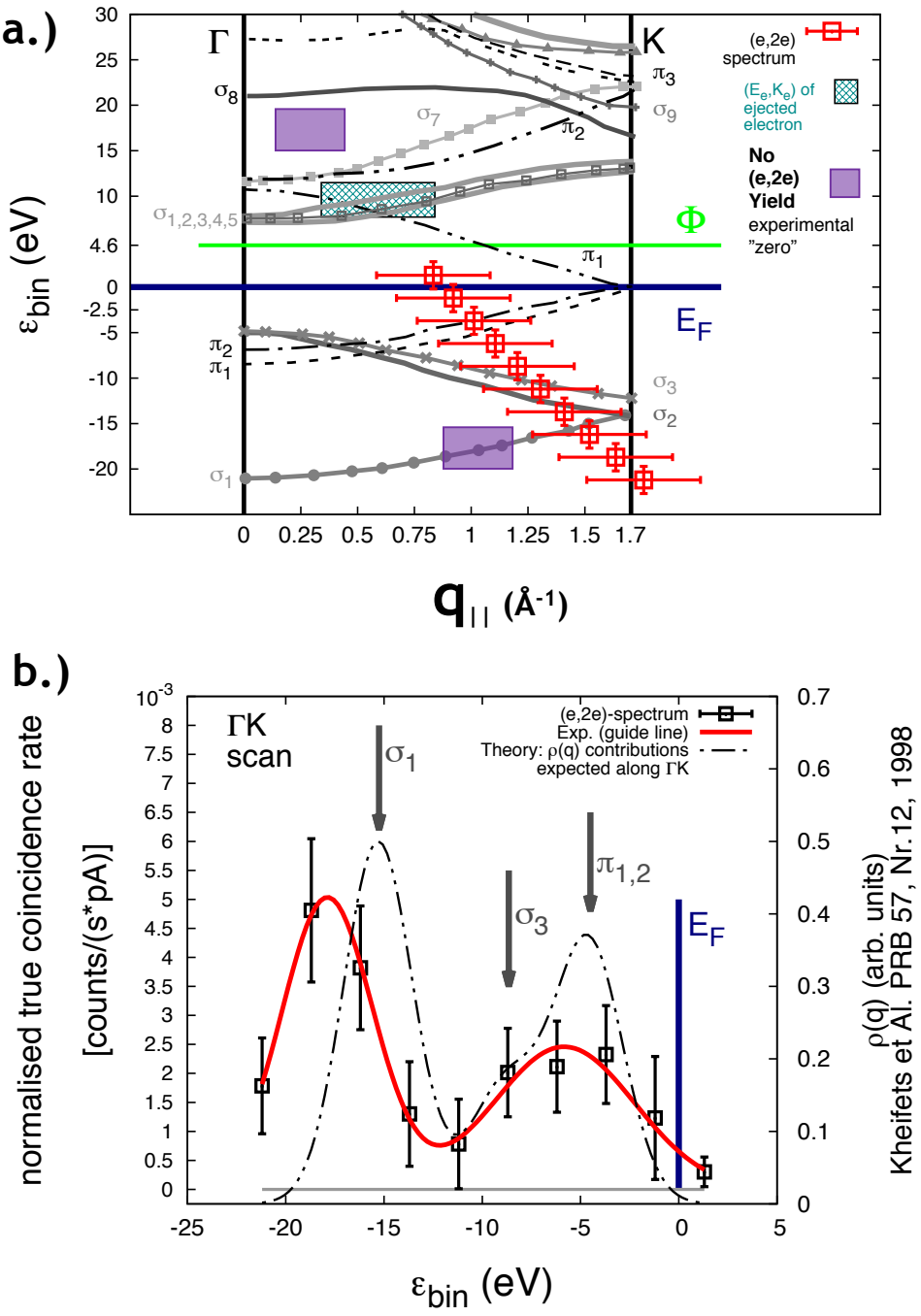

Figure 4.20: (a.) The "ΓK-scan-cut": (e,2e)-experiment performed at constant final state (green box) centered at $E_2 - E_{Fermi} \approx 10\,eV$ while scanning over the various initial states, for $\varepsilon_{bin} \in (-22.5; +3.7)\,eV$, indicated by the red data points. Initial and final states are superimposed over the band structure of Graphite from Ref. [185] to show sampled regions in phase-space. Panel (b.) displays the results of the experiment where the normalised (e,2e)-yield is given as a function of the binding energy of the recoil electron. Black data points were measured with ca. 16% error and are guided by the red line. Dashed-dotted black line represents an orientative trend for the momentum density, $\varrho(\vec{q})$ – scale on the right-hand side – expected according to [200, 159] in correspondence of the energy bands that were scanned throughout the experiment for the sole ΓK crystalline direction.

a reciprocal lattice vector of $\vec{G}_{\parallel}(\Gamma K)$=5.1Å^{-1} was considered. The parallel component of the bound electron ($q_{\parallel}$), as well determined via eq. (2.4), can be projected over the ΓK-crystalline direction, as shown by the red data points in panel (a.).

The perpendicular component $\Delta\vec{K}_{\perp}$ inside the crystal is different from the one outside, since both the incident and the scattered electrons (labelled with "0" and "1" respectively) undergo refraction at the surface and are subject to the crystal inner potential U_{in} =16 eV [195]. By determining the $\Delta\vec{K}_{\perp}^{in}$ component it is possible to obtain the $q_{\perp}$-value of the bound electron, this in turn could be projected over the ΓA-symmetry direction of the crystal (not shown).

As previously stated, in such an experiment, where the final state is kept fixed and the initial state is scanned for different E- and K-transfers, the (e,2e)-cross section is mainly moulded by the momentum density of the valence band. For this reason, in order to explain the measured trend in our TDCS (the red guiding line in plot (b.)) comparison with the expected momentum density distribution was attempted, while keeping in mind that the method used is merely a first-order approximation as stated above.

According to the TDCS – equation (2.12) – the availability of empty bands is as much important as the availability of the initially occupied states in order to generate SEs. This statement was tested by performing a single measurement with a low statistical uncertainty (long integration time) with an initial state falling on the σ_1-energy band and a final state falling in an E-gap above E_{vac} (states highlighted in Fig. 4.20 by the purple rectangles). The true coincidence rate, , was found to be below detectability (i.e. being an experimental "zero" with $R_{true} \approx 6 \times 10^{-4}$) thus confirming the statement. To highlight the relevance of the final state in the SEE-process, especially when working in the LE-regime, an (e,2e)-measurement was intentionally planned to obtain experimental proof sustaining the above-mentioned allegations.

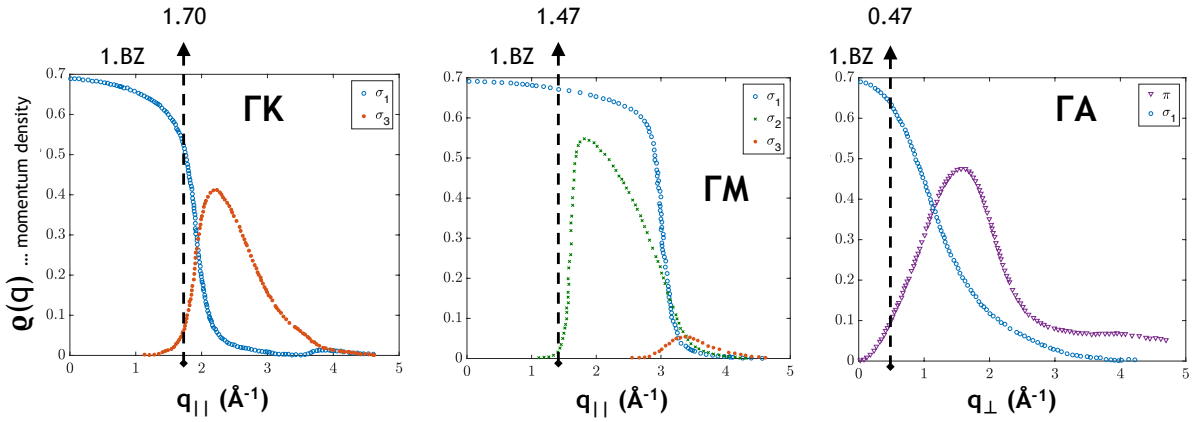

Figure 4.21: Electron momentum densities given along the three high symmetry directions from Ref. [200, 159].

Plot (b.) in figure 4.20 exhibits a dashed-dotted black line, which represents the estimated trend of $\varrho(\vec{q})$ for the experimental $q_{\parallel}$- and $q_{\perp}$-values corresponding to the positions in phase-space of those energy bands which were crossed during the experimental scan. Momentum densities $\varrho(\vec{q})$ for the three high-symmetry directions were calculated by Kheifets *et al.* in Ref. [159] and

are shown in figure 4.21 in units of reciprocal Ångstrom.

As visible from figure 4.21, the only energy bands contributing to the $\varrho(\vec{q})$ in the ΓK-direction are σ_1 and σ_3. However, in our experiment contributions to the TDCS from the $\pi_{1,2}$-energy bands are also obtained. This is not surprising, since the kinematics of the experiment samples an "in-between" (a mixed) crystalline direction comprising both ΓK and ΓA symmetries, hence having both parallel and perpendicular momentum components.

In correspondence of crossed energy bands in the experimental scan shown in panel (a.), values for $q_{\parallel}$ and $q_{\perp}$ were determined and compared with the calculated $\varrho(\vec{q})$-values given along the high-symmetries of ΓK and ΓA. Hence, the dashed-dotted black curve given in fig. 4.20 (b.) reports in arbitrary units values for $\varrho(\vec{q})$ obtained by means of this comparison.

By comparing the experimental trends of the TDCS (red line) with the approximative theoretical trend (black dashed-dotted line) in the binding energy spectrum of fig. 4.20 (b.), it is possible to find accordance (in the energy position) for the $\varrho(\vec{q})$-distribution coinciding with the σ_3- and $\pi_{1,2}$-bands. Whereas for σ_1, the experimental TDCS is shifted towards higher ε_{bin} with respect to the expected value, by ca. 2 eV.

The electron momentum density distribution for ΓA shown in the plot on the right-hand side of fig. 4.21 clearly exhibits a strong contribution to $\varrho(\vec{q})$ occurring in correspondence of the σ_1-band. This energy band (substantially) contributes to the $\varrho(\vec{q})$-distribution for directions of the electron momentum parallel and perpendicular to the $\hat{c}$-axis.

Considering that the (e,2e)-experiment was performed for intermediate directions of $\Delta\vec{K}$ (neither only $\parallel$ nor only $\perp$ to the $\hat{c}$-axis) it also posses a parallel and perpendicular components, which automatically implies that also the initial state of the electron is characterised by the pair $(\vec{q}_{\parallel}, q_{\perp})$. For this reason, the shift in energy observed for the yield of correlated electron pairs in correspondence of a σ_1-electron in its initial state could be assigned to the fact that the actual experiment is not performed along high-symmetry directions of the crystal. To this end, it would be necessary to compare the experimental (e,2e)-yield with the calculated TDCS (as given in equation (2.12)) for values of $\varrho(\vec{q}, \varepsilon_{bin})$ representative for the real intermediate/mixed crystalline direction. Similar results were obtained for the "ΓM-scan-cut" of which the results are presented in the same form as for the ΓK-experiment in figure 4.22 (a.) and (b.). The kinematics employed for this (e,2e)-experiment was tuned again according the "DL"-model, in such a way thus to have R66, collecting the scattered electrons aligned with the first order diffracted peak along the ΓM-symmetry direction, for a polar angle at the manipulator axis of $\theta_{man} = 231°$ as discussed on the basis of the diffraction pattern shown in fig. 4.19.

Also in this case, the TOF-analyser remained tuned on a fixed ejected electron energy E_e of $5\,\text{eV} \pm \Delta E_{res}$, however its collection angle θ_e (given wrt. the surface normal) was of 51.4°. The momentum vectors of both incident $\vec{k}_0$ and scattered $\vec{k}_s$ electrons were aligned along the optical axis of R66 under a polar angle of ca. 38.6° according to the "DL-model" previously described. The energies scanned for the initial state covered the same range as during the scan performed

along the ΓK-direction. The scan done along the in-plane ΓM-direction sampled regions in first and second Brillouin zone (see blue squares in fig. 4.22 (a.)). Also in this experiment both parallel and perpendicular components should be considered while performing the comparison between the measured TDCS and the estimated theoretical (e,2e)-yield as expected on the basis of the calculated momentum densities.

Similar first-order approximation analysis was conducted also in this case, when comparing the measured (e,2e)-yield, of which the trend is guided by the blue line in fig. 4.22 (b.), with the theoretically expected distribution for $\varrho(\vec{q}, \varepsilon_{bin})$ (given as black dashed-dotted line in the same plot). The analogy between the two curves is rather poor, in this case. Only the energy-position for the (e,2e)-yield measured in correspondence of the π-bands (at E_{Fermi}) corresponds to the calculated $\varrho(\vec{q})$ to some extent. Remarkably, some (e,2e)-intensity is observed around binding energy -10 eV, where the σ_3-band is crossed at BZ-boundary.

According to the calculated momentum density given along ΓM (shown in the middle plot of figure 4.21) the contribution to the $\varrho(\vec{q})$ given by σ_3 should be the least important one, moreover it appears at a value of $q_{\parallel} \approx 3.4 Å^{-1}$ which is much bigger than the value actually sampled during the scan.

It is well-known, that so-called "$\vec{G}$-assisted" events can Umklapp in the first BZ DoS that belong to further BZs hence contributing to the (e,2e)-signal. When the momentum of the electron (in this specific case its $q_{\parallel}$-component) happens to coincide with a value corresponding to a boundary in the Brillouin zone, a so-called Umklapp-process can re-project the momentum of this electron into another region in phase-space, with a q-value increased (or diminished) by the value of the $\vec{G}$-vector component for that crystalline direction. Due to this effect, sometimes is it possible to observe higher yields than expected for the original $q_{\parallel}$-component, due to additional contributions from other regions in phase-space. Even if a $\vec{G}$-assisted event were hypothesised, the in-plane $\vec{G}_{\parallel}$(ΓM) is $2.94 Å^{-1}$. For the correspondent $q_{\parallel}$-value, of this reciprocal lattice vector, the momentum density contribution given by σ_3 along ΓM results being nearly zero as well. After having excluded the hypothesis of a $\vec{G}$-assisted event, the appearance of some (e,2e)-intensity for this $q_{\parallel}$ and for ε_{bin} = -10 eV could be only explained on the basis of the intermediate direction of the experiment.

Again a shift in ε_{bin} of about 2–2.5 eV between the experimental TDCS (blue) and the theoretically predicted one (black dashed-dotted) is observed for the σ_1-band. By looking at the various energy bands given in fig. 4.22 (a.) and considering the experimental resolutions: in Δq, indicated by the horizontal bars, and in $\Delta E \sim 3$ eV[9], the measured (e,2e)-yield is found in fact at a lower value with respect to the E-bands of $\sigma_{1,2}$ as drawn in panel (a.), however the large resolution in momentum could lead to measuring intensity at lower ε_{bin} than expected in

[9]Note that the vertical bars plotted in panel (a.) merely indicate the energy steps of 2.5 eV as done during the experimental scan

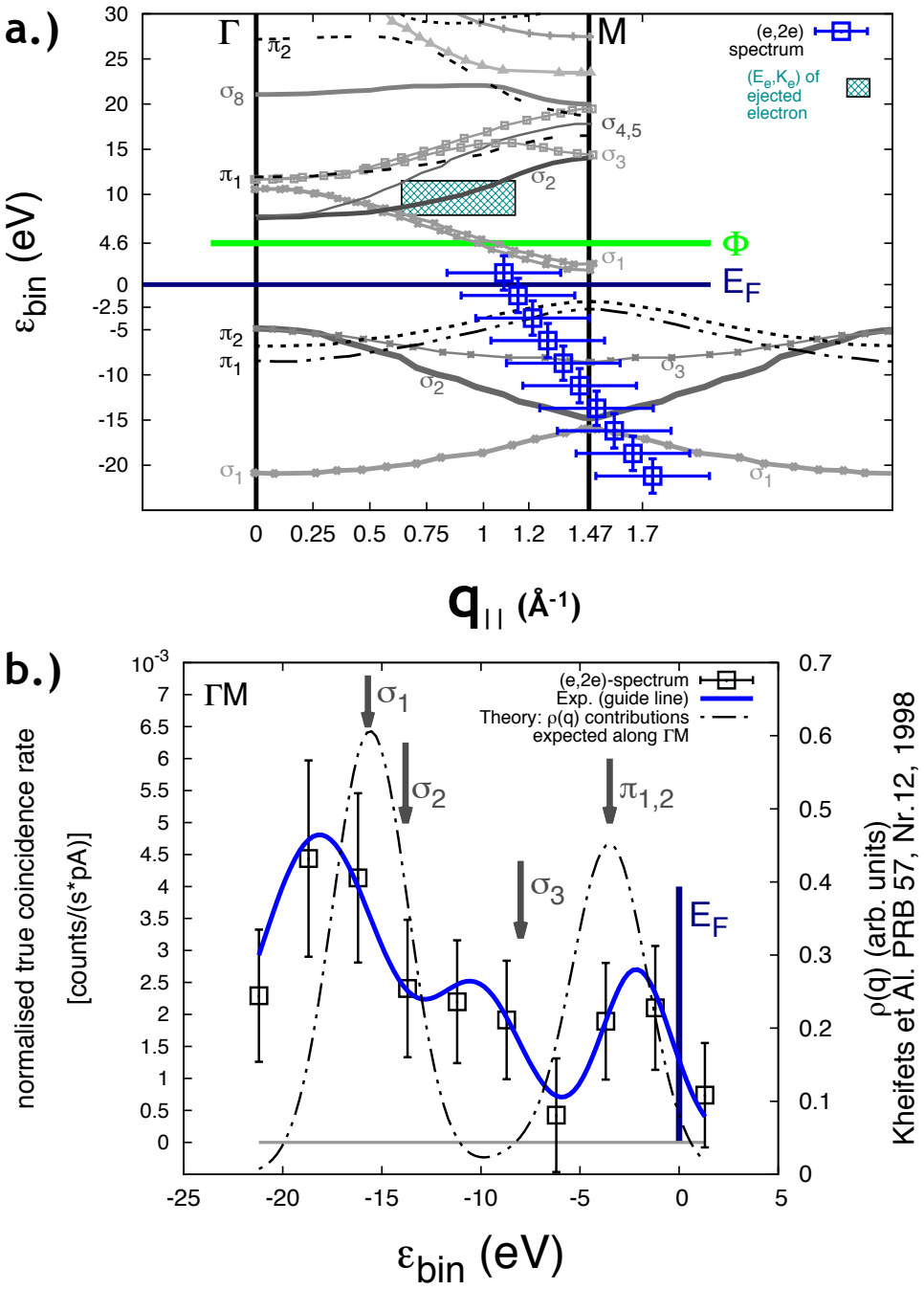

Figure 4.22: (a.) The "ΓM-scan-cut". Similarly as shown in case of the "ΓK-scan-cut" this (e,2e)-experiment was also performed for a constant final state (green box) centered at $E_2 - E_{Fermi} \approx 10\,eV$ while scanning over initial states with $\varepsilon_{bin} \in (-22.5; +3.7)\,eV$, indicated by the blue data points. Panel (b.) displays the results of the experiment where the normalised (e,2e)-yield is given as a function of the binding energy of the recoil electron. Black data points were measured with ca. 20% error and are guided by the blue line. Dashed-dotted black line represents an orientative trend for the momentum density, $\varrho(\vec{q})$ – scale on the right-hand side – expected according to [200, 159] in correspondence of the energy bands that were scanned throughout the experiment for the sole ΓM crystalline direction.

correspondence of σ_1-contributions measured in 2.BZ.

It shall be pointed out, also in this case, that the role played by the perpendicular component of the momentum in the initial state is not negligible. If we compare with the distributions of $\varrho(\vec{q})$ given along ΓA, in fact, a large contribution to the momentum density is observed exactly in correspondence of the σ_1-band (see right-hand side plot in figure 4.21).

For these experiments, the analysis and interpretation of the measured TDCS done on the basis of information entailed in former works [200, 159] was attempted only from a *qualitative* point of view. In spite of all the mentioned "aside-considerations" and limitations of the method used to inter-compare the actual experimental data with the theory presented by Kheifets *et al.* in their work, it was nonetheless possible to interpret to some extent spectral features revealed by the experimental TDCS. This preliminary analysis of the measured coincident SEE-yield, done on the basis of the calculated distributions of the $\rho(\vec{q})$ for the three main crystallographic directions in Graphite, showed that the observed spectral intensity mostly follows modulations of the $\rho(\vec{q})$ along these three symmetry directions.

Proper calculation of the (e,2e)-cross-section would allow to comment not only on the energy-positions of the observed (e,2e)-intensities, but also to compare with the predicted intensities. This final comment shall serve as a hint for future experiments and data analysis.

4.3.2 Al(100) vs. poly Al: (e,2e)

In nearly-free electron (NFE) metals like Aluminium the dominant inelastic scattering mechanism is represented by characteristic collective modes, also known as plasmons[10]. These characteristic excitations are due to the aggregate-coherent motion of electron-hole pairs in a conducting medium describable by a free-electron gas dielectric function. In this picture, plasmons are electron density fluctuations which at specific frequencies give rise to an instability in the dielectric function of the medium. In Al, these characteristic collective excitations correspond to the excitation of a surface plasmon, at $\Delta E = \hbar\omega_s = 10.5\,eV$, and of a bulk plasmon, at $\Delta E = \hbar\omega_b = 15\,eV$, and are recognisable as prominent and sharp peaks in the energy loss spectrum. For this reason, this material has been chosen as "test-ground" for several investigations dealing with these collective modes.

It was long believed [254, 93], that these excitation channels play a substantial role in the generation and ejection of LE-SEs. SEES acquired on Al-surfaces by Everhart *et al.* [92] exhibited some structures in the energy distribution of SEs. The energies at which they found these features superimposed over the rather bland SE-spectrum, corresponded to an ejected electron energy of $E_e = (\hbar\omega_s - \Phi) \approx 6.3\,eV$ in case of the surface plasmon and to $(\hbar\omega_b - \Phi) \approx 10.5\,eV$ in case of the bulk plasmon. Here, the workfunction, Φ for Al is 4.2 eV. On the basis of these (faint) spectral features, it was assumed plasmon losses being the main channel of excitation giving rise to these structures in the SE-spectrum.

However, by means of spectroscopic techniques delivering a double-differential information – such as the REELS and SEES described in previous sections – it is intrinsically difficult to determine to which extent inelastic processes contribute to the production of SEs in the LE-regime.

The first experimental proof drawing a direct link between these characteristic energy losses and the SE-spectrum was performed in 2008 by Werner *et al.* [147], where the role of surface and bulk plasmon decay in the SEE-process was investigated on an Aluminium (100) surface. In their work, it could be undoubtedly assessed that certain features in the SE-spectrum appear as the result of plasmon decay and that maxima in the (e,2e)-cross section are linked to correlated electron pairs, of which one is the inelastically scattered electron, that has lost $\Delta E = \hbar\omega_{s,b}$ and the other is the time-correlated secondary, which is emitted with $E_e = (\hbar\omega_{s,b} - \Phi)$.

Further experiments performed in recent years, both at TUV [148, 126] and at RM3 [150, 149] all demonstrated that secondary electron emission is particularly enhanced at plasmon frequencies. Aluminium was the privileged target in all these investigations.

The experimental evidence for this resonant behaviour of the SE-cross section to the characteristic frequencies of plasma, arose, among other things, interest also from the theoretical

[10] The quasi-particles resulting from the quantisation of this collective oscillation.

point of view. In 2012, Kouzavov and Berakdar proposed a model describing the phenomenon of plasmon-assisted electron-electron collisions leading to the emission of secondary electrons [164].

Most of the works mentioned in this preamble will be used in the following as a comparative platform to the present set of data.

The overall objective of this work consists in drawing a direct link between excitation and emission processes for the understanding of the underlying processes involved. For the reasons stated above, Aluminium represents an ideal candidate to study the many-body character of excitations occurring in the electronic sub-system of a solid, of which the plasmon is the main representative in the energy ranges at the focus of our investigations.

Since former (e,2e)-spectra already demonstrated that the singly excited plasmons represent one main energy transfer channel through which SEs are generated, one of the aims pursued in this work was to further examine the character of plural and multiply-excited plasmons and their role in the SE-emission process.

Comparison between TDCS from the single crystalline and the polycrystalline surface was made in the attempt to separate contribution to the SEY due to the long-range order of the sample from those induced by its electronic structure. The intention of this inquiry was to identify the underlying "building-block" of the scattering mechanism leading to the observed coincident SEY, independently from the degree of long-range order in a sample.

Figure 4.23 shows the result of an investigation of a single crystal Al(100)-surface bombarded by monochromatic PEs of 101.7 eV. The coincidence experiment was conducted in specular reflection for the TOF-analyser, where scattered electrons were detected under a polar angle of 30°. The SE-spectrum was collected under 60° emission angle by R66 and its electron optics was purposely tuned to obtain a high-transmission for the LE-range.

Each (e,2e)-experiment was conducted at a fix energy window, meaning that each analyser remained tuned on the selected kinetic energy over the whole duration of one experiment (one point-acquisition, which typically lasted 16–20 hours) after which the surface needed to be re-prepared (sputtered and annealed as explained in sections 3.1 and 3.3.4).

The central panel in fig. 4.23 displays the (e,2e)-yield obtained after merging all (e,2e)-experimental points measured over the total length of the investigation (ca. 110 acquisitions frames). The TDCS is displayed as a function of the energy lost by the incident electron (given along the ordinate axis) and of the kinetic energy of the emitted SEs (along the co-ordinate axis). The probability for their correlated detection is indicated by the colour scale in arbitrary units. On the left-hand side of the 2D-colour map, aligned with the ejected electron energy scale, the 2DCS displaying the energy distribution of SEs is shown in blue and just below the surface plot entailing the TDCS, a REELS (given with respect to energy loss scale) measured over the energy range of interest is shown in black. The scales of the two 2DCS are aligned with respect to the energy scales of the (e,2e)-cross section.

Prior to setting up each (e,2e)-coincidence measurement, the clean and ordered surface was re-aligned to the specular angle of TOF and both 2DCS of inelastically scattered and secondary electrons were measured under the exact same kinematics as the subsequent (e,2e)-coincidence measurement. Acquisition of single-electron spectra was routinely done not only to monitor the quality of the surface and its alignment, but foremost to use them to properly normalise the measured (e,2e)-cross section. To this end, generally both 2DCS were normalised to the

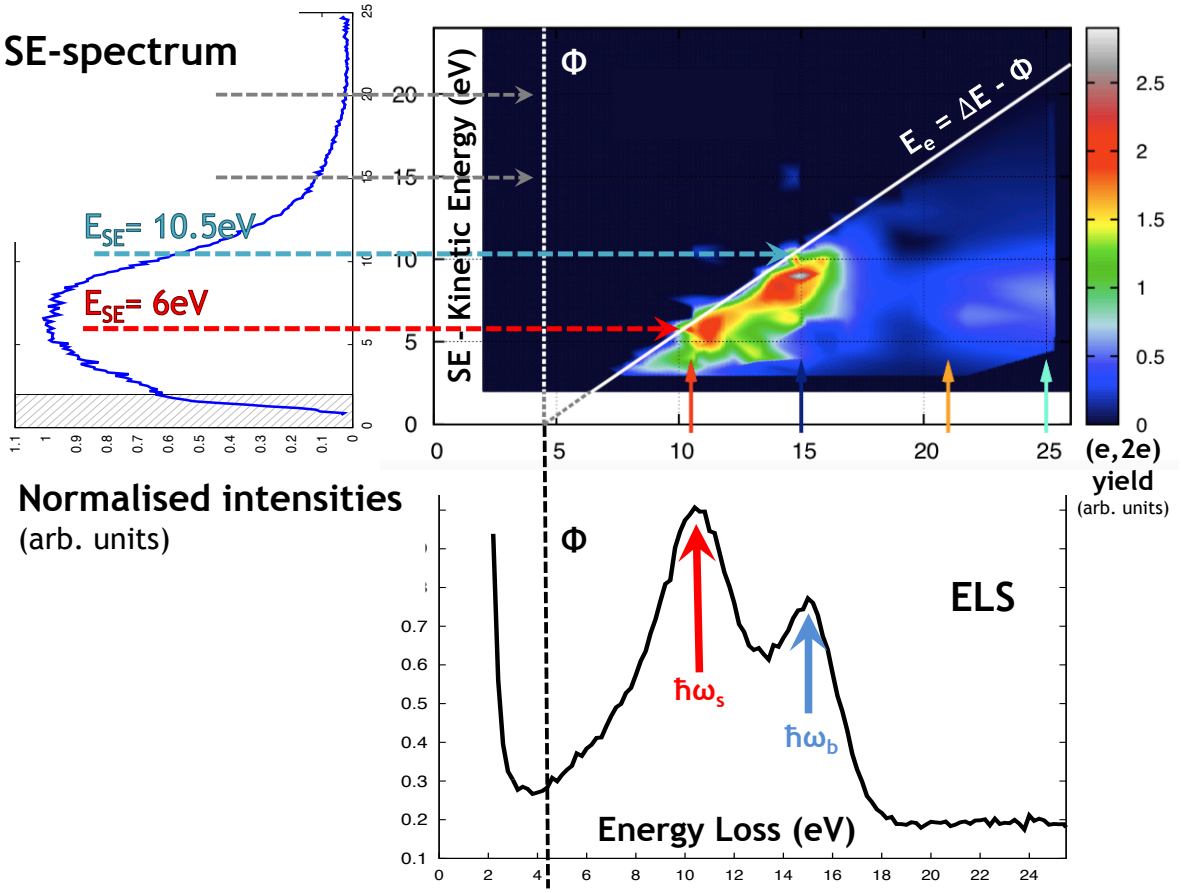

Figure 4.23: (2D-panel): Triple-differential Cross-section from Al(100) along with its correspondent double-differential electron spectra. The SE-spectrum (blue) was acquired using R66 under the exact same scattering conditions as during the (e,2e)-measurement. Both 2DCS were normalised to the maximum of the SE-peak and surface plasmon peak, respectively. The ELS (black) at the bottom was measured with TOF under specular reflection conditions (same as during the coincidence experiment). The 2D-plot displays the (e,2e)-yield (colour scale) obtained as a function of the energy lost by the primary electron (scale along the x-axis) and of the ejected electron energy (scale along the y-axis). [255]

maximum in their respective range and to the primary current. The REELS was normalised to the intensity of the $\hbar\omega_s$ and converted to energy loss scale, indicated at the bottom of the ordinate axis. It exhibits evident surface and bulk plasmon peaks at ∼10.5 eV (red arrow) and 15 eV (blue arrow), respectively. For higher energy transfers corresponding to the excitation energy of a doubly-excited plasmon the intensity in the ELS drops by a factor of 5 if compared to the intensity of the surface plasmon peak. The orange and light-blue arrows at the bottom of the

surface plot indicate energy positions for: (1.) a double surface plasmon, $2 \cdot \hbar\omega_s$ =21 eV and (2.) a doubly excited plasmon composed of $(\hbar\omega_s + \hbar\omega_b)$= 25 eV.

Similarly, also for the LE-regime, the 2DCS given by the SEES was acquired under the exact scattering conditions used in the following (e,2e)-experiment. The SE-spectrum was detected under a 60° emission angle, employing a set of lenses which was optimised for the kinetic energy range of interest.

After several optimisation procedures adopted, it was possible to obtain a constant transmission for energies ranging between 6 eV and 16 eV. Transmission for the LE-SEs with E_e <6 eV was no longer uniform, however after correcting the spectrum by using the determined transmission function, it was possible to obtain a reliable SE-spectral shape, which was comparable to spectra acquired by means of TOF, where the transmission was determined to be uniform down to 2-3 eV and to spectra taken from literature [243] (More details concerning the correction of SEES for the transmission function can be found in subsection 3.3.4.1). After this procedure transmission of LE-SEs through the electron optics of R66 was considered reliable for electron energies down to ca. 4 eV. This is the reason why the (e,2e)-yield shown in the false-colour map of fig. 4.23 goes down to ca. 3.5 eV (accounting for the experimental energy resolution) ejected electron energies, of which the scale is given along the co-ordinate axis.

The pass energies at either analyser were kept constant for each measurement frame and they were E_{pass} =40–45 eV for the scattered electrons at the TOF-analyser and E_{pass} = 22–25 eV for the acquisition of the SE-spectrum in R66.

As already hypothisised by the work conducted by Chung and Everhart [93] by the mere analysis of the two 2DCS, it is difficult to estimate to which extent the prominent inelastic scattering features of a surface and bulk plasmons contribute to the emission of secondary electron. However, the 2D-map displaying the (e,2e)-yield reveals regions in the TDCS with evidently higher intensity, which correlate SE-emission at these plasma frequencies. In fact, at exactly the characteristic energy losses of the singly excited plasmons, $\hbar\omega_s$ and $\hbar\omega_b$, the TDCS reaches its maximal values, thus undoubtedly indicating that the probability for SEE is highest in correspondence of these plasma frequencies.

This plasmon-resonant SE-emission behaviour was already observed in Ref. [147] on the single crystalline surface of Al(100) and again in 2013 [126] on the polycrystalline Al sample.

At the frequencies of the doubly excited plasmons – a double surface plasmon with 21 eV (indicated by the orange arrow in the 2D-map of fig. 4.23) and a doubly-excited plasmon composed of a surface and a bulk plasmon with 25 eV (light-blue arrow) – some intensity for correlated electron emission can be observed in the 2D-map, however with a (e,2e)-yield of the order of 0.7 arbitrary units (on the colour scale). The (e,2e)-yield obtained in correspondence of these doubly-excited plasma frequencies is diminished by a factor 3.6 with respect to the yield measured in correspondence of the single surface and bulk plasmon excitations. Furthermore, this (e,2e)-intensity measured in correspondence of these doubly-excited plasmons is found for

kinetic energies of the ejected electron corresponding to the emission of a SE escaping from the target as if it were generated by the decay of a single plasmon only. Since the emitted electron has a kinetic energy corresponding to the decay of a single plasmon, with $E_e = \hbar\omega_{s,b} - \Phi$, this suggests that the excitation and decay process of a double plasmon has an incoherent character. If these double-plasmon losses decayed coherently, the whole kinetic energy would be invested in the promotion of a single electron with $E_e = (2 \cdot \hbar\omega_{s,b}) - \Phi$. In this case, (e,2e)-intensity should be observed along the Fermi diagonal at higher ejected electron energies (indicated by the grey arrows in the SE-spectrum of fig. 4.23). However, the sole intensity visible in the TDCS is observed for ejected electrons with kinetic energies corresponding to the excitation/decay of a single plasmon loss.

These double-plasmon losses can either decay simultaneously emitting two SEs at once or in a sequential fashion, where one electron is emitted after the decay of each plasmon, thus also resulting in the emission of two distinct electrons. In our experiment, it is impossible to distinguish whether the decay of such a double plasmon occurs simultaneously or as a Markov-chain like process. Nonetheless, by means of this experiment it was possible to asses that the higher probability for SEE in case of double plasmon excitation/decay occurs incoherently resulting in the emission of two distinct electrons. It shall be noted, that this does not exclude the possibility for coherent double-plasmon decay, however for the measured (e,2e)-yield in this experiment, it can be affirmed that it is far more likely for a double-plasmon to decay in an electron pair than for it to give rise to one single SE.

As previously explained in the case of HOPG in subsection 4.3.1, the intensity contributions that are observed slightly above the Fermi level (white diagonal in fig. 4.23) are due to the experimental resolutions, which do not consent to observe a neat (step-function-like) intensity drop as expected at Fermi level. The energy resolution in these experiments can be in fact represented by a Gaussian with a FWHM of ca. 2.65 eV, which convoluted with the Fermi step yields the real slope measured in our spectra.

The data set presented in figure 4.23 will be compared to other (e,2e)-coincidence experiments in the following.

The series of measurements performed to obtain the (e,2e)-cross section shown in fig. 4.23 can be alternatively displayed as a function of the initial state of the bound electron prior to its emission, hence as a function of its binding energy, ε_{bin}, and parallel momentum, $q_{\parallel}$. Figure 4.24 represents the regions in the ($q_{\parallel}$, ε_{bin})-phase-space given along the ΓX-crystalline direction, which were sampled during the series of experiments shown in the precedent figure. The experimental points shown in fig. 4.24 are given in the reduced Brillouin zone scheme (RBZ) accounting for Umklapp-processes. The regions in phase-space sampled are mostly centred around the X-symmtry point, at the BZ-boundary. The differently coloured and numbered symbols (see legend) highlight experiments which were conducted to investigate SE-emission in correspondence of the various characteristic energy losses of both the singly- and doubly-excited plasmons. The blue rectangles

drawn around the blue triangles highlighting the experiments conducted in coincidence with the bulk plasmon loss symbolise the average experimental resolution obtained during each such an experiment. It is a well-known fact that in crystalline structures at the BZ-boundaries the presence

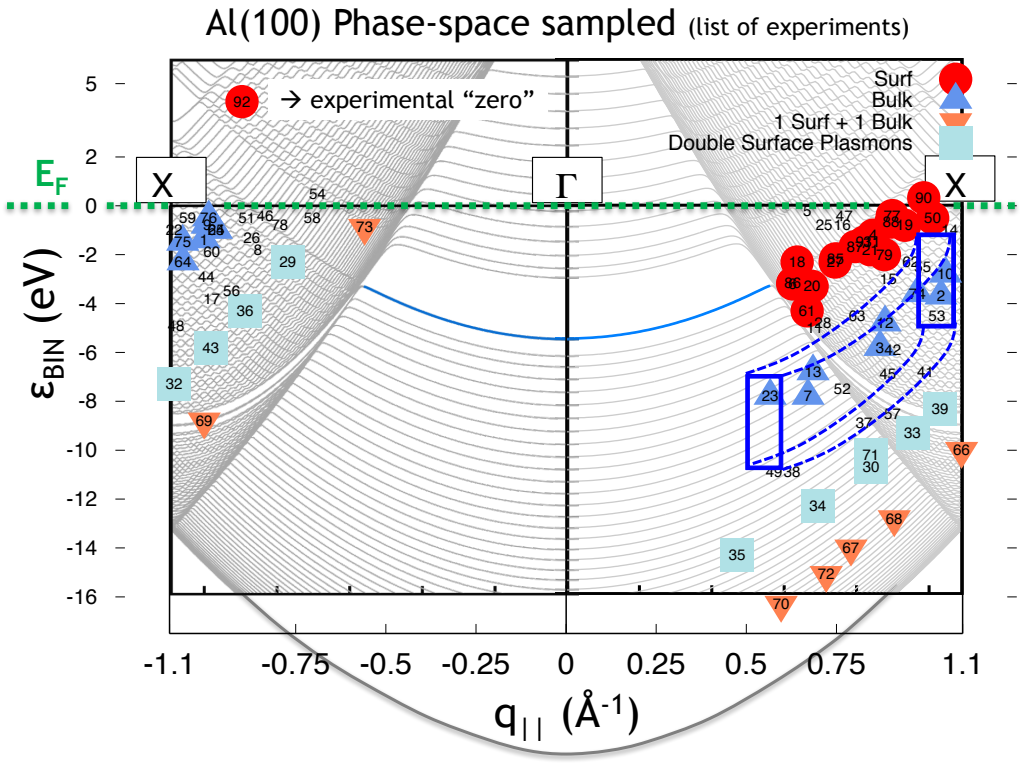

Figure 4.24: Regions in the Al(100) ($q_{\parallel}$,ε_{bin})-phase-space sampled by the series of (e,2e)-experiments. Experiments for which the SE-emission process was investigated in correspondence of a characteristic plasmon loss in Aluminium are highlighted in colours. The blue rectangular area symbolises the averagely momentum and energy resolutions obtained during an experiment. (The calculated BS used for this plot was extracted from Ref.[149].)

of the so-called Van Hove singularities in the DoS may either enhance or diminish the knock-out cross section [256]. The TDCS given as a function of ΔE versus E_e demonstrates that enhanced SE-emission occurs exactly in resonance with the singly-excited plasmon losses. For the kinematics achieved in the actual experiment, the regions in phase-space sampled in correspondence of these characteristic losses and for differently bound electrons (or correspondingly different kinetic energies of the secondary electrons) are proximate to the BZ-boundary at the X-symmetry point. The presence of such singularities in the DoS could be concurring with the already assessed plasmon-enhanced SE-emission. In spite of the fact that the actual experiment was conducted by investigating the (e,2e)-cross section at a BZ-boundary no additional enhancement could be observed at these symmetry points. Furthermore, the achieved experimental resolution (of $\Delta E_{res} \simeq 2.55\,\text{eV}$ and $\Delta q \simeq 0.13\,\text{Å}^{-1}$) does not permit to make any precise statement on the effect of Van Hove singularities on the emission of SEs.

Authors from Ref. [257] performed a calculation predicting the effects of these singularities

in the (e,2e)-cross section for other experiments done on single crystals. The sensitivity needed for an experiments needs to be much higher to accurately investigate the transition regions at BZ-boundary. Their calculation predicted that these kinks in the DoS have practically no effects on the emission of SEs in their (e,2e)-experiments.

In the following, a comparative analysis of the actual (e,2e)-experiment is performed with a data-set obtained from another (e,2e)-experiment and with the simulation based on the theoretical model proposed in Ref. [164]. Figure 4.25 entails three 2D-plots representing TDCSs from Aluminium. In this case, all three TDCSs are plotted as a function of the scattered electron energy (E_s) and of the ejected electron energy (E_e).

Panels (a.) and (b.) are two experimental (e,2e)-cross sections measured respectively on Al surfaces exhibiting different long-range order and acquired under two different kinematical conditions, each one of which illustrated on the right-hand side by a simple scheme. The (e,2e)-cross section shown in panel (a.) represents the actual experiment (already shown and discussed in fig. 4.23) measured on the Al(100) single crystal. Panel (b.) displays the results obtained on a polycrystalline Al surface [126, 217].

Both experimental results are compared to a numerical simulation (shown in panel (c.)) based on one theoretical model proposed in Ref. [164] which describes the SE-emission process as a plasmon-assisted electron-electron collision occurring in a metallic surface, in which screening properties are described by the dielectric response of the medium. Furthermore, in their theoretical framework, the effects of the surface dielectric response were incorporated into the treatment of the (e,2e)-process for the first time.

In metallic surfaces, the two main mechanisms for SEE are associated either to a direct knock-out process (where the SE is emitted as a consequence of direct scattering between the incident primary and the valence- or conduction-band electron) or to the relaxation of a collective excitation, such as plasmons, i.e. a *plasmon-assisted* event. For the simulation shown in panel (c.) of fig. 4.25 Kouzakov and Berakdar approximate the metal through a jellium, thus disregarding the role played by the band structure of the solid and the interconnected inter-band transitions, which in a jellium are free-electron-like. Therefore, when the energy loss undergone by the incident primary electron corresponds exactly to the characteristic excitation frequency of a plasmon, the screened Coulomb potential resonates to this frequency and this can lead to an enhanced emission of secondary electrons, at these specific energy losses. Numerical results based on this model allowed to inquire the role played by the plasmon in the dynamical screening of the electron-electron interaction.

Panel (c.) shows the numerical results for the correlated electron energy distribution obtained by using the random-phase approximation (RPA) to describe the dielectric response of a degenerate electron gas, by assuming an infinite surface barrier (IB), which is ideal within the specular reflection model (SRM) and, at last, in order to describe the electron transport in the metal, a

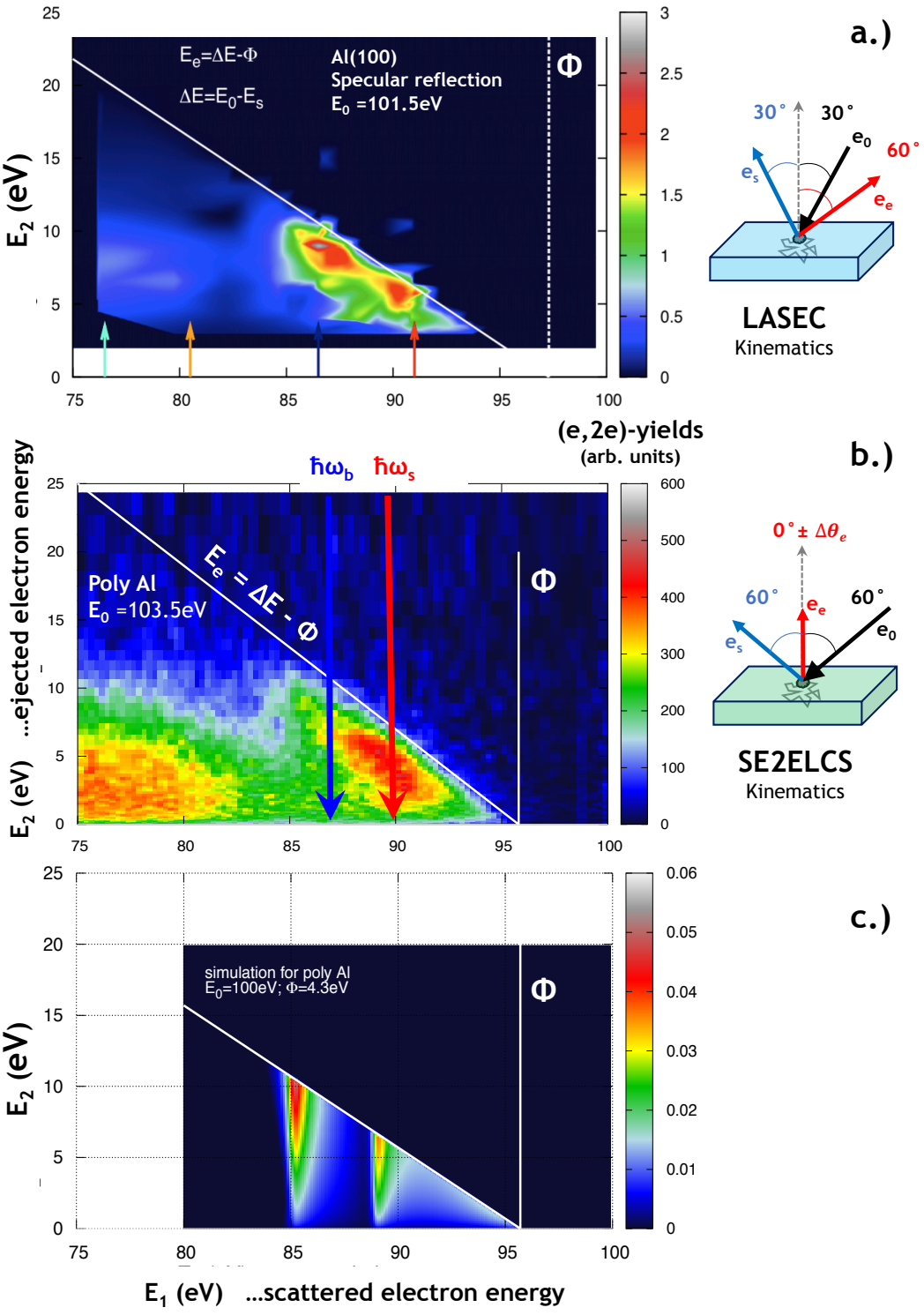

Figure 4.25: Intercomparison of two (e,2e)-coincidence data sets with one theoretical model presented in Ref. [164]. The experiments shown here were performed on two Aluminium surfaces exhibiting a different long-range order and under different kinematics (as shown on the right-hand side of each panel respectively). (a.) Triple-differential cross section from Al(100) – same data as shown in Fig. 4.23 displayed as a function of scattered and ejected electron energies. (b.) SE2ELCS from polycrystalline Al – same data as published in Ref. [126]. (c.) Simulation for polycrystalline Aluminium performed by Kouzakov and Berakdar also shown in Fig. 3 of Ref. [164].

hydrodynamical approximation (HA) was employed . The combination of all above-mentioned approximations and assumptions result in the simulation shown in panel (c.), which indeed resembles the most the experimental results presented in panels (a.) and (b.). The outcome of this model was compared to experimental (e,2e)-yields from Al(100) obtained by Werner et al. in 2008 [147], finding satisfactory accordance, thus confirming that in Al, the electron ejection-mechanism occurring in a direct electron-electron scattering process is decidedly enhanced at plasma frequencies.

In spite of the different long-range order of the specimens and the different kinematics employed during the acquisition of the TDCSs shown in panels (a.) and (b.), it is possible to immediately recognise that in either (e,2e)-cross section the highest coincidence yield is observed in the single-scattering regime and for scattered electron energies of $E_1 = 91\,eV$ and $86.5\,eV$, corresponding to the characteristic energy losses $\Delta E = E_0 - E_s$ of a surface and bulk plasmons, respectively. In correspondence of these characteristic energy losses, the ejected electrons escape from the target with the full energy loss undergone by the primary electron minus the target work function (with $E_e = (E_0 - E_s) - \Phi$). Hence, the resulting SE is the product of one single scattering event.

While in case of the single crystal (a.), the coincident SEY is similarly high at both plasmon frequencies, in the polycrystal (b.), in correspondence of the bulk plasmon energy there occurs to be a subtle decrease in intensity. This local minimum in the intensity was ascribed to the so-called "Begrenzungs"-effect [258, 259, 126]. Theoretical calculations show that the distribution of energy losses occurring in one individual surface excitation, also known as differential surface excitation probability (DSEP) peaks at the frequency of the surface plasmon, whereas it exhibits a negative excursion exactly in correspondence of the bulk plasmon frequency. On the other hand the distribution of energy losses in individual bulk losses, also known as differential inverse inelastic mean free path (DIIMFP) exhibits a maximum at the volume plasmon energy. The complementarity of DSEP and DIIMFP at the energy loss of the volume plasmon leads due to the presence of surface excitations to a diminished intensity of the volume excitations.

The fact that the Begrenzungs-effect seems to affect more the (e,2e)-yield in the polycrystalline sample could be ascribed to the fact that in this case the (e,2e)-cross section is averaged out over all possible symmetry directions. In the single crystal, instead, due the chosen Bragg-scattering condition only those inelastic events which are assisted by the diffraction process (elastic collision of the electron with the crystalline lattice) are selected and enhanced in a specific direction.

Independently from the long-range order of the target it seems that in both (e,2e)-cross sections the single vertex interaction picture is the fundamental mechanism behind the creation-emission process of a SE. Just like in the Al(100), also in the Al polycrystal, in correspondence of the doubly-excited plasmon losses there intensity appears for SEs with kinetic energies corresponding to the decay of one single plasmon. Panel (b.) does not exhibit any intensity along the Fermi level for higher energy transfers either, thus reconfirming that also in the polycrystalline surface plural plasmon losses decay incoherently.

The simulation shown in panel (c.) exhibits maximal (e,2e)-yield only at the plasmon frequencies. Moreover, at these energy losses the intensity of (e,2e)-events decreases rather slowly for ejected electron energies going from the Fermi level down to nearly 0 eV. Both experimental results exhibit at these plasma frequencies their maximal intensity right at the Fermi level, whereas this intensity tends to rapidly decrease for secondary electrons with lower kinetic energies. Furthermore, intensity in between plasmon peaks does not go down to zero. These discrepancies between experiment an simulation can be ascribed to (i.) the experimental resolution and (ii.) the analysers transmission. As previously mentioned, in case of the (e,2e)-measurement conducted in the LASEC laboratory, the transmission of the analyser collecting the slow ejected electrons was found to be uniform only down to ∼4 eV. Below this kinetic energy it was not possible to measure.

In figure 4.26 a more detailed inter-comparison between the three data-sets is performed. Panel (a.) shown the TDCS measured at RM3 on the Al(100) containing a rectangular area (highlighted in orange) selecting regions in the (e,2e)-spectrum along the Fermi level. All electron pairs contained in this rectangular area associate to each varying energy transfer (indicated along the ΔE-scale) an ejected electron with a given kinetic energy (given along the co-ordinate axis) for which the initial state exhibits a constant binding energy (ε_{bin}). The herewith obtained (e,2e)-yield represents a SEE-intensity given as a function of various energy loss transfers, however by keeping the initial state of the ejected electron nearly constant (with $\varepsilon_{bin} = const.$ and variable $q_{\parallel}$ of the bound electron).

To illustrate the corresponding region in the ($q_{\parallel}$,ε_{bin})-phase-space for these selected events, the same rectangular area is plotted in panel (b.) as a function of the initial state. All ejected electrons escape from the target as a consequence of different energy loss processes, however they all arise from a region in phase-space with constant binding energy right below the Fermi level.

Such a selection of electron pairs was performed on all three data-sets (experimental and numerical) presented in figure 4.25 and the resulting linear plot is shown in panel (c.) of fig. 4.26. The (e,2e)-yields shown in this linear plot are given as a function of the energy losses undergone by the incident electron. The black curve with open squares is the result obtained by the actual (e,2e)-experiment performed at RM3. The (e,2e)-intensity was normalised to the maximum intensity obtained in correspondence of the surface plasmon energy. The light-green dotted curve represents the selective (e,2e)-cross section of the SE2ELCS from poly Al. Kouzakov and Berakdar's simulated data are displayed as continuous dark-green line.

For all three cases, it is evident that in the energy loss range, characteristic for the single plasmon excitations, the SE-yield is strongly enhanced, thus confirming the electron scattering model describing plasmon-assisted SEE. Furthermore, in case of the RM3-experiment the achieved energy resolution permits to distinguish between the two plasmon contributions, as predicted from the theory (dark-green). When tuning out of the plasmon resonances, hence going towards higher energy transfers, the so-called "conventional" (e,2e)-regime is entered. There, emission of

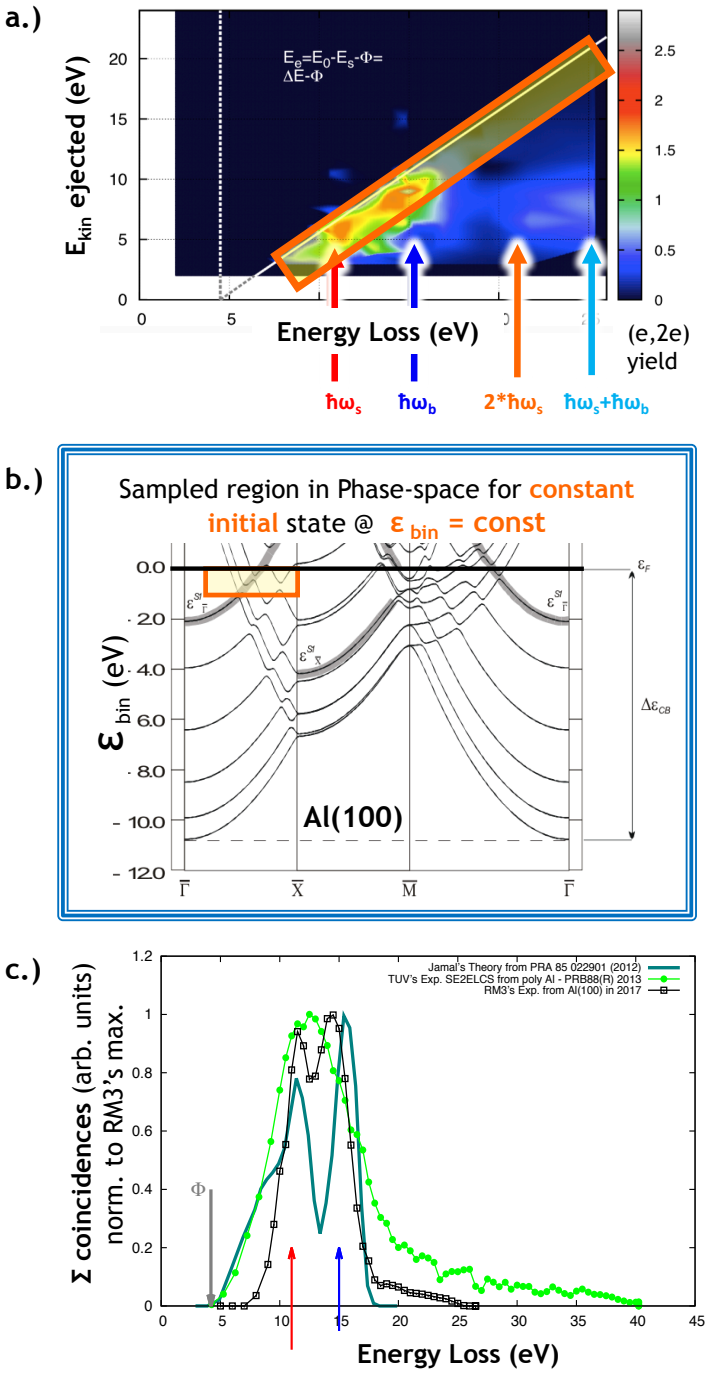

Figure 4.26: (a.) 2D-plot from Al(100): characteristic singly- and doubly-excited plasmons are indicated by coloured arrows. The orange rectangle highlights the area of selected (e,2e)-coincidence data which were acquired along the Fermi-level for different energy losses and ejected electron energies, while maintaining the binding energy of the initial state constant. (b.) same rectangular area as in (a.) given in terms of the "initial state", hence as a function of parallel momentum ($q_{\parallel}$) and binding energy (ε_{bin}) of the ejected electron prior to its emission. (c.) Linear spectrum of the (e,2e)-data selected in (a.) or (b.) along the Fermi level given as a function of the considered energy loss. Comparison is made between the two experiments performed on Al(100) (black curve with open squares), polycrystalline Al (light-green curve with filled circles) and the theoretical simulation from Ref. [164].

SEs can be induced by direct knock-out processes (as also state previously). For energy losses exceeding 20 eV, for all three cases an abrupt drop in intensity (of about one order of magnitude) can be seen in both experiments and theoretical calculations. This result re-confirms that SEE resonates at plasma frequencies and that the second probable mechanism for emission of SEs is far more improbable.

Similar data selection was performed for specific energy loss intervals, thus obtaining the (e,2e)-yield given as a function of the ejected electron energy at a specifically selected energy transfer. Examples for such a data analysis are shown in figures 4.27 and 4.28 where the selected energy losses correspond to the surface and volume plasma frequencies, respectively. In both figures, the upper panel illustrates the (e,2e)-cross section obtained from Al(100) wherein the selected rectangular regions are overlaid – a red rectangle for the surface plasmon and a blue for the bulk plasmon energy intervals. The lower panels, in either figure, display all linear spectra obtained from each analysed (e,2e)-data set after performing such a data-selection.

Along with the previously presented experimental and numerical data, for the two rectangular selections shown in figures 4.27 and 4.28, the inter-comparison is also performed with the (e,2e)-measurement in Ref. [147] on the same Al(100)-surface used in the LASEC laboratory for the actual experiment and for a same kinematics.

Figure 4.27 displays the (e,2e)-yield obtained in correspondence of the sole ΔE-interval corresponding to the $\hbar\omega_s \pm 0.5$ eV. The vertical red line indicates the Fermi level. Data points with errorbars – black squares and purple circles – represent the two data-sets of (e,2e)-experiments performed in the LASEC laboratory on the same Al(100)-sample (see legend). The black continuous line serves to guide the eye. The rectangular selection performed on the SE2ELCS data-set is given in light-green with open triangles, whereas the theoretical result is shown as dark-green continuous line.

To facilitate comparison, all data sets were normalised to the maximal yield measured in the (e,2e)-experiment conducted at RM3 in 2017. It shall be kept in mind that this normalisation method is founded on an arbitrary choice and that alternative methods could be also adopted. For all data-sets, the onset for SEE occurs (within the given energy resolutions) at the flexus point crossing the Fermi level (red arrow). Both (e,2e)-experiments conducted on the Al(100)-surface exhibit a similar trend and a rapid decay of intensity around 4 eV ejected electron energy, in dissonance to the theory predicted behaviour (dark green line). As previously mentioned this could be associated to the analysers transmission, which for example, in case of the actual experiment was reputed to be no longer reliable in the very low kinetic energy range.

The measured experimental "zero"-intensity is given by the two data points and their error bars at $\Delta E = (E_0 - E_s) = 15$ eV. The grey striped area represents the range of intensity contained within the "*experimental zero*" – i.e. this frequency range falls into the rate interval defining the frequency of truly uncorrelated coincidence events (accidental background) which sets the lower limit of

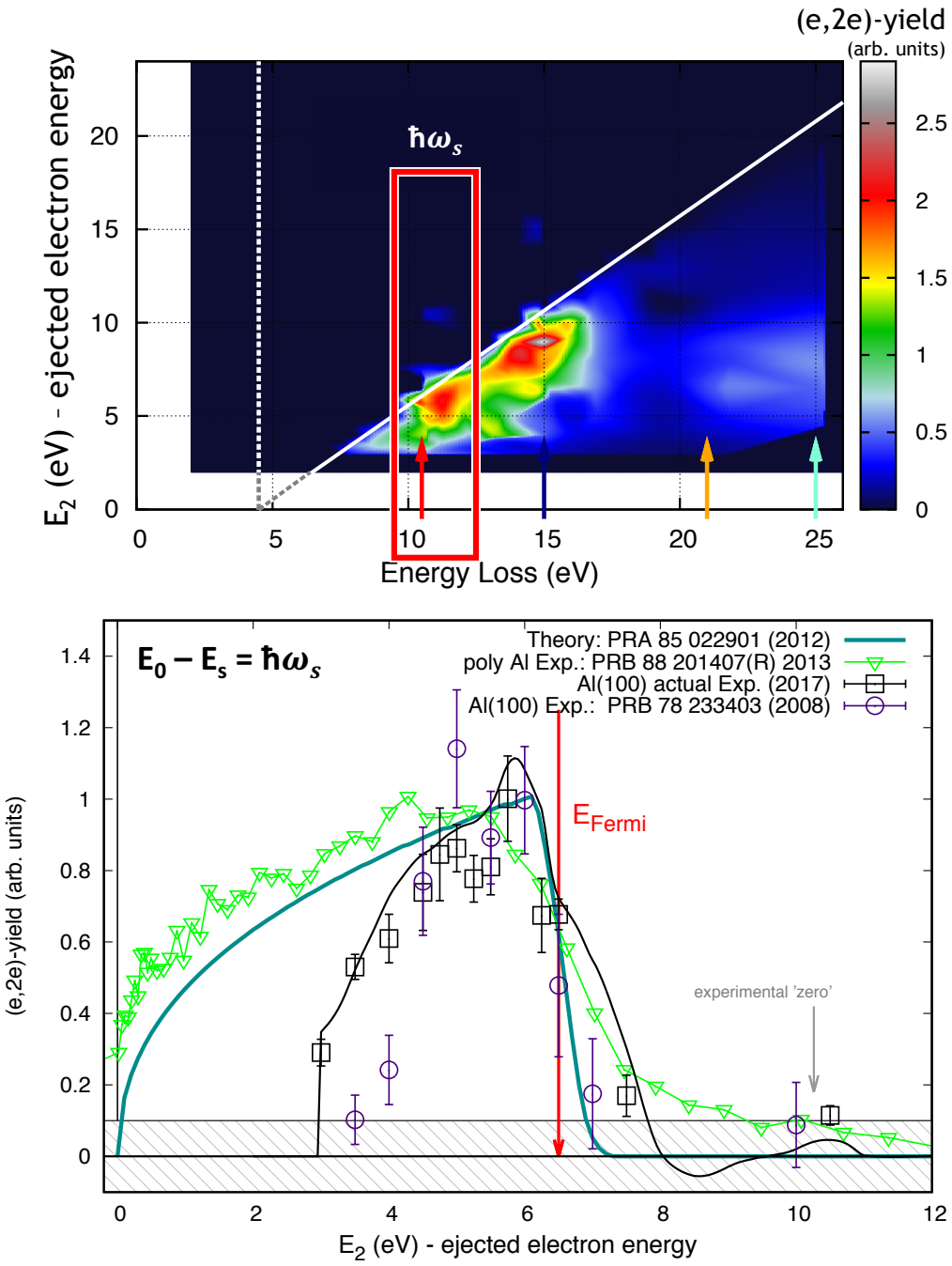

Figure 4.27: *Upper panel:* Selection of (e,2e)-data performed at the characteristic energy loss of a surface plasmon at $\hbar\omega$ =10.5 eV. *Lower panel:* Comparison among linear spectra displaying the (e,2e)-yield obtained within the selected constant energy loss interval centred around the surface plasmon loss given as a function of the ejected electron energy (abscissa). Experimental and simulated data sets are indicated in the legend.

sensitivity in our (e,2e)-experiments. An example for such an "experimental zero"-measurement was shown in paragraph 3.3.4.3.1 and is indicated as measurement "nr. 92" in figure 4.24, were all (e,2e)-measurements performed on Al(100) are displayed in phase-space.

In the specific case of measurement "nr. 92", the (e,2e)-experiment was purposely tuned to collect solely *uncorrelated* electron pairs, since their kinetic energies do not fulfil energy conservation. The (e,2e)-electron pair of choice was composed of an inelastically scattered electron with ca. 85 eV – hence after having suffered a characteristic energy loss corresponding to the excitation energy of a bulk plasmon ($\Delta E = \hbar\omega_s = 15\,eV$) – and an ejected electron with $E_e \simeq 15\,eV$, thus infringing energy conservation law (as previously explained in paragraph 3.3.4.3.1). Data points comprised in this area can therefore be regarded as null.

On the other hand, fairly good accordance is found between the SE2ELCS (light-green) and the simulation.

Inter-comparison among the various linear spectra obtained by the rectangular selection centred around the bulk plasmon energy, for an energy loss range of ca. $\hbar\omega_b \pm 0.5\,eV$, is shown in the lower panel of fig. 4.28. The same normalisation method was adopted also in this case. Whereas similar results were obtained for both RM3 measurements the intensity measured by SE2ELCS remains nearly constant also when going towards 0 eV-secondary electrons. Again, the experiments performed on the single crystal rapidly drop in intensity around 6 eV kinetic energy.

However, this diminished (e,2e)-yield occurring at 6 eV is not necessarily due to the analyser transmission in this case, since for such kinetic energies it was still uniform. According to theory though the measured drop in (e,2e)-intensity is still too abrupt. The unexpected nearly constant (e,2e)-intensity registered by SE2ELCS could yet not be clarified.

The inter-comparison of all these experimental data-sets with the theoretical prediction allow to assess that the onset for SE-emission occurs exactly at the Fermi level and that the maximal yield in correspondence of these two characteristic energy losses is expected to be right below the Fermi level. Whereas concerning the origin of the discrepancies between theory and experiments observed at lower kinetic energies (for $E_e \leq 4\,eV$) it is difficult to make a clear statement, since for this very low kinetic energy range it is notoriously difficult to tune the experimental equipment to perform reliable and precise measurements.

To definitively determine whether the (e,2e)-yield should rather gently decrease – as predicted by theory – when going towards lower kinetic energies for the ejected secondary, it would be necessary to repeat a series of dedicated (e,2e)-measurements with better energy resolution (of ca. 0.5 eV) and tuning the electron optical element of each analyser thus to obtain a uniform transmission down to ca. 1 eV energy.

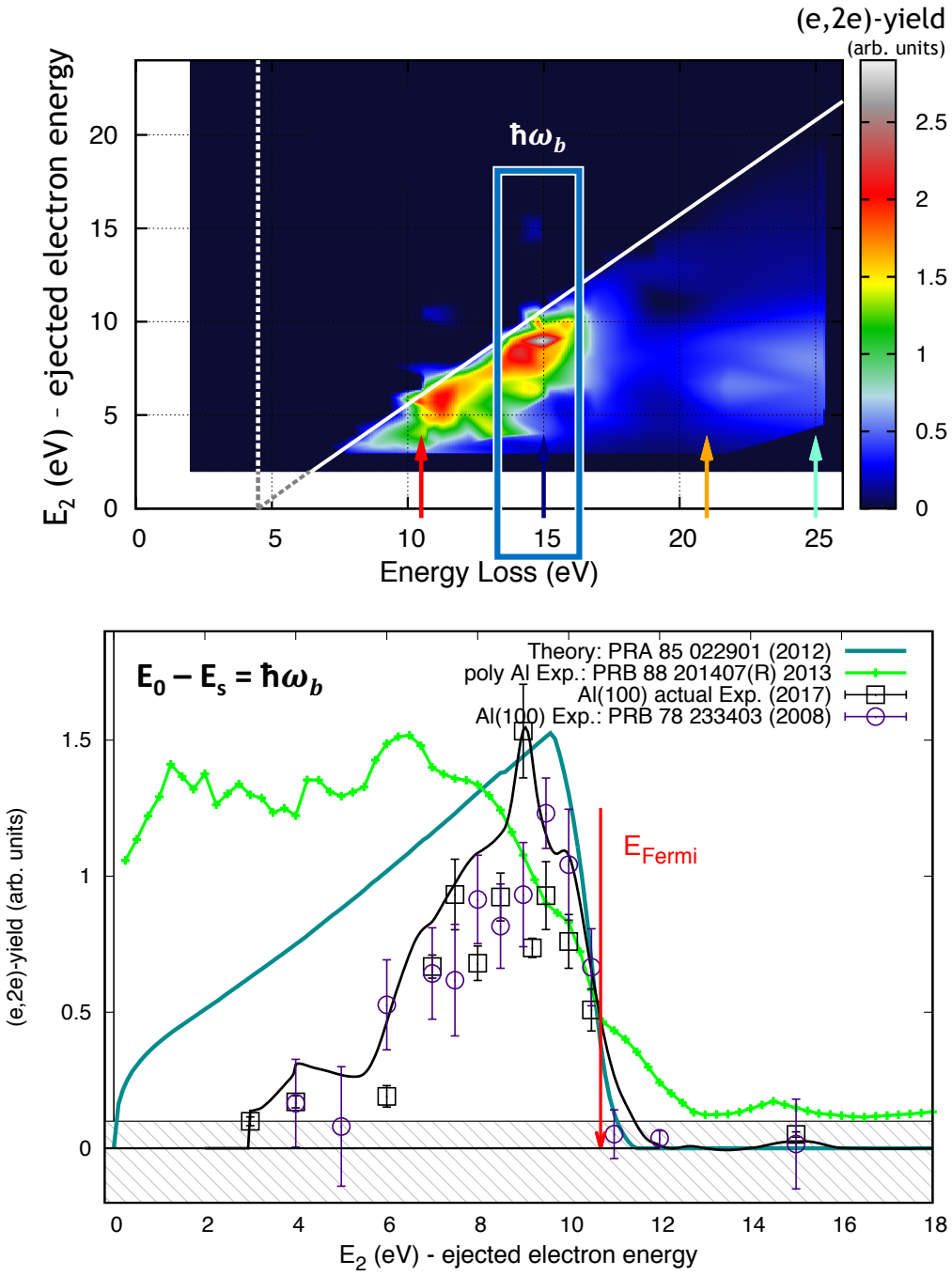

Figure 4.28: *Upper panel:* Selection of (e,2e)-data performed around the characteristic energy loss of a bulk plasmon at $\hbar\omega_s$ =15 eV. *Lower panel:* Comparison among linear spectra displaying the coincidence yield obtained at the constant energy loss interval selected, given as a function of the ejected electron energy (abscissa). Experimental and simulated data sets are indicated in the legend.

CHAPTER 5

Summary & Conclusions

Incoherent elastic scattering and the IMFP parameter are the pillars upon which rely the majority of the current available models describing SEE based on MC simulations. As discussed in chapter 2 and particularly in section 2.1, the majority of the models used nowadays to predict and describe SEE are based on approximations whose validity becomes questionable and ineffective when working in the low energy (LE) regime. Furthermore, most of these models do not account for the long-range order of solids, hence their description of electron scattering and transport is rather inadequate for crystalline surfaces, where interference effects play a relevant role.

By means of the scrutinising strategy adopted in this work, it was possible to unearth the fundamental interaction processes, as well as the other main ingredients – i.e. the electronic structure of the investigated target – that need to be considered when aiming at a complete description of the SEE-mechanism and of the SE-yield in the LE-regime. In fact, the information gathered in this work demonstrates, that for the LE-regime (below 100 eV) and for crystalline surfaces, the sole parameter of the IMFP and incoherent scattering no longer suffice to properly describe the creation-ejection mechanism of the low energetic secondaries (LE-SEs).

Especially for primary electron energies below 50 eV – the influence of the target band structure dominates both the *reflection* (REY or η) and *emission* (SEY or δ) behaviours of both incoming and emitted electrons. The series of LE-TEY measurements (presented in section 4.1 and subsections therein) has made clear that, for the proper interpretation of this measured energy- and angle-dependent yields, it is necessary to consider the unoccupied band structure (BS) of the irradiated solid. In fact, for landing electron energies between ~ 0 and 50 eV this integral response is made up by an interplay of reflectivity and emissivity and is ultimately dictated by the unoccupied Density-of-States (DoS) of the target. Only those free (impinging) electrons exhibiting wave-functions that can couple with a Bloch-wave of an empty band can penetrate the solid and interact with electrons of the target, thus eventually generating SEs. Otherwise, in presence of energy gaps, a rise in the LE-TEY is observed, however linked to a higher reflectivity,

induced by the (nearly) total reflection of the incoming electron, whose wave-function, does not match any empty state inside the solid. Hence, by means of the TEY measured in the LE-regime, it becomes evident that the BS above vacuum level modulates the flux of both the incident electron and of the ejected electron.

In view of the fact that, it is experimentally impossible to distinguish between true secondary electrons and backscattered primaries and that the quantity accessible to experiments is, as a matter of fact, a Total Electron Yield (TEY or σ) rather than a SEY, it would be more appropriate to apply a rigorous and consistent designation for this quantity in the literature; especially when measuring in the LE-range.

Furthermore, the relevant role played by the target electronic structure in the SEE-process was undoubtedly recognisable in observations made by means of (e,2e)-coincidence spectroscopy from HOPG (of which results were presented in subsection 4.3.1), when measuring the TDCS at a fixed final state, for an ejected electron of very low energy $\sim 4\,\mathrm{eV}$. Emission of these LE-SEs was studied in dependence of various energies and momenta transferred during the inelastic collision, hence by measuring the TDCS – given in eq. (2.12) – scanning through different initial states available in the $(\vec{q}_{\parallel};\, \varepsilon_{bin})$-phase-space.

By these measurements it was shown that, the availability of an occupied initial state constitutes a necessary however not sufficient condition to grant the promotion of a bound electron above vacuum level, i.e. a SE-emission event. In fact, the necessary and, only then, sufficient condition for the promotion of an electron to the conduction band is obtained if both the initial occupied and final unoccupied bands involved in the ionisation process, are available.

Accordingly, in the LE-regime – especially when the ejected electron energy is very low ($\lesssim 20\,\mathrm{eV}$) – the TDCS is strongly modulated by both DoS below and above vacuum level (JDoS). The higher the considered ejected electron energy, E_e, the less evident the role played by this "*selective initial–final JDoS*"[1], since in this case the emitted electron escapes from regions where the unoccupied DoS increases monotonically (continuum of states) and where the presence of forbidden regions (energy gaps) is strongly diminished.

When the (e,2e)-experiment involves such higher energetic SEs (with $\mathrm{E}_e \gtrsim 20\,\mathrm{eV}$), due to the increased presence of accessible escape channels, it is likely for this electron to be emitted, thus contributing to the measured (e,2e)-yield. While for these high energy SEs the momentum density above vacuum level increases, with increasing energy losses, $\Delta\mathrm{E}$, and momentum transfers, $\Delta\vec{K}$ the kinematical factor and the dipole matrix element decrease. Thus, in the electron spectrum range involving higher energy transfers, the overall (e,2e)-yield – i.e. the measured TDCS – is

[1] Here, by *selective JDoS* one refers to the fact that in such an (e,2e)-experiment both discrete initial and final electron states are fixed and therefore discriminated in one and the same experiment. The herewith obtained Joint-DoS is then given by the convolution of these discrete initial and final states only and not as defined in REELS, where the momentum density of each allowed initial state is convoluted with all available final states.

evidently attenuated.

In summary, (e,2e)-coincidence spectroscopy has made possible to correlate excitations due to the incoming electron with the resulting SE-features pinpointing the fundamental role of both initial and final states of the ionising event.

In HOPG, where the band structure exhibits a complex network of bands and a non-constant DoS, this aspect was particularly evident, whereas in the case of Aluminium, the NFE-like DoS in this target makes emission of SEs always possible, since availability of empty states was uniformly granted.

Furthermore, (e,2e)-results from Al(100) show, similarly as in previous works of Refs. [147, 148, 126, 149], that the ejection of a SE is predominantly induced and enhanced – i.e *assisted* – by the excitation/relaxation of plasmons. These collective modes represent one key mechanism in the production of these omni-present secondary electrons.

The aim of the present (e,2e)-studies conducted on Al(100) (discussed in subsection 4.3.2) was to investigate the role of these two predominant excitation channels - of a surface ($\hbar\omega_s$ =10.5 eV) and a bulk ($\hbar\omega_b$ =15 eV) plasmon - with respect to the relevance of the competing direct knock-out processes. The (e,2e)-cross section measured in an energy loss range where only direct electron–electron scattering is expected (e.g. ΔE= 19 eV) drops by a factor of at least 10, thus demonstrating that the plasmon-resonant channel pre-dominates with respect to direct electron–electron scattering.

In addition, by studying the (e,2e) probability distribution in the double scattering regime – i.e. where 2 plasmons are excited – it was possible to assess that generation of SEs measured in coincidence with a doubly excited plasmon exhibits an *incoherent* (sequential) character, thus leading to the emission of two SEs, each one ejected with a kinetic energy characteristic for the excitation of a single plasmon.

Consequently, by comparison of results obtained from (e,2e)-measurements done on the single crystalline Al surface and its polycrystalline counterpart, it could be found that independently from the primary energy and the kinematics chosen in an experiment, the elementary mechanism that leads to emission of SEs is a single ionising collision assisted by these collective electron excitations (plasmons) and/or coherent elastic scattering (diffraction). By means of these results it was possible to appraise that the single scattering event represents the fundamental process leading to the SE-cascade.

In fact, both (e,2e) and elastic-inelastic diffraction experiments performed in this work support the description of the ionising collision as happening inside the solid, hence the trajectories of the three unbound electrons (incoming, scattered and secondary) are refracted by the inner potential barrier in entering and exiting the sample surface. Inside the solids the incoming

electron undergoes diffraction from the crystal lattice (the specularly reflected beam is a 0^{th}-order diffraction). Each diffracted beam acts as a primary beam for the following ionising collision, whose cross section decreases rapidly with increasing momentum transfer (see equation (2.12)).

Consequently, all correlated pairs emerging from the surface are predominantly generated by diffracted beams pointing towards the surface and the (e,2e)-events in reflection geometry are equivalent to events generated in transmission geometry by monochromatic electron beams generated within the solid by diffraction. Due to the sharp dependence of the TDCS on the momentum transfer (i.e. the scattering angle), almost the totality of the single scattering (e,2e)-events occurs for the primary electron scattered along the diffraction/reflection direction (within a few degrees opening angle at the energies of the present experiments).

Although, in the single scattering regime, the measured (e,2e)-cross section unambiguously follows this "DL"-scattering scheme, making such single ionising process the building block applicable to explain the build-up of the SE-cascade, it shall be noted that, when entering in the multiple scattering regime it is questionable whether the scattered electrons preserve any "memory" on their original direction. This seems, in fact, highly unlikely since both elastic and transport mean free paths (EMFP and TMFP) are comparable to all relevant path lengths in this energy range.

In the single scattering regime, the "DL"-scattering model completely explains the measured (e,2e)-cross section, where initial and final states are fully defined.

For secondaries emitted with kinetic energies comprised within a LE-range, also characteristic for the multiple scattering regime (e.g. as shown in (e,2e)-measurements from HOPG performed at constant final state with $E_e = 4\,eV$) the obtained TDCS (figures 4.20 and 4.22) displayed as a function of the initial state exhibit some discrepancies with respect to the calculated momentum densities. On the one hand, these discrepancies were partially attributed to the fact that, in these experiments, not only electron bands along the two in-plane symmetry directions are invoked, but also the ΓA-symmetry direction should be considered. On the other hand, the mismatches between the measured TDCS and the expected momentum densities along ΓK and ΓM could be also linked to the fact that the 4 eV SEs arise in the course of a multiple scattering event, hence their initial state is no longer undoubtedly identifiable.

This demonstrates once more that *quantitative* interpretation of the SEE-process is highly complicated.

This homogeneous corpus of experimental evidences has allowed to develop a dependable description of the elementary emission of SEs that rests on the following grounds:

- In the LE-regime the TEY-response of a material is constituted by the interplay of reflectivity and emissivity of the target, which is dictated by its band structure.
- SEs are generated in single electron scattering events in which the full energy and momentum lost by the incident electron is transferred to a bound electron of the target.

- For the SE emission to be possible, energy and momentum transferred in the collision must be such to couple an initially occupied bound state of the target with an empty state above the vacuum level.
- The SE emission process is assisted by collective excitations, such as Plasmon, and by coherent diffractions from the crystal lattice.

The electron scattering model adopted and successfully applied till now to describe (e,2e)-coincidence experiments in reflection mode and for medium kinetic energies (above 100 eV) is based on the First Born Approximation (FBA) [154] (see sections 2.2 to 2.4). There, the incident electron is described as a plane wave, whereas the target electrons, initial and final states, are described by one-electron Bloch wave functions in the momentum space representation. In analogy to what is done in the three step model in photo-ionisation from solids, the ejected electron wave function within the solid, $\psi_e(E_e, \vec{k}_e)$, matches the energy and the parallel momentum component of the corresponding plane wave in the vacuum. The series of (e,2e)-measurements performed in this work demonstrate the applicability of this model also in the LE-regime.

In conclusion, a comprehensive elementary model for generation of SEs has been identified. Correct interpretation of measured (e,2e)-cross sections can be only performed, if the electronic structure of the irradiated target is considered both in the occupied and unoccupied states.

The SE generation probability fully depends on both energy and momentum conservation in the collision and band structure of the solid. This elementary generation model is applicable at each individual step of the SE generation cascade.

Appendices

APPENDIX A

HOPG: Repository of Ar-REELS

This appendix contains all Ar-REELS measured from HOPG along positions displayed in the diffraction pattern of fig. A.1. The excitation energy used for this series of measurements was $E_0 = 91.73$,eV.

By varying the angle of incidence (θ_{in}) and the angle of emission (θ_{out}) – these are indicated on the top and bottom scales of the diffraction pattern shown in figure A.1 – the parallel component of the exchanged momentum, $\Delta\vec{K}_{\parallel}$ is varied, thus for a very same discrete energy loss (ΔE) different excitation channels can be accessed, as previously explained in subsection 4.2.1. This in turn will result in a variation of the intensity and peak positions observed in a REEL-spectrum.

After having determined the crystalline order of the clean HOPG surface, angle-resolved REELS spectra were measured under a specific combination of (θ_{in}, θ_{out}), hence under various scattering conditions for which correspondent diffraction kinematics were obtained.

Figure A.1 shows the same diffraction pattern as in fig. 3.4 however it reports various numerical labels (blue, grey or purple) marking either specific diffraction peaks or regions in between peaks at which REELS were measured. Each numerical label is used to identify the correspondent REELS and combination of incident-emission angles used for its acquisition. Blue numbers were used to mark REELS acquired on diffraction peaks, purple numbers for spectra measured in between peaks (in regions of minima), whereas grey numbers label spectra measured on the ascending and descending slopes of the specular peak. REELS measured in specular reflection conditions are labelled by the index number #12 marked in red.

All REELS were normalised only to the primary current, I_0, but not to the area of the ELP. To properly interpret the variations – in intensity, in shape and in energy position – of the observed spectral features, both the *macroscopic* (characterised by the dielectric response of the material) and *microscopic* (characterised by the BS of the target; in particular by the joint-DoS as explained in subsections 4.2.2 and 4.2.4) pictures need to be considered.

Table (A.1) contains the complete list of Ar-REELS acquired at the different spots identified

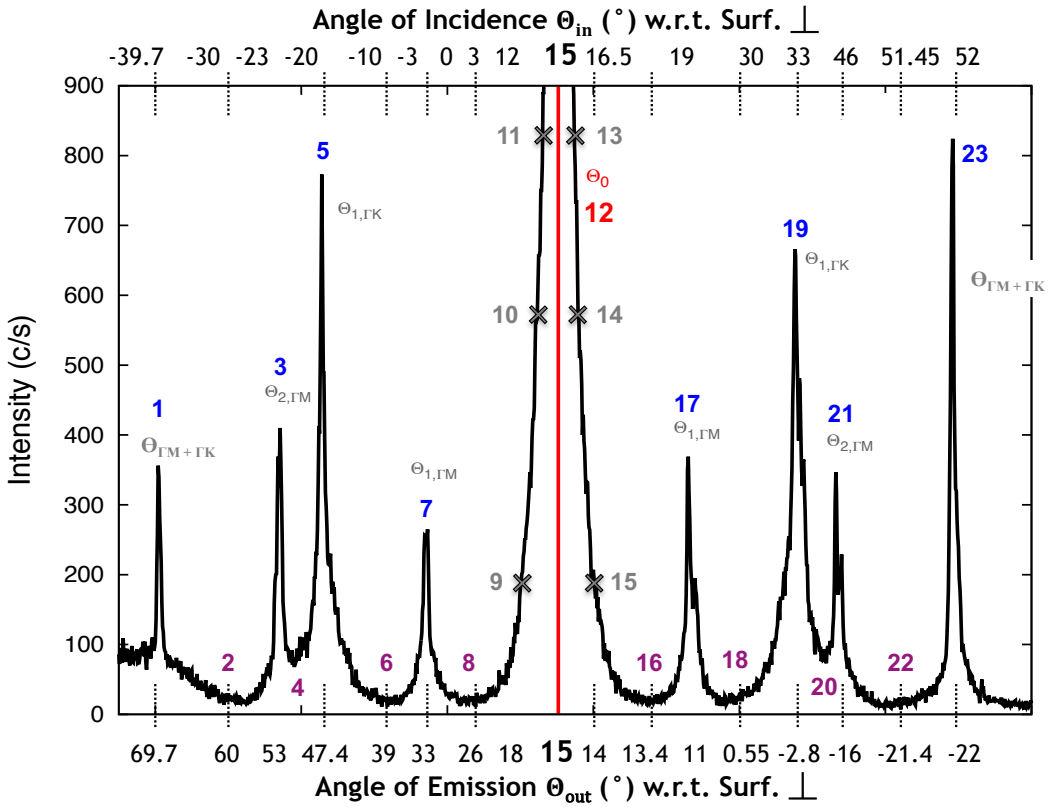

Figure A.1: Same diffraction pattern of HOPG from Fig. 3.4 labelled with coloured index-numbers to make connection to the Ar-REELS acquired under the specifically chosen combination of incident-emission angles. The colour code used for the labels is: *blue* for Ar-REELS acquired on diffraction peaks; *purple* for spectra measured in diffraction minima; *grey* for Ar-REELS measured on the ascending/descending slope of the specular peak and *red* for all REELS acquired at specular reflection. Table A.1 reports in detail all pairs of $(\theta_{in}, \theta_{out})$ used for the series of Ar-REELS shown in the following, along with the main spectral characteristics.

by the numerical indices displayed in fig. A.1. This table lists the scattering geometry as well as the intensities of relevant spectral features, such as ELP and plasmon losses.

The legend in all REELS shown in the following entail the combination of $(\theta_{in}, \theta_{out})$ used during the experiment (as given in Table (A.1)). The ELP was omitted from each figure leaving only the energy loss range of interest.

In addition to the index-labels, in the following it will be referred to all spectra acquired on the left-hand side of the 0^{th}-order Bragg peak in the diffraction pattern of fig. A.1 as *"LX"* and consequently to all those acquired on the right-hand side of the specular peak as *"RX"*. A series of figures will show all Ar-REELS plotted in various combinations. This is done to perform different types of inter-comparisons. For example, the REELS acquired on spot #5, on the 1^{st}-order diffracted peak along the ΓK-direction on the "LX"-side is compared with its counterpart on the "RX"-side, measured on spot #19. All "LX"-side REELS are inter-compared with their counterparts on the "RX"-side and the same type of comparison is also done among all REELS acquired in minima in-between peaks. In general all spectra (with ID-numbers ranging from 1 to

12), hence those which were acquired on the "LX" of the specular peak are plotted in red, whereas those acquired on the "RX"-side are plotted in blue. Further details are specified in each panel ranging from fig. A.2 to A.9.

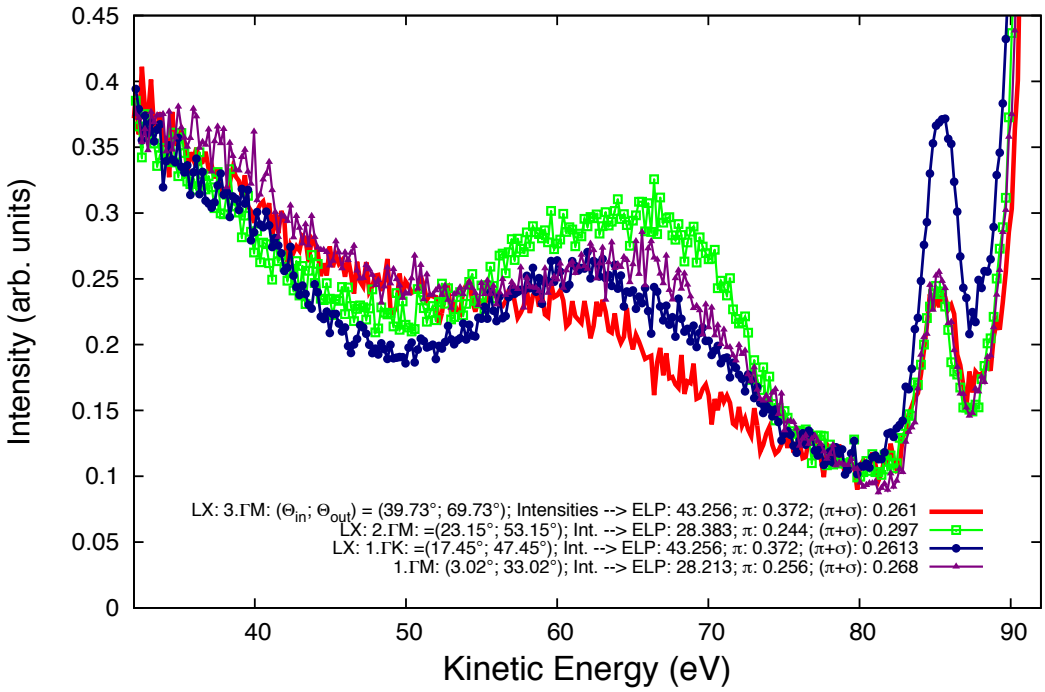

Figure A.2: Ar-REELS measured on "LX"-side diffraction peaks with ID No. [#]: 1, 3, 5 and 7 as labelled in fig.A.1.

ID No. [#]	θ_{in} [°]	θ_{out} [°]	ELP (arb. un.)	π (arb. un.)	$\pi + \sigma$ (arb. un.)	(I_π/I_{ELP}) [–]	$(I_{\pi+\sigma}/I_{ELP})$ [–]
1	-39.73	69.73	10.590	0.2394	0.2394	0.0226	0.0226
2	-31.15	61.15	1.489	0.0633	0.1735	0.0425	0.1165
3	-23.15	53.15	28.383	0.2440	0.2976	0.0086	0.0105
4	-20.55	50.55	4.028	0.2385	0.2604	0.0592	0.0646
5	-17.45	47.45	43.256	0.372	0.2613	0.0086	0.006
6	-9.05	39.05	1.648	0.0655	0.271	0.0397	0.1643
7	-3.02	33.02	28.213	0.2562	0.2680	0.0091	0.0095
8	3.45	26.55	2.1384	0.0707	0.167	0.0331	0.0751
9	12.00	18.00	41.448	0.7517	0.4936	0.0181	0.0119
10	13.48	16.52	116.824	1.516	0.771	0.0130	0.0066
11	14.35	15.65	204.041	1.600	0.7493	0.0078	0.0037
12	14.95	15.05	1261.06	1.7773	0.9206	0.0014	0.0007
13	14.95	15.05	703.97	2.5024	1.2772	0.0036	0.0018
14	14.85	15.15	900.00	1.8758	1.1246	0.0021	0.0012
15	15.98	14.02	151.380	1.800	1.2497	0.0120	0.0083
16	16.55	13.45	81.8843	1.5292	1.304	0.0187	0.0160
17	19.13	10.87	15.818	0.4135	0.5237	0.0261	0.0331
18	29.45	0.55	2.8667	0.106	0.3066	0.0370	0.01070
19	32.84	-2.84	24.031	0.1516	0.3717	0.0063	0.0155
20	39.45	-9.45	81.068	1.5292	1.3003	0.0189	0.0160
21	46.13	-16.13	9.7353	0.4773	0.2329	0.049	0.0240
22	51.45	-21.45	12.2335	0.1905	0.293	0.0156	0.024
23	52.08	-22.08	7.6182	0.2142	0.3167	0.0281	0.0416

Table A.1: Catalogue of Ar-REELS from HOPG acquired at each index-number displayed in fig. A.1. The table reports the used scattering conditions, the relative intensities obtained on the ELP and the characteristic losses of a π- and $\pi + \sigma$-plasmons and their relative intensity relations.

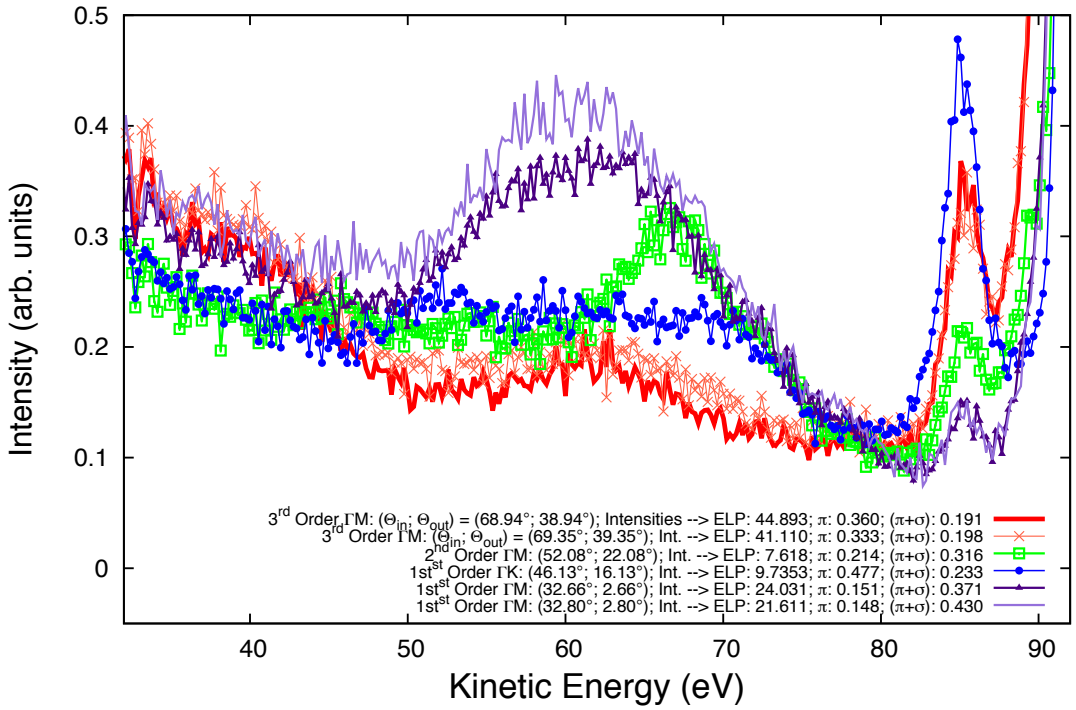

Figure A.3: Ar-REELS measured on "RX"-side diffraction peaks with ID No. [#]: 17, 19, 21 and 23 as labelled in fig.A.1.

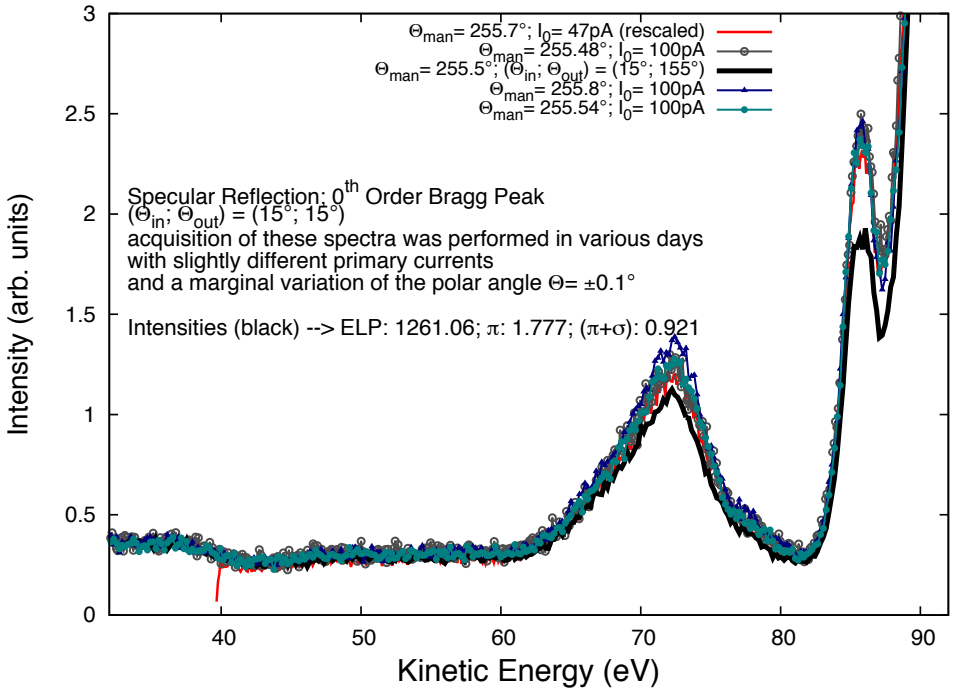

Figure A.4: Several REELS acquired in specular reflection condition on different days and after different cycles of annealing, also employing different primary currents of the electron beam. ID No. 12, highlighted in red in fig.A.1.

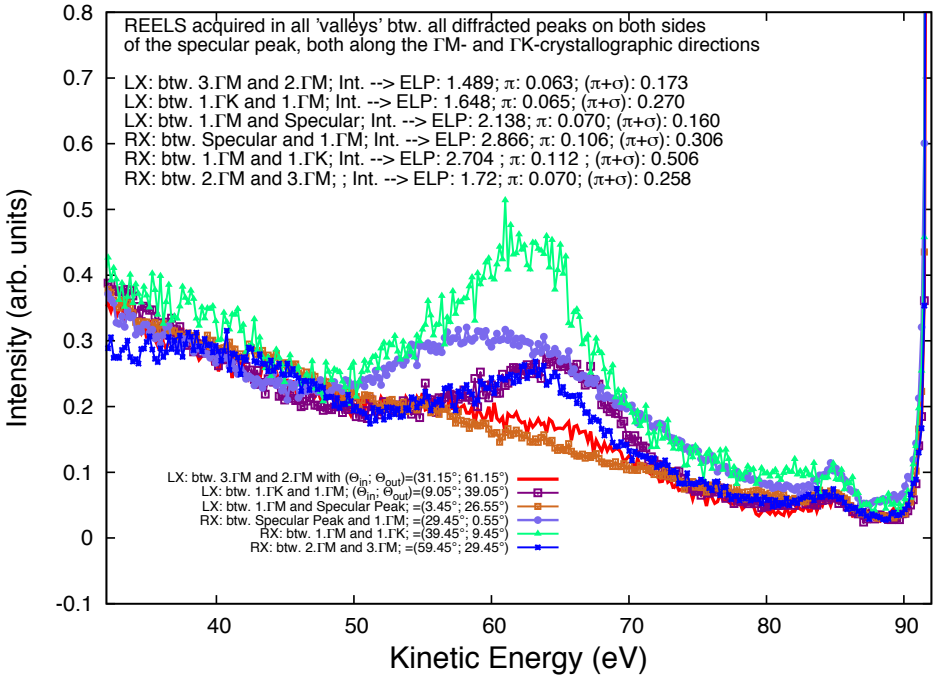

Figure A.5: Ar-REELS acquired in all minima ("valleys") in between diffraction peaks, on both sides of the specular peak. ID No. [#]: 2, 6, 8, 16, 18 and 22 (purple).

(a) REELS #4 acquired in the minimum btw. the 2^{nd} order diffraction peak along the ΓM-direction and the 1^{st} order diffraction along the ΓK-direction, both on the LX-side.

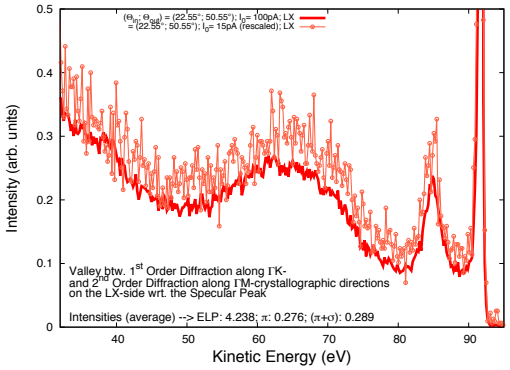

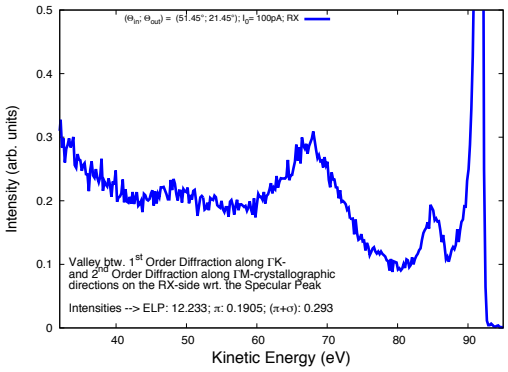

(b) REELS #20 acquired in the minimum btw. the 1^{st} order diffraction along the ΓK-direction and the 2^{nd} order diffraction peak along the ΓM-direction, both on the RX-side.

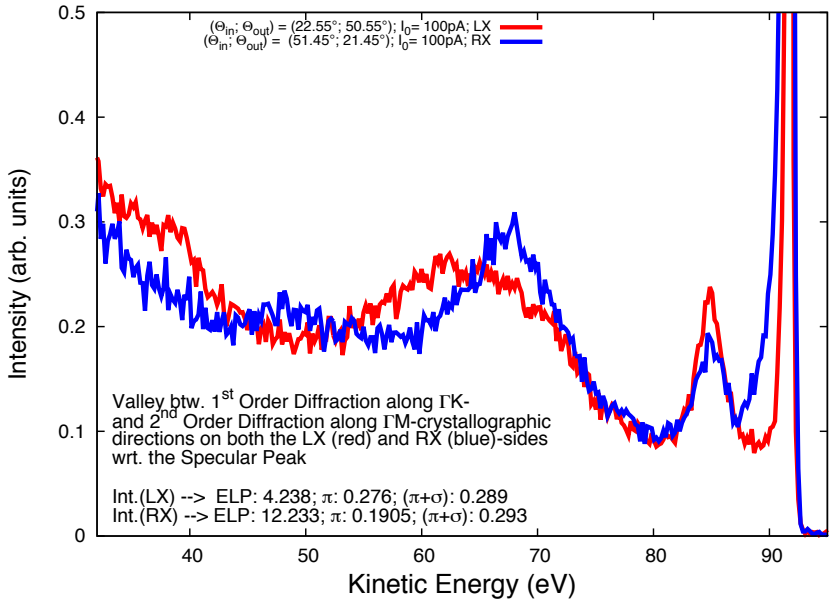

(c) Direct comparison between REELS #4 and #20, measured in reversed scattering conditions with respect to one another. Consult the legend for the effective pairs of $(\theta_{in}, \theta_{out})$.

Figure A.6: Inter-comparison of Ar-REELS measured in positions of minimal intensity in the diffraction pattern.

(a) Comparison btw. REELS acquired on the 1^{st}-order diffraction along the ΓK-direction. ID No. [#]: 5 (LX, red) and 19 (RX, blue).

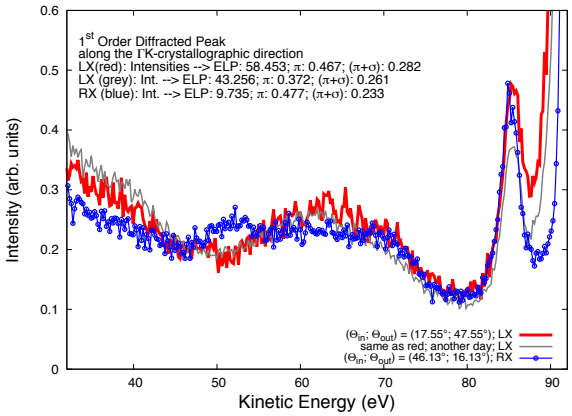

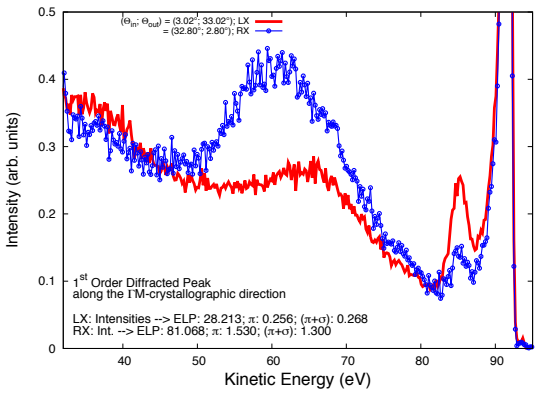

(b) Comparison btw. REELS acquired on the 1^{st}-order diffraction along the ΓM-direction. ID No. [#]: 7 (LX, red) and 17 (RX, blue).

(c) Comparison btw. REELS acquired on the 3^{rd}-order diffraction along the ΓM-direction. ID No. [#]: 1 (LX, red) and 23 (RX, blue).

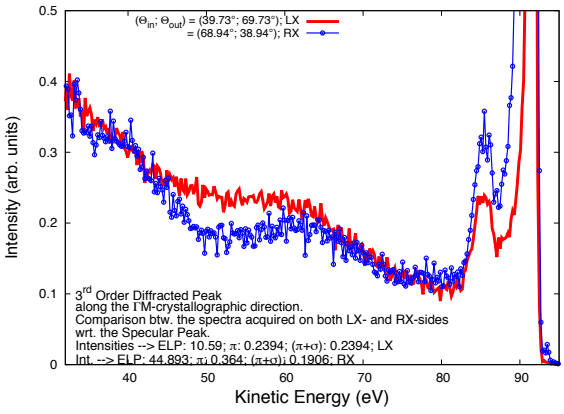

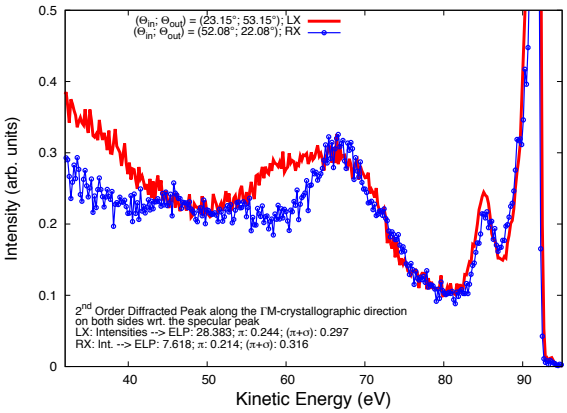

(d) Comparison btw. REELS acquired on the 2^{nd}-order diffraction along the ΓM-direction. ID No. [#]: 3 (LX, red) and 21 (RX, blue).

Figure A.7: Inter-comparison of Ar-REELS measured on diffraction peaks of different orders on both "LX"- and "RX"-sides.

(a) Comparison btw. REELS acquired on the LX-sided first order diffraction peaks along ΓK (ID No. 5) andΓM (ID No. 7) directions.

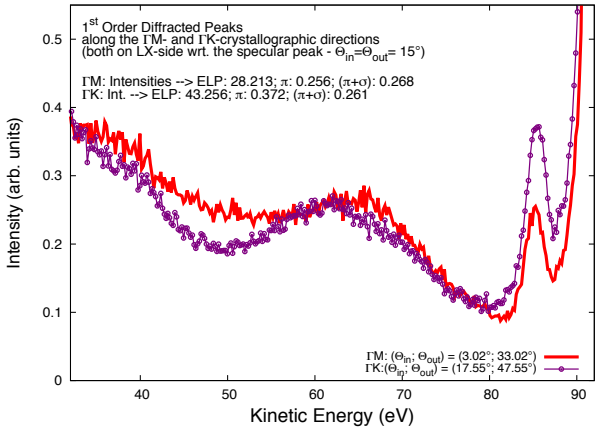

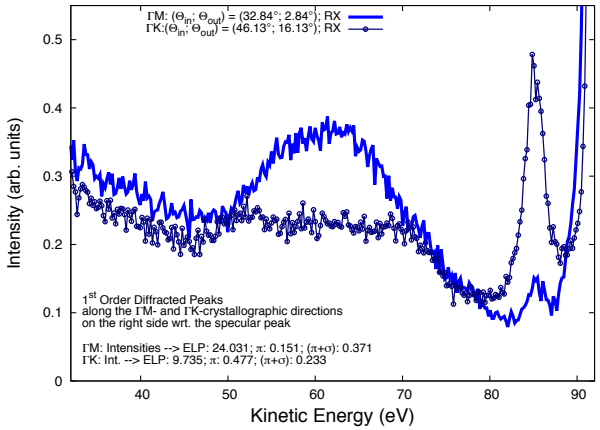

(b) Comparison btw. REELS acquired on the RX-sided first order diffraction peaks along ΓK (ID No. 19) andΓM (ID No. 17) directions.

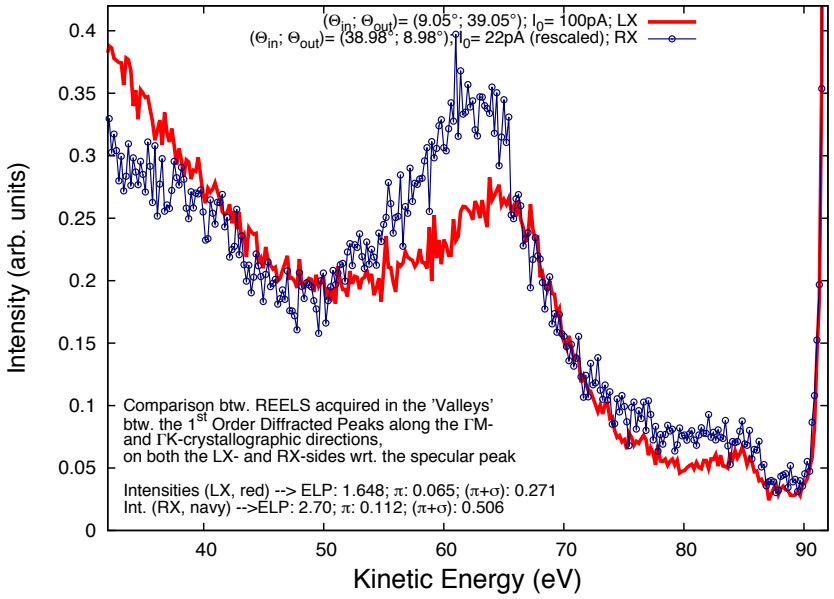

(c) Comparison btw. REELS acquired in the minima between the first order diffracted peaks along ΓK and ΓM on both sides of the specular peak. ID No. [#]: 6 (LX, red) and 18 (RX, blue).

Figure A.8: Comparison between REELS acquired on both LX and RX (wrt. specular peak).

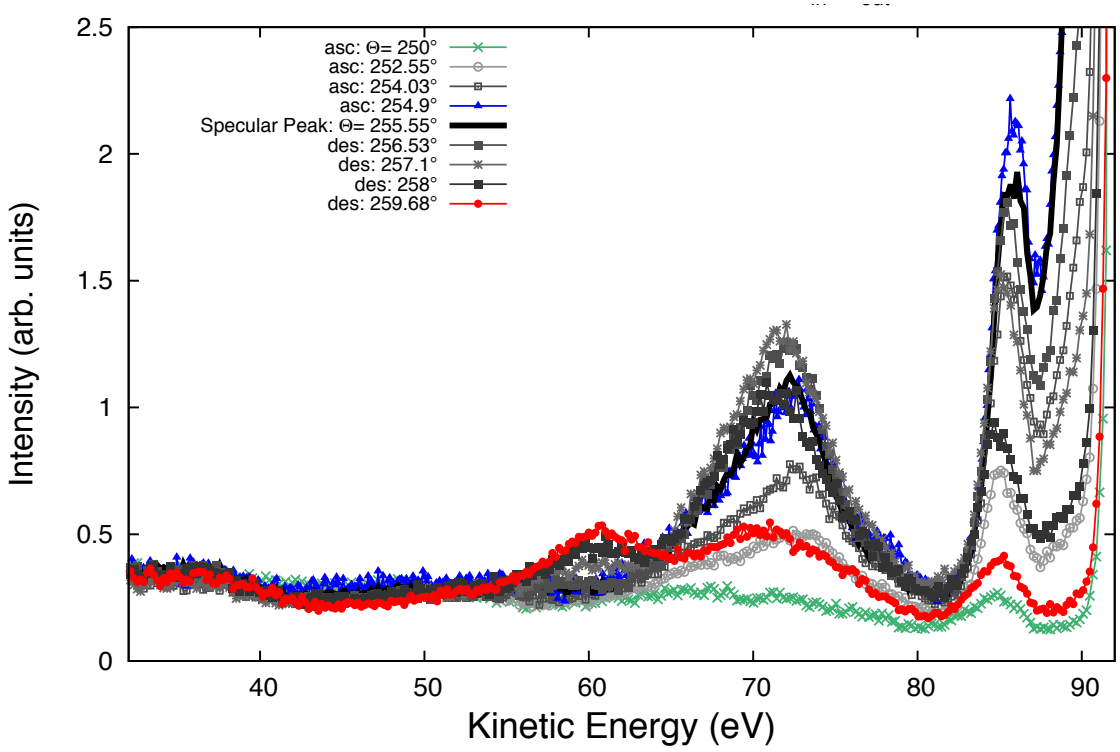

Figure A.9: Ar-REELS acquired on the "ascending" and "descending" slopes of the specular peak (measurements highlighted by grey index-number in fig. A.1). ID No. [#]: 9, 10, 11, 13, 14, and 15. The specular peak is plotted as thick black continuous line for reference.

Bibliography

[1] E. Goldstein. "Vorläufige Mitteilungen über elektrische Entladungen in verdünnten Gasen". In: *Monatsberichte d. Königlich Preussischen Akademie d. Wissenschaften* (1876), pp. 279–295 (cit. on p. 1).

[2] J. J. Thomson. In: *Philos. Mag.* 44 (1897), p. 293 (cit. on p. 1).

[3] I. Falconer. "J. J. Thomson and the discovery of the electron". In: *Physics Education* 32.4 (1997), p. 226. URL: http://stacks.iop.org/0031-9120/32/i=4/a=015 (cit. on p. 1).

[4] George E. Smith. "J. J. Thomson and The Electron: 1897–1899 An Introduction". In: *The Chemical Educator* 2.6 (1997), pp. 1–42. DOI: 10.1007/s00897970149a. URL: https://doi.org/10.1007/s00897970149a (cit. on p. 1).

[5] A. Becker. "Über die Rückdiffusion, Reflexion und Sekundärstrahlerregung langsamer Kathodenstrahlen". In: *Annalen der Physik* 383.19 (), pp. 253–276. DOI: 10.1002/andp.19253831904. URL: https://onlinelibrary.wiley.com/doi/abs/10.1002/andp.19253831904 (cit. on pp. 1, 25).

[6] F. Jona, J. A. Strozier Jr., and W. S. Yang. "Low-energy electron diffraction for surface structure analysis". In: *Reports on Progress in Physics* 45.5 (1982), p. 527. URL: http://stacks.iop.org/0034-4885/45/i=5/a=002 (cit. on p. 1).

[7] H. Seiler. "Secondary electron emission in the scanning electron microscope". In: *J. Appl. Phys.* 54.11 (1983), R1–R18 (cit. on pp. 1, 3, 12, 88, 130, 131, 136, 152).

[8] L. Reimer. *Transmission Electron Microscopy*. Springer, 1984 (cit. on p. 1).

[9] R. Shimizu and Z.-J. Ding. "Monte Carlo modelling of electron-solid interactions". In: *Rep. Prog. Phys.* 5 (1992), pp. 487–531 (cit. on pp. 1, 31, 33).

[10] J. Goldstein et al. *Scanning Electron Microscopy and X-ray Microanalysis*. New York, London: Plenum, 1992 (cit. on p. 1).

[11] R. F. Egerton. *Electron Energy-Loss Spectroscopy in the Electron Microscope*. 3rd ed. Springer US, 2011. ISBN: 144199582X,9781441995827. URL: http://gen.lib.rus.ec/book/index.php?md5=b50bddb4d2c2bb6bcdee3b6af63a17f9 (cit. on pp. 1, 5).

[12] D. L. Mills. "Interaction of low-energy electrons with surface lattice vibrations". In: *Prog. Surf. Sci.* 8.4 (1977), pp. 143 –180. DOI: https://doi.org/10.1016/0079-

6816(77)90008-9. URL: http://www.sciencedirect.com/science/article/pii/0079681677900089 (cit. on p. 1).

[13] M. Kimura, M. Inokuti, and M. A. Dillon. "Electron degradation in molecular substances". In: *Adv. Chem. Phys.* 84 (1993), p. 193 (cit. on p. 1).

[14] Léon Sanche. "Low-energy electron therapy". In: *Nature Materials* 14 (June 2015), 861 EP –. DOI: http://dx.doi.org/10.1038/nmat4333. URL: http://dx.doi.org/10.1038/nmat4333 (cit. on p. 2).

[15] Yi Zheng, J. Richard Wagner, and Léon Sanche. "DNA Damage Induced by Low-Energy Electrons: Electron Transfer and Diffraction". In: *Phys. Rev. Lett.* 96 (2006), p. 208101 (cit. on p. 2).

[16] Sylwia Ptasińska and Léon Sanche. "Dissociative electron attachment to hydrated single DNA strands". In: *Phys. Rev.* E75 (2007), p. 031915 (cit. on p. 2).

[17] A. Mozumder and Y. Hakano. *Charged Particle and Photon Interactions with Matter*. Boca Raton: CRC Press, 2004. ISBN: 0-7923-6526-7 (cit. on p. 2).

[18] Yi Zheng et al. "Role of Secondary Low-Energy Electrons in the Concomitant Chemoradiation Therapy of Cancer". In: *Phys. Rev. Lett.* 100 (2008), p. 198101 (cit. on p. 2).

[19] J. Wiza. "Microchannel plate detectors". In: *Nuclear Instruments and Methods* 162 (1979), p. 587. DOI: 10.1016/0029-554X(79)90734-1 (cit. on pp. 2, 95).

[20] H. Bruining. "Literature on the Application of SEE". In: *Physics & Applications of SEE*. Ed. by H. Bruining. Second Edition. Pergamon Science Series: Electronics and Waves–a Series of Monographs. Pergamon, 1962, pp. 175–176. ISBN: 978–0–08–009014–6. DOI: https://doi.org/10.1016/B978-0-08-009014-6.50015-6. URL: http://www.sciencedirect.com/science/article/pii/B9780080090146500156 (cit. on p. 2).

[21] Shu Xia Tao, Hong Wah Chan, and Harry van der Graaf. "Secondary Electron Emission Materials for Transmission Dynodes in Novel Photomultipliers: A Review". In: *Materials* 9.12 (2016). DOI: 10.3390/ma9121017. URL: http://www.mdpi.com/1996-1944/9/12/1017 (cit. on p. 2).

[22] H. Bruining. "9 - Some Examples of SEE causing Disturbing Effects". In: *Physics & Applications of SEE*. Ed. by H. Bruining. Second Edition. Pergamon Science Series: Electronics and Waves–a Series of Monographs. Pergamon, 1962, pp. 127–135. ISBN: 978–0–08–009014–6. DOI: https://doi.org/10.1016/B978-0-08-009014-6.50012-0. URL: http://www.sciencedirect.com/science/article/pii/B9780080090146500120 (cit. on p. 2).

[23] R. Cimino et al. "Can Low-Energy Electrons Affect High-Energy Physics Accelerators?" In: *Phys. Rev. Lett.* 93 (1 2004), p. 014801. DOI: 10.1103/PhysRevLett.93.014801. URL: https://link.aps.org/doi/10.1103/PhysRevLett.93.014801 (cit. on p. 2).

[24] M.A. Gusarova et al. "Multipacting simulation in accelerating RF structures". In: *nima* 599.100 (2009) (cit. on p. 2).

[25] M. A. Furman. "Electron Cloud Effects in Accelerators". In: *arXiv* 002.1310.1706 (2013), pp. 1–8 (cit. on p. 2).

[26] Kazuhito Ohmi. "Beam-Photoelectron Interactions in Positron Storage Rings". In: *Phys. Rev. Lett.* 75.8 (1995), pp. 1526–1529. DOI: 10.1103/PhysRevLett.75.1526 (cit. on p. 2).

[27] M. Taborelli et al. "Nine years of carbon coating development for the SPS upgrade: achievements and heritage". In: *Techn. Report CERN* CERN–ACC–2016–0010 (2015). URL: https://cds.cern.ch/record/2126930 (cit. on pp. 2, 65, 133).

[28] B. Henrist et al. "Secondary electron emission data for the simulation of electron cloud". In: *ECLOUD02 Workshop Proceedings* (2002), pp. 75–78. URL: http://cern.ch/conf-ecloud02/papers/allpdf/hilleret.pdf (cit. on p. 2).

[29] V. Baglin et al. "The secondary electron yield of technical materials and its variation with surface treatments". In: *Proceedgins of EPAC 2000*. 2000, pp. 217–221 (cit. on pp. 2, 13, 77, 125).

[30] R. Cimino et al. "Detailed Investigation of the Low-Energy Secondary Electron Yield (LE-SEY) of Clean Polycrystalline Cu and of Its Technical Counterpart". In: *IEEE Transaction (on Electron Devices)* 43.9 (2015), pp. 2954–2960. DOI: 10.1109/TPS.2015.2395451 (cit. on p. 2).

[31] W. H. Hartung et al. "In-situ measurements of the secondary electron yield in an accelerator environment: Instrumentation and methods". In: *Nuclear Instruments and Methods* 783 (5 2015), pp. 95–109 (cit. on p. 3).

[32] J.J. Scholtz, D. Dijkkamp, and R. W. A. Schmitz. "Secondary Electron Emission Properties". In: *Philips J. Res.* 5 (1996), pp. 375–389 (cit. on pp. 3, 12).

[33] A. Shih et al. "Secondary electron emission studies". In: *Appl. Surf. Sci.* 111 (1997), pp. 251–258 (cit. on pp. 3, 12, 16, 26, 88, 130, 136).

[34] Rachel M. Thorman et al. "The role of low-energy electrons in focused electron beam induced deposition: four case studies of representative precursors". In: *Beilstein J. Nanotechnol.* 6 (2017), pp. 1904–1926 (cit. on p. 3).

[35] H. Garret. "Spacecraft Charging, An Update". In: *IEEE Transaction. (on Plasma Science)* 28.6 (2000), pp. 2017–2028. DOI: 10.1109/27.902229. URL: https://ci.nii.ac.jp/naid/30019759798/en/ (cit. on p. 3).

[36] H. B. Garrett and Albert C. Whittlesey. "Introduction". In: *Guide to Mitigating Spacecraft Charging Effects*. Wiley-Blackwell, 2012. Chap. 1, pp. 1–5. ISBN: 9781118241400. DOI: 10.1002/9781118241400.ch1. eprint: https://onlinelibrary.wiley.com/doi/pdf/

10.1002/9781118241400.ch1. URL: https://onlinelibrary.wiley.com/doi/abs/10.1002/9781118241400.ch1 (cit. on p. 3).

[37] Joyce Dever et al. "Chapter 23 - Degradation of spacecraft materials". In: *Handbook of Environmental Degradation of Materials*. Ed. by Myer Kutz. Norwich, NY: William Andrew Publishing, 2005, pp. 465 –501. ISBN: 978-0-8155-1500-5. DOI: https://doi.org/10.1016/B978-081551500-5.50025-2. URL: http://www.sciencedirect.com/science/article/pii/B9780815515005500252 (cit. on p. 3).

[38] Z. Němeček et al. "Secondary electron emission and its role in the space environment". In: *AIP Conference Proceedings* 1925 (2018), p. 0 (cit. on p. 3).

[39] S. Luryi. "Hot electrons in semiconductor devices". In: *Hot Electrons in Semiconductors - Physics and Devices*. Ed. by N. Balkan. Oxford: Clarendon Press, 1999. Chap. 17 (cit. on p. 3).

[40] K Kanaya, S Ono, and F Ishigaki. "Secondary electron emission from insulators". In: *J. Phys. D: Appl. Phys.* 11.17 (1978), p. 2425. URL: http://stacks.iop.org/0022-3727/11/i=17/a=015 (cit. on pp. 3, 4).

[41] Jacques Cazaux. "Some considerations on the secondary electron emission, δ, from e^-–irradiated insulators". In: *Journal of Applied Physics* 85.2 (1999), pp. 1137–1147. DOI: 10.1063/1.369239. eprint: https://doi.org/10.1063/1.369239. URL: https://doi.org/10.1063/1.369239 (cit. on pp. 3, 12).

[42] E. W. McFarland and J. Tang. "A photovoltaic device structure based on internal electron emission". In: *Nature* 421.0 (2003), pp. 616–618 (cit. on p. 3).

[43] *Hot Carriers*. http://eesemi.com/hotcarriers.htm (cit. on p. 4).

[44] Arthur J. Nozik. "Utilizing Hot Electrons". In: *Nature Energy* 3 (2018), pp. 170–171 (cit. on p. 4).

[45] Jason Valentine. "Bridging the gap with hot electrons". In: *Nature Nanotechnology* 13 (2018), pp. 96–97 (cit. on p. 4).

[46] David B. Williams and C. Barry Carter. "Electron Sources". In: *Transmission Electron Microscopy: A Textbook for Materials Science*. Boston, MA: Springer US, 2009, pp. 73–89. ISBN: 978-0-387-76501-3. DOI: 10.1007/978-0-387-76501-3_5. URL: https://doi.org/10.1007/978-0-387-76501-3_5 (cit. on p. 5).

[47] Ludwig Reimer. "Electron Detectors and Spectrometers". In: *Scanning Electron Microscopy: Physics of Image Formation and Microanalysis*. Berlin, Heidelberg: Springer Berlin Heidelberg, 1998, pp. 171–205. ISBN: 978-3-540-38967-5. DOI: 10.1007/978-3-540-38967-5_5. URL: https://doi.org/10.1007/978-3-540-38967-5_5 (cit. on p. 5).

[48] Professor Dr. Stefan Hüfner (auth.) *Photoelectron Spectroscopy: Principles and Applications*. Springer Series in Solid-State Sciences 82. Springer Berlin Heidelberg, 1996. ISBN: 978-

3-662-03211-4,978-3-662-03209-1. URL: http://gen.lib.rus.ec/book/index.php?md5=d0088ddf4d8aabc9326e4631ae597fa2 (cit. on pp. 5, 10, 61, 82, 91).

[49] H. Ibach and D. L. Mills. *Electron Energy Loss Spectroscopy and Surface Vibrations*. first. Academic Press, 1982. ISBN: 0-12-369350-0 (cit. on pp. 5, 123).

[50] R. K. Zheng. "Electron Energy Loss Spectroscopy". In: *Microscopy and imaging science* 0 (2006), p. 0 (cit. on pp. 5, 150).

[51] H. Raether. *Excitation of Plasmons and Interband Transitions by Electrons*. Springer Tracts in Modern Physics. Springer, 1980. ISBN: 9783540096771. URL: https://books.google.at/books?id=8fRIPgAACAAJ (cit. on pp. 6, 47).

[52] H. Raether. *Surface plasmons on smooth and rough surfaces and on gratings*. Springer tracts in modern physics Bd. 111. Springer, 1988. ISBN: 9783540173632. URL: https://books.google.at/books?id=ZLwrAAAAYAAJ (cit. on p. 6).

[53] P. Schattschneider. "Fundamentals of Inelastic Electron Scattering". In: (1986) (cit. on p. 6).

[54] R. F. Egerton. "Electron energy-loss spectroscopy in the TEM". In: *IOP Publishing, Rep. Prog. Phys.* 72 (2009). Reports on Progress in Physics, p. 25 (cit. on pp. 6, 7).

[55] Richard A. Ferrell and John J. Quinn. "Characteristic Energy Loss of Electrons Passing Through Metal Foils: Momentum-Exciton Model of Plasma Oscillations". In: *Phys. Rev.* 108.3 (1957) (cit. on p. 6).

[56] I. Egri. "The Internal Structure of Plasmons". In: *Z. Phys. B Con. Mat.* 53 (1983), pp. 183–189 (cit. on p. 6).

[57] J.P. Goel, O.K. Harsh, and K.S. Srivastava. "Expression for the total number of electrons participating in plasmon oscillations in metals". In: *Physica B+C* 144.2 (1987), pp. 190–192. DOI: https://doi.org/10.1016/0378-4363(87)90033-7. URL: http://www.sciencedirect.com/science/article/pii/0378436387900337 (cit. on p. 7).

[58] I. Egri et al. "Evidence for internal structure of plasmons in electron energy loss spectra". In: *Surf. Sci.* 128 (1983), pp. 51–60 (cit. on p. 7).

[59] W. S. M. Werner. "Electron transport in solids for quantitative surface analysis". In: *Surf. Interface Anal.* 31 (2001), pp. 141–176 (cit. on pp. 7, 23, 32, 33).

[60] Wolfgang S. M. Werner and Peter Schattschneider. "On the energy dissipation process in incoherent electron scattering". In: *Journal of Electron Spectroscopy and Related Phenomena* 143.2 (2005). Electron Energy Loss Spectroscopy in the Electron Microscope, pp. 65–80. DOI: https://doi.org/10.1016/j.elspec.2004.03.011. URL: http://www.sciencedirect.com/science/article/pii/S0368204804004050 (cit. on pp. 7, 33).

[61] Philip Hofmann. *Surface Physics: An Introduction*. Philip Hofmann, 2016. ISBN: 978-87-996090-1-7 (cit. on pp. 8, 37, 54, 61, 67, 122).

[62] H. Lüth. *Solid Surfaces, Interfaces and Thin Films*. Sixth. Springer, 2010. ISBN: 978–3–319–10756–1 (cit. on pp. 10, 21, 37, 47, 122).

[63] O. Yu. Ridzel, V. Astasauskas, and W. S. M. Werner. "Low energy (1–100 eV) electron inelastic mean free path (IMFP) values determined from analysis of secondary electron yields (SEY) in the incident energy range of 0.1–10 keV". In: *J. Electron. Spectrosc. Relat. Phenom.* 0.0 (2018), p. 0 (cit. on pp. 10, 22, 33, 170, 171).

[64] R. E. Bunney. "Review of Literature Secondary Electron Emission". In: *NASA* 0.0 (1964), p. 0 (cit. on pp. 12, 16).

[65] A.J. Dekker. "Secondary Electron Emission". In: *Advances in Research and Applications*. Ed. by Frederick Seitz and David Turnbull. Vol. 6. Solid State Physics. Academic Press, 1958, pp. 251 –311. DOI: https://doi.org/10.1016/S0081-1947(08)60728-6. URL: http://www.sciencedirect.com/science/article/pii/S0081194708607286 (cit. on pp. 12, 16).

[66] A. Shih and C. Hor. "Secondary Emission Properties as a Function of the Electron Incidence Angle". In: *IEEE Transaction (on Electron Devices)* 40.4 (1993), p. 0 (cit. on p. 12).

[67] G. F. Dionne. "Origin of secondary electron emission yield-curve parameters". In: *J. Appl. Phys.* 46 (1975), p. 3347 (cit. on pp. 12, 25).

[68] J. R. M. Vaughan. "Secondary emission formulas". In: *IEEE Transaction (on Electron Devices)* 36.9 (1989) (cit. on pp. 12, 14).

[69] J. R. M. Vaughan. "A new formula for secondary emission yield". In: *IEEE Transaction (on Electron Devices)* 36.9 (1989), pp. 1963–1967. DOI: 10.1109/16.34278 (cit. on pp. 12, 14).

[70] Ai-Gen Xie et al. "A universal formula for secondary electron yield from metals". In: *Nuclear Instruments and Methods in Physics Research Section B: Beam Interactions with Materials and Atoms* 268.17 (2010), pp. 2565 –2570. DOI: https://doi.org/10.1016/j.nimb.2010.06.012. URL: http://www.sciencedirect.com/science/article/pii/S0168583X10005860 (cit. on p. 12).

[71] Y. Lin and D. C. Joy. "A new examination of secondary electron yield data". In: *Surf. Interface Anal.* 37 (2005), pp. 895–900. DOI: 10.1002/sia.2107 (cit. on pp. 12, 13, 27, 66, 125).

[72] C. Yin Vallgren et al. "Amorphous carbon coatings for the mitigation of electron cloud in the CERN Super Proton Synchrotron". In: *Physical Review Special Topics – Accelerators and Beams* 14.071001 (2011), p. 0 (cit. on pp. 13, 14, 125).

[73] L. A. Gonzalez et al. "The secondary electron yield of noble metal surfaces". In: *AIP Advances* 7.11 (2017), p. 115203. DOI: 10.1063/1.5000118. eprint: https://doi.org/10.1063/1.5000118. URL: https://doi.org/10.1063/1.5000118 (cit. on pp. 13, 125).

[74] N. Hilleret, C. Scheuerlein, and M. Taborelli. "The secondary-electron yield of air-exposed metal surfaces". In: *Appl. Phys. A* 76.1085 (2003), p. 0 (cit. on p. 14).

[75] Kenneth G. McKay. "Secondary Electron Emission". In: *Bell Telephon Laboratories* 0.0 (1948), pp. 66–120 (cit. on pp. 16, 25).

[76] J. Devooght, A. Dubus, and J. C. Dehaes. "Improved age-diffusion model for low-energy electron transport in solids. I. Theory". In: *Phys. Rev. B* 36 (10 1987), pp. 5093–5109. DOI: 10.1103/PhysRevB.36.5093. URL: https://link.aps.org/doi/10.1103/PhysRevB.36.5093 (cit. on pp. 16, 26).

[77] W. S. M. Werner. "Photon and Electron Induced Electron Emission from Solid Surfaces". In: vol. 225. Springer Tracts in Modern Physics. Springer, 2007, pp. 39–77 (cit. on p. 16).

[78] Olga Yu. Ridzel. "Interaction of slow electrons with matter for nanoscale characterisation of solids". PhD thesis. Technische Universität Wien, 2018 (cit. on p. 21).

[79] A. Bellissimo et al. "Secondary electron generation mechanisms in Carbon allotropes at low impact electron energies". In: *J. Electron Spectrosc. Relat. Phen.* (2018) (cit. on pp. 22, 30, 166, 168, 169).

[80] W. S. M . Werner. "Electron transport in solids for quantitative surface analysis". In: *Surf. Interface Anal.* 31 (2001), p. 141 (cit. on p. 21).

[81] Z.-J. Ding and R. Shimizu. "Monte Carlo study of backscattering and secondary electron generation". In: *Surface Science* 197.3 (1988), pp. 539 –554. DOI: https://doi.org/10.1016/0039-6028(88)90645-0. URL: http://www.sciencedirect.com/science/article/pii/0039602888906450 (cit. on pp. 22, 31).

[82] H. Bethe and J. Ashkin. *Experimental Nuclear Physics*. Ed. by E. Segré. New York: Wiley-VCH, 1953, p. 253 (cit. on p. 22).

[83] M. Rösler et al. "Historical Overview". In: *Particle Induced Electron Emission I*. Ed. by G. Höhler. Springer Tracts in Modem Physics. Berlin, Heidelberg: Springer, 1991, pp. 59–71. ISBN: 3–540–53431–8. DOI: https://doi.org/10.1007/BFb0041376 (cit. on p. 25).

[84] A. J. Dekker and A. van der Ziel. "Theory of the Production of Secondary Electrons in Solids". In: *Phys. Rev.* 86 (5 1952), pp. 755–760. DOI: 10.1103/PhysRev.86.755. URL: https://link.aps.org/doi/10.1103/PhysRev.86.755 (cit. on p. 25).

[85] H. Bruining. "Physics and application of secondary electron emission". In: *Pergamon* (1954) (cit. on pp. 25, 27).

[86] H. Bruining. "6 - Theory of SEE; the mechanism of excitation of Secondary Electrons". In: *Physics & Applications of SEE*. Ed. by H. Bruining. Second Edition. Pergamon Science Series: Electronics and Waves–a Series of Monographs. Pergamon, 1962, pp. 78–96. ISBN: 978-0-08-009014-6. DOI: https://doi.org/10.1016/B978-0-08-009014-6.50009-0. URL: http://www.sciencedirect.com/science/article/pii/B9780080090146500090 (cit. on p. 25).

[87] P. A. Wolff. "Theory of Secondary Electron Cascade in Metals". In: *Phys. Rev.* 95 (1 1954), pp. 56–66. DOI: 10.1103/PhysRev.95.56. URL: https://link.aps.org/doi/10.1103/PhysRev.95.56 (cit. on p. 26).

[88] J. Schou. "Transport theory for kinetic emission of secondary electrons from solids". In: *Phys. Rev. B* 22.5 (1980), p. 2141 (cit. on pp. 26, 152).

[89] P. Ganachaud and M. Cailler. "A monte-carlo calculation of the secondary electron emission of normal metals: I. the model." In: *Surf. Sci.* 83 (1979), pp. 498–518 (cit. on p. 26).

[90] P. Ganachaud and M. Cailler. "A monte-carlo calculation of the secondary electron emission of normal metals: II. results for aluminium." In: *Surf. Sci.* 83 (1979), pp. 519–530 (cit. on p. 26).

[91] T. Koshikawa and R. Shimizu. "A Monte Carlo calculation of low-energy secondary electron emission from metals". In: *J. Phys. D: Appl. Phys.* 7 (1974), pp. 1303–1315 (cit. on p. 26).

[92] T. E. Everhart et al. "Measurement of structure in the energy distribution of slow secondary electrons from aluminum". In: *J. Appl. Phys.* 47.7 (1976), pp. 2941–2945. DOI: 10.1063/1.323085. eprint: https://doi.org/10.1063/1.323085. URL: https://doi.org/10.1063/1.323085 (cit. on pp. 26, 182).

[93] M. S. Chung and T. E. Everhart. "Role of plasmon decay in secondary electron emission in the nearly-free-electron metals. Application to aluminum". In: *Phys. Rev. B* 15.10 (1977), pp. 4699–4715 (cit. on pp. 26, 182, 185).

[94] V. Heine. "The band structure of aluminium I. Determination from experimental data". In: *Proceedings Royal Society London A: Math., Phys. & Engin. Sciences* 240.1222 (1957), pp. 340–353. DOI: 10.1098/rspa.1957.0089. URL: http://rspa.royalsocietypublishing.org/content/240/1222/340 (cit. on pp. 26, 66).

[95] V. Heine. "The band structure of aluminium II. The convergence of the orthogonalized plane wave method". In: *Proceedings Royal Society London A: Math., Phys. & Engin. Sciences* 240.1222 (1957), pp. 354–360. DOI: 10.1098/rspa.1957.0090. URL: http://rspa.royalsocietypublishing.org/content/240/1222/354 (cit. on pp. 26, 66).

[96] V. Heine. "The band structure of aluminium III. A self-consistent calculation". In: *Proceedings Royal Society London A: Math., Phys. & Engin. Sciences* 240.1222 (1957), pp. 361–374. DOI: 10.1098/rspa.1957.0091. URL: http://rspa.royalsocietypublishing.org/content/240/1222/361 (cit. on pp. 26, 66).

[97] C. N. Berglund and W. E. Spicer. "Photoemission studies of copper and silver: Theory." In: *Phys. Rev.* 136 (1964), pp. 1030–1044 (cit. on p. 26).

[98] M. P. Seah and W. A. Dench. "Quantitative electron spectroscopy of surfaces: A standard data base for electron inelastic mean free paths in solids". In: *Surface and Interface Analysis* 1.1 (), pp. 2–11. DOI: 10.1002/sia.740010103. URL: https://onlinelibrary.wiley.com/doi/abs/10.1002/sia.740010103 (cit. on p. 27).

[99] H. A. Bethe. "On the Theory of Secondary Emission". In: *Phys. Rev.* 59 (1941), pp. 940–949 (cit. on p. 27).

[100] E. M. Baroody. "A Theory of Secondary Electron Emission from Metals". In: *Phys. Rev.* 78.6 (1950), pp. 780–787 (cit. on p. 27).

[101] A. O. Barut. "The Mechanism of Secondary Electron Emission". In: *Phys. Rev.* 93 (5 1954), pp. 981–984. DOI: 10.1103/PhysRev.93.981. URL: https://link.aps.org/doi/10.1103/PhysRev.93.981 (cit. on p. 27).

[102] R. G. Lye and A. J. Dekker. "Theory of Secondary Emission". In: *Phys. Rev.* 107 (4 1957), pp. 977–981. DOI: 10.1103/PhysRev.107.977. URL: https://link.aps.org/doi/10.1103/PhysRev.107.977 (cit. on p. 27).

[103] Keiji Ueno et al. "Characteristic Secondary Electron Emission from Graphite and Glassy Carbon Surfaces". In: *Japanese Journal of Applied Physics* 27.5A (1988), p. L759. URL: http://stacks.iop.org/1347-4065/27/i=5A/a=L759 (cit. on pp. 29, 59, 108, 123, 153, 156, 157).

[104] A. Hoffman, G. L. Nyberg, and S. Prawer. "High-energy angle-resolved secondary-electron emission spectroscopy of highly oriented pyrolytic graphite". In: *J. Phys. Condens. Matter* 2 (1990), pp. 8099–8106 (cit. on p. 29).

[105] M. S. Chung and T. E. Everhart. "Simple calculation of energy distribution of low-energy secondary electrons emitted from metals under electron bombardment". In: *Journal of Applied Physics* 45.2 (1974), pp. 707–709. DOI: 10.1063/1.1663306 (cit. on p. 30).

[106] V. Astašauskas. "Secondary Electron-Electron Energy Loss Coincidence Spectroscopy (SE2ELCS) on Surfaces". PhD thesis. Technische Universität Wien, 2018 (cit. on pp. 30, 124, 162, 166, 169).

[107] J. B. Pendry. *Low Energy Electron Diffraction*. London, New York: Academic Press, 1974 (cit. on pp. 31, 32).

[108] J. J. Barton M. L. Xu and M. A. Van Hove. "Electron scattering by atomic chains: Multiple scattering effects". In: *Phys. Rev.* 39 (1989), p. 8275 (cit. on pp. 31, 32).

[109] Y. Chen et al. In: *http://electron lbl gov/mscdpack/mscdpack.html* (1998) (cit. on p. 31).

[110] Aimo Winkelmann, Koceila Aizel, and Maarten Vos. "Electron energy loss and diffraction of backscattered electrons from silicon". In: *New Journal of Physics* 12 (2010), p. 053001. DOI: doi:10.1088/1367-2630/12/5/053001 (cit. on pp. 31, 32).

[111] S. L. Dudarev and M. I. Ryazanov. In: *Sov. Phys. JETP* 61 (1985), p. 2 (cit. on p. 31).

[112] S. L. Dudarev and M. J. Whelan. "Temperature dependence of elastic backscattering of electrons from polycrystalline solids". In: *Surf. Sci.* 311 (1994), p. L687 (cit. on p. 31).

[113] S. L. Dudarev, P. Rez, and M. J. Whelan. "Theory of electron backscattering from crystals". In: *Phys. Rev.* 51 (1995), p. 3397 (cit. on p. 31).

[114] P. Schattschneider and W. S. M. Werner. "Coherence in EELS". In: *J. Electron Spectrosc. Relat. Phen.* 143 (2005), pp. 81–95 (cit. on p. 31).

[115] B Davison. *Neutron Transport Theory*. London: Oxford University Press, 1955 (cit. on p. 31).

[116] V. V. Sobolev. *A Treatise on radiative transfer*. Princeton, NJ: van Nostrand, 1963 (cit. on p. 31).

[117] R. Shimizu and Z.-J. Ding. "Monte Carlo Modelling of electron–solid interactions". In: *IOP Publishing, Rep. Prog. Phys.* 55 (1992), pp. 487–531 (cit. on pp. 32, 33).

[118] Z.-J. Ding and R. Shimizu. "Monte Carlo simulation study of reflection-electron-energy-loss-spectroscopy spectrum". In: *Phys. Rev. B* 61.20 (2000), pp. 14128–14135 (cit. on p. 32).

[119] Z. J. Ding, X. D. Tang, and R. Shimizu. "Monte Carlo study of secondary electron emission". In: *Journal of Applied Physics* 89.1 (2001), pp. 718–726. DOI: 10.1063/1.1331645 (cit. on pp. 32, 33).

[120] A. Dubus et al. "Monte carlo evaluation of the influence of the interaction cross sections on the secondary-electron-emission yields from polycrystalline aluminum targets." In: *Phys. Rev. B* 47 (1993), pp. 11056–11073 (cit. on p. 32).

[121] ASTM International. "Standard Test Methods for Determining Average Grain Size". In: *ASTM International* E112.10 () (cit. on p. 32).

[122] M.-L. Xu, J. J. Barton, and M. A. Van Hove. "Electron scattering by atomic chains: Multiple-scattering effects". In: *Phys. Rev. B* 39 (12 1989), pp. 8275–8283. DOI: 10.1103/PhysRevB.39.8275. URL: https://link.aps.org/doi/10.1103/PhysRevB.39.8275 (cit. on p. 32).

[123] F. Salvat, A. Jablonski, and C. J. Powell. "ELSEPA - Dirac partial-wave calculation of elastic scattering of electrons and positrons by atoms, positive ions and molecules". In: *Comput. Phys. Commun.* 165 (2005), pp. 157–190 (cit. on p. 33).

[124] B. L. Henke, E. M. Gullikson, and J. C. Davis. "X-ray interactions: Photoabsorption, scattering, transmission, and reflection at E = 50-30, 000 eV, Z = 1-92". In: *Atomic Data and Nuclear Data Tables* 54.2 (1993), pp. 181–342. DOI: 10.1006/adnd.1993.1013. URL: https://www.sciencedirect.com/science/article/pii/S0092640X83710132?via{\%}3Dihub (cit. on p. 33).

[125] E. D. Palik. *Handbook of Optical Constants of Solids*. Academic Press, 1998. ISBN: 0125444206. URL: https://www.sciencedirect.com/science/book/9780125444156 (cit. on pp. 33, 67, 69).

[126] Wolfgang S. M. Werner et al. "Secondary-electron emission induced by in *vacuo* surface excitations near a polycrystalline Al surface". In: *Phys. Rev. B* 88.201407(R) (2013), p. 0 (cit. on pp. 33, 36, 37, 50, 73, 124, 162, 182, 185, 188–190, 199).

[127] C. T. Whelan et al. *(e, 2e) & Related Processes*. Vol. 414. NATO ASI Series (Series C: Mathematical and Physical Sciences). Springer, 1993 (cit. on pp. 35, 160).

[128] A. D'Andrea and R. Del Sole. "Theory of (e,2e) reaction near solid surfaces: application to Si". In: *Surf. Sci.* 71 (1978), pp. 306–326 (cit. on p. 35).

[129] Stefani G. "Electronic and Atomic Collisions". In: Elsevier Science Publishers B. V., 1988, pp. 163–175 (cit. on p. 35).

[130] U. Amaldi et al. "Use of a Two Channeltron Coincidence in a New Line of Research in Atomic Physics". In: *Rev. Sci. Instrum.* 40.1001 (1969) (cit. on p. 35).

[131] R. Camilloni, A. Giardini Guidoniand R. Tiribelli, and G. Stefani. "Coincidence Measurement of Quasifree Scattering of 9-keV Electrons on K and L Shells of Carbon". In: *Phys. Rev. Lett.* 29 (1972), p. 618 (cit. on p. 35).

[132] G. Stefani, R. Camilloni, and A. Giardini Guidoni. "Absolute (e,2e) coplanar symmetric cross sections measured for valence orbitals of Ne". In: *J. Phys. B: Atom Mol. Phys.* 12.15 (1979), p. 0 (cit. on p. 35).

[133] E. Weigold et al. "The (e,2e) reaction in molecules: Momentum space wave function of H_2". In: *Physics Letters A* 44.7 (1973), pp. 531 –532. DOI: https://doi.org/10.1016/0375-9601(73)91008-6. URL: http://www.sciencedirect.com/science/article/pii/0375960173910086 (cit. on p. 35).

[134] I. E. McCarthy and E. Weigold. "Wavefunction mapping in collision experiments". In: *Rep. Prog. Phys.* 51.6 (1988), pp. 299–392 (cit. on p. 35).

[135] I. E. McCarthy and E. Weigold. "Electron momentum spectroscopy of atoms and molecules". In: *Reports on Progress in Physics* 54.6 (1991), p. 789. URL: http://stacks.iop.org/0034-4885/54/i=6/a=001 (cit. on p. 35).

[136] D. Voreades. "Secondary electron emission from thin carbon films". In: *Surf. Sci.* 60 (1976), pp. 325–348 (cit. on pp. 35, 36).

[137] I. E. McCarthy and E. Weigold. "Electron momentum spectroscopy of solid surfaces". In: *Contemporary Physics* 35.6 (1994), pp. 377–384. DOI: 10.1080/00107519408222127. eprint: https://doi.org/10.1080/00107519408222127. URL: https://doi.org/10.1080/00107519408222127 (cit. on p. 35).

[138] Y.Q Cai et al. "Direct imaging of the valence electronic structure of solids by (e,2e) spectroscopy". In: *Solid State Communications* 95.1 (1995), pp. 25 –29. DOI: https://doi.org/10.1016/0038-1098(95)00222-7. URL: http://www.sciencedirect.com/science/article/pii/0038109895002227 (cit. on p. 35).

[139] M. Vos and I.E. McCarthy. "Observing electron motion in solids". In: *Rev. Mod. Phys.* 67.3 (1995), pp. 713–723 (cit. on p. 35).

[140] S. Iacobucci et al. "An angular resolved electron energy loss investigation of highly oriented pyrolitic graphite electronic structure". In: *J. Electron Spectrosc. Relat. Phen.* 67.3 (1994), pp. 479 –488. DOI: https://doi.org/10.1016/0368-2048(93)02033-I. URL: http://www.sciencedirect.com/science/article/pii/036820489302033I (cit. on pp. 35, 37, 59, 165).

[141] J. Kirschner, O. M. Artamonov, and S. N. Samarin. "Two-electron coincidence spectroscopy of scattering events at surfaces". In: *Phys. Rev. Lett.* 69 (1992), p. 1711 (cit. on pp. 35, 36).

[142] S. Samarin et al. "Application of (e,2e) spectroscopy for studying surface states of W(001)". In: *J. Electron Spectrosc. Relat. Phen.* 96 (1998), pp. 61–67 (cit. on pp. 35, 37).

[143] H. Müllejans and A. L. Bleloch. "Ratio between the energy-loss spectrum in coincidence with secondary electrons and the normal energy-loss spectrum for thin carbon films in the carbon K-edge region." In: *Phys. Rev. B* 46.13 (1992), pp. 8597–8599 (cit. on p. 36).

[144] F. J. Pijper and P. Kruit. "Detection of energy-selected secondary electrons in coincidence with energy-loss events in thin carbon foils". In: *Phys. Rev. B* 44.17 (1991), pp. 9192–9200 (cit. on p. 36).

[145] J. Drucker and M. R. Scheinfein. "Delocalized secondary-electron generation studied by momentum-resolved coincidence-electron spectroscopy". In: *Phys. Rev. B* 47.23 (1993), pp. 15973–15975 (cit. on p. 36).

[146] M. R. Scheinfein, J. Drucker, and J. K. Weiss. "Secondary-electron production pathways determined by coincidence electron spectroscopy". In: *Phys. Rev. B* 47.7 (1993), pp. 4068–4071 (cit. on p. 36).

[147] W. S. M. Werner et al. "Role of surface and bulk plasmon decay in secondary electron emission". In: *Phys. Rev. B* 78 (2008), p. 233403 (cit. on pp. 36, 50, 90, 162, 182, 185, 190, 193, 199).

[148] W. S. M. Werner et al. "Contribution of Surface Plasmon Decay to Secondary Electron Emission from an Al Surface". In: *Appl. Phys. Lett.* 99 (2011), p. 184102 (cit. on pp. 36, 162, 182, 199).

[149] A. Ruocco et al. "Surface state mediated plasmon decay in Al(100)". In: *Phys. Rev. B* 95.155408 (2017) (cit. on pp. 36, 37, 162, 182, 187, 199).

[150] G. Di Filippo et al. "Plasmon resonant (e, 2e) spectroscopy on Be(0001)". In: *Phys. Rev. B* 94.155422 (2016) (cit. on pp. 36, 162, 182).

[151] J. Kirschner, O. M. Artamonov, and S. N. Samarin. "Angle Resolved Energy Correlated Coincidence Electron Spectroscopy of Solid Surfaces". In: *Phys. Rev. Lett.* 75.12 (1995), pp. 2424–2427 (cit. on p. 36).

[152] R. Feder et al. "Low-energy $(e, 2e)$ spectroscopy from the W(001) surface: Experiment and theory". In: *Phys. Rev. B* 58 (24 1998), pp. 16418–16431. DOI: 10.1103/PhysRevB.58.16418. URL: https://link.aps.org/doi/10.1103/PhysRevB.58.16418 (cit. on p. 36).

[153] S. Iacobucci et al. "Reflection (e,2e) experiments: a novel surface spectroscopy". In: *J. Electron Spectrosc. Relat. Phen.* 76 (1995). Proceedings of the Sixth International Conference on Electron Spectroscopy, pp. 109 –114. DOI: https://doi.org/10.1016/0368-2048(95)02508-1. URL: http://www.sciencedirect.com/science/article/pii/0368204895025081 (cit. on pp. 37, 40, 41).

[154] A. Liscio et al. "Two-step-wise interpretation of highly asymmetric, grazing angle (e,2e) on solids: A real momentum spectroscopy for surfaces and overlayers". In: *Phys. Rev. B* 77.085116 (2008). DOI: 10.1103/PhysRevB.77.085116 (cit. on pp. 37, 40–44, 163, 164, 168, 201).

[155] S. Samarin et al. "Emission of correlated electron pairs from Au(111) and Cu(111) surfaces under low-energy electron impact: Contribution of surface states, d-states and spin effects". In: *J. Electron Spectrosc. Relat. Phen.* 198 (2015), pp. 26–30 (cit. on p. 37).

[156] A. Morozov et al. "Spin-correlation imaging of electrons in ferromagnets". In: *Phys. Rev. B* 65 (10 2002), p. 104425. DOI: 10.1103/PhysRevB.65.104425. URL: https://link.aps.org/doi/10.1103/PhysRevB.65.104425 (cit. on p. 37).

[157] S. Samarin et al. "Spin-orbit coupling in tungsten by spin-polarized two-electron spectroscopy". In: *Phys. Rev. B* 70 (7 2004), p. 073403. DOI: 10.1103/PhysRevB.70.073403. URL: https://link.aps.org/doi/10.1103/PhysRevB.70.073403 (cit. on p. 37).

[158] F. O. Schumann et al. "Spin-Resolved Mapping of Spin Contribution to Exchange-Correlation Holes". In: *Phys. Rev. Lett.* 104 (2010), p. 087602 (cit. on p. 37).

[159] A. S. Kheifets et al. "Mechanism of the low-ejection-energy (e,2e) reaction on a graphite surface". In: *Phys. Rev. B* 57.12 (1998) (cit. on pp. 37, 40, 59, 163, 164, 171, 176, 177, 180, 181).

[160] O. M. Artamonov, S. N. Samarin, and J. Kirschner. "(e,2e) electron spectroscopy of surfaces". In: *Appl. Phys. A* 65 (1997), pp. 535–542 (cit. on pp. 40, 41).

[161] S. Iacobucci et al. "On the ionisation mechanism of reflection (e,2e) events". In: *AIP Conference Proceedings* 360 (1996), p. 825. DOI: 10.1063/1.49766 (cit. on p. 41).

[162] S. Iacobucci et al. "Fully resolved kinematics of grazing-incidence (e,2e) experiments". In: *Surf. Sci.* 454–456 (2000), pp. 1026–1030 (cit. on p. 41).

[163] W. Steinmann. "Optical Plasma Resonances in Solids". In: *Phys. Stat. Sol.* 28.437 (1968) (cit. on p. 47).

[164] K. A. Kouzakov and J. Berakdar. "Plasmon-assisted electron-electron collisions at metallic surfaces". In: *Phys. Rev. A* 85 (2012), p. 022901 (cit. on pp. 48, 49, 124, 162, 183, 188, 189, 192).

[165] J. Lindhard. "On the properties of a gas of charged particles". In: *Mat. Fys. Medd. Dan. Vid.* 28.8 (1954), pp. 1–57 (cit. on p. 48).

[166] H. Ibach. *Physics of Surfaces and Interfaces*. first. Springer, 2006. ISBN: 3540347097 (cit. on pp. 54, 65).

[167] Hans Lüth. "Preparation of Well-Defined Surfaces, Interfaces and Thin Films". In: *Solid Surfaces, Interfaces & Thin Films*. Berlin, Heidelberg: Springer, 2010, pp. 29–65. ISBN: 978-3-642-13592-7. DOI: 10.1007/978-3-642-13592-7_2. URL: https://doi.org/10.1007/978-3-642-13592-7_2 (cit. on pp. 54, 55, 137).

[168] Christopher C. Davis John H. Moore and Michael A. Coplan. *Building Scientific Apparatus*. Cambridge: Cambridge University Press, 2009. ISBN: 978–0–521–87858–6 (cit. on p. 54).

[169] Dr. Walter Umrath. *Grundlagen der Vakuumtechnik*. Bonner Strasse 498, Köln, Deutschland: Leybolb Oerlikon (cit. on p. 54).

[170] L. A. Gonzalez et al. "The secondary electron yield of noble metal surfaces". In: *AIP Advances* 7 (2017), p. 115203 (cit. on pp. 54, 125).

[171] Hiroshi Watanabe, Katsuo Takahashi, and Masaya Iwaki. "Structural characterization of ion implanted HOPG and glass-like carbon by laser Raman spectroscopy". In: *Nuclear Instruments and Methods in Physics Research Section B: Beam Interactions with Materials and Atoms* 80-81 (1993), pp. 1489 –1493. DOI: https://doi.org/10.1016/0168-583X(93)90827-S. URL: http://www.sciencedirect.com/science/article/pii/0168583X9390827S (cit. on p. 55).

[172] Vincent B. Crist. "Argon Implanted into Graphite, by XPS". In: *Surface Science Spectra* 1.4 (1992), pp. 376–380. DOI: 10.1116/1.1247636 (cit. on p. 55).

[173] Cedric J. Powell et al., eds. KLUWER ACADEMIC PUBLISHERS, 2002. ISBN: 0–306–45887–X (cit. on pp. 55, 61).

[174] T E. Madey A W. Czanderna and Cedric J. Powell. Plenum Press, New York, NY, 1998 (cit. on p. 55).

[175] Omer Sise et al. "Novel and traditional fringing field correction schemes for the hemispherical analyser: comparison of first-order focusing and energy resolution". In: *Meas. Sci. Technol.* 18.7 (2007), p. 1853. URL: http://stacks.iop.org/0957-0233/18/i=7/a=009 (cit. on pp. 56, 94).

[176] E. M. Metodiev et al. "Fringe electric fields of flat and cylindrical deflectors in electrostatic charged particle storage rings". In: *Phys. Rev. ST Accel. Beams* 17 (7 2014), p. 074002. DOI: 10.1103/PhysRevSTAB.17.074002. URL: https://link.aps.org/doi/10.1103/PhysRevSTAB.17.074002 (cit. on p. 56).

[177] Alessandra Bellissimo. "I would like to thank my colleagues from the Technical Univesity of Vienna, Wolfgang Werner and Vytautas Astašauskas for having provided me with these grids." Thanking Note. 2018 (cit. on p. 56).

[178] Agar Scientific. *Data Sheet AGG303: Colloidal Graphite - Aquadag.* 2010 (cit. on pp. 57, 62).

[179] A. liscio. "Spettroscopie di coincidenza elettrone-elettrone per lo studio di superfici ad incidenza radente". PhD thesis. Università degli Studi Roma Tre, 1993 (cit. on p. 57).

[180] P. Costa Pinto et al. *Carbon Coating of the SPS Dipole Chambers.* Tech. rep. Geneva: CERN, 2015. URL: https://cds.cern.ch/record/1567024/files/arXiv:1308.1305.pdf (cit. on p. 58).

[181] R. C. Tatar and S. Rabii. "Electronic properties of graphite: A unified theoretical study". In: *Phys. Rev. B* 25 (6 1982), pp. 4126–4141. DOI: 10.1103/PhysRevB.25.4126. URL: https://link.aps.org/doi/10.1103/PhysRevB.25.4126 (cit. on pp. 59, 166).

[182] D. D. L.Chung. "Review Graphite". In: *J. Mat. Sci.* 37 (2002), pp. 1–15 (cit. on p. 59).

[183] V. Pantin et al. "Electronic properties of high oriented pyrolitic graphite: Recent discoveries". In: *J. Phys. Chem. Solids.* 67 (2006), pp. 546–551 (cit. on pp. 59, 60).

[184] P. R. Wallace. "The Band Theory of Graphite". In: *Phys. Rev.* 71 (1947), p. 622 (cit. on p. 59).

[185] R. F. Willis, B. Fitton, and G. S. Painter. "Secondary-electron emission spectroscopy and the observation of high-energy excited states in graphite: Theory and experiment". In: *Phys. Rev. B* 9 (4 1974), pp. 1926–1937. DOI: 10.1103/PhysRevB.9.1926. URL: https://link.aps.org/doi/10.1103/PhysRevB.9.1926 (cit. on pp. 59, 151, 175, 176).

[186] F. Maeda et al. "Unoccupied-electronic-band structure of graphite studied by angle-resolved secondary-electron emission and inverse photoemission". In: *Phys. Rev. B* 37 (9 1988), pp. 4482–4488. DOI: 10.1103/PhysRevB.37.4482. URL: https://link.aps.org/doi/10.1103/PhysRevB.37.4482 (cit. on pp. 59, 108, 123, 153, 156, 157).

[187] A. K. Solanki et al. "Band structure and optical properties of graphite". In: *Solid State Commun.* 100.9 (1996), pp. 645–649 (cit. on p. 59).

[188] A. G. Marinopoulos et al. "Ab initio study of the optical absorption and wave-vector-dependent dielectric response of graphite". In: *Phys. Rev. B* 69 (24 2004), p. 245419. DOI: 10.1103/PhysRevB.69.245419. URL: https://link.aps.org/doi/10.1103/PhysRevB.69.245419 (cit. on pp. 59, 155, 166).

[189] S. K. Mahatha, S. Menon S. R. Krishnakumar, and T. Balasubramanian. "Unoccupied electronic structure of graphite probed by angle-resolved photoemission spectroscopy". In: *Phys. Rev. B* 84 (11 2011), p. 113106. DOI: 10.1103/PhysRevB.84.113106. URL: https://link.aps.org/doi/10.1103/PhysRevB.84.113106 (cit. on p. 59).

[190] Preben J. Møller and Mohamed H. Mohamed. "An experimental study of the energy dependence of the total yield due to the incidence of low- energy electrons onto graphite surfaces". In: *JPC* 15.6 (1982), pp. 6457–6462 (cit. on pp. 59, 108, 130, 156).

[191] L. Papagno et al. "Graphite: Electronic and structural properties studied by electron-energy-loss and secondary-electron-emission spectroscopy". In: *prb* 26 (Aug. 1982), pp. 2320–2322. DOI: 10.1103/PhysRevB.26.2320 (cit. on pp. 59, 108, 156).

[192] U. Diebold et al. "Angle resolved electron energy loss spectroscopy on graphite". In: *Surf. Sci.* 197 (3 1987), pp. 430–443 (cit. on pp. 59, 165).

[193] I. Schäfer, M. Schlüter, and M. Skibowski. "Conduction-band structure of graphite studied by combined angle-resolved inverse photoemission and target current spectroscopy". In: *Phys. Rev. B* 35.14 (1987) (cit. on pp. 59, 130, 153, 163).

[194] A. Hoffman, R. Brener, and C. Cytermann. "Extended fine structure in the secondary electron emission spectra of graphite and glassy carbon". In: *Surf. Interface Anal.* 22.1–12 (), pp. 590–593. DOI: 10.1002/sia.7402201125. eprint: https://onlinelibrary.wiley.com/doi/pdf/10.1002/sia.7402201125. URL: https://onlinelibrary.wiley.com/doi/abs/10.1002/sia.7402201125 (cit. on pp. 59, 108, 156).

[195] A. Ruocco et al. "Scattering mechanism of electrons interacting with surfaces in specular reflection geometry: Graphite". In: *Phys. Rev. B* 59.20 (1999), pp. 13359–13364 (cit. on pp. 59, 136, 148, 177).

[196] V. N. Strocov et al. "Three-dimensional unoccupied band structure of graphite: Very-low-energy electron diffraction and band calculations". In: *Phys. Rev. B* 61 (2000), pp. 4994–5001. DOI: 10.1103/PhysRevB.61.4994 (cit. on pp. 59, 60, 130, 134).

[197] Kenneth W. Shung. "Dielectric function and plasmon structure of stage-1 intercalated graphite". In: *Phys. Rev.* B34 (1986), p. 979 (cit. on pp. 59, 163).

[198] Bojana Visič et al. "Optical properties of exfoliated MoS_2 coaxial nanotubes - analogues of graphene". In: *Nanoscale Research Letters* 6 (2011), p. 593 (cit. on p. 59).

[199] Gao C. et al. "Spectral momentum density of graphite from (e,2e) spectroscopy: Comparison with first-principles calculation." In: *Phys. Rev. B* 37(8) (1988), pp. 3914–3923 (cit. on pp. 59, 171).

[200] A. S. Kheifets and M. Vos. "Spectral electron momentum density calculations in graphite". In: *J. Phys.-Condens. Mat.* 7 (1995), pp. 3895–3904 (cit. on pp. 59, 163, 166, 171, 176, 177, 180, 181).

[201] S. Rioual et al. "Momentum distribution and valence-band reconstruction in graphite by grazing incidence (e,2e) spectroscopy". In: *Phys. Rev. B* 57.4 (1998), p. 0 (cit. on pp. 59, 163, 164, 168, 175).

[202] R. Klucker, M. Skibowski, and W. Steinmann. "Anysotropy in the Optical Transitions from the π and σ Valence Bands of Graphite". In: *physica status solidi (b)* 65.2 (1974), pp. 703–710. DOI: 10.1002/pssb.2220650230. URL: https://onlinelibrary.wiley.com/doi/abs/10.1002/pssb.2220650230 (cit. on pp. 59, 151, 155).

[203] S. Bose et al. In: *New J. Phys.* 12 (2010), p. 023028 (cit. on pp. 60, 157).

[204] M. Pisarra et al. "Unoccupied electronic states of few-layer graphene". In: *arXiv* (2018), pp. 1–19 (cit. on pp. 60, 157, 158).

[205] Gregory A. Fiete and Eric J. Heller. "Colloquium: Theory of quantum corrals and quantum mirages". In: *Rev. Mod. Phys.* 75 (3 2003), pp. 933–948. DOI: 10.1103/RevModPhys.75.933. URL: https://link.aps.org/doi/10.1103/RevModPhys.75.933 (cit. on pp. 60, 74).

[206] I. E. Tamm. "On the possible bound states of electrons on a crystal surface". In: *Phys. Zs. Sowjetunion* 1 (1932), p. 733 (cit. on p. 60).

[207] W. Shockley. "On the Surface States Associated with a Periodic Potential". In: *Phys. Rev.* 56.4 (1939), p. 317 (cit. on p. 61).

[208] H. W. B. Skinner. "The soft x-ray spectroscopy of the solid state". In: *Reports on Progress in Physics* 5.1 (1938), p. 257. URL: http://stacks.iop.org/0034-4885/5/i=1/a=323 (cit. on p. 66).

[209] Walter A. Harrison. "Band Structure of Aluminum". In: *Phys. Rev.* 118 (5 1960), pp. 1182–1189. DOI: 10.1103/PhysRev.118.1182. URL: https://link.aps.org/doi/10.1103/PhysRev.118.1182 (cit. on p. 66).

[210] G. V. Hansson and S. A. Flodström. "Photoemission from surface states and surface resonances on the (100), (110) and (111) crystal faces of aluminium". In: *Phys. Rev. B* 18.4 (Aug. 1978) (cit. on pp. 66, 67, 109).

[211] Harry J. Levinson, F. Greuter, and E. W. Plummer. "Experimental band structure of aluminum". In: *Phys. Rev. B* 27 (2 1983), pp. 727–747. DOI: 10.1103/PhysRevB.27.727. URL: https://link.aps.org/doi/10.1103/PhysRevB.27.727 (cit. on p. 66).

[212] H. Ehrenreich, H. R. Philipp, and B. Segall. "Optical Properties of Aluminum". In: *Phys. Rev.* 132 (5 1963), pp. 1918–1928. DOI: 10.1103/PhysRev.132.1918. URL: https://link.aps.org/doi/10.1103/PhysRev.132.1918 (cit. on pp. 66, 67, 141).

[213] M. I. Marković and A. D. Rakić. "Determination of optical properties of aluminium including electron reradiation in the Lorentz-Drude model". In: *Optics & Laser Technology* 22.6 (1990), pp. 394 –398. DOI: https://doi.org/10.1016/0030-3992(90)90093-J. URL: http://www.sciencedirect.com/science/article/pii/003039929090093J (cit. on p. 66).

[214] W. S. M. Werner, K. Glantschnig, and C. Ambrosch-Draxl. "Optical Constants and Inelastic Electron-Scattering Data for 17 Elemental Metals". In: *J. Phys. Chem. Ref. Data* 38.4 (2009), pp. 1013–1092 (cit. on pp. 66, 68).

[215] Alessandra Bellissimo. "I would like to thank my colleagues from TUV (in particular Wolfgang S. M. Werner) who made available the BRUCE library by means of which it was possible to access to a series of data, e.g. collected optical data from Palik, which were used to produce this plot." Thanking Note Nr.2. 2019 (cit. on p. 69).

[216] G. I. Kanel et al. "Dynamic yield and tensile strength of aluminum single crystals at temperatures up to the melting point". In: *Journal of Applied Physics* 90.1 (2001), pp. 136–143. DOI: 10.1063/1.1374478. eprint: https://doi.org/10.1063/1.1374478. URL: https://doi.org/10.1063/1.1374478 (cit. on p. 68).

[217] Alessandra Bellissimo. "Electron Induced Secondary Electron Emission Studies of Polycrystalline Aluminium and various Carbon Allotropes by Means of (e,2e)-Coincidence Spectroscopy". Diploma thesis. Technische Universität Wien, 2014 (cit. on pp. 73, 124, 162–165, 188).

[218] B. Henrist et al. "The Variation of the Secondary Electron Yield and of the Desorption Yield of Copper under Electron Bombardment: Origin and Impact on the Conditioning of the LHC". In: *Proceeding of EPAC 2002* (2002) (cit. on p. 74).

[219] E. Rudberg and J. C. Slater. "Theory of Inelastic Scattering of Electrons from Solids". In: *Phys. Rev.* 50 (2 1936), pp. 150–158. DOI: 10.1103/PhysRev.50.150. URL: https://link.aps.org/doi/10.1103/PhysRev.50.150 (cit. on p. 74).

[220] J. L. Robins and J. B. Swan. "Characteristic Electron Energy Loss Spectra of the Transition Metals, Ti to Cu". In: *Proceedings of the Physical Society* 76.6 (1960), p. 857. URL: http://stacks.iop.org/0370-1328/76/i=6/a=306 (cit. on p. 74).

[221] C. J. Powell. "The Origin of the Characteristic Electron Energy Losses in Ten Elements". In: *Proceedings of the Physical Society* 76.5 (1960), p. 593. URL: http://stacks.iop.org/0370-1328/76/i=5/a=301 (cit. on p. 74).

[222] F. Forstmann and J. B. Pendry. "Surface States on *d*-Band Metals". In: *Z. Phys.* 235 (1970), pp. 75–84 (cit. on p. 74).

[223] P. Heimann et al. "*d*-like surface-state bands on Cu(100) and Cu(111) observed in angle-resolved photoemission spectroscopy". In: *Phys. Rev. B* 20 (8 1979), pp. 3059–3066. DOI: 10.1103/PhysRevB.20.3059. URL: https://link.aps.org/doi/10.1103/PhysRevB.20.3059 (cit. on p. 74).

[224] Armando Euceda, D. M. Bylander, and Leonard Kleinman. "Self-consistent electronic structure of 6- and 18-layer Cu(111) films". In: *Phys. Rev. B* 28 (2 1983), pp. 528–534. DOI: 10.1103/PhysRevB.28.528. URL: https://link.aps.org/doi/10.1103/PhysRevB.28.528 (cit. on p. 74).

[225] H. Eckardt, L. Fritsche, and Noffke J. "Self-consistentrelativistic band structure of the noble metals". In: *J. Phys. F: Met. Phys.* 4 (1984), pp. 97–112 (cit. on pp. 75, 76).

[226] S. A. Kolomov and L. T. Chadderton. "Total Current Spectroscopy". In: *Surf. Sci.* 90 (1979), pp. 359–380 (cit. on pp. 77, 80, 130).

[227] Kimball Physics Inc. *Electron Source ELG-2 / EGPS-1022*. 2010. URL: https://scilab.co.jp/product/vacuum/download/elg_2_2.pdf (cit. on pp. 79, 83, 126).

[228] "CRC Handbook of Chemistry and Physics: A Ready-Reference of Chemical and Physical Data". In: *Journal of the American Chemical Society* 127.12 (2005). Ed. by David R. Lide, pp. 4542–4542. DOI: 10.1021/ja041017a. eprint: https://doi.org/10.1021/ja041017a. URL: https://doi.org/10.1021/ja041017a (cit. on pp. 82, 87, 133, 141, 143).

[229] Hans Lüth. "Scattering from Surfaces and Thin Films". In: *Solid Surfaces, Interfaces & Thin Films*. Berlin, Heidelberg: Springer, 2010, pp. 133–213. ISBN: 978-3-642-13592-7. DOI: 10.1007/978-3-642-13592-7_4. URL: https://doi.org/10.1007/978-3-642-13592-7_4 (cit. on pp. 85, 130).

[230] Masashi Shiraishi and Masafumi Ata. "Work function of carbon nanotubes". In: *MRS Proceedings* 633 (2000), A4.4. DOI: 10.1557/PROC-633-A4.4 (cit. on p. 88).

[231] Giovanni Stefani. *Appunti su Analisi di Particelle Cariche*. Teaching notes. 2016 (cit. on p. 91).

[232] R E Imhof, A Adams, and G C King. "Energy and time resolution of the 180 degrees hemispherical electrostatic analyser". In: *Journal of Physics E: Scientific Instruments* 9.2 (1976), pp. 138–142. DOI: 10.1088/0022-3735/9/2/024. URL: https://doi.org/10.1088%2F0022-3735%2F9%2F2%2F024 (cit. on p. 94).

[233] Omer Sise and Theo J. M. Zouros. "Position, Energy, and Transit Time Distributions in a Hemispherical Deflector Analyzer with Position Sensitive Detector". In: *Journal of Spectroscopy* (2015) (cit. on p. 94).

[234] Damiano Sbaraglia. *SIMION Simulations for the electron optical elements in R66*. Report on SIMION simulations for the electron optical elements in R66. 2011 (cit. on p. 95).

[235] Andrea Fondacaro. *Riassunto ELPHOS*. Report on the first test experiments performed employing R66, formerly known as "ELPHOS" analyser. 2002 (cit. on p. 95).

[236] Hamamatsu Photonics K. K. *MCP (Microchannel plate) and MCP assembly*. URL: https://www.hamamatsu.com/resources/pdf/etd/MCP_TMCP0002E.pdf (cit. on p. 95).

[237] RoentDek Handels GmbH. *MCP Delay Line Detector Manual* (cit. on p. 95).

[238] Elettra Sincrotrone Trieste. *THR–02–ST Advanced 4–channel time converter*. Sincrotrone Trieste S.C.p.A. Strada Statale 14 - km 163.5 in AREA Science Park; 34149 Basovizza; Trieste Italy (cit. on p. 96).

[239] Marco Sbroscia. *Software di acquisizione dalla elettronica THR02-ST*. Report on SW for (e,2e)-coincidence acquisition. 2016 (cit. on p. 97).

[240] Alessandra Bellissimo. *Software for planning and evaluating an (e,2e)-coincidence experiment*. FORTRAN code for the calculation of the kinematics, for the prediction of the flight-times and for the evaluation of an (e,2e)-coincidence experiments. Università degli Studi Roma Tre, Dipartimento di Scienze, 2017 (cit. on pp. 101, 116, 170, 171).

[241] G. Stefani, L. Avaldi, and R. Camilloni. *Electron Correlation in ionization and related coincidence techniques*. New York : Kluwer Academic/Plenum Publishers, pp. 161–187 (cit. on pp. 101, 103).

[242] E. Harting and F. H. Read. *Electrostatic Lenses*. Amsterdam, Oxford, New York: Elsevier Scientific Publishing Company, 1976 (cit. on p. 106).

[243] P. Riccardi et al. "Secondary electron emission spectra from clean and cesiated Al surfaces: the role of plasmon decay and data analysis for applications". In: *Journal of Physics: Condensed Matter* 22.30 (2010), p. 305004. URL: http://stacks.iop.org/0953-8984/22/i=30/a=305004 (cit. on pp. 109, 185).

[244] R. Khalid. "Secondary electron emission studied by Secondary electron electron energy loss coincidence spectrometry (SE2ELCS)". PhD thesis. Technische Universität Wien, 2013 (cit. on pp. 124, 162).

[245] A. Dittmar-Wituski, M. Naparty, and J. Skonieczny. "Angle-dependent total current spectroscopy of graphite surfaces of various anisotropy". In: *J. Phys. C: Solid State* 18.12 (1985), p. 2563. URL: http://stacks.iop.org/0022-3719/18/i=12/a=017 (cit. on pp. 126, 127).

[246] A. Dittmar-Wituski, M. Naparty, and J. Skonieczny. "Simple method for simultaneous measurement of work function changes and electron reflectivity variation". In: *Journal of Physics E: Scientific Instruments* 17.12 (1984), p. 1139. URL: http://stacks.iop.org/0022-3735/17/i=12/a=015 (cit. on p. 130).

[247] I. Bartoš. "ELECTRONIC STRUCTURE OF CRYSTALS VIA VLEED". In: *Prog. Surf. Sci.* 59.1-4 (1998), pp. 197–206 (cit. on p. 130).

[248] G. Capart. "Band structure calculations of low energy electron diffraction at crystal surfaces". In: *Surface Science* 13.2 (1969), pp. 361 –376. DOI: https://doi.org/10.1016/0039-6028(69)90197-6. URL: http://www.sciencedirect.com/science/article/pii/0039602869901976 (cit. on p. 130).

[249] A. Howie. “Problems of interpretation in high resolution electron microscopy”. In: *J. Microsc.* 129.2 (1982), pp. 239–251 (cit. on p. 131).

[250] R. Eckhardt. “Stan Ulam, John von Neumann, and the Monte Carlo method”. In: *Los Alamos Science* (1987). Special issue, pp. 131–141 (cit. on pp. 143, 144).

[251] Bouchard C. and Carette J. D. “The surface potential barrier in secondary emission from semiconductors”. In: *Surface Science* 100 (1980), pp. 251–268. DOI: 10.1016/0039-6028(80)90456-2 (cit. on p. 152).

[252] Kevin Jensen. *Advances in Imaging and Electron Physics*. Ed. by Peter Hawkes. first. Vol. 149. Academic Press, 2007. ISBN: 9780123742070 (cit. on p. 152).

[253] C. T. Whelan et al. *New directions in Atomic Physics*. Kluwer Academic/Plenum Publishers, 1999. ISBN: 0306461811 (cit. on p. 160).

[254] C. V. von Koch. “Evidence of plasmons in secondary electron emission spectra”. In: *Phys. Rev. Lett.* 25.12 (1970), pp. 792–794 (cit. on p. 182).

[255] Alessandra Bellissimo. “I would like to thank my colleague Olga Ridzel for her Matlab expertise which has helped to re-order the data to produce this surface plot.” Thanking Note Nr.1. 2018 (cit. on p. 184).

[256] Léon Van Hove. “The Occurrence of Singularities in the Elastic Frequency Distribution of a Crystal”. In: *Phys. Rev.* 89 (6 1953), pp. 1189–1193. DOI: 10.1103/PhysRev.89.1189. URL: https://link.aps.org/doi/10.1103/PhysRev.89.1189 (cit. on p. 187).

[257] V. G. Levin, V. G. Neudachin, and Yu. F. Smirnov. “On Investigation of the Structure of Energy Bands Using Quasielastic Knock-Out of an Electron by an Electron (e, 2e)”. In: *Phys. Stat. Sol. (b)* 49 (1972), p. 489 (cit. on p. 187).

[258] C. J. Tung et al. “Differential cross sections for plasmon excitations and reflected electron-energy-loss spectra”. In: *Phys. Rev. B* 49.23 (1994), pp. 16684–16692 (cit. on p. 190).

[259] Wolfgang S.M. Werner. “Surface and bulk plasmon coupling observed in reflection electron energy loss spectra”. In: *Surf. Sci.* 526.3 (2003), pp. L159 –L164. DOI: https://doi.org/10.1016/S0039-6028(02)02684-5. URL: http://www.sciencedirect.com/science/article/pii/S0039602802026845 (cit. on p. 190).

List of Tables

List of Figures

Curriculum Vitae

Alessandra Bellissimo, Physicist, Dipl.-Ing.

Information
address: Via Posillipo 66, Viale Costa, Villino "Consiglia" cap. 80123 Naples, Italy
mobile: +39 (345) 432 5019 *(temporary)*
skype: bellissimo.alessandra
email (1): bellissimo.alessandra@gmail.com
email (2): bellissimo@fis.uniroma3.it *(temporary)*
Place of Birth: Naples, Italy
Date of Birth: 11.05.1982
Nationality: Italian & British

Languages
Italian mother tongue
German mother tongue
English full functional proficiency
French general functional proficiency

Personal Skills

initiative & self-sufficiency; curiosity & problem solving; detail-oriented & logic
collaborative & helping; team player & leader; direct/easy-going communication
organisation & management; responsibility & self-awareness
adaptability & flexibility; preciseness & punctuality

Technical Skills

Handling of UHV-technology, Analysers & Detectors, Electron Optics, Electronics.
surface analysis techniques : EELS, XPS, UPS, (e,2e), TEY & SEY, LEED.
surface preparation : sputtering & annealing

IT-skills

FORTRAN: ⋆⋆⋆⋆; Gnuplot: ⋆⋆⋆⋆;
Bash & Awk ⋆⋆⋆; LabView: ⋆ *(user knowledge)*; Origin: ⋆⋆

Interests

Professional:

Fundamental Mechanisms of LEEs & SEE; Investigation of Microscopic Properties of Materials; Highly interested in widening my field of expertise; Studying & Cross-linking

Personal:

if only there were some more time, I would also dabble in...

Classical Music, Art, Writing & Poetry, Photography, Travelling, Drawing & Painting, Nature, Hiking, Swimming, Cooking

... but in reality I mostly concentrate on work

Experience

Scientific Career

- **09/15 – 08/18** Early Stage Researcher (ESR) of a Marie Curie Initial Training Network (MC–ITN)of the European Commission (EC) (grant number 606988, FP7-PEOPLE-2013-ITN)

The project of "**SIMDALEE2**" (= **S**ources, **I**nteraction with **M**atter, **D**etection and **A**nalysis of **L**ow **E**nergy **E**lectrons 2; www.simdalee2.net) is a research and training network dedicated to the investigation of Low Energy Electrons (**LEEs**) near surfaces. My research focusses onto the investigation of the fundamental mechanisms of interaction of LEEs with solids leading to the creation and ejection Secondary Electrons (**SEs**). Among routinely used electron spectroscopic techniques, such as X-ray Photoelectron Spectroscopy (**XPS**), Electron Energy Loss Spectroscopy (**EELS**), Ultra-Violet PES or **UPS** and **Auger** spectroscopy, in my research I make use of **(e,2e)-coincidence** spectroscopy, performed in the laboratories of University of Roma Tre and of the Technical University of Vienna. Furthermore, I have been measuring the Total/Secondary Electron Yield (**TEY**/**SEY**) of several materials, ranging from single crystalline targets to their polycrystalline or amorphous counterparts, by using experimental techniques available in the laboratories of the Vacuum Surfaces and Coatings (VSC) group at CERN. The aim of these investigations, conducted by using all above-listed electron spectroscopic techniques, is to disentangle the different mechanisms making up the TEY and to study into depth the fundamental microscopic properties relevant to the yield of SEs in a material.

Experience & **Competences:**

- Operation of Ultra-High-Vacuum & Surface Analysis instrumentation
- Experience in assembling, commissioning and calibrating Electron Analysers (Hemispherical Electron Analyser (HMA) & Time-of-Flight spectrometer (TOF))
- Knowledge of Materials & Surface Preparation Techniques for UHV-environment
- Surface characterisation by a variety of Electron Spectroscopic Techniques *(as mentioned above)*
- Planning and running of complex experiments
- Data Analysis & interpretation
- Writing software to analyse experimental data
- Solving of problems (hardware, software and of organisational nature)

– Writing scientific reports

The know-how listed above has been acquired over a period of *6 years* I spent working towards both Dipl.-Ing. and PhD.

Previous Non-Scientific Experiences

2003 – 2009 **Owner** & **Manager of a gastronomic business** in Vienna, Austria
(during interruption of university curriculum)

Founded and successfully ran a small restaurant and ice-cream place with the collaboration of a partner. After this experience, from which I gained many organisational, management and economic skills I returned to my academic education.

Education

- **30/11/18 – now** PhD thesis *(approved by external referees in January 2019)*
- **09/15 – 08/18** Doctoral School in Material Sciences, Nanotechnology and Complex Systems; Università degli Studi Roma Tre, Dipartimento di Scienze, Via della Vasca Navale 84, I–00146, Rome, Italy

---

During the past three years, the objective of my research was focussed on the investigation of the fundamental mechanisms relevant to the generation-ejection of SEs from solids under electron bombardment. To this end several spectroscopic techniques were employed, each one of which investigating a different aspect of the SEE-phenomenon, thus revealing different processes yielding SEs in a material, setting a particular emphasis on the low-energy impact range. Acquisition of differential-cross sections (DCS) with an increasing degree of differentiation – ranging from TEY measurements, double-differential cross-sections (2DCS) obtained by means of EELS and SEES, as well as triple-differential CS (TDCS) obtained by means of electron pair spectroscopy or (e,2e). This comprehensive investigation has led to the disentanglement of the elementary processes that need to be accounted for the understanding of the SE-generation probability, that fully take into account both energy and momentum conservation in the collision and the band structure of the solid, furthermore identifying the mostly relevant excitation and relaxation channels inducing generation and emission of SEs. The PhD work was furthermore embedded in an international and interdisciplinary context, such as the one offered by the ITN-project of SIMDALEE2 which provided me with a broad scientific perspective on the matter.

- **2001 – 2002** & **2009 – 2014** Diplom Ingegneur (Dipl.-Ing or MSc)
Technische Universität Wien, Institut für Angewandte Physik, Wiedner Hauptstraße 8–10/134, A–1040 Vienna, Austria

---

I obtained my degree – after 6 years of interruption (see section "Non-Scientific Experiences") – with a university curriculum mostly oriented towards solid state Physics. I pursued my experimental thesis work, entitled **"Electron Induced Secondary Electron Emission Studies of Polycrystalline Aluminium**

and various Carbon Allotropes by Means of (e,2e)-Coincidence Spectroscopy", from 2013 – 2014. The main objective of this thesis was to investigate the phenomenon of SEE in well-known materials, such as Al and various C-allotropes. By means of various electron spectroscopic techniques, among which also (e,2e)-coincidence spectroscopy, it was possible to identify relevant excitation processes involved in the creation-ejection mechanisms of these SEs.

- **1998 – 2001** Secondary school degree (Matura), Bundes Real Gymnasium Perchtoldsdorf, (Vienna) Austria
  Secondary school with emphasis on scientific subjects.

- 1992 – 1998 Secondary school, Centro Scolastico Belforte, Naples, Italy
  Multilingual secondary school.

Schools & Training

2015 **XIII SILS School on Synchrotron Radiation:** *Fundamentals, Methods and Applications* Grado (Italy), September 14–25; **url:** XIII SILS
Participation and attendance of lectures and poster presentation.

Publications

- *Phys.Rev. B* **88** 201407(**R**), 2013
  Secondary-electron emission induced by in vacuo surface excitations near a polycrystalline Al surface; Wolfgang S.M. Werner, Francesc Salvat-Pujol, Alessandra Bellissimo, Rahila Khalid, Werner Smekal, Mihály Novák, Alessandro Ruocco and Giovanni Stefani
  doi: https://link.aps.org/doi/10.1103/PhysRevB.88.201407
- *Surface Science* **635** Suppl. C, L1 – L3 (2015)
  Reflection electron energy loss spectrum of single layer graphene measured on a graphite substrate; Wolfgang S.M. Werner, Alessandra Bellissimo, Roland Leber, Afshan Ashraf and Silvina Segui
  doi: https://doi.org/10.1016/j.susc.2014.12.016
- *Journal of Electron Spectroscopy (submitted 2018)*
  Secondary Electron Generation Mechanisms in Carbon Allotropes at Low Impact Electron Energies; Alessandra Bellissimo, Gian Marco Pierantozzi, Alessandro Ruocco, Giovanni Stefani, Olga Yu. Ridzel, Vytautas Astašauskas, Wolfgang S.M. Werner, Mauro Taborelli
- *Journal of Electron Spectroscopy (submitted 2018)*
  Optical and Electronic properties of amorphous Silicon Dioxide by single and double electron spectroscopy; Vytautas Astašauskas, Alessandra Bellissimo, Pavel Kuksa, Christian Tomastik, Henryk Kalbe and Wolfgang S.M. Werner

Contributions to International Conferences

- 2017 **oral** **FisMat 2017**, ICTP, Trieste (Italy), October 1–6; **url:** fismat2017
  A. Bellissimo, A. Ruocco, M. Sbroscia, G.M. Pierantozzi, F. Offi, S. Iacobucci and G. Stefani;
  Title: *Mastering the low energy secondary electron emission from single crystal surfaces by plasmons excitations*
- 2017 **oral** **SIMDALEE 2017**, Hotel Flamingo, Pula (Italy), September 18–22; **url:** simdalee2017
  A. Bellissimo, A. Ruocco, M. Sbroscia, S. Iacobucci, G.M. Pierantozzi and G. Stefani
  Title: *On the relevance of plasmon assisted generation of secondary electrons*
- 2017 **poster** **SIMDALEE 2017**, Hotel Flamingo, Pula (Italy), September 18–22; **url:** simdalee2017
  A. Bellissimo, G. Stefani, H. Neupert and M. Taborelli
  Title: *Unraveling relevance of the different electron generation mechanisms to the Total Electron Yield (TEY)*
- 2017 **poster** **ElCoGS 2017**, Università Roma Tre, Rome (Italy), July 8–9; **url:** ElCoGS17
  A. Bellissimo, A. Ruocco, M. Sbroscia, G.M. Pierantozzi, F. Offi, S. Iacobucci and G. Stefani
  Title: *(e,2e)-spectroscopy as discriminatory tool: disentangling relevant SEE-mechanisms in Aluminium*
- 2017 **oral** **XXIII AIV Conference**, Convitto della Calza, Florence (Italy), April 4–7; **url:** XXIII AIV
  A. Bellissimo, H. Neupert, G. Stefani and M. Taborelli
  Title: *Carbon Allotropes Secondary Electron Emission: Can we reliably measure it?*
- 2016 **oral** **16^{th} Joint Vacuum Conference (JVC16)**, Portoroz (Slovenia), June 6–10; **url:** JVC16
  A. Bellissimo, W. S.M. Werner, G. Stefani, A. Ruocco, F. Salvat-Pujol, R. Khalid, W. Smekal and M. Novák
  Title: *Benchmark Spectra for Secondary Electron Emission by Means of (e,2e)-Coincidence Spectroscopy*
- 2015 **oral** **ECASIA 2015**, Granada (Spain), September 28 – October 1; **url:** ECASIA2015
  A. Bellissimo, W. S.M. Werner, F. Salvat-Pujol, R. Khalid, W. Smekal and M. Novák, A. Ruocco and G. Stefani
  Title: *Benchmark Spectra for Secondary Electron Emission via (e,2e)-Coincidence Spectroscopy*
- 2015 **poster** **XIII SILS School**, Grado (Italy), September 14–25; **url:** XIII SILS
  A. Bellissimo, W. S.M. Werner, A. Ruocco, G. Stefani, F. Salvat-Pujol, R. Khalid, M. Novák, A. Ashraf, S. Segui and W. Smekal
  Title: *Secondary Electron Electron-Energy Loss Coincidence Spectroscopy (SE2ELCS) of Aluminum and various Carbon Allotropes*
- 2015 **oral** **LEE 2015**, Schloß Hernstein, Vienna (Austria), September 7–11; **url:** LEE 2015
  A. Bellissimo, W. S.M. Werner, F. Salvat-Pujol, R. Khalid, A. Ashraf, W. Smekal and S. Segui
  Title: *Correlation Effects in Graphitic Materials from Secondary Electron Electron-Energy Loss Coincidence Spectroscopy (SE2ELCS)*
- 2014 **invited poster** **International Symposium on Spin-Polarized Electron Physics and Nanomagnetism**, Halle (Germany), July 10–13
  A. Bellissimo, W. S.M. Werner, F. Salvat-Pujol, R. Khalid, M. Novák, W. Smekal and G. Stefani
  Title: *Electron Induced Secondary Electron Emission Studies of Polycrystalline Aluminum and various Carbon Allotropes by Means of Coincidence Spectroscopy*
- 2014 **oral** **15^{th} Joint Vacuum Conference (JVC15)**, Kaiserwasser, Vienna (Austria), June 15–18; **url:** JVC15

A. Bellissimo, W. S.M. Werner, F. Salvat-Pujol, R. Khalid, M. Novák, W. Smekal and G. Stefani
Title: *Electron Induced Secondary Electron Emission Studies of Polycrystalline Aluminum and various Carbon Allotropes by means of Coincidence Spectroscopy*

- 2014 **poster** **IR-Raman Workshop**, Technical University of Vienna (Austria), April 4–8
A. Bellissimo, W. S.M. Werner, M. Chudzicki, A. Tasneem, J. Ofner, B. Lendl
Title: *sp_2-content of carbon allotropes a comparative study using Raman- and Electron Spectroscopy*
- 2013 **poster** **71^{st} IUVSTA Workshop on Characterisation of Nanostructures by means of Electron Beam Techniques**, Schloß Hernstein, Vienna (Austria), June 24–28; **url:** IUVSTA71
A. Bellissimo, W. S.M. Werner, F. Salvat-Pujol, R. Khalid, M. Novák and G. Stefani
Title: *Secondary Electron Electron Energy Loss Coincidence Measurements of Polycrystalline Aluminium*
- 2009 **attendance of lectures** **60^{th} IUVSTA Workshop on Low Energy Spectroscopy and Simulations**, Haus der Forschung, Vienna (Austria), November 11–13
Participation and attendance of lectures

Invited Seminars

- 2017 Title: ***(e,2e) and TEY: How and Why***
ETH Zürich, Department of Physics, Zürich (Switzerland), November 22
Survey of experimental results obtained by means of different electron spectroscopy techniques for the investigation of secondary electron emission in the low-energy range.
- 2017 Title: ***(e,2e) and TEY: How and Why***
VSC-seminar at CERN, Geneva (Switzerland), August 8
Presentation of the results obtained by means of (e,2e)-coincidence spectroscopy and complementary measurements of Total Electron Yield conducted on a set of single crystal surfaces and their polycrystalline or amorphous counterpart, at CERN within a collaborative work

Organisation of Conferences

- **SIMDALEE 2017**, Hotel Flamingo, Pula (Italy), September 18–22, 2017;
url: simdalee2017
part of the organising committee
- **ElCoGS 2017**, Aula Magna, Universitá di Roma Tre, Roma (Italy), July 8–9, 2017;
url: ElCoGS17
part of the local organising committee
- **LEE 2017**, Schloß Hernstein, Vienna (Austria), September 7–11;
url: LEE 2015
part of the local organising & scientific committee
- **15^{th} Joint Vacuum Conference (JVC15)**, Kaiserwasser, Vienna (Austria), June 15–18;
url: JVC15
part of the local organising & scientific committee